



UNIVERSITÀ DI BOLOGNA "ALMA MATER STUDIORUM"

DOTTORATO DI RICERCA IN GEOFISICA  
XXIV CICLO

Settore concorsuale 04/04  
Settore scientifico disciplinare GEO/10

**Fault delineation and stress orientations  
from the analysis of background, low  
magnitude seismicity in Southern  
Apennines (Italy)**

---

**Tesi di dottorato  
Emanuela Matrullo**

**Tutore**  
Prof. R. De Matteis

**Coordinatore**  
Prof. M. Dragoni

**Supervisore**  
Dott. A. Emolo

2012



*“You've got to find what you love.  
And that is as true for your work as it is for your lovers.  
Your work is going to fill a large part of your life, and the only way  
to be truly satisfied is to do what you believe is great work.  
And the only way to do great work is to love what you do.  
If you haven't found it yet, keep looking. Don't settle.  
As with all matters of the heart, you'll know when you find it.  
And, like any great relationship, it just gets better and better as the  
years roll on. So keep looking until you find it.  
Don't settle....Stay Hungry. Stay Foolish....”*

*Steve Jobs*



# Table of Contents

Table of Contents	5
Introduction	7
<i>Chapter 1: Stress field determination</i>	
1. Introduction	13
2. Aspects of stress tensor	14
2.1 Stress tensor	15
2.2 Rock Failure and Faulting	20
3. Indicators of stress	27
4. Stress inversion from earthquakes	30
4.1 Stress tensor from initial polarities of a population of earthquakes	32
<i>Chapter 2: Geological and geophysical setting of the investigated area</i>	
1. Introduction	45
2. The Southern Apennines	48
2.1 Geodynamic and tectonic evolution	48
3. The Campania-Lucania region: crustal setting	57
4. Historical and instrumental seismicity	67
<i>Chapter 3: The Network and data collection</i>	
1. Introduction	75
2. The network and data-collection	76
3. Statistical features of the analyzed seismicity	81
4. Data set creation and validation	84
5. Discussion and conclusion	88
<i>Chapter 4: 1D velocity model, interpretation of station corrections and earthquake locations</i>	
1. Introduction	89
2. 1D P-wave velocity model estimation	92
2.1 Hypocenter stability test	98

2.2 Station corrections	100
2.3 3D P-wave Velocity Model and station corrections interpretation	102
3. S-wave velocity structure	106
4. Earthquakes Location comparison	107
4.1 Synthetic examples on earthquake location	111
5. HypoDD relocation	114
5.1 Synthetic example	116
5.2 Double difference location in the studied area	118
6. Discussions and conclusions	122
<i>Chapter 5: Focal mechanisms and stress field determination</i>	
1. Introduction	125
2. Focal mechanisms	126
2.1 Focal mechanisms of the studied area	127
3. Stress inversion	135
3.1 Bootstrap method, confidence ellipses and error estimation	136
3.2 Stress inversion for the studied area	138
3.3 Velocity model influence on stress parameters	141
3.4 Analysis on spatial variations of the stress fields	145
4. Discussion and conclusion	147
<i>Chapter 6: Seismotectonic implication</i>	
1. Introduction	149
2. Fault identification and regional stress field from the analysis of background microseismicity	150
3. Seismotectonic and geodynamic interpretation	156
4. Final remarks	163
Conclusion	167
Bibliography	171
Acknowledgments	185

# Introduction

In active seismic regions knowing the precise location, geometry and character of fault structures is of great interest for studies of tectonic processes, ongoing Earth's deformation, and hazard assessment. One important issue is whether the background, low magnitude seismicity allows to identify the faults causative of moderate to large earthquakes and to infer information about the present stress field acting in the area. The main limitations of using micro-seismicity to study active faults generally derive from the relatively large hypocentral errors due to network geometry, number and accuracy of arrival time readings, the inaccuracy of the crustal velocity model but also from the possible uncorrelation of microearthquake occurrence with faults and regional stress regime responsible of large earthquakes. Thanks to the development of regional dense seismic networks, it is possible nowadays to have high quality recordings of small earthquakes that can be used to highly improve the accuracy in location, focal mechanism and stress field estimation, so that their relationship with major faults can be quantitatively assessed. Several studies worldwide have shown that high precision earthquake locations produce sharpening of seismicity patterns allowing to determine the fine-scale fault geometry and extent (Rubin *et al.*, 1999; Waldhauser and Ellsworth, 2000; Hauksson and Shearer, 2005; Lin *et al.*, 2007). Most of these studies concern the seismicity of California, a region characterized by a dominant strike-slip tectonics, suitable for the identification of streaks of microearthquakes along active fault surfaces. Only few microseismicity studies performed in normal/thrust tectonic stress environments show a robust correlation between the background low magnitude seismicity and location and geometry of active faults causative of large earthquakes (Evans *et al.*, 1985; Suarez *et al.*, 1990; Rigo *et al.*, 1996). This is specifically the case of the Apenninic chain in Italy, where the background microseismicity, recorded by the permanent National Seismic Network of the Istituto Nazionale di Geofisica e Vulcanologia (INGV), shows a quite diffused

pattern of locations, spread across the axis chain, with a poor correlation with existing and known fault structures. On the other hand, several examples exist, showing that the locations of aftershocks recorded immediately after a moderate to large event accurately delineate the geometry of the fault planes and can be used to estimate the stress field thanks to the high quality of data and the improved techniques of analysis (e.g. Chiaraluce *et al.*, 2003).

The goal of this thesis is to show that refined analyses of background, low magnitude seismicity in the dominant normal-faulting tectonic region of Southern Apennines allow to delineate the main active faults and to accurately estimate the directions of the regional tectonic stress. This region is among the areas of Italy with the highest seismic potential and it has been the target of a project of a prototype system for Earthquake Early Warning (Zollo *et al.*, 2009). Moreover this area is characterized by complex geological-structural architecture. This complexity is related to the deformation of three main paleogeographic domains: the Lagonegro Basin located between the Western Carbonate and Apulia Carbonate Platforms. The tectonics of this area is accommodated by the collision between the Adriatic micro-plate and the Apenninic belt, derived by the convergence between the Euro-Asian and African plates. The eastward migration of the thrust-belt-foredeep-foreland system caused by the west-dipping subduction process of the Adriatic microplate is related to the opening of the Tyrrhenian basin (Patacca *et al.*, 1990). The background seismicity is mainly distributed along the axis of the Apenninic chain and it is characterized by low to moderate magnitude earthquakes ( $M < 3$ ). The most recent destructive earthquake occurred in the Irpinia region on November 23, 1980,  $M$  6.9 and has been studied in detail by many authors using different geophysical data sets (Westaway and Jackson, 1987; Bernard and Zollo, 1989; Pantosti and Valensise, 1990). The 1980 earthquake was a pure normal faulting event; it occurred on approximately 60 Km long, NW-SE striking, fault segments with three main rupture episodes at 10, 18 and 39 s from the first shock. Since 1980, the largest event that occurred within the epicentral area of the

1980 earthquake was the April 3, 1996 earthquake ( $M_L=4.9$ ), also characterized by a normal faulting mechanism (Cocco *et al.*, 1999). Two moderate magnitude seismic sequences occurred between 1990 and 1991 in the Potenza region located about 40 Km SE of the 1980 Irpinia aftershock area (Ekstrom, *et al.*, 1994). The two mainshocks ( $M_L=5.2$  and  $M_L=4.7$ ) and the larger events of the sequences were characterized by strike-slip faulting mechanisms with preferred fault planes having an E-W orientation (Di Luccio *et al.*, 2005).

The low magnitude earthquake data ( $0.1 < M_L < 3.2$ ) analyzed in this work have been acquired by the National Seismic Network and the Irpinia Seismic Network (ISNet), a dense and wide dynamic network deployed around and over the active fault system affecting the region and managed by the permanent research enterprise AMRA - Analysis and Monitoring of Environmental Risk.

The availability of high quality data-set has allowed us to perform several analyses to characterize the area from a seismological point of view and to increase the details of the knowledge about this complex crustal structure. We want to underline here the innovation of the contribution obtained from the analysis of background micro-seismicity in studies of active tectonics. This gives a new perspective to the application of the high quality records of background seismicity for the identification and characterization of active fault systems, which can integrate the information provided by low magnitude seismicity about the active stress regime.

Taking into account the peculiarities of the investigated area and of the tectonic environment, different methods must be adopted in order to better define the fault structures.

The definition of the fault structures requires accurate localization and it cannot be exempt from the correct understanding of the propagation medium. This is important to reduce uncertainties and distortion in the position of hypocenters that may result in artifacts such as apparent lineations (Michelini and Lomax, 2004). Three-dimensional (3D) features of the propagation medium are generally

unknown, and so simplified one dimensional (1D) velocity models are generally used in the earthquakes location.

The known strong lateral variation of the elastic properties of the medium in the investigated area called into question the representativeness of the 1D velocity model and the role of the static station corrections for the earthquakes location. In this kind of studies it's important a detailed study for the velocity model determination and an accurate analysis on the effects that the use of 1D velocity models to represent the true three dimensional velocity distribution induces on earthquake locations. The effects of an unsuitable velocity model on hypocenter locations can be minimized by using relative earthquake location methods (Frèchet, 1985; Got *et al.*, 1994). An additional improvement in the location precision can be also obtained by improving the accuracy of the relative arrival-time readings using waveform cross-correlation methods (Waldhauser, 2002).

These features make it possible to obtain sharp streaks of microearthquakes especially for strike slip vertical faults as is the case examined in the region of Potenza. But an additional complexity in tectonic settings characterized by extensional regime is due to the presence of normal faults with a dip from  $50^{\circ}$  to  $70^{\circ}$ . And so the epicentral characteristics of the seismicity could not display linear trends as for near vertical faults. The study of the focal solutions can in these cases provide information on the presence of random or highly organized structures and can help to understand the orientation and the geometry of the fault planes.

In order to better understanding the geodynamic processes and interpret the seismicity and the fault systems from a seismotectonic point of view, it's important to define the stress field acting in the area. Several inversion techniques are used to determine the stress field and its possible spatial variations using earthquakes data. In particular the background seismicity and the aftershocks of a strong earthquake represent the only tools to study the state of stress acting in a region in depth. It's important to underline that the ability of the inversion to find an acceptable "best" stress tensor is equally as important as

to define meaningful errors on the stress directions. This is especially important if we are to look for spatial variations in the stress field, even in relatively small regions of space as the case examined.

The work carried out in the present research thesis is organized as follows.

The first chapter starts with a brief recall of the fundamental concepts of stress. We describe the different methodologies used to estimate the state of stress, including the use of fault data, information on borehole breakouts and focal mechanisms of earthquakes. In particular, we focus on the algorithm developed by Rivera L. and Cisternas A. (1990) that allows for the simultaneous estimation of the orientation and shape of the stress tensor and the individual fault plane solution given a population of earthquakes.

In the second chapter we describe the investigated area from a geological point of view. This is an important tool to understand the structural complexity of the analysed area, where the geological and geophysical knowledge reveal a significant lateral variation of the elastic properties of the medium along a direction perpendicular to Apenninic belt and characterized by a complex systems of faults with dominant normal-faulting tectonic.

In the third chapter we discuss about the creation and validation of seismological dataset recorded by ISNET and INGV networks. The presence in the studied area of an *a hoc* regional dense seismic network, allowed us to build a high quality recordings of small earthquakes and to obtain a dataset of very accurate arrival time readings and polarity of the P-wave first motion. This is important to improve the accuracy in location, velocity model, focal mechanism and stress field estimation.

In the fourth chapter we estimate a “minimum” P-wave velocity model together with station corrections. We analyze the role of the station corrections and the effects on the earthquakes location in an area characterized by important lateral velocity variation. This study is supported by several synthetic tests and by the comparison with the location in a three dimensional model availed for the area.

The application of a methodology called Double Difference (DD; Waldhauser and Ellsworth, 2000) technique is used in order to improve the earthquake locations and permit to better delineate the fault systems.

In the first part of fifth chapter we illustrate the methodology behind the construction of the focal mechanism and compute the fault plane solutions for the selected earthquakes. In the second part we analyze the problem of the stress field determination using earthquakes data. A new method to compute the error on the stress field orientations will be implemented. We study the velocity models influence on the estimated parameters. The spatial variations of the stress field it will be investigated. The results of this analysis allow us to define the geometry of fault systems and to understand the geodynamic acting in the area. Finally, in the sixth chapter we propose our interpretation of the results presented in the previous chapters. An accurate discussion from a seismotectonic and geodynamic point of view concludes this work.

# Chapter 1

## Stress field determination

---

### 1. Introduction

The state of stress in the lithosphere is the result of the forces acting upon and within it. Knowledge of the magnitude and distribution of these forces can be combined with mechanical, thermal and rheological constraints to provide a better understanding of geodynamic and deformational processes (Bott, 1959; McKenzie, 1969). Stress makes geologic processes happen, and geologic processes make stress. Plate tectonics, glacial rebound, landslides, tidal deformation, phase changes, fluid flow, rock folding, and crystallization are example of processes that generate, modify, and consume stress within the Earth. Gravitational forces acting on and within the Earth are intimately connected to the stress state, and earthquakes occur when the shear stress exceeds the failure level for the fault.

In this section we want to analyze the state of stress in the brittle crust resulting from relatively large scale lithospheric process so that knowledge of crustal stress can be used to constrain the forces involved in these processes. Any quantitative description of seismic wave propagation or of earthquake physics requires the ability to characterize the internal forces between different parts of the medium, called stress. To better understand the nature and distribution of forces within the crust is essential to recall the fundamental concepts of the theory of stress, with particular reference to the determination of the principal axes of stress.

We briefly describe the different methodologies that allow us to obtain an estimate of the state of stress, including the use of fault data, information on borehole breakout and focal mechanisms of earthquakes. In particular we describe the algorithm developed by Rivera L. and Cisternas A. (1990) that

allows for the simultaneous estimation of orientation and shape of the stress tensor and the individual fault plane solution given a population of earthquakes from first P-motion polarities.

## 2. Aspects of stress tensor

Stress is a well-defined physical quantity throughout the interior of any fluid or solid material. Basic rules of force balance on a small material element lead to the construction of the stress tensor, which can be viewed as three mutually perpendicular force dipoles acting on the faces of the material element (Aki and Richards, 1980). These three dipoles are commonly referred to as principal stresses, and the units stress are force per unit area ( $1\text{Pa} = 1\text{Nm}^{-2}$ ).

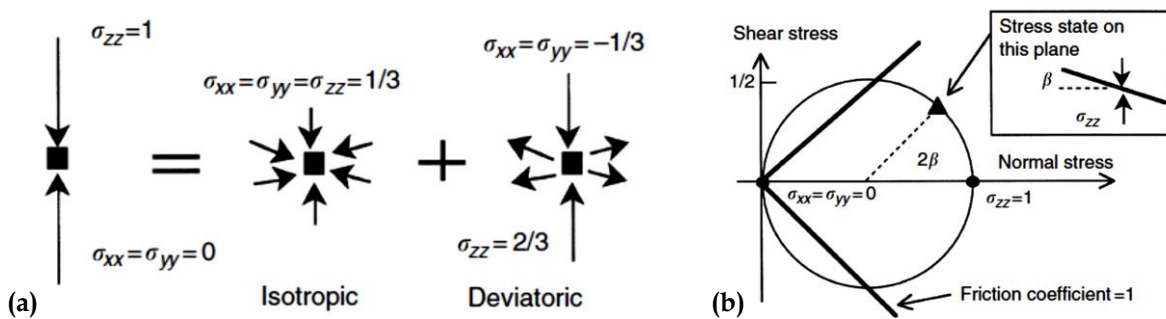


Figure 1.1 Stress tensor for a single vertical force dipole ( $\sigma_{zz}$ ) represented by isotropic and deviatoric components (a) or by Mohr's circle (b) (modified from Ruff, 2002).

The most important mathematically subdivision of the stress tensor is into the isotropic and deviatoric parts. As shown in Figure 1.1, isotropic part is formally defined as one-third the trace of the stress tensor; in other words pressure is the average value of the principal stresses.

Figure 1.1 also illustrates how a stress tensor for a single force dipole is decomposed into the isotropic part and deviatoric part.

A common description of the stress state is to quote the "normal" and "shear" stresses with respect to a particular plane slicing through the material. In this context *normal* stress refers to the force component acting perpendicular to the plane, whereas *shear* stress refers to the force component acting parallel to the plane. In the matrix representation of stress, *normal* and *shear* stresses are the

diagonal and off-diagonal components of the stress tensor after it has been rotated to a new coordinate system that coincides with the plane orientation.

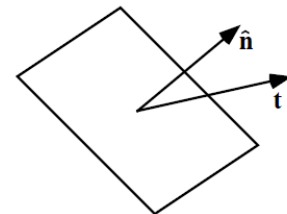
Mohr's circles provide a clever geometric visualization of this view of the stress state (Figure 1.1).

As a plane is rotated from an initial orientation that is normal to the maximum principal stress, then shear stress along the plane increases from its initial value of zero.

## 2.1 Stress tensor

In this paragraph, the theoretical treatment is from Shearer, (2009).

Consider an infinitesimal plane of arbitrary orientation within a homogeneous elastic medium in static equilibrium. The orientation of the plane may be specified by its unit normal vector,  $\hat{\mathbf{n}}$ . The force per unit area exerted by the side in the direction of  $\hat{\mathbf{n}}$  across this plane is termed the traction and is represented by the vector  $\mathbf{t}(\hat{\mathbf{n}}) = (t_x, t_y, t_z)$ .



If  $\mathbf{t}$  acts in the direction shown here, then the traction force is pulling the opposite side toward the interface. This definition is the usual convention in seismology and results in extensional forces being positive and compressional forces being negative. In some other fields, such as rock mechanics, the definition is reversed and compressional forces are positive. There is an equal and opposite force exerted by the side opposing  $\hat{\mathbf{n}}$ , such that  $\mathbf{t}(-\hat{\mathbf{n}}) = -\mathbf{t}(\hat{\mathbf{n}})$ . The part of  $\mathbf{t}$  which is normal to the plane is known as *normal stress*, the one which is parallel is called *shear stress*. In case of a fluid, there are no shear stresses and  $\mathbf{t} = -P \hat{\mathbf{n}}$ , where  $P$  is the pressure.

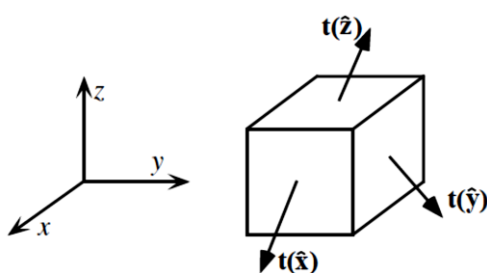


Figure 1.2 The traction vectors  $\mathbf{t}(\hat{\mathbf{x}})$ ,  $\mathbf{t}(\hat{\mathbf{y}})$ , and  $\mathbf{t}(\hat{\mathbf{z}})$  describe the forces on the faces of an infinitesimal cube in a Cartesian coordinate system (from Shearer, 2009)

In general, the magnitude and direction of the traction vector will vary as a function of the orientation of the infinitesimal plane. Thus, to fully describe the internal forces in the medium, we need a general method for determining  $\mathbf{t}$  as a function of  $\hat{\mathbf{n}}$ . This is accomplished with the *stress tensor*, which provides a linear mapping between  $\hat{\mathbf{n}}$  and  $\mathbf{t}$ .

The stress tensor,  $\sigma$ , in a Cartesian coordinate system (Figure 1.2) may be defined<sup>1</sup> by the tractions across the  $yz$ ,  $xz$ , and  $xy$  planes:

$$\sigma = \begin{bmatrix} t_x(\hat{x}) & t_x(\hat{y}) & t_x(\hat{z}) \\ t_y(\hat{x}) & t_y(\hat{y}) & t_y(\hat{z}) \\ t_z(\hat{x}) & t_z(\hat{y}) & t_z(\hat{z}) \end{bmatrix} = \begin{bmatrix} \sigma_{xx} & \sigma_{xy} & \sigma_{xz} \\ \sigma_{yx} & \sigma_{yy} & \sigma_{yz} \\ \sigma_{zx} & \sigma_{zy} & \sigma_{zz} \end{bmatrix} \quad (1.1)$$

Since the solid is in static equilibrium, the equilibrium conditions reduces the number of independent parameters in the stress tensor to six, respect to nine that are present in the most general form of a second-order tensor.

$$\sigma = \sigma^T = \begin{bmatrix} \sigma_{xx} & \sigma_{xy} & \sigma_{xz} \\ \sigma_{yx} & \sigma_{yy} & \sigma_{yz} \\ \sigma_{zx} & \sigma_{zy} & \sigma_{zz} \end{bmatrix} \quad (1.2)$$

The traction across any arbitrary plane of orientation defined by  $\hat{\mathbf{n}}$  may be obtained by multiplying the stress tensor by  $\hat{\mathbf{n}}$ , that is,

$$t(\hat{\mathbf{n}}) = \sigma \hat{\mathbf{n}} = \begin{bmatrix} t_x(\hat{\mathbf{n}}) \\ t_y(\hat{\mathbf{n}}) \\ t_z(\hat{\mathbf{n}}) \end{bmatrix} = \begin{bmatrix} \sigma_{xx} & \sigma_{xy} & \sigma_{xz} \\ \sigma_{yx} & \sigma_{yy} & \sigma_{yz} \\ \sigma_{zx} & \sigma_{zy} & \sigma_{zz} \end{bmatrix} \begin{bmatrix} \hat{n}_x \\ \hat{n}_y \\ \hat{n}_z \end{bmatrix} \quad (1.3)$$

This can be shown by summing the forces on the surfaces of a tetrahedron (the *Cauchy tetrahedron*) bounded by the plane normal to  $\hat{\mathbf{n}}$  and the  $xy$ ,  $xz$ , and  $yz$  planes. The stress tensor is simply the linear operator that produces the traction vector  $\mathbf{t}$  from the normal vector  $\hat{\mathbf{n}}$ , and, in this sense, the stress tensor exists independently of any particular coordinate system. For a practical purpose, we

---

<sup>1</sup>Often the stress tensor is defined as the transpose of (1.1) so that the first subscript of  $\sigma$

select a specific reference frame writing the stress tensor as a  $3 \times 3$  matrix in a Cartesian geometry.

The stress tensor will normally vary with position in a material; it is a measure of the forces acting on infinitesimal planes at each point in the solid. Stress provides a measure only of the forces exerted across these planes. However, other forces may be present (e.g., gravity); these are denoted as *body forces*.

### 2.1.1 Principal axes of stress

For a given state of stress, the traction vector acting on each surface within a material has components both normal and tangential to it. Since the stress tensor is real and symmetric, it is always possible to find a reference frame which makes it diagonal. The three axis defining this reference frame are called the principal stress axis. We can consider some surfaces specially oriented such that the shear tractions on them vanish. These surfaces can be characterized by their normal vectors, called *principal stress axis*; the normal stresses on this surface are called *principal stresses*. This concept is fundamental for the earthquake source mechanisms.

Thus, for any stress tensor, it is always possible to find a direction  $\hat{\mathbf{n}}$  such that there are no shear stresses across the plane normal to  $\hat{\mathbf{n}}$ , that is,  $\mathbf{t}(\hat{\mathbf{n}})$  points in the  $\hat{\mathbf{n}}$  direction. In this case

$$\begin{aligned}\mathbf{t}(\hat{\mathbf{n}}) &= \lambda \hat{\mathbf{n}} = \boldsymbol{\sigma} \hat{\mathbf{n}} \\ \boldsymbol{\sigma} \hat{\mathbf{n}} - \lambda \hat{\mathbf{n}} &= 0 \\ (\boldsymbol{\sigma} - \lambda \mathbf{I}) \hat{\mathbf{n}} &= 0\end{aligned}\tag{1.4}$$

where  $\mathbf{I}$  is the identity matrix and  $\lambda$  is a scalar multiplicative constant. This is an eigenvalue problem that has a non-trivial solution only when the determinant vanishes<sup>2</sup>:

$$\det[\boldsymbol{\sigma} - \lambda \mathbf{I}] = 0\tag{1.5}$$

---

<sup>2</sup>A nontrivial solution exists only for values of  $\lambda$  such that the matrix is singular (has no inverse), which occurs when its determinant is zero

This is a cubic equation with always three solutions, the eigenvalues  $\lambda_1$ ,  $\lambda_2$ , and  $\lambda_3$ . Furthermore, since  $\sigma$  is symmetric and real, the eigenvalues are real. Corresponding to the eigenvalues are the eigenvectors  $\hat{\mathbf{n}}(1)$ ,  $\hat{\mathbf{n}}(2)$ , and  $\hat{\mathbf{n}}(3)$ . The eigenvectors are orthogonal and define the *principal axes* of stress. The planes perpendicular to these axes are termed the *principal planes*. We can rotate  $\sigma$  into the  $\hat{\mathbf{n}}(1)$ ,  $\hat{\mathbf{n}}(2)$ ,  $\hat{\mathbf{n}}(3)$  coordinate system by applying a similarity transformation

$$\boldsymbol{\sigma}^R = \mathbf{N}^T \boldsymbol{\sigma} \mathbf{N} = \begin{bmatrix} \sigma_1 & 0 & 0 \\ 0 & \sigma_2 & 0 \\ 0 & 0 & \sigma_3 \end{bmatrix} \quad (1.6)$$

Where  $\boldsymbol{\sigma}^R$  is the rotated stress tensor and  $\sigma_1$ ,  $\sigma_2$ , and  $\sigma_3$  are the *principal stresses* (identical to the eigenvalues  $\lambda_1$ ,  $\lambda_2$ , and  $\lambda_3$ ). Here  $\mathbf{N}$  is the matrix of eigenvectors

$$\mathbf{N} = \begin{bmatrix} n_x^{(1)} & n_x^{(2)} & n_x^{(3)} \\ n_y^{(1)} & n_y^{(2)} & n_y^{(3)} \\ n_z^{(1)} & n_z^{(2)} & n_z^{(3)} \end{bmatrix} \quad (1.7)$$

By convention, the three principal stresses are sorted by size, such that  $|\sigma_1| > |\sigma_2| > |\sigma_3|$ . The maximum shear stress occurs on planes at  $45^\circ$  to the maximum and minimum principle stress axes. In the principal axes coordinate system, one of these planes has normal vector  $\hat{\mathbf{n}} = (1/\sqrt{2}, 0, 1/\sqrt{2})$ . The traction vector for the stress across this plane is

$$\mathbf{t}(45^\circ) = \begin{bmatrix} \sigma_1 & 0 & 0 \\ 0 & \sigma_2 & 0 \\ 0 & 0 & \sigma_3 \end{bmatrix} \begin{bmatrix} 1/\sqrt{2} \\ 0 \\ 1/\sqrt{2} \end{bmatrix} = \begin{bmatrix} \sigma_1/\sqrt{2} \\ 0 \\ \sigma_3/\sqrt{2} \end{bmatrix} \quad (1.8)$$

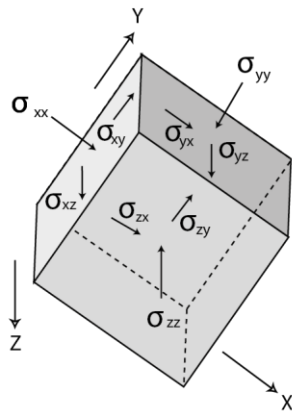
This can be decomposed into normal and shear stresses on the plane:

$$\mathbf{t}_N(45^\circ) = \mathbf{t}(45^\circ) \cdot (1/\sqrt{2}, 0, 1/\sqrt{2}) = (\sigma_1 + \sigma_3)/2 \quad (1.9)$$

$$\mathbf{t}_S(45^\circ) = \mathbf{t}(45^\circ) \cdot (1/\sqrt{2}, 0, -1/\sqrt{2}) = (\sigma_1 - \sigma_3)/2 \quad (1.10)$$

and we see that the maximum shear stress is  $(\sigma_1 - \sigma_3)/2$ .

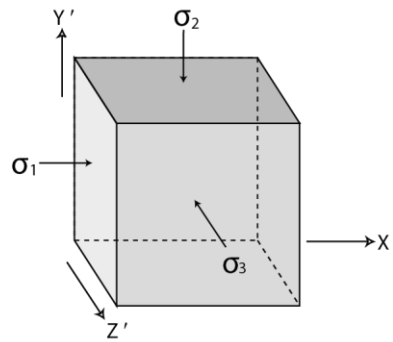
Stress description of stresses in 3D



$$\sigma = \begin{bmatrix} \sigma_{xx} & \sigma_{xy} & \sigma_{xz} \\ \sigma_{yx} & \sigma_{yy} & \sigma_{yz} \\ \sigma_{zx} & \sigma_{zy} & \sigma_{zz} \end{bmatrix}$$

(a)

Principal stress tensor



$$\sigma' = \begin{bmatrix} \sigma_1 & 0 & 0 \\ 0 & \sigma_2 & 0 \\ 0 & 0 & \sigma_3 \end{bmatrix}$$

(b)

Figure 1.3 (modified from (Zoback *et al.*, 2002) Definition of stress tensor in an arbitrary Cartesian coordinate system, rotation of stress coordinate system through a tensor transformation, and principal stresses as defined in a coordinate system in which shear stresses vanish.

If  $\sigma_1 = \sigma_2 = \sigma_3$ , then the stress field is called *hydrostatic* and there are no planes of any orientation in which shear stress exists. In a fluid the stress tensor can be written (where  $P$  is the pressure)

$$\sigma = \begin{bmatrix} -P & 0 & 0 \\ 0 & -P & 0 \\ 0 & 0 & -P \end{bmatrix} \tag{1.11}$$

### 2.1.2 Deviatoric stress

Stresses in the deep Earth are dominated by the large compressive stress from the hydrostatic pressure. Often it is convenient to consider only the much smaller *deviatoric* stresses, which are computed by subtracting the mean normal stress (given by the average of the principle stresses, that is  $\sigma_m = (\sigma_1 + \sigma_2 + \sigma_3)/3$ ) from the diagonal components of the stress tensor, thus defining the deviatoric stress tensor

$$\boldsymbol{\sigma}_D = \begin{bmatrix} \sigma_{xx} - \sigma_m & \sigma_{xy} & \sigma_{xz} \\ \sigma_{xy} & \sigma_{yy} - \sigma_m & \sigma_{yz} \\ \sigma_{xz} & \sigma_{yz} & \sigma_{zz} - \sigma_m \end{bmatrix} \quad (1.12)$$

It should be noted that the trace of the stress tensor is invariant with respect to rotation, so the mean stress  $\sigma_m$  can be computed by averaging the diagonal elements of  $\sigma$  without computing the eigenvalues (i.e.,  $\sigma_m = (\sigma_{11} + \sigma_{22} + \sigma_{33})/3$ ). In addition, the deviatoric stress tensor has the same principal stress axes as the original stress tensor. The stress tensor can then be written as the sum of two parts, the hydrostatic stress tensor  $\sigma_m \mathbf{I}$  and the deviatoric stress tensor  $\boldsymbol{\sigma}_D$

$$\boldsymbol{\sigma} = \sigma_m \mathbf{I} + \boldsymbol{\sigma}_D = \begin{bmatrix} -p & 0 & 0 \\ 0 & -p & 0 \\ 0 & 0 & -p \end{bmatrix} + \begin{bmatrix} \sigma_{xx} + p & \sigma_{xy} & \sigma_{xz} \\ \sigma_{xy} & \sigma_{yy} + p & \sigma_{yz} \\ \sigma_{xz} & \sigma_{yz} & \sigma_{zz} + p \end{bmatrix} \quad (1.13)$$

Where  $p = -\sigma_m$  is the mean pressure. For isotropic materials, hydrostatic stress produces volume change without any change in the shape; it is the deviatoric stress that causes shape changes.

## 2.2 Rock Failure and Faulting

At low temperatures and pressures rock is a brittle material that will fail by fracture if the stresses become sufficiently large. Fractures are widely observed in surface rocks of all types. When a lateral displacement takes place on a fracture, the break is referred to as a fault. When the stress on the fault reaches a critical value, the fault slips and an earthquake occurs. The elastic energy stored in the adjacent rock is partially dissipated as heat by friction on the fault and is partially radiated away as seismic energy. This is known as *elastic rebound*. Fault displacements associated with the largest earthquakes are of the order of 30 m (Turcotte *et al.*, 2002).

Here we provide quantitative definitions of the different types of faults in terms of the relative magnitudes of the principal stresses.

Since voids cannot open up deep in the Earth, displacements on faults occur parallel to the fault surface. For simplicity we assume that the fault surface is planar; in fact, faulting often occurs on curved surfaces or on a series of surfaces that are offset from one another.

A number of studies or reviews of rock failure, faulting and reology currently exists (Lockner D.A. *et al.*, 2002). For a theoretical development or a numerical modeling, it is common to assume that earthquakes occur on preexisting fault zones. The Earth's crust is generally permeated with preexisting fractures and it is known that earthquakes occur on these.

### 2.2.1 Faulting

Generally, an earthquake may be idealized as movement across a planar fault of arbitrary orientation (Shearer, 2009; Figure 1.4). The fault plane is defined by its strike ( $\phi$ , the azimuth of the fault from north where it intersects a horizontal surface) and dip ( $\delta$ , the angle from the horizontal). For non-vertical faults, the lower block is termed the foot wall; the upper block is the hanging wall. The slip vector is defined by the movement of the hanging wall relative to the foot wall; the rake,  $\lambda$ , is the angle between the slip vector and the strike. Upward movement of the hanging wall is termed reverse faulting, whereas downward movement is called normal faulting. Reverse faulting on faults with dip angles less than  $45^\circ$  is also called thrust faulting; nearly horizontal thrust faults are called overthrust faults. In general, reverse faults involve horizontal compression in the direction perpendicular to the fault strike whereas normal faults involve horizontal extension. Horizontal motion between the fault surfaces is termed strike-slip. If an observer, standing on one side of a fault, sees the adjacent block move to the right, this is termed right-lateral strike-slip motion (with the reverse indicating left-lateral motion). To define the rake for vertical faults, the hanging wall is assumed to be on the right for an observer looking in the strike direction. In this case,  $\lambda = 0^\circ$  for a left-lateral fault and  $\lambda = 180^\circ$  for a right-lateral fault. The

strike is defined between  $0^\circ$  and  $360^\circ$ , the dip is defined between  $0^\circ$  and  $90^\circ$ , the rake is defined between  $0^\circ$  and  $360^\circ$ .

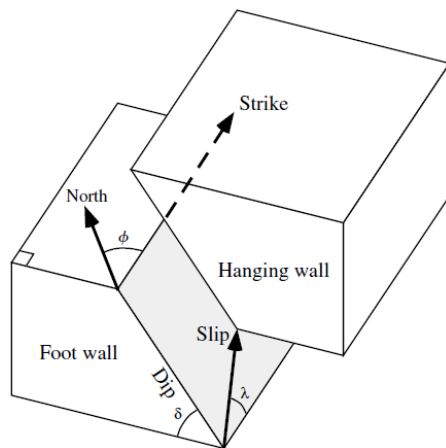


Figure 1.4 A planar fault is defined by the strike and dip of the fault surface and the direction of the slip vector (from Shearer, 2009)

We can choose to generally describe the state of stress in terms of the principal coordinate system. We remember that the principal coordinate system is the one in which shear stresses vanish and only three principal stresses  $|\sigma_1| > |\sigma_2| > |\sigma_3|$  fully describe the stress field. The reason why this concept is so important is that as the Earth's surface is in contact with a fluids (either air or water) and cannot support shear tractions, it is a principal plane (Zoback *et al.*, 2002). Thus, one principal axis is generally expected to be normal to the Earth's surface with either two principal stresses in an approximately horizontal plane. Although it is clear that this must be true very close to the Earth's surface, compilation of earthquake focal mechanism data and other stress indicators (describe below) suggest that it is also generally true at the depth of the brittle-ductile transition in the upper crust (Zoback, 1992 ; Brudy *et al.*, 1997). Assuming this case, we must define only four parameters to describe the state of stress at depth; one stress orientation (usually taken to be the azimuth of the maximum horizontal compression  $S_{Hmax}$ ) and three principal stress magnitudes:  $S_V$ , the vertical stress corresponding the weight of the overburden;  $S_{Hmax}$ , the maximum principal horizontal stress; and  $S_{hmin}$ , the minimum principal horizontal stress.

This obviously helps to make stress determination in the crust a tractable problem.

Considering the magnitude of the greatest, intermediate, and minimum principal stress at depth ( $\sigma_1$ ,  $\sigma_2$  and  $\sigma_3$ ) in terms of  $S_V$ ,  $S_{Hmax}$  and  $S_{Hmin}$  in the manner proposed by Anderson (Anderson 1951; Figure 1.5).

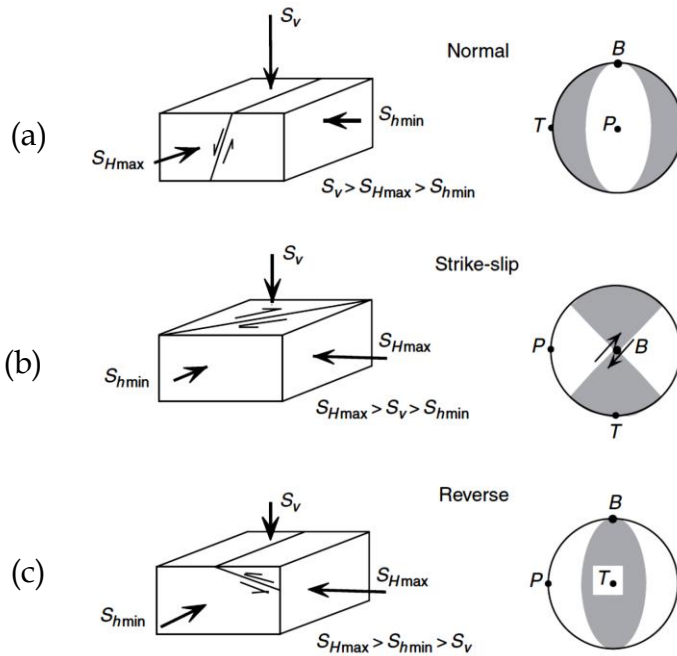


Figure 1.5 E.M. Anderson's classification scheme for relative stress magnitudes in normal, strike-slip and reverse faulting regions. Corresponding focal mechanisms are shown to the right.

The two horizontal principal stresses in the Earth,  $S_{Hmax}$  and  $S_{Hmin}$  can be described relative to the vertical principal stress,  $S_V$ , whose magnitude corresponds to the overburden. Mathematically, this is equivalent to the integration of density from the surface to the depth of interest,  $z$ . In other words;

$$S_V = \int_0^z \rho(z')g dz' \approx \bar{\rho} g z \quad (1.14)$$

Where  $\rho(z)$  is the density as a function of depth,  $g$  is gravitational acceleration (is supposed constant, at shallow depth) and  $\bar{\rho}$  is mean overburden density.

For this section we assume that the stresses in the  $x$ ,  $y$ , and  $z$  directions are the principal stresses ( $x$  and  $z$  in horizontal plan, and  $y$  is vertical). The theoretical treatment is from Turcotte *et al.*, 2002.

We will first consider thrust faulting (Figure 1.5 c), which occurs for example when the oceanic lithosphere is thrust under the adjacent continental (or oceanic) lithosphere at an ocean trench. Thrust faulting also plays an important role in the compression of the lithosphere during continental collisions. Idealized thrust faults are illustrated in Figure 1.6. Compressional stresses cause displacement along a fault plane dipping at an angle  $\beta$  to the horizontal. As a result of the faulting, horizontal compressional strain occurs. Thrust faults can form in each of the two conjugate geometries shown in Figure 1.6a and b.

The vertical component of stress  $\sigma_{yy}$  is the overburden or lithostatic pressure ( $\sigma_{yy} = \rho gy$ ). The vertical deviatoric stress  $\Delta\sigma_{yy}$  is zero. To produce the thrust faults in Figure 1.6, a compressional deviatoric stress applied in the  $x$  direction  $\Delta\sigma_{xx}$  is required,  $\Delta\sigma_{xx} > 0$ . The horizontal compressional stress  $\sigma_{xx} = \rho gy + \Delta\sigma_{xx}$  therefore exceeds the vertical lithostatic stress  $\sigma_{xx} > \sigma_{yy}$ .

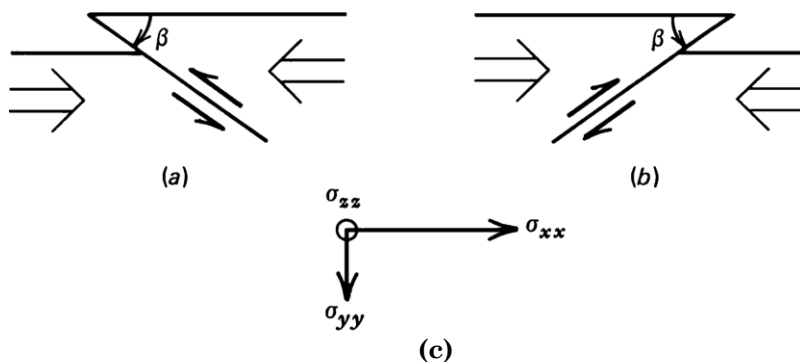


Figure 1.6 Thrust faulting. Two conjugate thrust faults with dip angles  $\beta$  are shown in (a) and (b). The principal stresses illustrated in (c) are all compressional with magnitudes  $\sigma_{xx} > \sigma_{zz} > \sigma_{yy}$ .

For the fault geometry shown in Figure 1.6 it is appropriate to assume that there is no strain in the  $z$  direction. In this situation of plane strain we can use to relate the deviatoric stress component  $\Delta\sigma_{zz}$  to  $\Delta\sigma_{xx}$  and we can write

$$\Delta\sigma_{zz} = \nu\Delta\sigma_{xx}^{(3)} \quad (1.15)$$

---

<sup>3</sup> Poisson's ratio

The deviatoric stress in the  $z$  direction is also compressional, but its magnitude is a factor of  $\nu$  less than the deviatoric applied stress. Therefore the horizontal compressional stress,

$$\sigma_{zz} = \rho gy + \Delta\sigma_{zz} = \rho gy + \nu\Delta\sigma_{xx} \quad (1.16)$$

exceeds the vertical stress  $\sigma_{yy}$ , but it is smaller than the horizontal stress  $\sigma_{xx}$ . Thrust faults satisfy the condition  $\sigma_{xx} > \sigma_{zz} > \sigma_{yy}$ . The vertical stress is the least compressive stress.

Just as thrust faulting accommodates horizontal compressional strain, normal faulting accommodates horizontal extensional strain. Normal faulting (Figure 1.5 a) occur for example on the flanks of ocean ridges where new lithosphere is being created. Normal faulting also occurs in continental rift valleys where the lithosphere is being stretched. Applied tensional stresses can produce normal faults in each of the two conjugate geometries shown in Figure 1.7.

The displacements on the fault planes dipping at an angle  $\beta$  to the horizontal lead to horizontal extensional strain. Normal faulting is associated with a state of stress in which the vertical component of stress is the lithostatic pressure  $\sigma_{yy} = \rho gy$  and the applied deviatoric horizontal stress  $\Delta\sigma_{xx}$  is tensional ( $\Delta\sigma_{xx} < 0$ ).

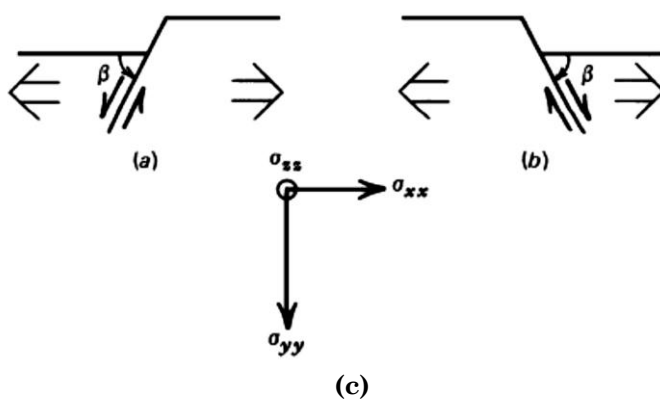


Figure 1.7 Normal faulting. Two conjugate normal faults with angle of dip  $\beta$  are shown in (a) and (b). The principal stresses illustrated in (c) have magnitudes related by  $\sigma_{yy} > \sigma_{zz} > \sigma_{xx}$ .

$$\text{The horizontal stress, } \sigma_{xx} = \rho gy + \Delta\sigma_{xx} \quad (1.17)$$

is therefore smaller than the vertical stress,  $\sigma_{yy} > \sigma_{xx}$ .

The plane strain assumption is again appropriate to the situation in Figure 1.7, and Equation (1.15) is applicable. Consequently, the deviatoric stress in the  $z$  direction  $\Delta\sigma_{zz}$  is also tensional, but its magnitude is a factor of  $\nu$  smaller than the deviatoric applied stress. The total stress,

$$\sigma_{zz} = \rho gy + \nu \Delta \sigma_{xx} \quad (1.18)$$

is smaller than  $\sigma_{yy}$  but larger than  $\sigma_{xx}$ . Normal faults satisfy the condition  $\sigma_{yy} > \sigma_{zz} > \sigma_{xx}$ , where the vertical stress is the maximum compressive stress. Both thrust faults and normal faults are also known as dip-slip faults since the displacement along the fault takes place on a dipping plane.

A strike-slip fault (Figure 1.5b) is a fault along which the displacement is strictly horizontal. Thus there is no strain in the  $y$  direction. The situation is one of plane strain with the nonzero strain components confined to the horizontal plane. Two conjugate strike-slip faults are shown in Figure 1.8. The fault planes make an angle  $\psi$  with respect to the direction of the principal stress  $\sigma_{xx}$ . The fault illustrated in Figure 1.8a is right lateral and the one in Figure 1.8b is left lateral.

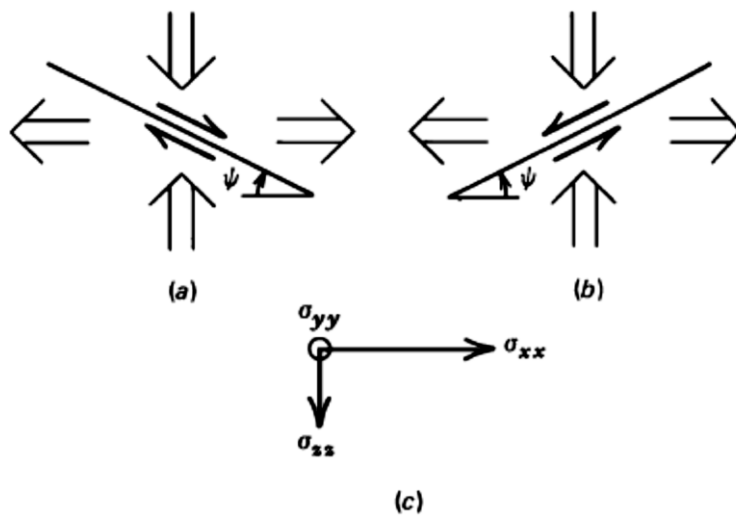


Figure 1.8 Strike-slip faulting in plan. Two conjugate strike-slip faults inclined at an angle  $\psi$  to the direction of the principal stress  $\sigma_{xx}$  are shown in (a) and (b). The principal stresses illustrated in (c) are related by  $\sigma_{zz} > \sigma_{yy} > \sigma_{xx}$ .

The state of stress in strike-slip faulting consists of a vertical lithostatic stress  $\sigma_{yy} = \rho gy$  and horizontal deviatoric principal stresses that are compressional in one direction and tensional in the other.

The case shown in Figure 1.8 has

$$\Delta \sigma_{xx} < 0 \quad \Delta \sigma_{zz} > 0 \quad (1.19)$$

One can also have

$$\Delta \sigma_{xx} > 0 \quad \Delta \sigma_{zz} < 0. \quad (1.20)$$

One horizontal stress will thus be larger than  $\sigma_{yy}$  while the other will be smaller.

For the situation given by Equation (1.19) we have

$$\sigma_{zz} > \sigma_{yy} > \sigma_{xx}, \quad (1.21)$$

while Equation (1.20) gives

$$\sigma_{xx} > \sigma_{yy} > \sigma_{zz}. \quad (1.22)$$

For strike-slip faulting, the vertical stress is always the intermediate stress. A special case of strike-slip faulting occurs when

$$|\Delta\sigma_{xx}| = |\Delta\sigma_{zz}| = \tau_0. \quad (1.23)$$

This is the situation of pure shear. The stress  $\tau_0$  is the shear stress applied across the fault. In pure shear the angle  $\psi$  is  $45^\circ$ . The displacement on an actual fault is almost always a combination of strike-slip and dip-slip motion. However, one type of motion usually dominates.

### 3. Indicators of stress

The techniques for determining the state of stress within the Earth were developed in engineering, geology and energy. From a geological point of view, it is important to know the state of stress inside the Earth in order to understand how the plates move, why, where and when earthquakes occur, why and how the structures are formed.

Information about the state of stress in the lithosphere can be obtained through several methods: geological data and recent volcanic alignments, in situ stress measurements, fault plane solutions of earthquakes.

#### 3.1 Geologic stress indicators

From a geological point of view, there are different types of data that can be used to determine the in situ stress state, as the orientations of igneous dykes or volcanic alignments, which are formed in a plane normal to the least principal stress (Nakamura, 1977) and fault slip data, in particular the inversion of a set of kinematic indicators (or slickenside data) on the faults. The relationship between the faults and the directions of the principal axes of stress, according to the

Coulomb fracture criterion, suggests that the fault data may be used to determine the orientations of principal stress. The reliability of each estimate of the stress depends on the nature of the faults and the retention of features that indicate their movement.

### **3.2 In situ measurements**

Numerous techniques have been developed to measure stress in deep. Amadei and Stephansson (1997) and Engelder (1993) discuss many of these measurement methods.

The methods of determining stress orientation from observations in wells and boreholes and stress-induced borehole breakouts which access the crust at depths greater than 100m, are especially useful. These techniques are based on the observation that when a well or borehole is drilled, the stresses that were previously supported by the exhumed material are transferred to the region surrounding the hole. The resulting stress concentration is explained by the elastic theory.

The most common methods to determine the stress orientations from observations in wells and boreholes are stress-induced wellbore breakouts. The breakouts represent an important source of information thanks to the global distribution of oil exploration wells and since the breakouts can provide information on the stress field in regions where there are no available data of earthquakes or faults.

#### **3.3.3 Earthquake Focal Mechanisms**

The earthquake fault mechanisms represent an important tool to study the state of stress acting in a tectonic province at great depth. Consequently, the focal mechanisms have been frequently used to estimate the nature of the stress tensor in the seismogenic zones.

The focal mechanism describes the radiation pattern coming from the hypocenter of an earthquake and is related to the distribution of amplitude, polarity and/or polarization of the initial impulse of the phases P and/or S coming to the seismic stations located around the epicenter of an earthquake. The orientation of the fault plane and auxiliary plane (which bound the compressional and extensional quadrants of the focal plane mechanism) define the orientation of the P (compressional), B (intermediate) and T (extensional) axes. These axes are sometimes incorrectly assumed to be the same as the orientation of  $\sigma_1$ ,  $\sigma_2$  and  $\sigma_3$ .

If friction is negligible on the faults in question (but higher in surrounding rocks), there can be considerable difference (15-20°) between the P, B and T axes and principal stress directions (McKenzie, 1969). An earthquake focal plane mechanism always has the P and T axes at 45° to the fault plane and the B axes in the plane of the fault.

It is necessary to underline that only for an homogeneous body axes P and T represent the principal axes of stress. The pressure and tension axes give the directions of maximum compression and tension in the Earth only if the fault surface corresponds to a plane of maximum shear. Since this is usually not true, the fault plane solution does not uniquely define the stress tensor orientation (although it does restrict the maximum compression direction to a range of possible angles). Thus, there is not an exact match between P and T axes and the orientations of the maximum compressive stress ( $\sigma_1$ ) and minimum compressive stress ( $\sigma_3$ ).

The same stress field may be responsible for dislocations on planes differently oriented. Given a set of focal mechanisms of earthquakes generated by the same stress field, the principal directions of stress can be determined through the use of inversion techniques, based on the slip kinematics and on the assumption that fault slip will always occur in the direction of maximum shear stress on a fault plane (among other Gephart and Forsyth, 1984; Micheal, 1984; Angelier, 1990).

## 4. Stress inversion from earthquakes

The orientations of fault planes and slip directions indicated by a population of earthquake focal mechanisms can be used to determine best fit regional principal stress directions and a measure of relative stress magnitudes under the assumption of uniform stress in the source region. These analyses allow for the possibility that failure occurs on preexisting zones of weakness of any orientation. The idea is to determine a uniform stress field compatible with the different failure mechanisms that characterize several earthquakes.

However, if there are a variety of different focal mechanisms within a region of uniform stress, then both the principal stress directions and a measure of relative stress magnitudes may be determined. This is possible because on each fault plane, slip occurs in the direction of resolved shear stress (Bott, 1959); with this constraint each observation places a strong restriction on the stresses that generated the fault motion. It happens that each focal mechanism is consistent with only a relatively limited family of stress tensors. By inspecting the overlap of families of stresses associated with a number of focal mechanisms, we can define the range of stresses which may have acted over the region.

The principal stress orientations and a scalar which describes the relative magnitudes of the principal stresses can be determined directly from earthquake focal mechanisms through the use of inversion techniques (Armijo and Cisternas, 1978; Ellsworth and Zhonghuai, 1980; Angelier, 1984; Gephart and Forsyth 1984; Michael 1987a,b).

The basic assumptions of these methods are:

- the stress orientation is spatially uniform within the volume containing the event locations;
- the tangential traction on fault plane is parallel to the slip direction;
- enough variety on the fault plane orientations.

The accuracy of these inversion techniques depends on the uncertainty of the focal mechanisms and the fault/auxiliary plane ambiguity.

In Ellsworth and Zhonghuai (1980) method the orientation of the fault plane is taken as perfectly known, and the inverse method involves minimizing, in a least squares sense, the component of shear stress perpendicular to the observed slip direction (or, equivalently, minimizing the sine of the angle between the observed and predicted slip directions) by adjusting the orientation and relative magnitude of the (uniform) principal stresses. This is not the appropriate minimization for earthquake focal mechanism data because it implicitly assumes that the only errors are in the measurement of the direction of slip on the plane, whereas there is often substantial uncertainty in the orientation of the fault plane as well.

Angelier *et al.*, (1982) develop a technique which allowed for error in the orientation of the fault plane. Armijo and Cisternas (1978) developed an alternative approach in which they assumed that the data were exact but that the stress tensor varied in the region of study. They then found the orientation of the principal stresses that minimized the variations required in the relative sizes of the stresses needed to fit the data perfectly. But in this approach there clearly are errors in the observations and non-uniformity in the stress tensor may involve variation in principal stress directions as well as variation in stress magnitudes.

All these inversion techniques, when applied to earthquake focal mechanism data suffer from uncertainty as to which nodal plane is the true fault plane. These methods require that the investigator select the preferred nodal plane from each fault plane solution. Of course, normally this is done on the basis of knowledge of the local geology and tectonics. Often, however, there is no objective means to make this selection.

Gephart and Forsyth (1984) method automatically identifies one the preferred nodal plane from each focal mechanism as a more reasonable fault plane than the other for a given stress model following a grid search methodology.

The algorithm developed by Michael (1987a) is based on that formulation. The basic characteristic of this algorithm is the computation of the confidence limits

of the principal stress axes directions. Confidence limits are computed by a statistical tool known as bootstrap resampling.

The peculiarity of the technique developed by Rivera *et al.*, 1990 is to obtain the stress tensor, not from previously determined focal mechanisms, but rather from the original data of polarities of P arrival and take-off angles for source-station pairs. This method could be useful when the number of the polarities is scarce to compute reliable focal mechanisms.

#### 4.1 Stress tensor from initial polarities of a population of earthquakes

An algorithm for the simultaneous estimation of the orientation and shape of the stress tensor and the individual fault plane solutions for a population of earthquakes will be now introduced. It corresponds to a synthesis of the methods used by Brillinger *et al.*, (1980) to obtain focal mechanisms and by Armijo and Cisternas (1978) for stress tensor analysis in microtectonics. The input data are the polarities of the P arrival and take-off angles for the set of source-station pairs. The method distinguishes, in general, which one of the nodal planes corresponds to the fault and gives the direction of the slip (Rivera L. and Cisternas A., 1990).

##### 3.2.1 The Method

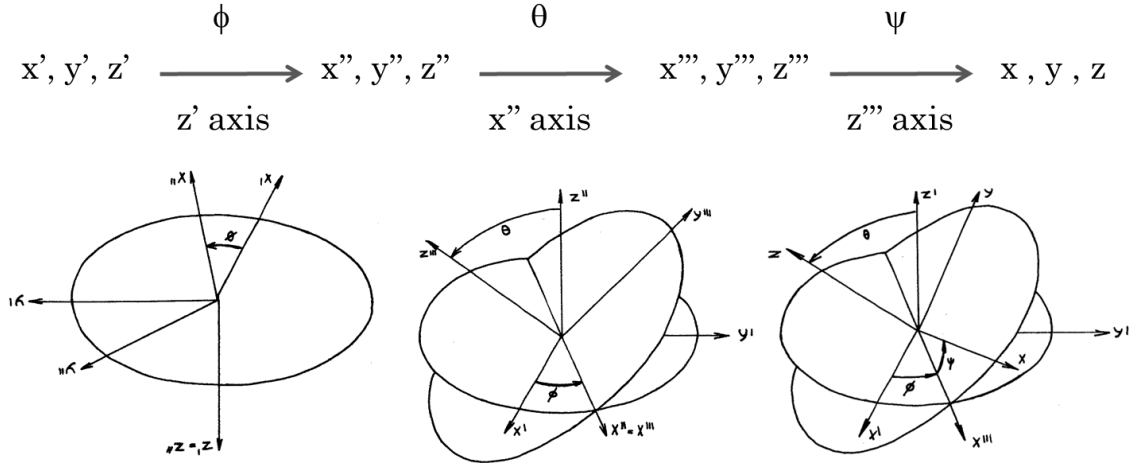
We used the method of Rivera L. and Cisternas A., (1990) in which the first-motion data, instead of the mechanic solutions, are directly used for inversion. The data are the raw first-motion polarities for a set of events.

The basic assumptions of the method are the same of other methods that found the principal stress orientations directly from earthquake focal mechanisms(e.g., Gephart and Forsyth 1984; Angelier 1984; Michael 1987;).

We define the stress tensor  $\Sigma$  (referred to the main axes):

$$\Sigma = \begin{bmatrix} \sigma_x & 0 & 0 \\ 0 & \sigma_y & 0 \\ 0 & 0 & \sigma_z \end{bmatrix} \quad (1.29)$$

We can obtain this form from geographic coordinates  $x', y', z'$  after a rotation using appropriate Eulerian angles ( $\phi, \theta, \psi$ ).



The coordinate change after the rotation is represented by the matrix (Goldestein, 1959):

$$\mathbf{M} = \begin{bmatrix} \cos \psi \cos \phi - \cos \theta \sin \psi \sin \phi & \cos \psi \cos \phi + \cos \theta \sin \psi \sin \phi & \sin \psi \sin \theta \\ -\sin \psi \cos \phi - \cos \theta \sin \psi \sin \phi & -\sin \psi \cos \phi + \cos \theta \sin \psi \sin \phi & \cos \psi \sin \theta \\ \sin \theta \sin \phi & -\sin \theta \sin \phi & \cos \theta \end{bmatrix} \quad (1.30)$$

To describe the relative magnitudes between three principal axis we define the parameter  $R = (\sigma_z - \sigma_x) / (\sigma_y - \sigma_x)$  with  $\sigma_y > \sigma_x$  (Armijo and Cisternas, 1978; Armijo 1982). The R-value is a scalar quantity describing the relative stress magnitudes (the shape of stress ellipsoid).

And under specific conditions (when z-axis is near the vertical,  $\theta < 15^\circ$ ), we can interpret R directly with the tectonic regime (for example with  $R=0$  we have uniaxial compression or with  $R=1$  uniaxial extension (Armijo 1968)).

If for example  $R > 1$  we have  $\sigma_z > \sigma_y > \sigma_x$  and so  $\sigma_z = \sigma_1$ ;  $\sigma_y = \sigma_2$ ;  $\sigma_x = \sigma_3$ .

If  $0 < R < 1$  we have  $\sigma_y > \sigma_z > \sigma_x$  and so  $\sigma_y = \sigma_1$ ;  $\sigma_z = \sigma_2$ ;  $\sigma_x = \sigma_3$ .

If  $R < 0$  we have  $\sigma_y > \sigma_x > \sigma_z$  and so  $\sigma_y = \sigma_1$ ;  $\sigma_x = \sigma_2$ ;  $\sigma_z = \sigma_3$ .

It is convenient to express this quantity through an angle  $\theta_r \in (-\pi/2, \pi/2)$ , the new variable is defined by:

$$R = \frac{1}{2}(1 + \sqrt{3} * \tan(\theta_r)) \quad (1.31)$$

And so under specific conditions, we have compression with  $\theta_r \in (-\pi/2, -\pi/6)$ , slip with  $\theta_r \in (-\pi/6, \pi/6)$  and extension with  $\theta_r \in (\pi/6, \pi/2)$ .

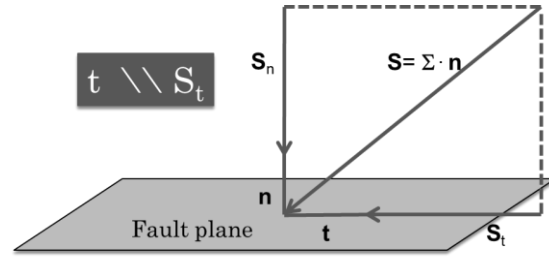
Thus, we can describe the state of stress with these three angular parameter  $\phi$ ,  $\theta$ ,  $\psi$ ,  $\theta_r$ .

The method is based on two fundamental hypothesis.

The first one is the “*Bott's hypothesis*”:

we assume that the slip vector ( $t$ ) on the fault plane is parallel to the tangential stress ( $S_t$ ).

The fault plane is described by the unit normal vector  $\mathbf{n} = (l, m, n)^T$  where  $l, m, n$  are the components in the system of the principal axes of stress.



We define the stress acting on this fault  $S = \Sigma \mathbf{n}$  and we decompose  $S$  in a normal and tangential component :

$$\mathbf{S}_n = (\mathbf{n}^t \mathbf{S}) \mathbf{n} = (\mathbf{n}^t \Sigma \mathbf{n}) \mathbf{n} \text{ (projection of } \mathbf{S} \text{ on } \mathbf{n}) \quad (1.32a)$$

$$\mathbf{S}_t = \mathbf{S} - \mathbf{S}_n = \Sigma \cdot \mathbf{n} - (\mathbf{n}^t \Sigma \mathbf{n}) \mathbf{n} \quad (1.32b)$$

and so

$$\mathbf{S}_t = \begin{bmatrix} \sigma_x l \\ \sigma_y m \\ \sigma_z n \end{bmatrix} - \begin{bmatrix} (\sigma_x l^2 + \sigma_y m^2 + \sigma_z n^2) l \\ (\sigma_x l^2 + \sigma_y m^2 + \sigma_z n^2) m \\ (\sigma_x l^2 + \sigma_y m^2 + \sigma_z n^2) n \end{bmatrix} \quad (1.33)$$

and for the three direction

$$(S_t)_x = (\sigma_x(1 - l^2) - \sigma_y m^2 - \sigma_z n^2) l = \dots = (\sigma_y - \sigma_x) (- (m^2 + n^2 R)) l$$

$$(S_t)_y = (\sigma_y - \sigma_x) (1 - (m^2 + n^2 R)) m$$

$$(S_t)_z = (\sigma_y - \sigma_x) (R - (m^2 + n^2 R)) n$$

We defined  $K = m^2 + n^2 R$  and so  $\mathbf{S}_t = (\sigma_y - \sigma_x) (-Kl, (1-K) m, (R-K)n)^t$

For the Bott's hypothesis the unitary vector on the direction of the strike ( $t$ )

$$\mathbf{t} = \text{unit} \begin{bmatrix} -Kl \\ (1-K)m \\ (R-K)n \end{bmatrix} \quad (1.34)$$

with  $R = (\sigma_z - \sigma_x) / (\sigma_y - \sigma_x)$  and  $K = m^2 + n^2 R$

The normal unitary vector in geographic coordinates is

$$\mathbf{n}' = (\sin \delta \sin \phi_s, -\sin \delta \cos \phi_s, \cos \delta)^t \quad (1.35)$$

The relation  $\mathbf{n} = \mathbf{M}\mathbf{n}'$  allows us to move on to the coordinates system of principal axis (l,m, n) using the rotation matrix  $\mathbf{M}$  in (1.34) to found t.

It must be given to geographical coordinates across the relation  $\mathbf{t}' = \mathbf{M} \mathbf{t}$ .

To resume the Bott's hypotesis, we have slip vector as a function of the parameters  $\phi, \theta, \psi, \theta_R, \phi_s, \delta$ .

The second hypotesis is "double couple point source".

The theoretical amplitude of the P-wave radiation pattern for a double couple point source is (Aki and Richards, 1980):

$$A_P = 2 (\mathbf{r}^t \mathbf{n}) (\mathbf{r}^t \mathbf{t}) \quad (1.36)$$

Where  $\mathbf{r}$  is the unit vector in the source-observer direction. This amplitude is a function of the orientation of the fault plane ( $\mathbf{n}$ ), and of the orientation and shape of the stress tensor ( $\phi, \theta, \psi; R$ ).

### *Forward problem*

Then the *forward problem* can be defines in the following manner: suppose we know the stress parameters and we assume a fault plane corresponding to the i-th earthquake ( $\mathbf{n}_i$ ). Then we compute the unit slip vector  $\mathbf{t}_i$  and hence the polarity  $Y_{ij}$  of P arrival at the j-th station in this way :  $Y_{ij} = \text{sign} (A_{ij})$

Where  $Y_{ij} = +$  we have compression and where  $Y_{ij} = -$  dilatation

$$Y_{ij} = Y_{ij} (\phi, \theta, \psi; \phi_s(i), \delta (i) ; \phi(j), i_\xi(j) )$$

where  $\phi, \theta, \psi$  describe the orientation of stress tensor;  $\phi_s(i), \delta (i)$  describe the fault plane for each earthquake; and  $\phi(j), i_\xi(j)$  describe the position of the station on focal sphere.

### *Inverse problem*

For our problem, given a set of polarities  $Y_{ij}$  of the initial motion of waves from  $N$  earthquakes recorded at  $M$  stations, our aim is to obtain the orientation and the shape of the stress tensor that is compatible with it and the fault plane of each individual earthquake.

Rivera formalized this problem with a probabilistic approach using a maximum likelihood algorithm (Brillinger *et al.*, 1980).

The model parameters are the 3 orientation parameters,  $\phi$ ,  $\theta$ ,  $\psi$ , for the stress tensor, 1 parameter for the stress ratio  $R$  and  $2N$  parameters,  $\phi_{si}$  and  $\delta_i$  with  $i=1,2,\dots,N$ , for the fault planes where  $\phi_{si}$  and  $\delta_i$  are strike and dip of the fault plane of event  $i$ , and  $N$  is the number of events used for the inversion.

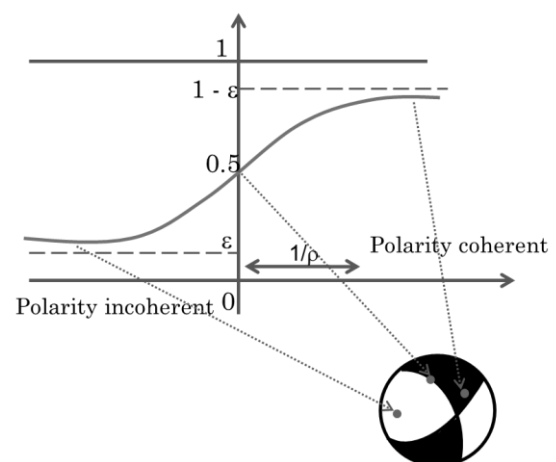
Then if we want to represent these parameters by a vector we can write  $m = (\phi, \theta, \psi, R, \phi_{si}, \delta_i = 1, 2, \dots, N)$ .

The algorithm described by Rivera L. and Cisternas A. (1990), the likelihood function  $L(m)$  is defined to measure the agreement between the first-motion data and the predicted polarities. In the definition of  $L$ , the contribution of each polarity is weighted as a function of the amplitude of the predicted P-wave radiation pattern.

The sample space is the set of all the possible outcomes of measuring polarities at the given source-station pairs. The probability of having a compression at a given station from a given earthquake is

$$P = \varepsilon + (1 - 2\varepsilon) \Phi(\rho A) \quad (1.37)$$

Where  $\varepsilon$  is a parameter that allows for errors in reading polarities ( $\varepsilon \in [0, 0.5]$ );  $\Phi$  is the normal cumulative function and  $\rho$  is a factor dependent on the amplitude of the signal (distance, magnitude, quality factor) and can be interpreted as an indicator of the accuracy of the take-off angle of the ray.



The probability to obtain a coherent lecture (A positive) is larger than 0.5. It increases with the size of the radiation pattern and tends to  $(1-\varepsilon)$ . Instead for the negative lecture the probability is smaller than 0.5 (it tends to  $\varepsilon$ )  $\varepsilon \in [0, 0.5]$ . For a seismogram with a good signal/noise ratio  $\varepsilon$  is equal to 0.

The parameter  $\rho$  governs the slope of this probability. With a large  $\rho$  the function is like a step.

The probability of reading a dilatation is  $1-P (Y = +)$ . The logarithm of the probability that a set of observed polarities  $Y_{ij}$  correspond to a model producing a theoretical amplitudes  $A_{ij}$  is given by the expression (Buforn, 1985):

$$L = - \sum \log \frac{1}{2} [ (1+Y_{ij} (1-2\varepsilon) \{2\Phi(\rho A_{ij}) -1 \} ] \quad (1.38)$$

Where  $L$  is a function of the parameters of the model through the theoretical amplitudes  $A_{ij}$ .

The parameters of the stress tensor and the orientation of the fault planes are chosen so that they maximize the likelihood function  $L$ . An initial model  $(\phi, \theta, \psi, \theta_R, \mathbf{n}_i)$  is modified in an iterative process up to the point where a given convergence criterion is satisfied. Since the dimension of the parameter space involved in the inversion is large, the calculations were carried out by using a quasi-Newton method (Harwell Scientific software Library).

The algorithm takes a given starting model  $\mathbf{m}_0$ , uses the gradient of  $L$  to sweep the model space, improves the fit, and iterates until a small enough gradient is found (Rivera and Kanamori 2002). Because of the binary nature of the data and the non-linearity of the problem, the procedure just described does not necessarily converge to the best solution, and can settle at a local minimum.

### *Error estimation*

Rivera *et al.*, 1990 followed the maximum likelihood procedure described by Brillinger *et al.*, (1980) in the estimation of uncertainties of the model parameters.

We compute the information matrix  $I(\lambda)$

$\lambda$  : estimated value of the parameters of the model ( $R$ , Euler's angles, and position of each poles of the fault planes on the sphere).

$$I(\lambda) = \left[ \sum_{ij} \left( \frac{\partial P_{ij}}{\partial \lambda_m} \frac{\partial P_{ij}}{\partial \lambda_n} \right) / \{P_{ij}(1 - P_{ij})\} \right] \quad (1.41)$$

Where the average is performed over all the possible configurations in the sample space, and the sum is made over all the pairs station-source.

The covariance matrix is then obtained as the inverse of the information matrix  $C = [I(\lambda)]^{-1}$  and then we can estimate the confidence ellipses of the poles of the fault planes on the focal sphere, and of the main axes of the stress tensor, together with the variance of the shape factor.

### *Analysis of the discrimination between fault and auxiliary planes*

We have seen in the equation (1.34) that the stress tensor determines the slip vector on a given fault plane, and hence the second nodal plane of the focal mechanism. The action of the same stress tensor on this second plane will not general, a slip vector orthogonal to the first plane.

The discrimination is not possible in some cases:

- If the stress tensor has a cylindrical symmetry ( $R=\pm\infty$  ;  $R=0$  ;  $R=1$ )
- if the normal to the fault plane happens to be orthogonal to one of the main axis of the tensor (in other words, if the fault plane passes through one of the principal axes of stress ( $l=0, m=0, n=0$ ))

# Chapter 2

## Geological and geophysical setting of the investigated area

---

### 1. Introduction

The Campania-Lucania region is located in the axial portion Southern Apennines, an Adriatic-verging fold-and-thrust belt, tectonically stacked over the flexured southwestern margin of the Apulia foreland.

The chain is located between the Tyrrhenian back-arc basin to the west and the Bradano foredeep to the east. During the Middle Miocene - Late Pliocene, several compressive tectonic phases, associated with the collision between the African and European margins, caused thrusting and stacking of different units toward stable domains of the Apulia foreland (whose sedimentary cover is formed by the Apulia Carbonate Platform, ACP). From Late Tortonian to Early Pleistocene, the system rapidly migrated to east as a consequence to “eastward” retreat of the sinking foreland lithosphere (Malinverno and Ryan, 1986; Patacca and Scandone, 1989, Patacca *et al.*, 1990).

The current structural complexity of the chain is also due to the different paleogeographic domains involved in the Southern Apennines tectonic units. The basinal facies successions allowed ductile deformation, while the carbonate platform successions mainly show a brittle behavior (D’Argenio *et al.*, 1974; Improta *et al.*, 2003). In addition, the deformation did not proceed cylindrically, but it was characterized by out-of-sequence thrust-propagation processes (Roure *et al.*, 1991). During the Late Pliocene - Early Pleistocene time span, the fold-and-thrust belt evolved tectonically by forming different arcs: the NNW-SSE-trending Molise-Sannio arc, to the north, and the WNW-ESE-trending Campania-Lucania arc, to the south.

Since the Middle Pleistocene, the fold-and thrust-belt started to uplift and to be affected by a NE-SW extensional tectonic regime, which caused the development of extensional fault systems along the core of the chain, which cut the preexisting compressional stack further complicating the internal geometry of the thrust belt. The extensional stress regime is still active along the chain axis, as indicated by the analysis of surface geological indicators, as well as of breakout, seismic and GPS data (Pantosti and Valensise, 1990; Frepoli and Amato, 2000; Montone *et al.*, 2004; DISS Working Group, 2010; Devoti *et al.*, 2008; Pasquale *et al.*, 2009; De Matteis *et al.*, 2012 under revision) and is responsible for the present-day seismicity in the Apennines chain. The background seismicity is mainly distributed along the axis of the chain and it is characterized by low to moderate magnitude earthquakes. It has to be noted, however, that the seismicity that occur between the Apennines chain and the Adriatic foreland may nucleate at depth between 10 and 25 km (Valensise *et al.*, 2004).

In particular, the Campania-Lucanian region is one of the most active seismic zones of the Apennines chain. Large destructive earthquakes occurred both in historical and recent times in this region, which was struck on 23 November 1980 by one of the strongest events ( $M 6.9$ ) in the past century. Detailed seismological studies on this earthquake have demonstrated the complexity of its source mechanism, which consists of at least three normal-faulting ruptures nucleated in a time range of 40 s on approximately 60 km long, NW-SE striking, three individual fault segments (Westaway and Jackson, 1987; Bernard and Zollo, 1989; Pantosti and Valensise, 1990; Amato and Selvaggi, 1993 ).

More than 30 years after this event, the seismotectonic environment that encompasses the fault system on which the 1980 earthquake occurred, shows a continuous background seismic activity including moderate-sized events. Since 1980, a normal faulting mechanism earthquake ( $M_L=4.9$ ) happened within the epicentral area of the 1980 earthquake on 3 April 1996. Moreover, two moderate magnitude seismic sequences occurred between 1990 and 1991 ( $M_L=5.2$  and  $M_L=4.7$  for the two mainshocks) in the Potenza region, located about 40 km to

the SE of the 1980 Irpinia aftershock area (Ekstrom, 1994). These latter sequences were characterized by dextral strike-slip faulting mechanisms and E-W strike (Di Luccio *et al.*, 2005, Boncio *et al.*, 2007).

The crustal tectonic setting of the Campania-Lucanian region has been defined by several geological and geophysical studies like tomographic studies (Amato and Selvaggi 1993, Chiarabba and Amato 1994, De Matteis *et al.*, 2010), analysis and joint interpretation of gravity data, seismic reflection lines and subsurface information from many deep wells (Improta *et al.*, 2003), in many cases carried out for hydrocarbon exploration purposes (Mostardini and Merlini, 1986; Patacca and Scandone, 1989, 2001; Casero *et al.*, 1991; Roure *et al.*, 1991; Menardi Noguera and Rea, 2000; Scrocca *et al.*, 2005).

The inferred crustal models show considerable lateral variations of the medium properties moving perpendicularly to Apennines belt. This variability is consistent with the presence of the Apulia Carbonate Platform, Western Carbonate Platform and basinal deposits successions, which form different tectonic units piled in the thrust stack. In addition, major lithological variations are evident along the strike of the mountain range, the most relevant being an abrupt deepening of the Apulia Carbonate Platform to the southeastern part of the investigated region (Improta *et al.*, 2003).

In the epicentral region of the 1980 event, the structural setting of the buried Apulia Carbonate Platform and underlying Permo-Triassic basement appears to be correlated with the P-wave velocity variations in the upper crust and with the aftershocks distribution. The structural highs of the Apulia Platform correspond to high-velocity regions, where aftershocks and coseismic slip of the mainshock are concentrated. This correlation suggests that the lithological heterogeneities in the upper crust, and in particular the Apulia Carbonate Platform units play a primary role in the rupture propagation and aftershocks distribution (Amato and Selvaggi, 1993; Improta *et al.*, 2003).

## 2. The Southern Apennines

Moving from north-east to south-west, i.e. from the foreland to the chain, the Southern Apennines are characterized by four main structural domains: the Apulian foreland, the Bradanica foredeep, the Apennines chain and the Tyrrhenian basin (Patacca and Scandone, 1987; Figure 2.1).

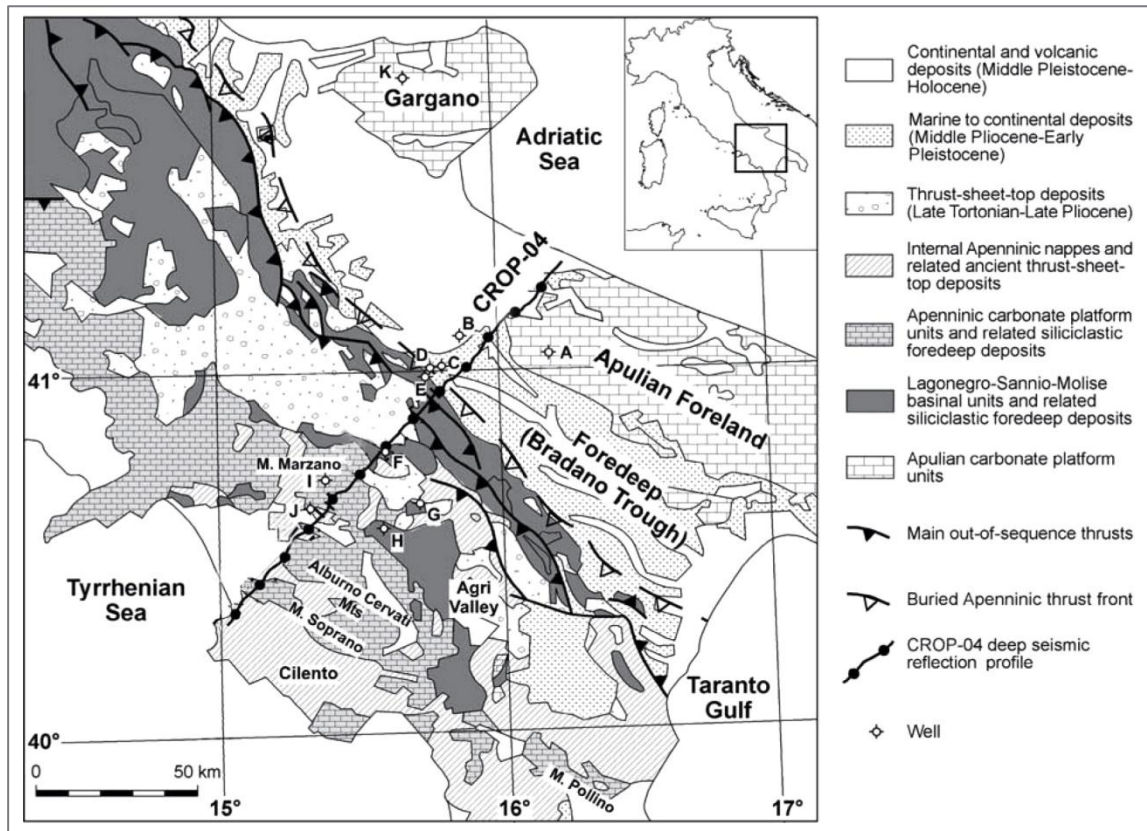


Figure 2.1 Simplified geologic map of Southern Apennines (from Scrocca *et al.*, 2005). Letters refer to deep wells (A, Puglia 1; B, Gaudioiano 1; C, Bellaveduta 1; D, Lavello 5; E, Lavello 1; F, S. Fele 1; G, M. Foi 1; H, Vallauria 1; I, S. Gregorio Magno 1; J, Contursi 1; K, Gargano 1).

The Apulian foreland, with its Meso-Cenozoic sedimentary cover (ACP - Apulia Carbonate Platform), is considered a stable area with respect to the Apennines, being only marginally involved in the tectonic movements that affect the Apennines chain. The few not negligible active faults that characterize this foreland are mainly E-W trending, subvertical right-lateral shear zones (e.g., the Mattinata fault in the Gargano promontory). The stratigraphic succession consists of continental and shallow marine Permo-Triassic deposits (Verrucano).

These are covered by Triassic evaporites, limestones and dolomites. In turn, they are topped by carbonate platform deposits, with a thickness ranging from 4 km in the Gargano area to more than 6 km in Salento, as confirmed by deep well data and seismic reflection lines (Roure *et al.*, 1991).

Towards SW, the foreland plunges below a partially deformed foredeep basin (Bradanic foredeep; Figure 2.1). Along the eastern side of the Bradanic foredeep, Plio-Pleistocene terrigenous deposits stratigraphically cover the flexured ACP (Casnedi, 1988). Moving westward, toward the front of the orogenic wedge, the buried Apulia foreland progressively dips below the rootless tectonic units of the Apennines and it is in turn involved in the folds and thrusts of the belt (Roure *et al.*, 1991).

The orogenic stack overlying the ACP is formed by thrust sheets coming from the deformation of the stratigraphic successions associated with the following main paleogeographic domains (Figure 2.2; Patacca *et al.*, 1992):

- shallow-water, shelf-margin and basinal facies successions (Lagonegro Basin, LB, Middle Triassic-Miocene), paleogeographically located between the ACP and the Western Carbonate Platform. The LB units are formed by two complementary parts of the lithostratigraphic succession: (i) a Triassic-Lower Cretaceous succession, consisting of siliciclastic deposits and dolomites, cherty limestones, radiolarites and siliceous claystones with limestones; and (ii) an Upper Cretaceous-Lower Miocene clayey succession mainly composed of carbonate resediments, arenaceous turbidites, varicoloured clays and quartzarenites, covered by Upper Miocene siliciclastic foredeep deposits and calcareous turbidites;
- the Western Carbonate Platform succession (WCP; or Apenninic Carbonate Platform), overthrusts on the LB units. It consists of a Mesozoic and Paleogene carbonate deposits succession, topped by Upper Miocene siliciclastic foredeep deposits; the latter were deposited on the WCP during its foredeep phase, thus before its involvement in the orogenic wedge;

- Jurassic-Miocene deep-sea succession sedimented on a thinned continental crust and now outcropping along the Tyrrhenian side of the Apennines and the northern boundary of the Calabrian Arc. It consists of varicoloured clays, arenaceous turbidites and carbonate resediments, and often appear as a chaotic tectonic *mélange*. The related tectonic units, the Sicilide Complex (SIC), overthrusts the WCP units. They have been incorporated in the thrust belt before the opening of the Tyrrhenian Basin and are the structurally highest units of the Southern Apennines.

Syntectonic terrigenous sequences unconformably cover the thrust sheets stack and represent the infill of Upper Tortonian to Lower Pleistocene satellite basins (Patacca and Scandone, 2001).

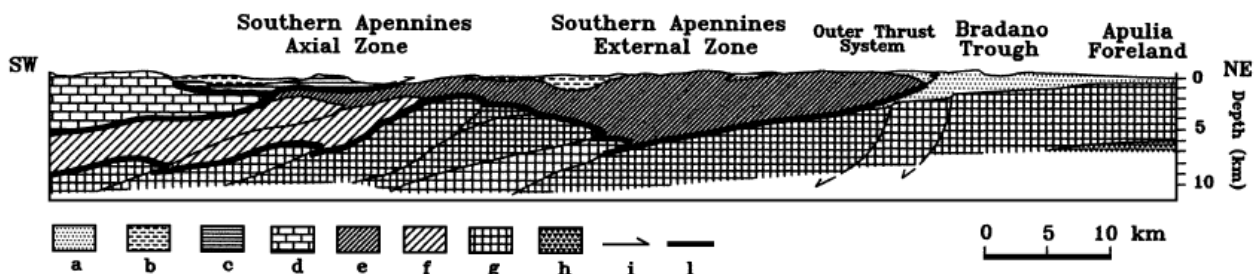


Figure 2.2 Schematic section of the shallow structure of the Southern Apennines across the Irpinia region. Legend : (a) Plio-Pleistocene deposits of the Bradano Trough; (b) thrust sheet-top successions (Upper Miocene-Lower Pleistocene); (c) Sicilide nappes (Paleogene-Lower Miocene); (d) Western Carbonate Platform (Mesozoic- Paleogene) and Upper Miocene flysch deposits associated with the foredeep phase; (e) Lagonegro Basin upper succession (Upper Cretaceous-Upper Miocene); (f) Lagonegro Basin lower succession (Lower Triassic-Lower Cretaceous); (g) Apulia Carbonate Platform (Triassic-Upper Miocene); (h) Verrucano Fm. (Permian-Lower Triassic); (i) thrusts and normal faults; (l) boundary of the main tectono-stratigraphic units (from Improta *et al.*, 2003).

Our knowledge on the upper crustal structure benefits from intense hydrocarbon exploration carried out in the study region. On the basis of industrial seismic reflection lines and deep well data, the tectonic structure of the Southern Apennines has been well reconstructed to a depth of about 10 km (Mostardini and Merlini, 1986; Patacca and Scandone, 1989, 2001; Casero *et al.*, 1991; Roure *et al.*, 1991; Menardi Noguera and Rea, 2000; Scrocca *et al.*, 2005).

According to the first reconstructions of the Southern Apennines (Mostardini and Merlini, 1986), the tectonic-stratigraphic units of this thrust belt are uprooted from the crystalline basement that is not involved in the accretion prism (thin-skinned model).

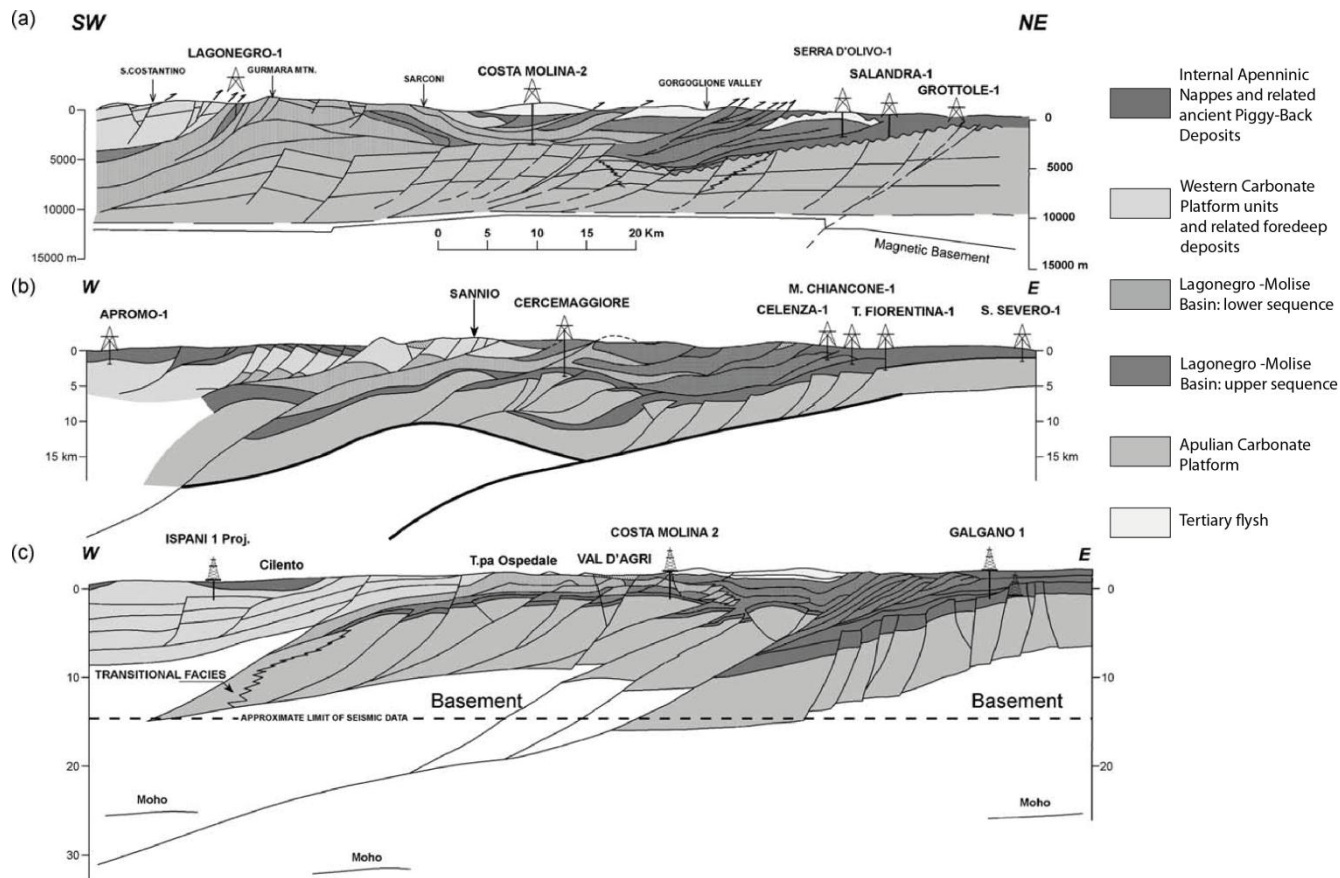


Figure 2.3 Comparison among different sections crossing the Southern Apennines and showing the alternative interpretations for the involvement of the crystalline basement in the deformation (Shiner *et al.*, 2004) : (a) Mostardini Merlini (1986); (b) Casero *et al.*, (1988) ; (c) Menardi Noguera and Rea (2000).

On the contrary, Casero *et al.*, (1988) and Roure *et al.*, (1991) suggested an involvement of the underlying crystalline basement (thick-skinned model) in the Neogene deformation. In addition, they suggested a crust thickening from Apulia foreland to the chain, where the crust is estimated to be about 50 km thick (Roure *et al.*, 1991). This thickness is plausible only assuming the basement involvement in the accretionary wedge. Such involvement allows explaining about 120 km shortening in the sedimentary cover, which is only partly compensated by a crustal thickening of the basement (Casero *et al.*, 1988). The basement involvement in the chain was confirmed by more recent investigations

(Figure 2.3) (e.g., Menardi Noguera and Rea, 2000; Improta *et al.*, 2003; Butler *et al.*, 2004).

This topic, however, is still matter of debate. For instance, the interpretation of a crustal seismic reflection profile (CROP04, located in Figure 2.1) by Scrocca *et al.*, (2005) constrains the orogenic wedge to a depth of about 15 km and maintains that the basement remains essentially undeformed and dips westward below the accretionary prism. This implies a total shortening of the allocthonous units (i.e. WCP, LB, ACP) estimated to be greater than 280-300 km (Figure 2.4).

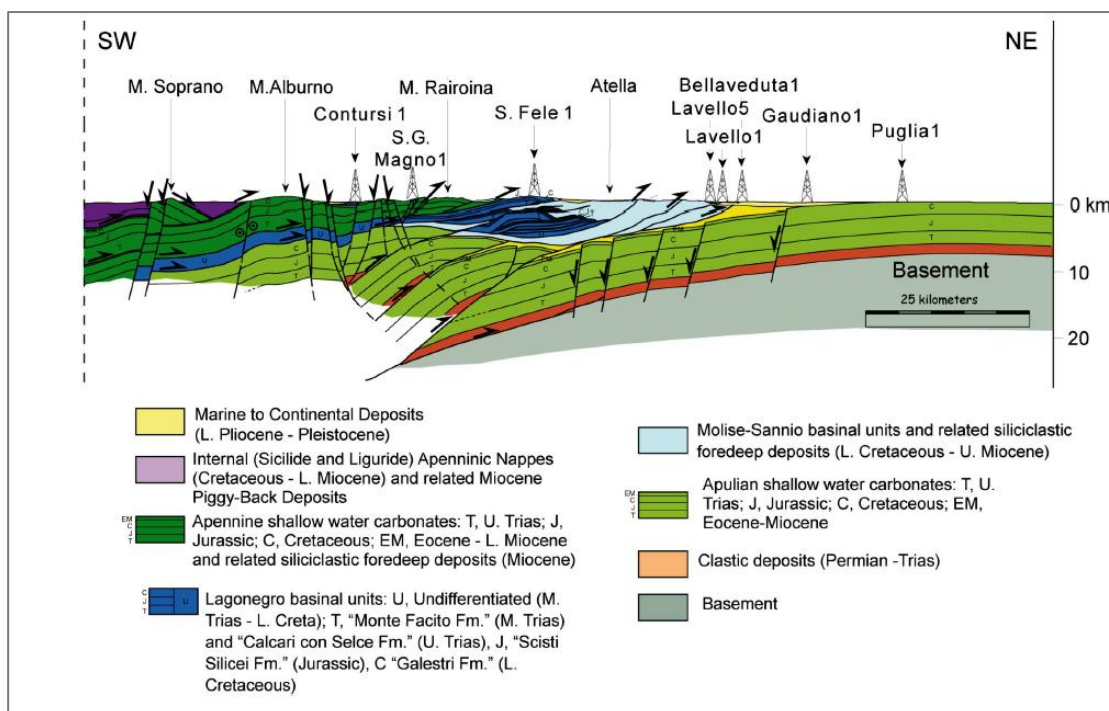


Figure 2.4 Regional geological cross-section built along the CROP-04 seismic reflection profile (Located in Figure 2.1) (Scrocca et a., 2005; Scrocca, 2010).

Finally, the back-arc basin, coinciding with the Tyrrhenian Sea, is the result of the extension that began in the late Miocene. It is characterized by crustal thinning and formation of new oceanic crust. The extensional tectonics in the Tyrrhenian basin gives rise to the formation of a series of depressions along the peri-Tyrrhenian margin of the Apennine chain (e.g., the Campanian Plain ).

Mainly E to NE-directed thrusting in the Apennines and associated foredeep-thrust-top basin sedimentation progressed toward the Adriatic foreland up to the Middle Pleistocene. Much of the Apennine chain has been dissected by normal and strike-slip faults that locally postdate thrust structures (e.g.,

Cavinato and De Celles, 1999). In the interior of the chain, these faults control Miocene-Pliocene basins and therefore are coeval with the thrust structures active further to the east. Indeed the entire chain has been convincingly described as a paired tectonic belt with extension in the orogenic hinterland balancing orogenic contraction on the forelandward side of the orogen (e.g., Lavecchia, 1988).

At ca. 800 ka, a major geodynamic change occurred, and a new tectonic regime was established in the Apennine chain and adjacent foothill areas. This is particularly well documented and widely accepted for the central and southern Apennines (e.g., Cinque *et al.*, 1993). Here, according to most authors, SW-NE-oriented active extension dominates over the core of the whole chain, as shown by breakout data and seismicity (Montone 2004), as well as by geological and geomorphological analyses (e.g., Galadini, 1999; D'Agostino 2001). In particular, along the topographic divide of the southern Apennines this extension accounts for large earthquakes generated by NW-SE striking normal faults (CPTI Working Group, 1999; Boschi 2000; Galadini 2000; Valensise and Pantosti, 2001, and references therein).

However, the 2002 Molise earthquakes, generated by E-W right-lateral faults located to the NE of the southern Apennines, supplied living evidence that in this part of the chain, toward the foreland, NW-SE normal faulting gives way to E-W, right-lateral, seismogenic faults.

These structures extend for tens of kilometers below the outer front of the southern Apennine orogenic wedge and, toward the east, below the foredeep deposits up to the foreland. Their present-day activity is suggested by both geological and seismological data, but their inception and growth date back to Mesozoic times. Therefore their activity is interpreted as the reactivation of inherited zones of weakness.

Major E-W oriented shear zones have been singled out roughly between the latitudes 40.300 N and 42.300 N, both onshore and offshore (Di Bucci and Mazzoli, 2003; Valensise *et al.*, 2004, Di Bucci 2010, and references therein).

Among them, the best constrained runs through the source region of the 2002 Molise earthquakes, continues toward the east crossing the mesoseismal area of the 1627 Gargano earthquake, then connects with the Mattinata fault and the Gondola line offshore (Di Bucci 2006).

## 2.1 Geodynamic and tectonic evolution

The convergence between the Africa and Eurasia plates has dominated the evolution of the Mediterranean basin since the Cretaceous, controlling the generation, spatial distribution and shape of all mountain chains and of the intervening basins. The structural setting of Apennines orogen is the result of several deformation events related to two main stages of geodynamic evolution of the region.

The first deformation event, occurred between the Cretaceous and the Oligocene, was characterized by the convergence between the European and the African plates and related subduction of the African lithosphere beneath the European one (Scandone, 1980). At the boundary between the Oligocene and Miocene, the Sardo-Corsican block underwent a counterclockwise rotation, which led to the opening of the Alghero-Provençal Basin (Cherchi *et al.*, 1982).

The second deformation event, which took place from the Tortonian, caused the opening of the Tyrrhenian basin and the eastward migration of the Apennines chain-foredeep-foreland system. This deformation event was characterized by a change in the tectonic evolution.

In particular, in the Southern Tyrrhenian basin, the intense extensional process caused the formation of new oceanic crust up to 10 km thick (Nicolich, 1989). The difference between the oceanic Ionian lithosphere, subducting underneath the Calabrian Arc, and the Adriatic continental lithosphere, subducting underneath the Southern Apennines, is reflected by the respectively different entity of flexural retreat (Lucente *et al.*, 1999).

The analysis of the tectonic evolution of the Apennine chain, in fact, reveals that from the Tortonian age the stress field which prevailed in that area was not

directly the NW-SE convergence between African and European plates, but rather the Adriatic lithosphere subduction, that induced the opening of the Tyrrhenian Sea and the Apennines thrusting (Luongo, 2002).

The model that can consistently interpret the coexistence of extensional processes along the inner side of the Apennine chain, the active compression along its outer front and the migration time of the entire system from west to east is still under discussion. From the Tortonian age, the beginning of the geodynamic processes recorded by the Tyrrhenian–Apennine system could be represented by the rise of the mantle in the center of the Tyrrhenian Sea and by its eastward migration with the formation of a convective cell (Luongo, 2002). In support to this hypothesis, the crustal structure of the Tyrrhenian domain, characterized by crustal thickness ranging from 6 to 15 km, as confirmed by the heat flow values (Della Vedova *et al.*, 1984) and the positive gravimetric anomalies, is compatible with an upwelling asthenosphere.

The east-southeastward younging of the Tyrrhenian-Apennine subduction system (Malinverno and Ryan, 1986; Royden 1987; Gueguen 1998; Rosenbaum and Lister, 2004), followed by the asthenospheric wedging at the retreating subduction hinge beneath the Southern Apennines and the southern Tyrrhenian Sea (Doglioni 1996), appear to have slowed and buckled during the Late Pleistocene after the collision with the thick continental lithosphere of the Apulia foreland at the front of the belt (Doglioni *et al.*, 1994).

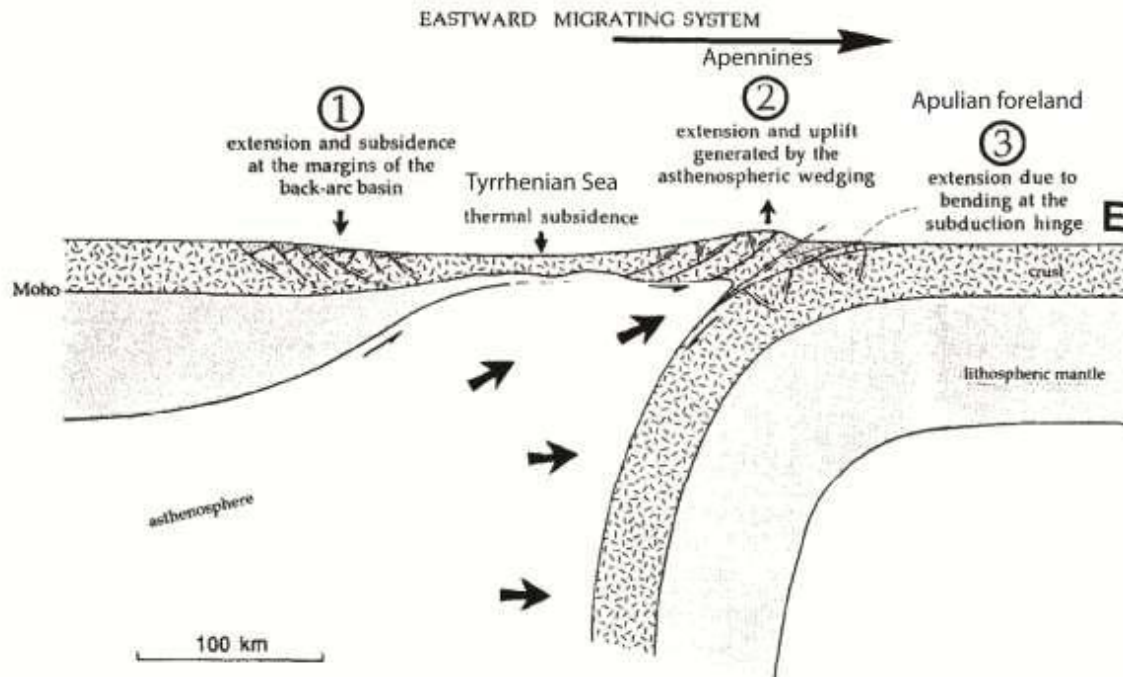


Figure 2.5 Representation of subduction system in Southern Italy (W-E section) and of the three different types of extensional environments (from Doglioni, 1996).

Three different types of extensional environments may be observed in an E-W section of the subduction system (e.g., see Figure 2.4): (i) the extension generated by horizontal stretching during back-arc opening, with the basal decollément at stretched lithosphere-asthenosphere boundary; (ii) the extension coeval with the uplift, that may be interpreted as due to the bending of the subducted lithosphere and to the upward push generated by the asthenospheric wedging at the subduction hinge; and (iii) the Apulia foreland extension, generated by the bending of the subducting lithosphere. It has normal faults terminating in the neutral crustal zone of folding, where flexural slip may form (Doglioni 1996). Many studies indicate that an extensional regime is active and responsible for most of the current seismicity in the Southern Apennines (Montone *et al.*, 2004). For instance, geodetic observations, together with seismological studies, reveal that the Apennine chain is undergoing a NE-trending extension, with seismic deformation rates higher in the southern portion (Di Luccio *et al.*, 2005; D'Agostino *et al.*, 2008).

As seen in the previous section, however, to the NE of the southern Apennines, toward the foreland, NW-SE active normal faulting gives way to E-W, right-

lateral, seismogenic faults. This is observed in a geodynamic setting characterized by the juxtaposition of various first-order structures, including (1) the Adriatic-Ionian-Hyblean foreland, formed by both continental and oceanic lithosphere; (2) a slab plunging into the southern Tyrrhenian asthenosphere; (3) the Tyrrhenian Sea, a young oceanic-type basin that is still undergoing significant stretching; (4) a continuous fold-and-thrust belt with variable strike, degree of shortening and uplift rates; and (5) the presence of active volcanoes. Di Bucci *et al.*, (2010) suggest that the Africa-Eurasia convergence acts in the background of all these structures, playing a primary and unifying role in the seismotectonics of the whole region.

This circumstance stems from a thorough investigation of foreland areas, where the effects of plate convergence are not masked by other regional-scale deformation phenomena. This is because the active tectonics signature that can be retrieved from field data is dominated by processes that are strictly related to the evolution of the mountain chains, such as the extension at the core of the orogenic stack and the compression at the leading front of the accretionary wedge (Di Bucci *et al.*, 2010).

We can conclude that, for the Italian peninsula, this interpretation model implicitly suggests to consider the active tectonics of the foreland and of the related chain separately. The foreland dynamics deals with long wavelength intraplate deformation, and therefore subtends the shallower and more local tectonic activity of the chain.

### **3. The Campania-Lucania region: crustal setting**

As already said in the previous sections, the Campania-Lucania region can be divided into four sectors, each of them characterized by distinct geological features (e.g., Improta *et al.*, 2003; Figure 2.6).

In the southwestern sector, the Meso-Cenozoic carbonate sequences of the WCP prevail, cropping out in the Picentini, Marzano and Maddalena massifs. In the Picentini and Marzano massifs, the carbonate platform sequences are highly

fractured and reach about 4000 m of total thickness. As clearly shown in few tectonic windows located in the Picentini massif, the WCP overthrusts the basal facies of the LB tectono-stratigraphic units. The overthrusting of the WCP is further documented by subsurface data from deep well logs (e.g., Contursi 1 well located in Figure 2.1; Improta *et al.*, 2003).

The extensional tectonics is responsible for the development of the Picentini and Marzano horsts and of the Sele graben, which are bounded by NW- and SE-dipping normal faults. Along the northeastern foothills of the Picentini and Marzano massifs and in the Sele graben, the WCP and its Upper Miocene, siliciclastic cover are overthrust by the Sicilide Complex, which mainly consists of varicolored clays. South of the Picentini massif, beneath the Sele plain, large southwest-dipping normal faults lower the buried carbonates of the WCP, which rapidly dips beneath Plio-Pleistocene marine and continental sediments. In turn, these deposits reach a 3 km maximum thickness in the Tyrrhenian offshore (Mostardini and Merlini, 1986).

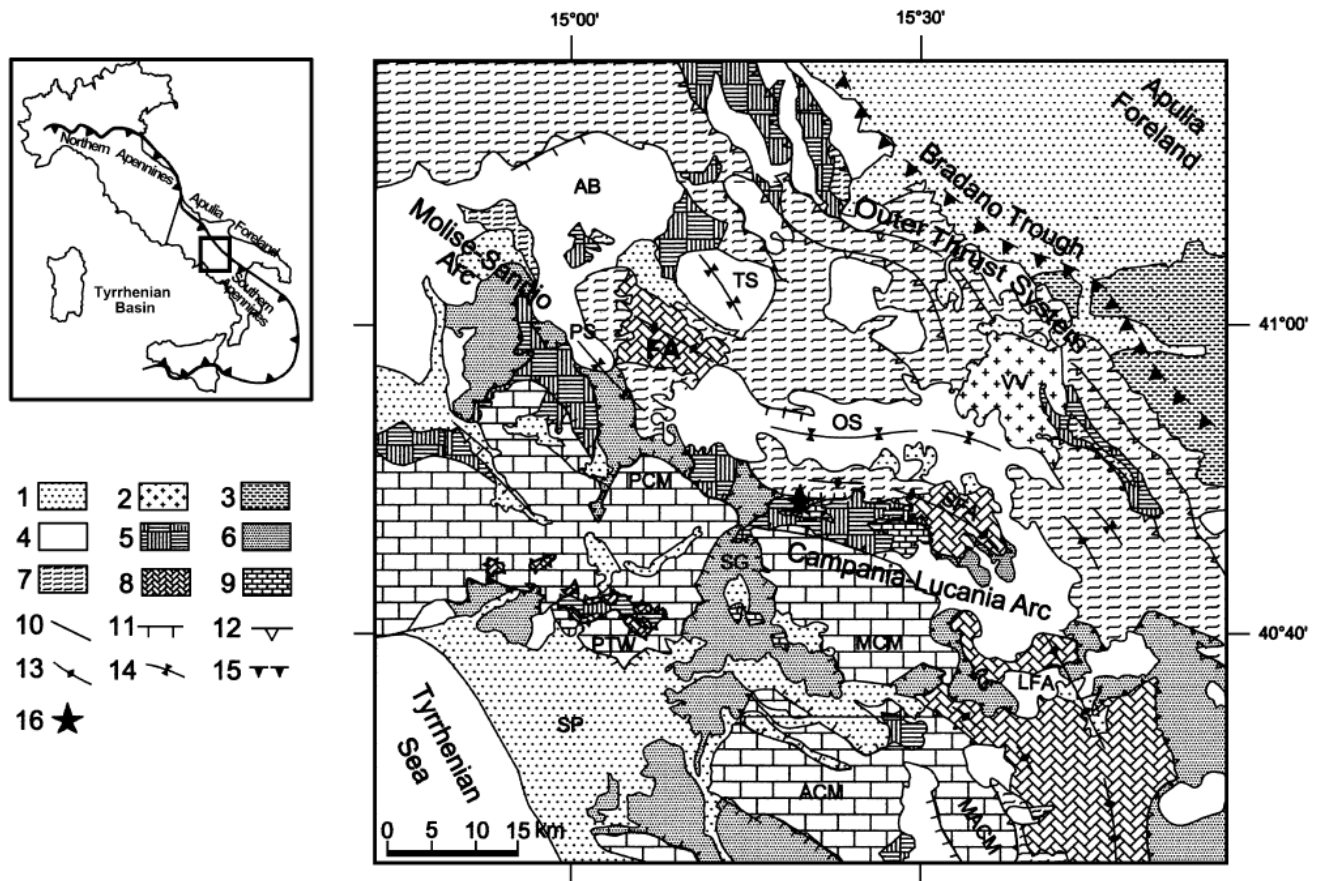


Figure 2.6 Geological map of the Irpinia region (Improta *et al.*, 2003). Legend : 1–Middle Pleistocene and Holocene deposits; 2–volcanites of the Vulture Volcano (Middle– Upper Pleistocene); 3–Bradano sedimentary cycle (Lower– Middle Pleistocene); 4–thrust sheet– top syntectonic clastic sequences (Upper Messinian– Early Pleistocene); 5–Upper Miocene siliciclastic flysch deposits (including the thrust sheet –top succession of the S. Bartolomeo Fm., Lower Messinian); 6–Sicilide and Sannio Complexes (Paleogene–Lower Miocene); 7–Tertiary deposits of the Lagonegro Basin; 8– Lagonegro Basin lower sequence (Lower Triassic –Lower Cretaceous); 9–Western Carbonate Platform (Mesozoic–Paleogene); 10–faults; 11–normal faults; 12–thrusts; 13–axis of antiform; 14–axis of synform; 15–buried frontal ramp of the Apennines thrust sheets; 16– epicenter of the 1980, Irpinia earthquake (from Westaway and Jackson, 1987). AB, Ariano Basin; TS, Trevico synform; PS, Paternopoli synform; FA, Frigento antiform; OS, Ofanto synform; SFA, S. Fele antiform; LFA, Lifo antiform; VV, Vulture Volcano; PCM, Pientini carbonate massif; MCM, Marzano carbonate massif; MACM, Maddalena carbonate massif; ACM, Alburno carbonate massif; PTW, Pientini tectonic windows; SG, Sele River graben; SP, Sele plain.

In the northwestern sector of the Campania-Lucania region, which corresponds to the southern edge of the Molise–Sannio arc (Patacca *et al.*, 1992), Upper Messinian–Early Pleistocene thrust sheet–top clastic sequences are widespread. These sequences, which cover Tertiary deposits of the Lagonegro Basin (LB) and Sannio Complex (SAC), form the infill of the Ariano Basin, as well as of the Paternopoli and Trevico synclines. The NW–SE-trending Paternopoli and Trevico

synclines are separated by the broad Frigento antiform, where siliceous claystones with limestones (Galestri Fm., Lower Cretaceous) of the LB crop out.

The northeastern sector extends from the outermost Apennine thrust system towards the Bradano Trough. Tertiary deposits of the LB, SAC and (Sicilide complex) SIC, as well as their covers of thrust sheet-top clastic sequences, are folded and thrust along the edge of the Bradano foredeep (Mostardini and Merlini, 1986; Casero *et al.*, 1988). Eastwards, post-orogenic shelf-to-continental clastic deposits of the Bradano sedimentary cycle (Lower-Middle Pleistocene, Patacca and Scandone, 2001) and Pleistocene volcanites of the Vulture Volcano seal the Apennine frontal thrust.

The southeastern sector includes the northern and central part of the Campania-Lucania arc (Patacca *et al.*, 1992). In this region, Mesozoic rocks of the LB are widespread. The Jurassic-Lower Cretaceous part of the succession (radiolarites, siliceous claystones) is exposed in the WNW-ENE trending San Fele antiform. On its southwestern side, the LB deposits are overthrust by the WCP units with their Upper Miocene siliciclastic flysch cover. Conversely, on the northeastern side, the San Fele antiform involves thrust sheet-top clastic sequences representing the Pliocene infill of the Ofanto Basin. This is a deep and narrow synform extending with a W-E direction between the Frigento and San Fele antiforms, thus with a trend that differs from the overall NW-SE direction of the Apennine structures. To the north, the Pliocene deposits of the Ofanto Basin lie only on Tertiary deposits of the LB and SIC, mainly consisting of varicolored clays.

The entire LB lower sequence, including the Triassic deposits (siltstones and dolomites, cherty limestones), crops out between the Lifo antiform, which strikes NNW-SSE, and the Maddalena carbonate massif. On the eastern foothills of the Maddalena massif, the WCP and the SIC overthrust the LB units.

The classical geological investigations to define the structural setting of the Irpinia region have been strongly improved by geophysical studies carried out in this area. Among other geophysical methods, a valuable contribution is provided

by seismic tomography, which helped to define the structure of the upper crust in the area and, in particular, to identify lithological heterogeneities interpreted as due to fault zones (Amato and Selvaggi, 1993; Chiarabba and Amato, 1994). In addition, the crustal structure was also reconstructed from the interpretation of 15 gravimetric profiles by Improta *et al.*, (2003). These researchers, through the modeling of gravimetric anomalies, constrained by seismic reflection data and well logs drilled for hydrological purposes, obtained 15 density sections for the study area. Each density range was associated with known major lithological units. The final model obtained shows significant lateral density variations, probably related to the NW-SE trends of the geological structures.

The Bouguer anomalies map, low-pass filtered for  $\lambda > 40$  km (Figure 2.7a), provides informations on the deep crust in Irpinia (Carrozzo *et al.*, 1981; Improta *et al.*, 2003). This map shows anomalies regularly trending NW-SE, with a minimum of -5 mGal in the Sannio region and a maximum of +10 mGal in correspondence with the Campania-Lucania arc. To the west of the axial zone of the chain, along the Tyrrhenian margin, a maximum of about +45 mGal can be observed, while in the east, along the Adriatic side, a maximum reaching approximately +60 mGal is observed.

The presence of these two maxima can be correlated with the depth and the trend of the Moho discontinuity in this part of the Southern Apennines. In the Apulia foreland area, the Adriatic Moho is located at a depth of about 30 km and plunges toward SW, reaching about 35 km depth beneath the Campania-Lucania arc. Near the Tyrrhenian coast, instead, the Tyrrhenian Moho is constrained at a depth of about 20-25 km (Nicolich, 1989). A step has been hypothesized between the two Moho surfaces.

The Piana del Sele tectonic depression corresponds to the SW-NE trending minimum, with a value of 32 mGal, which contrasts with the main NW-SE regional trend.

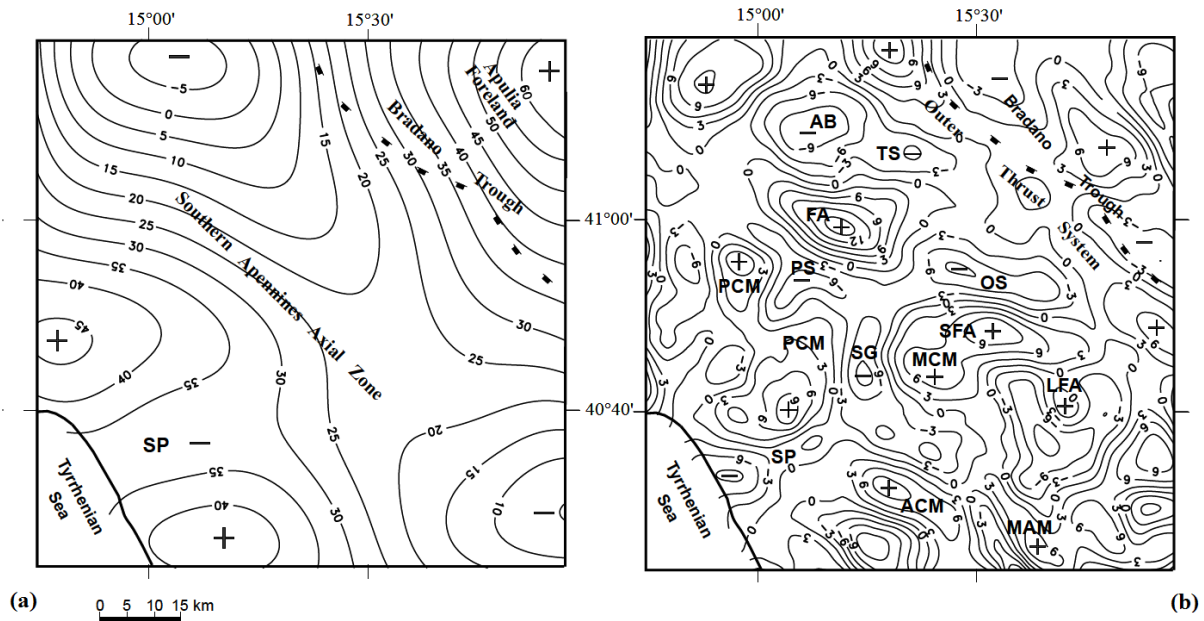


Figure 2.7 (a) : Map of the low-pass filtered Bouguer anomalies ( $\lambda > 40$  km) for the Irpinia region and surrounding areas; contour interval is 5mGal. (b) : Map of residual Bouguer anomalies for the same area; contour interval is 3 mGal. Legend : + indicate the relative maximum of the anomaly instead - the relative minimum; SP = Sele Plain; AB = Ariano Basin; TS = Treviso Synform; PS = Paternopoli Synform; FA = Frigento Antiform; OS = Ofanto Synform; SFA = San Fele Antiform; LFA = Lifo Antiform; PCM = Picentini Carbonate Massif; MCM = Marzano Carbonate Massif; ACM = Alburno Carbonate Massif; SG = Sele river Graben; (from Improta *et al.*, 2003).

The residual Bouguer anomaly map (Figure 2.7b) shows a quite complex pattern due to the presence of antiformal and synformal structures (Improta *et al.*, 2003). The largest anomalies fit with the San Fele and Frigento antiformal structures.

The Frigento anomaly is NW-SE oriented with a maximum of +15 mGal, probably due to the rise of the Apulia Carbonate Platform in this area. The San Fele Bouguer anomaly differs from Frigento one either for the maximum value (+9 mGal) either for the lower frequency content. These differences cannot be explained with lithological variations in the uppermost crust, suggesting the hypothesis of a considerable deepening of the ACP beneath the S. Fele antiform, with respect to the Frigento one, in agreement with the information provided by the deep wells and the seismic reflection data.

In the map of the anomaly of Bouguer residuals (Figure 2.7b), all the synforms filled by Pliocene thrust sheet-top clastic sequences are also well defined. The Ofanto syncline is correlated with a WNW-trending narrow anomaly (-9 mGal).

This anomaly is characterized by two sharp gradients towards its western and southern margins, probably due to the presence of important, shallow lateral lithological variations towards the Frigento and San Fele antiforms, respectively. Finally, the Sele graben is associated with a narrow negative anomaly (-9 mGal), which strikes N-S and separates the gravity high of the Marzano horst to the east (+ 6 mGal) from the gravity high of the Picentini horst to the west (+ 3 mGal).

In the epicentral area of the 1980 Irpinia earthquake (see the paragraph 4 for more details), a correlation was found between the geometry of the high density and high velocity structures of the buried Apulia units with the trend of the P-wave velocity anomalies as obtained from seismic tomography (Amato and Selvaggi, 1993). The structural highs of the buried Apulia units correspond to regions with high P-wave velocity values, where the "aftershocks" and the coseismic slip of the main events are concentrated. This correlation suggests that the geometry of the buried Apulia units plays a primary role in the rupture propagation. The velocity anomalies map (Figure 2.8b), in a layer from 0 to 3 km depth, shows a NNE-SSW trend of the anomaly at the northwest boundary of the epicentral region. This trend can be correlated with the ACP structural high of the Frigento antiform. To the southeast, this anomaly is characterized by a remarkable change in the velocity gradient, which decreases from 5.6 km/s to 4.2 km/s. This change can be interpreted as correlated with the plunge of the Apulia units from 0.25 km to 5 km depth, to the east of Frigento. Conversely, the high-velocity anomalies (5.2–5.4 km/s), which are present in the central sector of the epicentral region may be correlated with the extent of the carbonate thrust sheets of the Western Platform, whereas the low-velocity anomalies (4.4–4.8 km/s) located northeastward may be associated with the Ofanto synform, as already suggested by Amato and Selvaggi (1993).

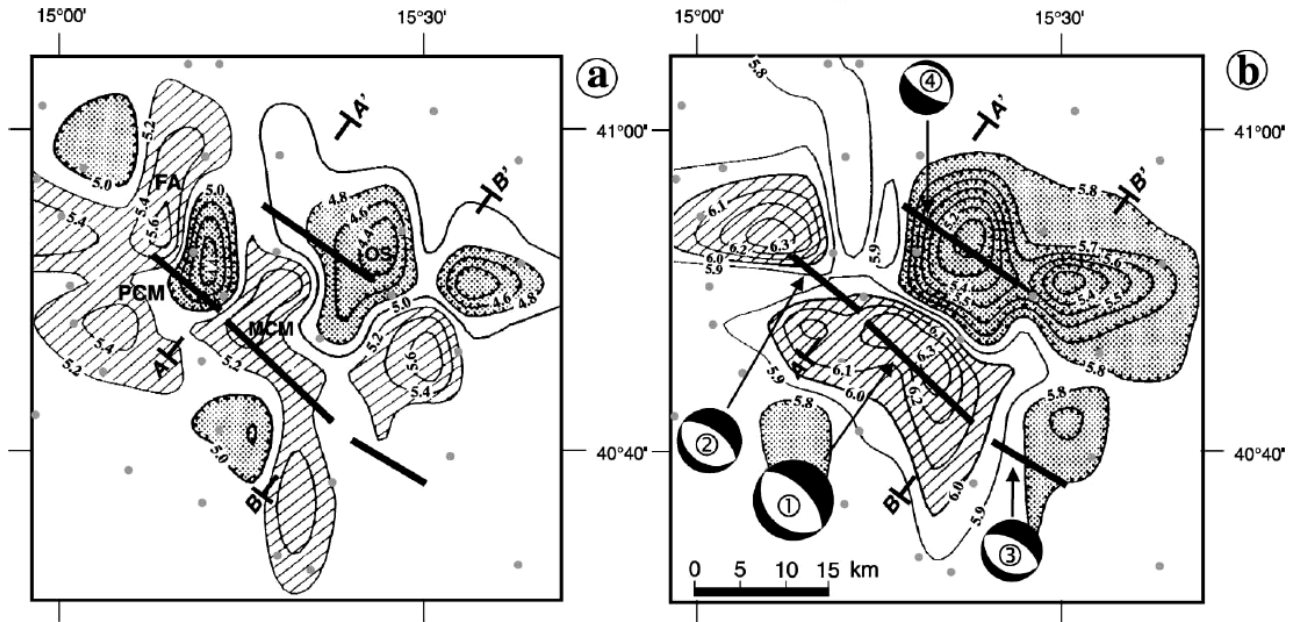


Figure 2.8 P wave velocity anomalies at the depth of 0-3 km (a) and 3-6 km (b) in the epicentral zone of the 1980 Irpinia earthquake (Improta *et al.*, 2003). The fault segments (black lines) and the focal mechanisms of the 4 sub-events are taken from Pantosti and Valensise, 1990 ( 1. Marzano segment, 2. Picentini segment, 3. San Gregorio segment, 4. Ofanto segment).

Between 3 and 6 km depth, however, the velocity anomalies map (Figure 2.8) is characterized by high velocities (between 6 and 6.3 km/s) to the north and south-west, and by low velocities (5.0-5.7 km/s) to the southeast. This distribution is well correlated with the morphology of the APC. In particular, the deepening of the ACP down to 5.5–6.0 km depth beneath the Ofanto synform corresponds to a pronounced WNW-trending negative anomaly in the tomographic image. In conclusion, the correlations outlined here indicate that the velocity structure in the upper crust is strongly influenced by the geometry of the ACP, whose structural lows and highs give rise to pronounced low- and high-velocity anomalies, respectively.

The aftershock distribution of 1980 earthquake (Amato and Selvaggi, 1993) suggests further considerations on the fault geometry and rupture propagation to the surface (Figure 2.9). The 1980 Irpinia aftershocks are confined in the upper crust at a depth between 0 and 12 km. This depth range corresponds to high-speed crustal volumes correlated in part with the massive carbonates of the Picentini and Marzano Mounts (Chiarabba *et al.*, 1996). Moreover, in these areas

the largest coseismic slip occurred, as indicated by strong motion data (Cocco and Pacor, 1993). An unexpected seismic behavior of the crustal volume corresponding to the Sele River Valley was revealed by the aftershocks analysis conducted by Amato and Selvaggi (1993), who studied the seismicity recorded in the months after the 1980 mainshock and found a marked decrease of activity in correspondence to the valley.

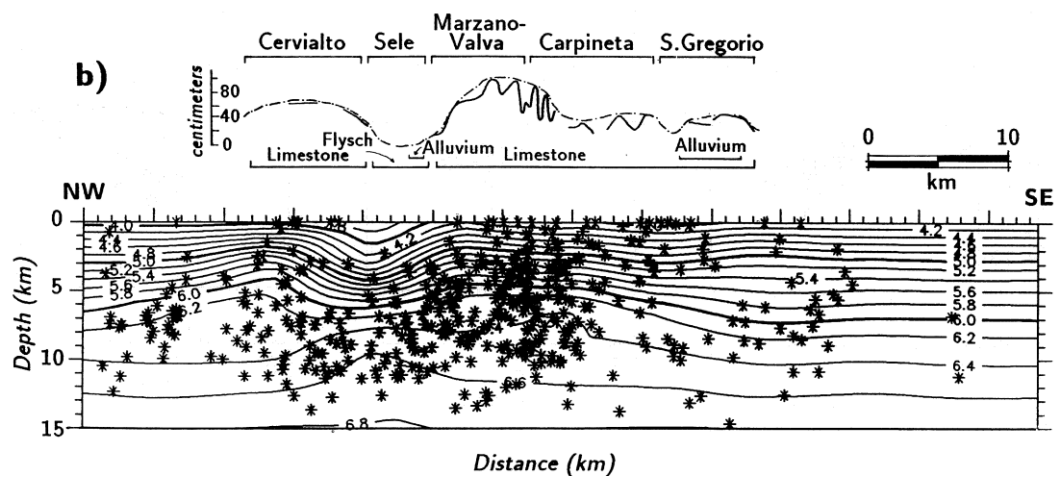


Figure 2.9 Section parallel to the main faults (Amato and Selvaggi, 1993). The stars denote the aftershocks of the Irpinia Earthquake. The seismicity is clustered beneath the Marzano-Valva sub-segments, where the most relevant surface deformation was observed (about 1 m). The Sele Valley, where any surface deformation was measured, is characterized by a low velocity zone coincident with a seismicity gap in the shallower 7 km depth. The surface slip has been inferred from the study performed by Pantosti e Valensise (1990).

According to Chiarabba and Amato (1994), rupture propagated through high-velocity areas, while the low-velocity zones are regions where rocks mechanical properties did not allow the surface deformation. Comparing the aftershocks distribution with crustal lithologies and 1980 seismogenic faults along sections crosscutting the fault system (faults acting from 0 s to 38 s, Figure 2.10; Improta *et al.*, 2003) we can observe that faulting activated the whole Mount Marzano fault segment, from 10-12 km depth up to the surface, where WCP deposits crop out. This fault segment is associated with a clear surface displacement (Westaway and Jackson, 1987; Pantosti and Valensise, 1990).

The rupture propagation of the Ofanto segment has been controlled by the vertical extent of the ACP: the rupture stopped crossing the low-density Tertiary

basinal terrains (mainly consisting of clayey successions) and the Pliocene clastic sequences of the Ofanto synform (Improta *et al.*, 2003).

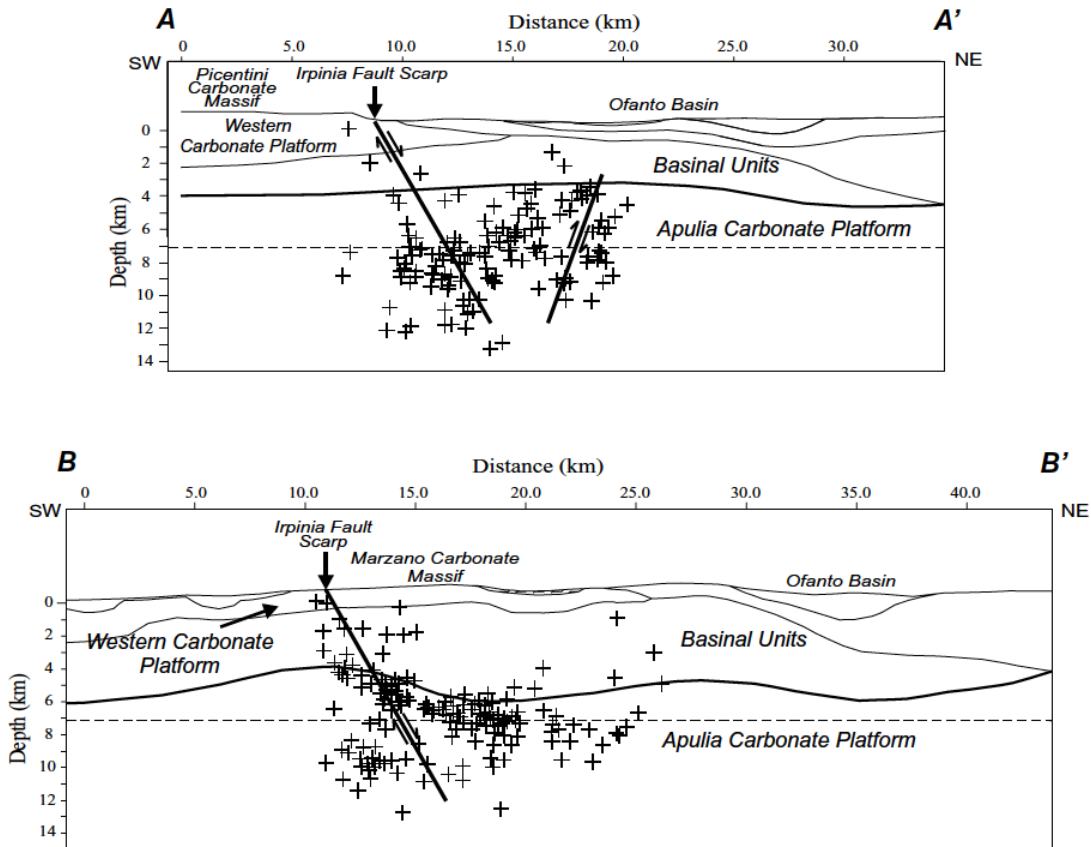


Figure 2.10 Fault segments and aftershocks of the 1980 Irpinia Earthquake, superimposed on two vertical sections, crossing the study area (from Improta *et al.*, 2003 and reference therein). The extent and the position of the fault segments are in agreement with the faulting model proposed by Pantosti and Valensise (1990). The aftershocks are mainly located in the Apulian Carbonate Platform Amato and Selvaggi, 1993.

Within the sedimentary units overlying to the ACP, the earthquake hypocenters are rare, and concentrate around the Mt. Marzano fault segment (Figure 2.10). Improta *et al.*, (2003), based on seismic reflection lines and on gravimetric and well data, suggest a rise of the Apulia Platform units in correspondence with the fault. The top Apulia is interpreted at 3.5-4 km depth, according to both a high velocity zone ( $V_p = 6.1-6.3$  km / s) identified by Amato and Selvaggi (1993) in the depth range between 3 and 6 km, and the location of the highest slip-rate on the fault surface, i.e. 1.0-1.2 m/s (Cocco and Pacor, 1993). These pieces of

information confirm that the rupture propagation and the aftershocks distribution are strongly controlled by the geometry of the buried Apulia carbonate units, which in this area represent the main lithological and rheological discontinuity in the upper crust (Improta *et al.*, 2003).

#### 4. Historical and instrumental seismicity

The Southern Apennines are a tectonically active region of Italy that accommodates the differential motions between the Adria and Tyrrhenian domains (Jenny *et al.*, 2006), to which almost all of the seismicity occurring in this region can be ascribed.

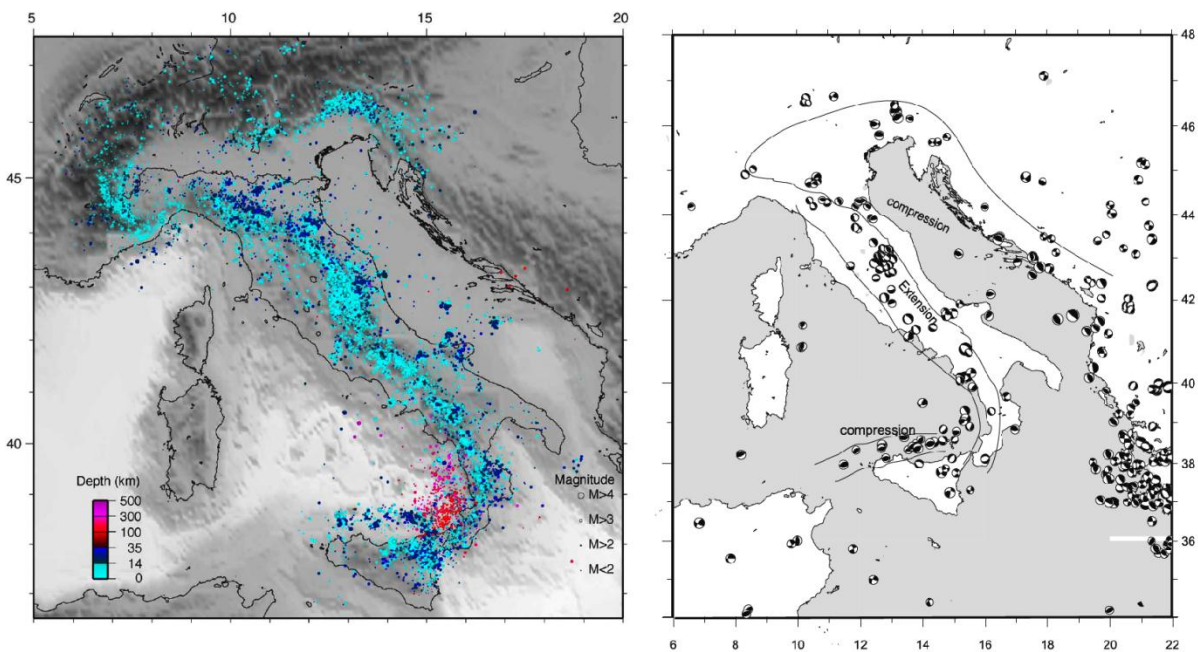


Figure 2.11 On the left : Hypocentral distribution of about 45,000 selected seismic events in the last 20 years (from Chiarabba 2005). Color scale, continuously varying, indicates the earthquakes depth (blue colours for the crustal seismicity and red colors for the mantle seismicity). The different size of circles represents the magnitude scale as indicated in the lower right corner. On the right : CMT and RCMT (Pondrelli *et al.*, 2002) solutions for the MN4.5 seismicity since 1976. The extension along the Apennines belt, as well as the compression around the Adria lithosphere and in the northern Sicily offshore are evident.

According to recent in-situ stress analysis (Montone 2004), seismological data, in particular earthquakes location, size and focal mechanisms, support the Southern Apennines as being characterized by an extensional tectonic regime

(Figure 2.11). Several geological and geophysical studies indicate that this extensional regime is still active and is responsible for the present-day seismicity of the southern Apennines region.

The investigated area is part of the Campania-Lucania region, where most of the earthquakes are concentrated within a long, narrow seismic belt, 30-50 km-large. In particular, two different crustal depths characterize the earthquakes: to the west, shallower earthquakes (depths <20 km) mark the chain axis (Irpinia area), whereas to the east, deeper earthquakes (about 20-40 km) are located in the foreland, both buried below the outer margin of the chain (Potentino area) and the foredeep, and exposed in the Apulia region (Figure 2.12). These two seismic zones are also characterized by different focal solutions, which indicate pure extension to the west (Irpinia area), and a strike-slip regime to the east.

Historically, the area have experienced many large and disastrous seismic events, among which those that occurred, for instance, in 1694, 1851, 1857 and 1930 (Figure 2.12), with the most recent event (November 23, 1980, M 6.9) represented by the complex normal-faulting Irpinia earthquake, which caused about 3,000 deaths and huge damage to the historical and civil heritage (Westaway and Jackson, 1984; Bernard and Zollo, 1989).

The November 23, 1980, M 6.9 earthquake had a complex source rupture, with distinct rupture episodes (Bernard and Zollo, 1998). Paleoseismological studies on two different sites along the fault (D'Addezio *et al.*, 1991, Pantosti *et al.*, 1993) showed that at surface, the fault activated by the 1980 earthquake had been active in the past 10.000 years, producing surface breaks similar to those observed during the 1980 earthquake.

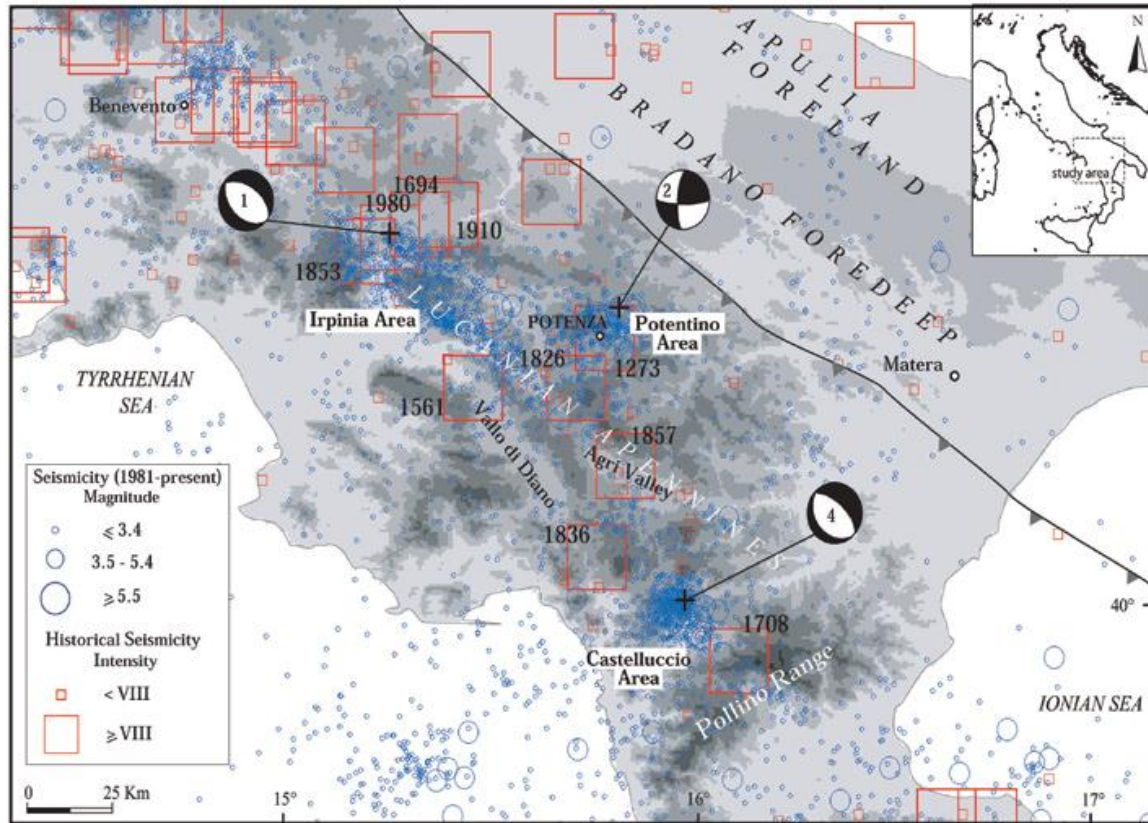


Figure 2.12. In blue, instrumental seismicity in Southern Italy from 1981 to 2005 (Castello *et al.*, 2005). In red the historical earthquakes from CPTI04 catalog (CPTI Working Group, 1999). The focal mechanisms (Pondrelli *et al.*, 2002) are related to: 1. Irpinia 1980, 2. Potenza 1990 and 1991, and 4. Castelluccio 1998 earthquakes (from Frepoli *et al.*, 2005).

This earthquake was well studied and the amount of data available has allowed a very detailed definition of the geometry, size and kinematics of the fault segments that were activated during this seismic event. The Irpinia earthquake, among those of high magnitude, still remains the best documented in the Mediterranean region, in particular for the detailed knowledge of the fracture process. Westaway and Jackson (1987) and Pantosti and Valensise (1990) used jointly seismometer and accelerometer records and geological and geodetic observations to propose a reconstruction of the fault geometry and the trend of temporal function of the source. Bernard and Zollo (1989), instead, carried out a detailed analysis of the near-source ground motion and of the geodetic data (joining the teleseismic waveforms analyzed by Westaway and Jackson in 1987 with the studies conducted on the aftershocks by Deschamps and King in 1984)

to constrain the timing, geometry and kinematics of the fracture process for each sub-event (Figure 2.13).

The earthquake nucleation originated at a depth of 12 km near Laviano (Westaway and Jackson 1987). In the first phase of the process, the initial fracture propagated through different sub-episodes towards SE and NW along a first, NE-dipping fault segment, defining a complex propagation mechanism (Bernard and Zollo, 1989) along the Marzano fault.

The second rupture started at the southeastern end of the first episode of rupture, after about 18 seconds, and propagated for about 20 km to the southeast, on a low angle normal fault dipping  $20^\circ$  to NE. This episode is associated with a second fault segment showing surface evidence. The third and final rupture episode occurred after 39 s from the first one. This subevent involved a steep normal fault dipping  $70^\circ$  to SW (therefore antithetic to the previous faults) and located at 11 km to the NE of the Marzano fault. The precise orientation of this fault segment is still debated.

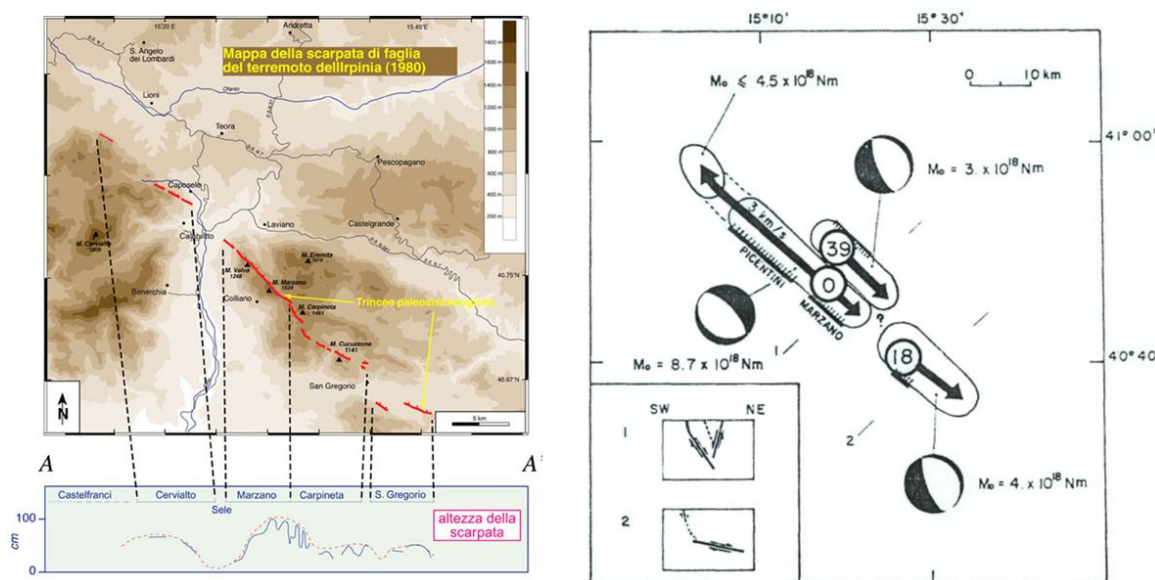


Figure 2.13 On the left: Surface evidence of the faults (0 s and 40 s): on the top the mapping of morphological evidence; on the bottom the displacement occurred during the earthquake along the fault (modified from Pantosti and Valensise, 1990). On the right: Representation of rupture kinematics (Bernard and Zollo, 1989).

Most of the authors (Westaway and Jackson, 1987; Bernard and Zollo, 1989; Pantosti and Valensise, 1990) agree that the failure propagated principally towards NW, not affecting the Sele River Valley. The accelerometric data analysis (Bernard and Zollo, 1989) showed that there was no significant contribution to the seismic radiation from the area of the Sele River Valley. Similarly, the analysis of fault scarps, initially recognized by Westaway and Jackson (1987) and later studied in detail by Pantosti and Valensise (1990), showed how these were disrupted in the vicinity of the Sele River Valley. The other sub-breaking episodes identified by Westaway and Jackson (1987) showed a lack of activity in that area.

The 1980 Irpinia earthquake made clear four fundamental aspects of the generation process of earthquakes in this area of the Apennines:

1. it produced primary surface faulting clearly visible, being the maximum surface displacement of about 1.2 m, and 38 km-long (Pantosti and Valensise, 1980), thus consistent with the length produced by the breakdown in depth;
2. it was generated by a main NW-SE striking, NE dipping normal fault;
3. many of the failure surfaces did not correspond with the tectonic features previously mapped, and they were irrespective of the topography, cutting the high portion of the Apennine chain, in correspondence of the carbonate reliefs of Mt. Marzano - Mt. Carpineta;
4. although their location had been well constrained by seismic and geodetic data and from the failure surfaces, the seismogenic faults were not visible in the seismic reflection profiles acquired for the oil exploration (e.g., Mostardini and Merlini, 1986).

These points constrain the Irpinia fault system as newly formed; its age of inception has been ascribed to the Middle Pleistocene (Pantosti *et al.*, 1993).

The Potenza area (Basilicata) was hit by two seismic sequences occurred 10-11 years (1990-1991) after the devastating 1980 Irpinia earthquake. These sequences were approximately located 40 km to SE of the 1980 earthquake. On may 5th,

1990, the mainshock ( $M_w$  5.7; Ekstrom, 1994) damaged the town of Potenza and the surrounding villages ( $I_0$ =VII MCS). On May 26th, 1991, another mainshock ( $M_w$  5.2) struck the same area causing additional damage.

The depth of the 1990–1991 seismic sequence is mostly concentrated between 15 and 23 km. Both mainshocks of these sequences were characterized by right-lateral kinematics on the E-W-striking nodal plain characterizing both fault plain solutions. Moreover, the epicenters as well depicted an E-W striking distribution. The Potenza sequences, as for epicentral distributions and hypocentral depths, and for fault kinematics, is strictly comparable to what observed for the 2002 Molise earthquakes (e.g., Vallée and Di Luccio, 2004). Both the Potenza and Molise sequences are quite different to the seismicity characterizing the axis of the overall Southern Apennines chain (Figure 2.14; Di Luccio *et al.*, 2005).

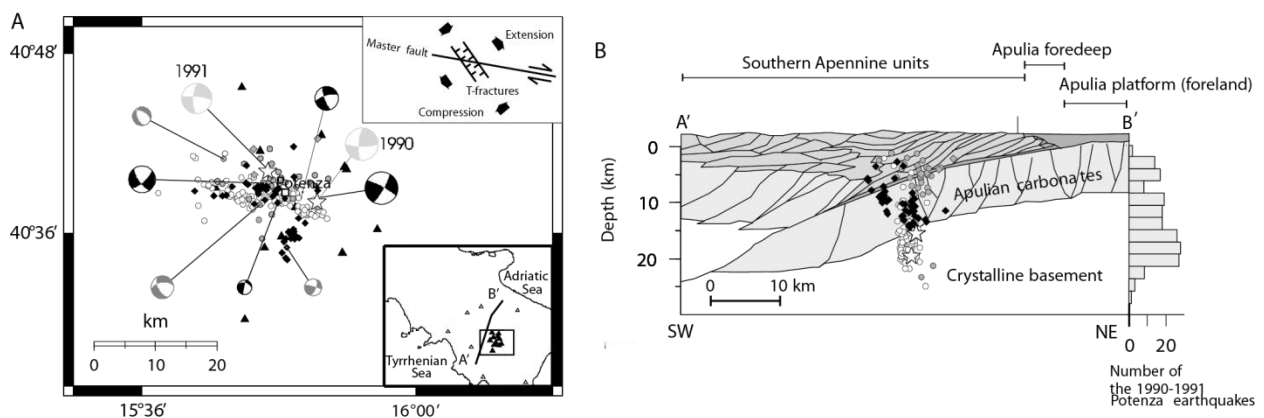


Figure 2.14 Modified from Di Luccio *et al.*, 2005 Relocated epicentres (A) of the 1990–1991 Potenza sequences. The focal solutions are also shown. (B) Hypocentral distribution of earthquakes is shown on a geological cross-section (simplified from Menardi Noguera and Rea, 2000) oriented orthogonal to the main alignment of seismicity. The number of the 1990–1991 events vs. depth is also shown.

The hypocentral location corresponds to the upper part of the middle crust underlying the Apulian sedimentary cover, at the footwall of the easternmost Apennine thrust system. This seismicity occurs therefore in the buried foreland, beneath the orogenic wedge. In this perspective, these seismic sequences have been interpreted as generated by E-W striking, crustal fault zones within the Apulia foreland (Di Bucci 2006; Boncio *et al.*, 2007).

The current seismicity distribution follows the pattern of the fault segments known as activated during the historical earthquakes. This underlines the presence of sub-parallel, NW-SE striking faults along the belt (e.g., Irpinia fault system), and of nearby E-W striking faults, transversely cutting the chain, as in the Potenza region.

In conclusion, considering the background seismicity, also in this case the hypocentral distribution in Irpinia is concentrated in the uppermost 15 km of the crust, but for the Sele River Valley area, where a seismicity gap in the uppermost 8 km depth is observed, in correspondence with a thick sedimentary cover. The focal mechanisms are compatible with the dominant NE-SW extensional regime. Consistently, the background seismicity in the Potenza region exhibits focal mechanisms with dextral strike-slip motion and larger hypocentral depths, down to 25 km within the Apulian carbonates and the underlying crystalline basement, with E-W striking, sub-vertical distribution (De Matteis *et al.*, 2012 under revision).



# Chapter 3

## The Network and data collection

---

### 1. Introduction

The main limitations of using micro-seismicity to study active faults generally derive from the relatively large hypocentral errors due to network geometry, number and accuracy of arrival time readings, the inaccuracy of the crustal velocity model.

Thanks to the development of regional dense seismic networks, it is possible to have high quality recordings of small earthquakes. This allows to individuate with high precision manually the arrival time readings and polarity of the P-wave first motion that can be used to highly improve the accuracy in location, focal mechanism and stress field estimation.

We analyzed the recent instrumental seismicity of Campania-Lucania region.

The microearthquakes data analyzed in this work have been acquired by the National Seismic Network (INGV) and the Irpinia Seismic Network (ISNet).

In this chapter we briefly present the network and data collection.

For this study we have analyzed 17202 records from 1312 events with local magnitude ranging between 0.1 and 3.2, recorded by ISNet and INGV stations from August 2005 to April 2011.

In order to demonstrate that the current events belong to background seismicity rather than being aftershocks of the previous large earthquakes, we compared the Omori's law computed fitting data after M=6.9, November 23, 1980 mainshock for different temporal periods and our data.

To obtain a high quality dataset, we manually picked the first P- and S-wave arrival times on the raw waveforms. A weighting factor was assigned to the reading of the first P- and S-wave arrival times according to the estimated

uncertainties (decreasing weighting factors were associated to uncertainties of  $<0.05$ ,  $0.05-0.10$ ,  $0.10-0.20$ ,  $0.20-0.50$ ,  $>0.50$  s).

## 2. The network and data-collection

Active faults of interest in the Southern Italy are located in Campania-Lucania Apennines (Figure 3.1). The improvement of the station coverage and the increased number of three component broad band sensors of the Italian seismic network with a multi-component seismic network, high density in this area is of fundamental importance for the mitigation of seismic risk of the region and allow us to achieve more accurate seismotectonic information about this area thanks the possibility to create high quality database of arrival time to highly improve the accuracy in location, focal mechanism and stress field estimation.

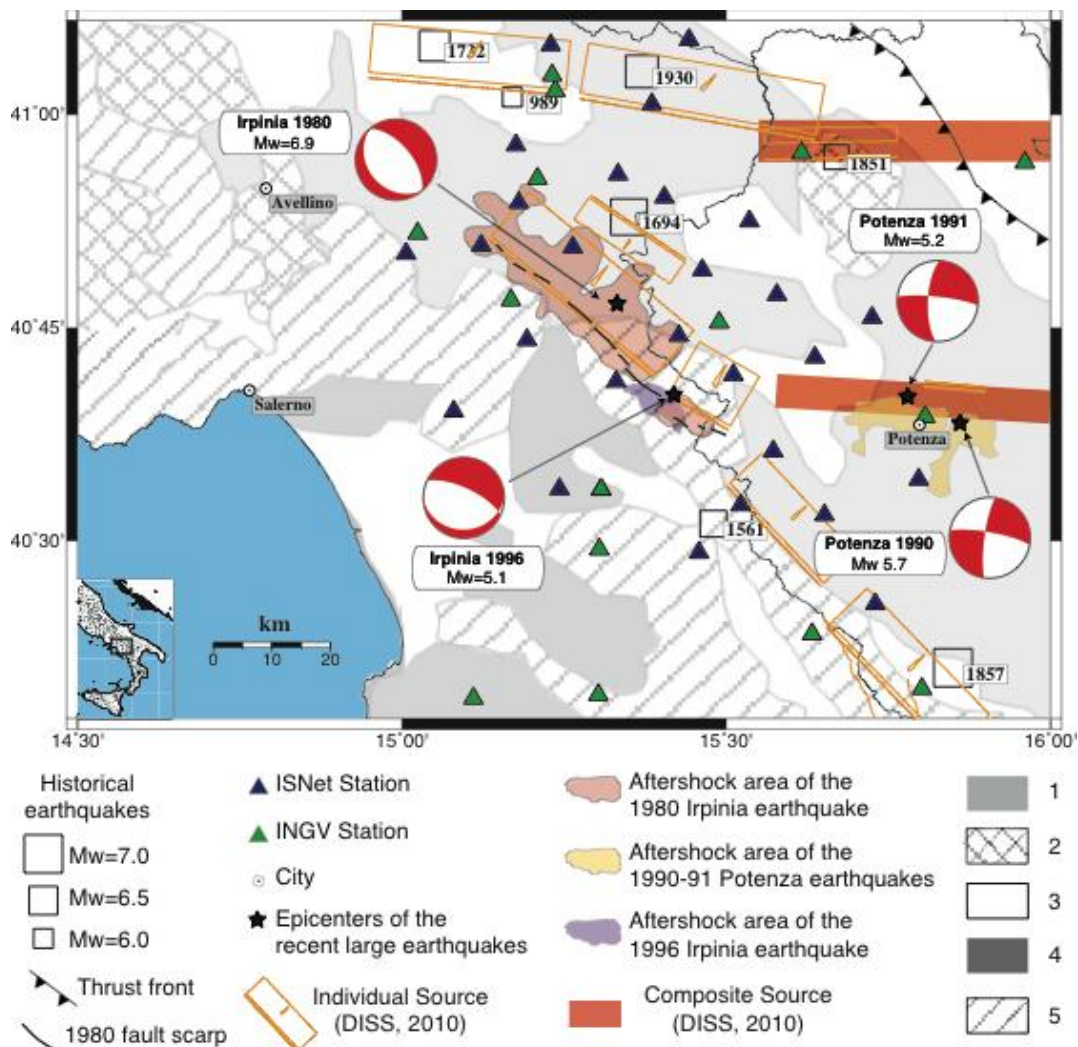


Figure 3.1 (previous page) Simplified geological map of Campania-Lucania region integrated with: seismogenic sources (*DISS Working Group, 2010*); locations of main historical earthquakes; focal mechanisms of large instrumental earthquakes and their aftershock zones; locations of the ISNet (blue triangle) and INGV (green triangle) stations. 1 Molise-Sannio-Lagonegro pelagic basin and related foredeep deposits; 2 Apennine carbonate platform; 3 Apulia carbonate platform; 4 Pliocene-Quaternary terrigenous deposits; 5 Ligurides and Sicilides.

## 2.1 The Italian National Seismic Network (INGV)

The new Italian National Seismic Network (INGV network) is a relative dense network of

broadband stations deployed for monitoring Italian seismicity.

In 2000 the INSN started a migration from a sparse shortperiod network to a dense broadband network. At present the INGV network consists of about 250 stations to monitor a country of 300.000 km<sup>2</sup> with a typical station spacing of 40 km (Olivieri *et al.*, 2008).

The network relies on a variety of digitizers and sensors and is continuously evolving. At present 120 stations are equipped with 40-sec velocity sensors (Trillium 40 s or Guralp CMG-40), and 23 stations have Lennartz 5-sec sensors; all are equipped with 24-bit digitizers. The MedNet Network contributes to the INSN with 14 very broadband stations (STS-1 and STS-2 sensors) deployed in Italy. Some of the sites also have an accelerometer, but since these data are not transmitted in real time, we did not use them in this study. The data streams are telemetered to Rome via various telemetry systems including satellite IP connections, dedicated leased telephone lines, and the public administration network.

We analyzed the event recorded at a total of 16 INGV station placed in the Campania-Lucanian region (Figure 3.1).

## 2.2 The Irpinia seismic network (AMRA)

Since 2005 the seismic activity in this area is monitored by a permanent seismic network operated by the AMRA (Analisi e Monitoraggio del Rischio Ambientale) consisting of 26 stations, each with six-component sensors, covering an area of 100km x 70km with an average inter-station distances of less than 10

km, consisting of multiple nodes in the data acquisition and processing, with organization into sub-networks (Weber *et al.*, 2007; Zollo *et al.*, 2009).

ISNet (Irpinia Seismic Network) is equipped with sensors that can record unsaturated seismic signals from small to large magnitude earthquakes. To ensure a high dynamic range, indeed, each station is equipped with two types of three-component sensors: strong-motion accelerometers and velocity instruments. Twenty-two sites are equipped with a Guralp CMG-5T accelerometer and a set of short period ( $T_0=1$  s) Geotech S13-J. The remaining sites have a Guralp CMG-5T and broadband Nanometrics Trillium (0.025-50 Hz band) sensors. The choice of using these sensors, arises from the necessity to record of events with different characteristics. The velocimeter are designed for registration of weak or distant events and are dedicated to the study of Earth's internal structure. The accelerometers are usually used in the recording of strong soil movements, to study in detail the seismic source and the effects of earthquakes on structures.

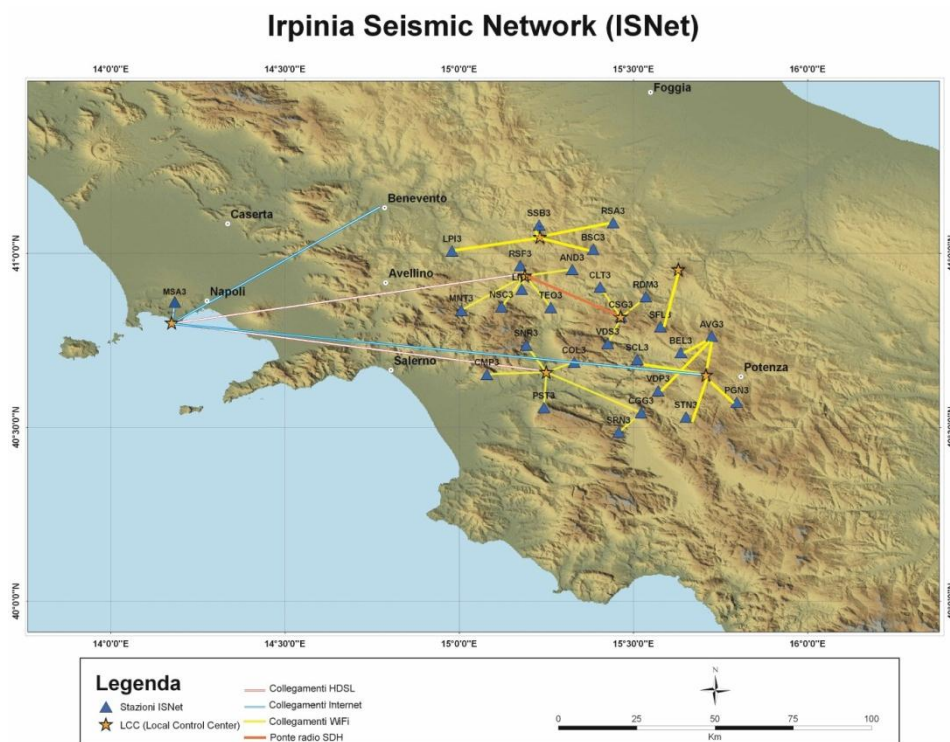


Figure 3.2 Irpinia Seismic Network architecture. The triangles indicates the seismic stations. The stars indicates the Local Control Center. Each LCC refer an average of 5-6 seismic stations (link are indicated with yellow line). The LCC is in communication with the operative center in the Naples University.

A further classification of the sensors is made on the basis of the frequency in which the instrument accurately reproduces the input signal. The “short period” sensors, characterized by a frequency of 1-2 Hz, have a response curve that is flat for frequencies higher than the natural frequency, and decays more or less rapidly towards lower frequencies, while the “long period” sensors are sensitive to low frequencies. The “Broad-band” sensors, are constructed with special technical devices that allow to have a flat response curve from zero to several hundred Hertz.

The seismic signals are acquired at the seismic station and transmitted in real time via radio (Wi-Fi) to a Local Control Center (LCC). Each LCC refer an average of 5-6 seismic stations. Figure 3.2 illustrates the locations that comprise ISNet. The LCC is in communication with the operative center in the Naples University.

### 2.3 Data collection

We analyzed the recent instrumental seismicity of Campania-Lucanian region in the area where the Irpinia earthquake on November 23, 1980 (M 6.9) occurred (Figure 3.3).

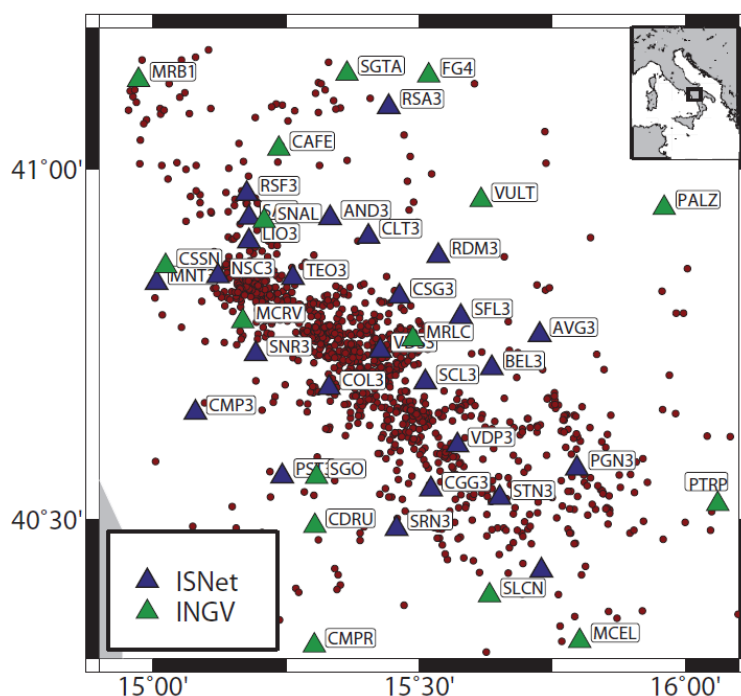


Figure 3.3. Earthquakes distribution of analyzed seismicity (red circles). Locations of the ISNet (blue triangle) and INGV (green triangle)

The dataset collected by ISNet is extended and integrated by the inclusion of the closest stations of the Italian Seismic Network, managed by INGV (Istituto Nazionale di Geofisica e Vulcanologia), allowing for a better quality in the determination of the hypocentral parameters.

The complete studied dataset consists of 17202 traces (considering only one component) recorded by 42 ISNet and INGV stations from 1312 microearthquakes occurred from August 2005 to April 2011 (De Matteis *et al.*, 2011)

The distribution of the analyzed waveform records as a function of the epicentral distance and magnitude is displayed in Figure 3.4. The spanned magnitude range is 0.1–3.2 (inside the seismic network) with a maximum epicentral distance of 150 km, whereas most of records are acquired at less than 50 km hypocentral distance.

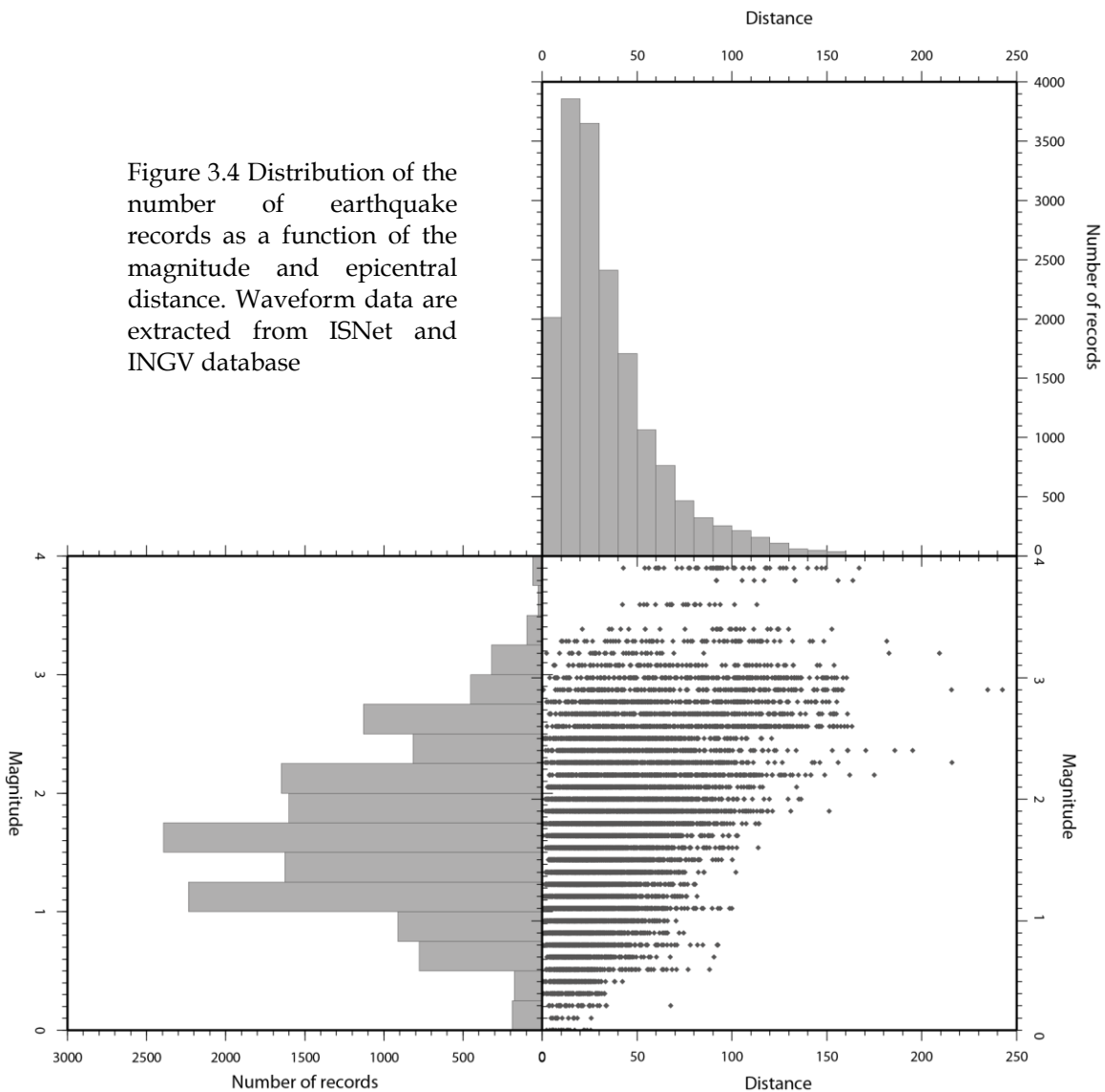


Figure 3.4 Distribution of the number of earthquake records as a function of the magnitude and epicentral distance. Waveform data are extracted from ISNet and INGV database

### 3. Statistical features of the analyzed seismicity

Statistical studies of earthquake occurrences have frequently been carried out since the early years of seismology. To obtain reliable results from statistical analysis, a sufficient amount of high-quality data is necessary. It's important to underline that the results of a statistical analysis must be tested for better understand their significance.

#### 3.1 Temporal distribution of the earthquakes

A first goal of this thesis was to prove that the current seismic events can be ascribed to the background seismicity rather than be interpreted as aftershocks of the previous large earthquakes.

Generally aftershocks rates and magnitudes follow several well-established empirical laws. The first of this is the Omori's Law. This law controls the rate of aftershocks with time. In particular Omori's law, or more correctly the modified Omori's law, is an empirical relation for the temporal decay of aftershock rates. Omori (1894) showed that the frequency of felt aftershocks per day  $n(t)$ , following the 1891 Nobi, central Japan, earthquake ( $M=8.0$ ) decreases regularly with time according to the equation:

$$n(t) = K/(c + t) \quad (3.1)$$

where:

- $n(t)$  is the rate of earthquakes measured in a certain time  $t$  after the main shock,
- $K$  is the amplitude, and
- $c$  is the "time offset" parameter.

The modified version of Omori's law, now commonly used, was proposed by Utsu in 1961 (Utsu, 1961; Utsu *et al.*, 1995).

$$n(t) = \frac{K}{(c+t)^p} \quad (3.2)$$

Where  $p$  modifies the decay rate and typically falls in the range 0.7–1.5. According to these equations, the rate of aftershocks decreases quickly with time. The rate of aftershocks is proportional to the inverse of time since the mainshock. For our case, on the basis of the last 30 years catalogue  $M \geq 3$  we tested with a statistical hypothesis test if the current seismicity rate obey the modified version of Omori's law as inferred from literature studies (Alessio *et al.*, 1995; Murru *et al.*, 2009) (Figure 3.5). The result of the  $\chi^2$  test indicates that at a significance level of 1% the hypothesis is not compatible with our data, thus the earthquakes in the last 20 years do not match the Omori's law rate decay but represent the background seismicity whose mean rate is represented in Figure 3.5 (De Matteis *et al.*, 2012 under revision).

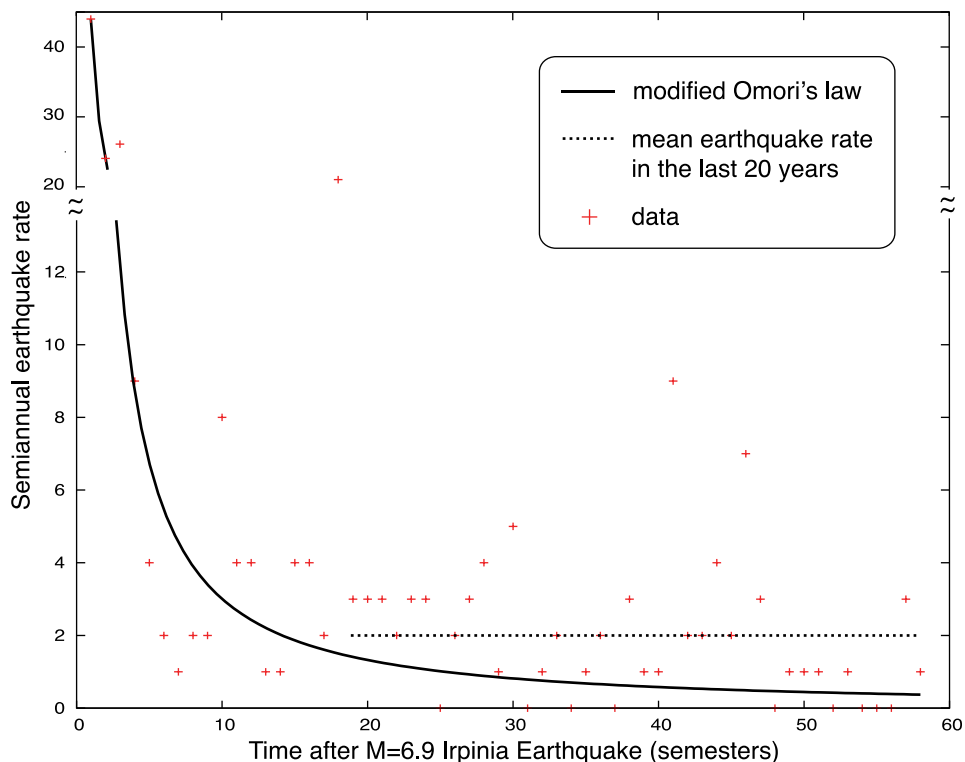


Figure 3.5 Semiannual rate of earthquakes with  $M \geq 3$  following the M 6.9 November 23, 1980 earthquake. Solid curve represent the modified Omori's law as inferred from literature studies.

### 3.2 Size Distribution of Earthquakes:Gutenberg Richter Law

In general, smaller earthquakes are much more frequent than larger ones.

In seismology, the Gutenberg–Richter law (GR law) expresses the relationship between the magnitude and total number of earthquakes in any given region and time period of at least that magnitude (Gutenberg and Richter, 1954).

$$\log_{10} N = a - bM \quad \text{or} \quad N = N_{\text{tot}} 10^{a-bM}$$

Where  $N$  is the number of events having a magnitude  $\geq M$  and  $a$  and  $b$  are constants.

The  $a$ -value simply indicates the total seismicity rate of the region. This is more easily seen when the GR law is expressed in terms of the total number of events:

$$N = N_{\text{tot}} \cdot 10^{-bM}$$

where,  $N_{\text{tot}} = 10^a$ , the total number of events.

The constant  $b$  is typically equal to 1.0 in seismically active regions. There is some variation with  $b$ -values in the range 0.5 to 1.5 depending on the tectonic environment of the region.

The Gutenberg Richter law is generally followed for the estimation of the detection threshold. The recurrence curve method uses the seismicity actually recorded by a seismic network to compute the Gutenberg Richter exponential decay function and compares the data recorded by each single station with the ones recorded by the whole network. Plotting the frequency-magnitude curve for a given station, we expect the same slope both at large and small magnitudes (or even a flat level or a positive slope) at small magnitudes, because some of the small events detected by the network do not come out of the noise at that station. The magnitude at which the curve changes its slope is the detection threshold for such a station. Since this magnitude is a function of the distance, data need to be grouped by distance or an attenuation law should be used to reduce the data at the same distance (Cao and Gao, 2002; Wiemer and Wyss, 2002).

In Figure 3.6 we plotted the completeness threshold predicted by the Gutenberg-Richter (GR) law. The law was computed using all the seismic events acquired

by the ISNet stations since January 2008 and located inside the network. The cumulative frequency-magnitude distribution was built by grouping the earthquakes in classes of magnitude having width of 0.3.

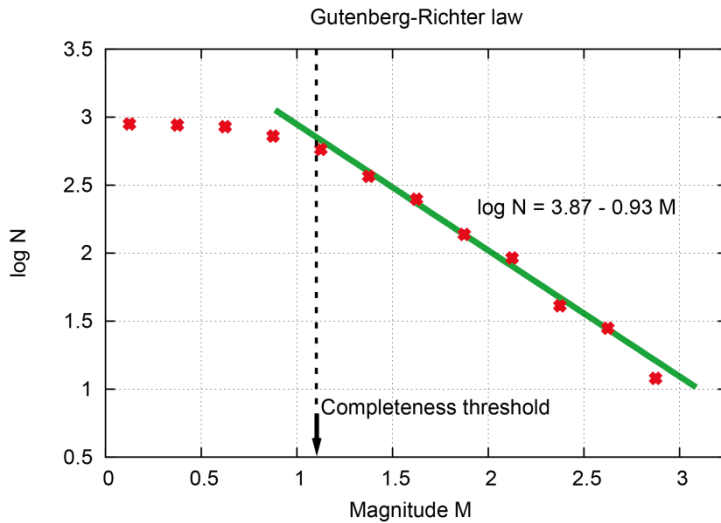


Figure 3.6 Gutenberg-Richter law computed for events inside ISNet. The dots represent the cumulative frequency-magnitude distribution of events occurred since January 2008. The relationship is obtained performing a fit over the linear part of dots distribution. The completeness magnitude is estimated at about 1.1.

Finally, the coefficients of the GR law were retrieved by a linear fit performed on the associated cumulative distribution. To investigate the completeness threshold, several linear fits were performed including points at smaller magnitude and the minimum magnitude to be included in the fit was defined as the point beyond it the quality of the fit started to degrade as compared to the previous curves. The estimated completeness threshold of the seismic catalog is 1.1, in the middle of the network where the recorded seismicity of the area is mainly concentrated (Vassallo *et al.*, in press).

#### 4. Data set creation and validation

To obtain a high quality dataset, we manually picked the first P-wave and S-wave arrival times of the background seismicity on the waveforms of earthquakes recorded at a minimum number of four stations. A weighting factor was assigned to the reading of the first P- and S-wave arrival times according to the estimated uncertainties

Weights	Picking accuracy (s)
0	<= 0.05
1	0.05 – 0.1
2	0.1 – 0.2
3	0.2 – 0.5
4	> 0.5

(decreasing weighting factors were associated to uncertainties of <0.05, 0.05-0.10, 0.10-0.20, 0.20-0.50, >0.50 s).

A first evaluation of picking consistency has been performed analyzing the “modified Wadati diagram” (we plot the difference of Ts vs difference of Tp for each couple of stations; Chatelain, 1978), which also provides an estimate of an average  $V_P/V_S$  ratio.

In the “modified Wadati diagram” diagram, we consider for each event, for each couple of station (i,j), the difference between phases  $P_i - P_j$  (x-axis) and  $S_i - S_j$  (y-axis) arrival time. This time difference can be expressed as:

$$P_i - P_j = \frac{(x_i - x_j)}{V_P}$$

and

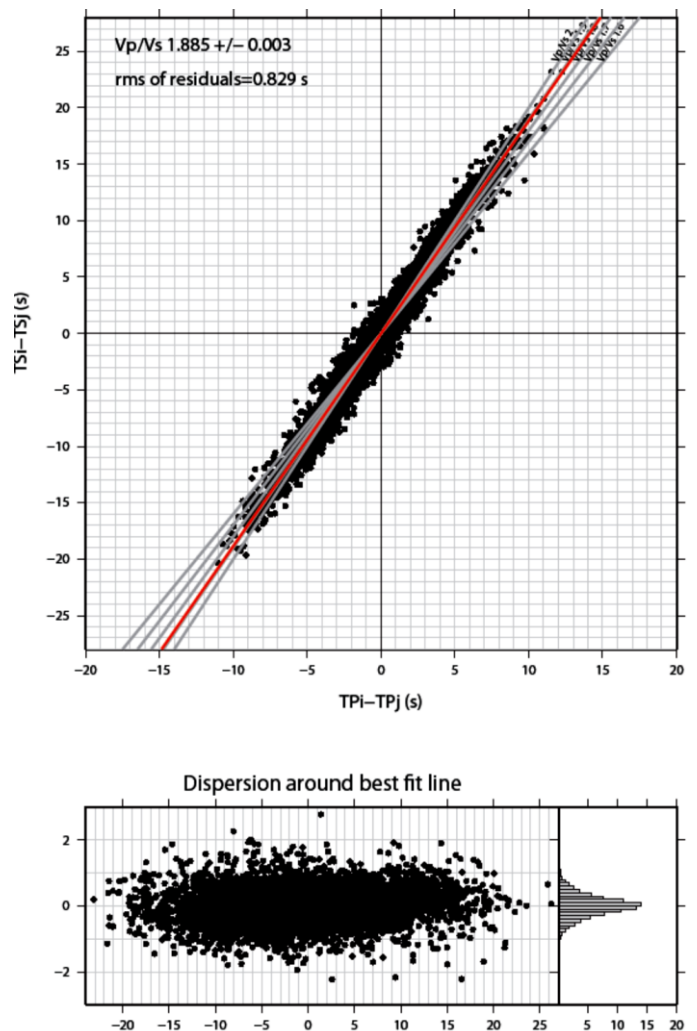
$$S_i - S_j = \frac{(y_i - y_j)}{V_P}$$

Each point is determined by the difference in reading times for the same event, and so the representation does not depend on the earthquake origin time.

Assuming an homogeneous half space, the data should fall along a straight line with a slope equal to the  $V_P/V_S$  ratio. By fitting the difference between P-phases ( $P_i - P_j$ ) versus the difference between S-phases ( $S_i - S_j$ ) arrival time for all pairs of stations, we estimate the value of the slope  $V_P/V_S$  through the equation:

$$(P_i - P_j) = V_P/V_S (S_i - S_j)$$

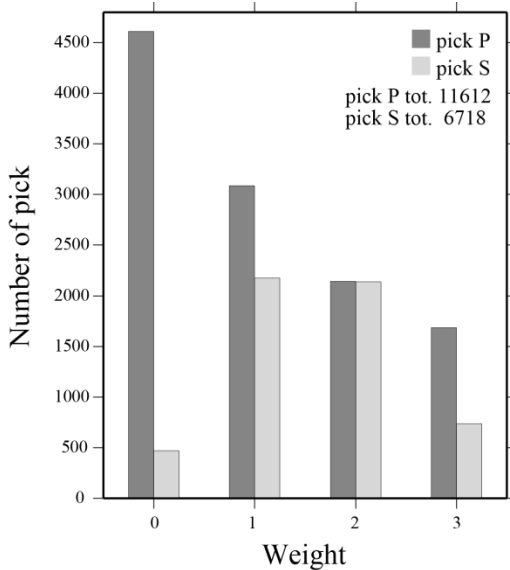
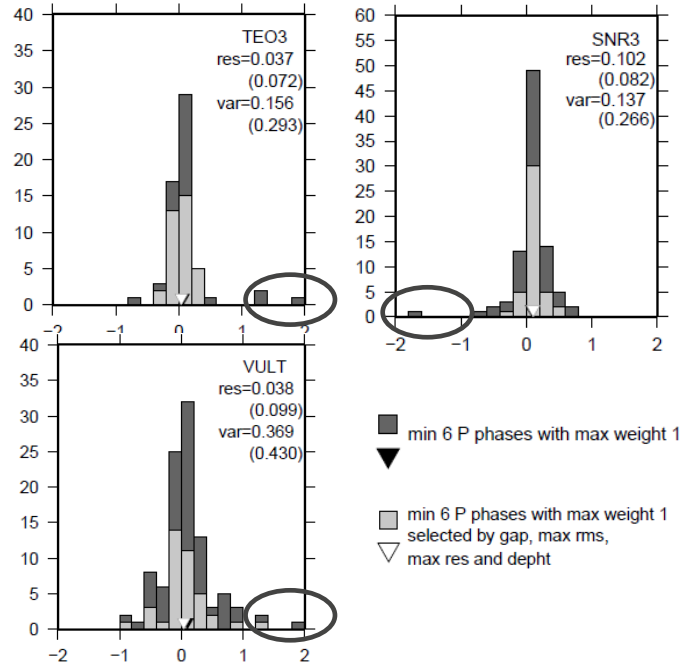
From our data the observed ( $P_i - P_j$ ) and ( $S_i - S_j$ ) arrival time pairs were well distributed around a linear trend where the least square best fit line provided a



$V_P/V_S$  ratio of 1.88 with a root mean square (RMSE) of 0.03, and linear correlation coefficient ( $R^2$ ) of 0.98.

The arrival times that departed significantly from this trend have been identified and removed.

Then, the picking quality has been assessed by performing a preliminary location in an homogeneous media ( $V_p=5.5\text{Km/s}$ ;  $V_p/V_s=1.88$ ) using the code NonLinLoc (Lomax *et al.*, 2000) and looking, for each station, for outliers on the histograms of residuals (difference between the observed and the calculated travel time). We performed a selection removing the picks significantly outside the distribution of residuals ( $> 1$  s).



In addition, we have chosen not to consider for our analysis the readings of weight 4 (with error greater than 0.5s on the identification of the seismic phase).

The final data consists of 11612 P- and 6718 S- arrival time readings. The analysis of the distribution of the number of picks as a function of the weight assigned give us information about the quality of the considered dataset. In particular considering the P-phase (dark grey) we can note the high number of lecture with good quality (weight 0 and 1).

We can see a fair number of S-phase pick (light grey) with lower quality respect the P-phase. S-phases are notoriously less clear phases of P as we can see the example in Figure 3.7.

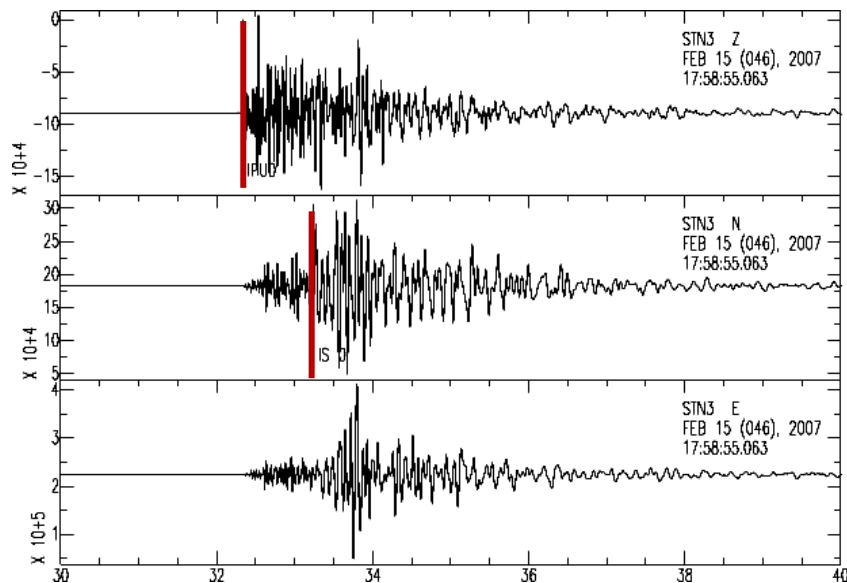
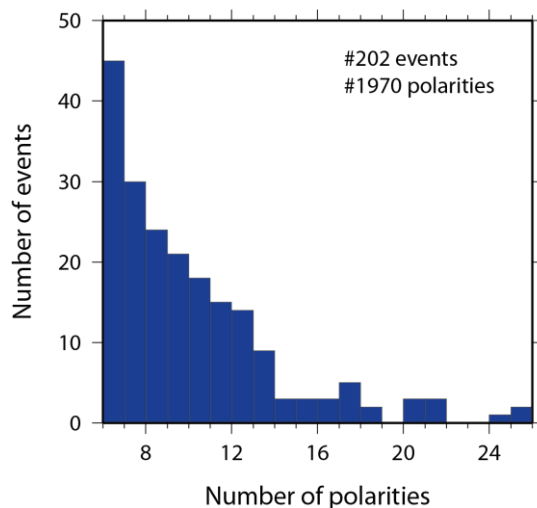


Figure 3.7 Example of P and S seismic phase individuation.



On the best quality traces, we also read the polarity of the P-wave first motion an essential parameter for the analysis carried out. Therefore, the readings were detected polarity characterized by “up” and “down”. We read a total of 3418 Up and 1749 Down. In the histogram we represent the number of earthquakes as a function of the number of polarities.

We consider only the earthquakes with at least 6 polarity read, that is the minimum number to obtain a reliable estimation of focal mechanism and for the stress tensor analysis, and inside the seismic network. For this set of 202 events, we read 1299 Up and 671 Down.

## 5. Discussion and conclusion

In this chapter we have discussed about the analysis and interpretation of seismological data recorded by ISNET and INGV network implemented during this thesis work.

We briefly presented the network architecture of the integrated seismic networks, and data collection. Statistical studies of earthquake occurrences allowed us the opportunity to estimate the detection threshold of the seismic network and to prove that the current seismic events can be ascribed to the background seismicity rather than be interpreted as aftershocks of previous large earthquakes.

The presence in the studied area of a regional dense seismic network, allowed us to build a high quality recordings of small earthquakes. High accuracy of arrival time and polarities of the P-wave first motion readings, give us the possibility to improve the accuracy in location, velocity model, focal mechanism and stress field estimation as we shall see in later chapters.

# Chapter 4

## 1D velocity model, interpretation of station corrections and earthquake locations

---

### 1. Introduction

Regional seismicity analysis for the study of seismotectonic processes, earthquakes recurrence, and earthquakes interaction requires precise knowledge of the spatial distribution of the earthquake hypocenters.

The earthquake location consists in determining the spatial coordinates and time of origin of the rupture nucleation, using the arrival times of seismic primary waves (P and S), from the theoretical relationship that links the observed data to the model parameters to be determined (Lay-Wallace, 1995). This implies the calculation of the travel times between an earthquake hypocenter and the recording stations, using a known velocity model between hypocenter and station. The computed travel times are in general nonlinear functions of hypocenter estimate and so the problem is non-linear. Generally, it has been performed by linearizing the equation linking observed arrival times to location parameters (spatial parameters and origin time; Geiger's algorithm, 1910) and solved with iterative methods such as Gauss-Newton, conjugated gradient and damped least squares (Buland, 1976; Lee *et al.*, , 1981; Pavlis, 1986). These methods require travel time derivative near an estimated hypocenter and that they are susceptible to instabilities when the problem is ill-conditioned. These algorithms are fast but often not accurate in the hypocentral solution, because, since they have to perform the calculation of partial derivatives, they often use not very representative parameterizations of the velocity model in the region of space between source and receiver. Furthermore, error estimation with

linearized methods is based on the assumption of normally distributed, that is, Gaussian, location parameters; this can be significantly wrong in ill-conditioned solutions, in which the true probability density can be multimodal (Presti *et al.*, 2004).

The use of linearized, maximum-likelihood methods in the past has been justified by the fast computation, at a time when computers were very slow. But in the last 20 years several techniques have been developed that do not make use of the inverse problem linearization and that perform an hypocentral coordinates investigation, using much more complicated velocity model parameterizations, taking into account the true complexity of the geological subsurface (Tarantola and Vallette, 1982; Moser *et al.*, 1992; Wittlinger *et al.*, 1993).

The accuracy of hypocenter locations is controlled by several factors, including the network geometry, available phases, arrival-time reading precision, and knowledge of the crustal structure (Pavlis, 1986; Gomberg 1990; Michelini and Lomax, 2004).

Simplified one-dimensional (1D) velocity models are generally used for monitoring purposes also in geologically complex seismogenic areas. In this case one can partially account for the velocity lateral variations by including station and/or source terms in the location procedure (Douglas, 1967; Pujol, 1988; Hurokawa and Imoto, 1992; Shearer, 1997) and/or by jointly inverting the travel-time data for hypocenters and velocity structure (Crosson, 1976; Ellsworth, 1977; Thurber, 1983; Kissling *et al.*, 1995; Waldhauser and Ellsworth, 2000). The effects of an unsuitable velocity model on hypocenter locations can also be minimized by using relative earthquake location methods (Frèchet, 1985; Fremont and Malone, 1987; Got *et al.*, 1994). We can again improve location precision by improving the accuracy of the relative arrival-time readings using waveform cross-correlation methods (Waldhauser, 2002). The combined use of these procedures results in earthquake location uncertainties in the range of a few meters to tens of meters. These fine-scale details on the seismicity reveal us the

complex geometry of the fault system defining the structures, from the kilometer to the meter scale. In fact many studies have shown a clear distribution in the hypocenter location both in the analysis of seismicity catalog (Shearer *et al.*, 2005) and in the analysis of the aftershocks distribution (Chiaraluce 2003). However, an accurate knowledge of the velocity structure of the studied region is necessary to prevent artifacts in the relative position of hypocenters: inappropriate choice of the velocity model, can lead to significant distortions and bias in the hypocenter positions (Michelini and Lomax, 2004).

Studies focused on the 1D velocity model definition are of great interest, since the elastic proprieties of the Earth mainly change with depth due to sedimentation, compaction and thermal processes, and tis make it difficult to retrieve a three dimensional (3D) velocity model. Moreover 3D tomographic models strongly depend on the 1D reference model: inadequate initial reference models may, in fact, severely distort tomographic images or introduce artifacts that lead to misinterpretations of the results.

However, in regions with strong lateral variations and irregular topographic surface, large location errors or systematic effect in earthquake location can be introduced by the use of simplified 1D layered velocity models. For most of the tectonically active regions, the geological structures are complex and can only be represented by fully 3D velocity models.

In this chapter we want to analyze the effects that the use of 1D models to represent the true 3D velocity distribution of a geologically complex area has on earthquake locations. We study the case of Campania-Lucania region (Southern Italy) where the geological and geophysical knowledge reveal a significant lateral variation of the elastic properties of the medium.

In particular we analyzed the role of static station corrections in the use of 1D velocity models for earthquake location.

We used the micro-earthquake data set consisting of 1312 events that occurred from August 2005 to April 2010 by integrating the data recorded at 42 seismic stations of various networks placed in the area described in chapter 3.

High quality P-wave first arrival travel time have been used to a) determine a P-wave “minimum 1D velocity model” following the approach of Kissling *et al.*, (1995), by a joint inversion of layered velocity model, station corrections and hypocenter locations; b) determine a 3D crustal velocity model, using a linearized and iterative tomographic algorithm (Latorre et al, 2004; Vanorio et al, 2005).

The comparison between the final locations, computed using the 1D model, and the locations obtained with the 3D model allows us to highlight systematic effects. Station corrections generally are strongly coupled to the velocity very just below the stations and partly account for the three-dimensionality of the velocity field that cannot be adequately represented by 1D model (Kissling *et al.*, 1995). In our case where the lateral heterogeneity are significant even at great depths (5-6 km), we expect that the station corrections play an important role and we want to investigate their relation with the complex geological structure.

Finally to minimize errors due to un-modeled 3D velocity anomalies and to improve earthquake location we relocated the earthquakes using the double-difference technique (HypoDD, Waldhauser and Ellsworth, 2000).

## 2. 1D P-wave velocity model estimation

The seismic wave travel time is a non-linear function of the hypocentral parameters and the seismic velocities sampled along the ray path between hypocenter and station. This dependence on hypocentral parameters and seismic velocity is called “coupled hypocenter-velocity model problem” (Crosson, 1976; Kissling 1988; Thurber 1992). It can be linearized and written in matrix notation as (Kissling *et al.*, 1995):

$$t = Hh + Mm + e = Ad + e \quad (4.1)$$

where  $t$  is the vector of travel time residuals,  $H$  is the matrix of partial derivatives of travel time with respect to hypocentral parameters,  $h$  is the vector of hypocentral parameter adjustments,  $M$  is the matrix of partial derivatives of travel times with respect to model parameters,  $m$  is the vector of velocity

parameter adjustments,  $e$  is the vector of travel time errors, including contributions from errors in measuring the observed travel times, errors in the calculated travel times due to errors in station coordinates, use of the wrong velocity model and hypocentral coordinates, and errors caused by the linear approximation,  $A$  is the matrix of all partial derivatives and  $d$  is the vector of hypocentral and model parameter adjustments.

In order to better constrain the hypocentral locations we performed an analysis for the best P-wave one-dimensional (1D) velocity model of the study area using the software VELEST (Kissling *et al.*, 1995). The non-linear problem can be linearized and the solution is obtained iteratively, where one iteration consists of solving both the complete forward problem and the complete inverse problem once. The inverse problem is solved by inversion of the damped least square matrix. For a more detailed description of VELEST methodology the reader is referred to Kissling (1995).

Since the Earth's crust is more complicated than a simple flat homogeneous layers model, this assumption introduces unavoidable errors in the process of earthquake location. In this formulation the station corrections play a key role, in fact part of the travel time residuals not explained by the 1D structure is included into the station correction (Scarfi *et al.*, 2009).

In the inversion process we have considered only the event with the following features: at least five P- arrival time readings, azimuthal gap smaller than  $200^\circ$ , a maximum location error (both horizontal and vertical) of 10 km and maximum RMS of 0.5 s. The final data set is composed of 4620 first P arrival time readings, corresponding to 390 localized events. Time picking accuracy was estimated in a range of 0.05-0.5 s. In Figure 4.1 we show the selected earthquakes (dark gray circles), and the ray covering with gray lines (Matrullo *et al.*, 2011a).

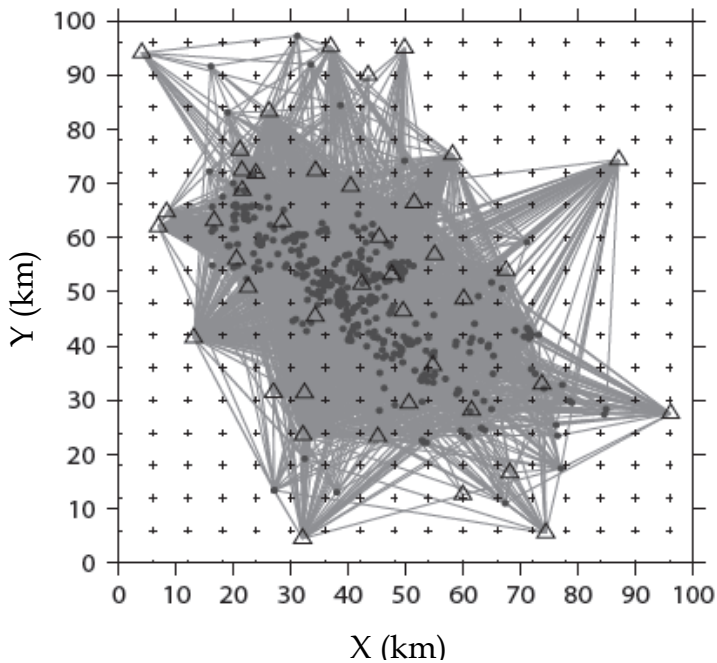


Figure 4.1 The ray covering (gray lines) considering the selected earthquakes (dark gray circles) in a Cartesian coordinate system. The stations are indicated with a triangle.

A critical factor for the linearized inverse problem, stressed by several authors (Kissling, 1988; Thurber, 1992; Kissling 1995), is the importance of the starting velocity model that affects the whole process of inversion. In order to solve the problem related to the selection of the starting model we performed several inversions using different 1D initial velocity models.

We used several 1D velocity models available in the literature for the study region at different spatial scale and resulting from the analysis of the 1997 to 2002 Italian Seismic Catalogue (Chiarabba *et al.*, 2005), or the recent seismicity of the Lucanian Apennines and Bradano foredeep (Maggi *et al.*, 2009) or the aftershocks of the 1980 Irpinia earthquake (Amato and Selvaggi, 1993; Bernard and Zollo, 1989; De Matteis *et al.*, 2010).

These velocity models, displayed in Figure 4.2a, show a very broad range of P-wave velocities in the first kilometers that decrease with depth. Also the number of interfaces and their depth are very different: this probably reflects the actual complexity of the area. Moreover, to explore a wider region of the model parameter space, we considered three homogeneous and three constant gradient velocity models (Figure 4.2b). Some additional layers every 1 km were

introduced for each considered model since the code VELEST does not invert for changes in layer thickness.

Damping factors for the hypocentral parameters, station delays and velocity parameters were selected optimizing the data misfit reduction and the parameter resolution. We chose to avoid low velocity layers to not introduce instabilities in the inversion process. We considered an initial damping coefficient of 0.01 for the hypocentral parameters and station delays and 0.1 for the velocity parameters. In this first step we invert several times in order to reduce number of layers were possible by combining adjacent. Afterwards, damping parameters for velocity variations and station corrections were selected optimizing the data misfit reduction and the parameter resolution, and we use a damping of 0.01 for the hypocentral, 0.1 for the station and 1.0 for the velocity parameters.

For each starting velocity model the convergence to a stable solution is obtained after 15-20 iterations and the final models (Figure 4.2b) are characterized by RMS values ranging between 0.12 and 0.13 s.

To select all the velocity models with the same RMS from a statistical point of view we applied the statistical Test F choosing the 95 per cent significance level. The selected models present the same characteristics: a low P-wave velocity shallow layer (1-3 km depth) with values ranging from 2.5 km/s to 4.5 km/s, a middle layer with thickness of 4-5 km and velocity between 5 km/s and 6 km/s and finally a smoothly increases with depth. The retrieved range of velocity models show a very broad range of P-wave velocities in the first kilometers that decreases with depth (Figure 4.2b). It represents the degree of uncertainty on the values of velocity and on the depth of the interfaces we found.

The average velocity model has been used as starting model for a further inversion whose solution represents the best "Minimum 1D model" (dotted line in Figure 4.2b). This final model satisfies the following requirements: 1) earthquake locations, station delays and velocity values do not vary significantly in subsequent iterations; 2) the total RMS value of all events is significantly

reduced with respect to the first routine earthquake locations. We obtained a RMS reduction of about 61% of RMS with a final value of 0.12 s.

The retrieved “Minimum 1D model” presents a P-wave velocity shallow layer (until 2 km depth) of 3.2 km/s (Figure 4.2b dotted line). This is consistent as average P-wave velocity value due to the known strong lateral velocity variations due to different lithologies varying from Carbonate Platform domain (P-wave velocity of 5.3 – 6.0 km/s) to thrust sheet- top clastic sequence (P-wave velocity of 2.0 – 2.4 km/s; the seismic velocities range is referred to Improta 2003).

A layer of 4 km thick (from 2 to 6 km in depth) is characterized by a velocity of 4.7 km/s compatible with the seismic velocity of the Lagonegro Basins units (Improta *et al.*, 2003).

The transition to the domains of Apulian Platform domain occurs gradually passing across a layer of 2 km thick with a velocity of 5.5 km/s. The retrieved velocity value of 6.2 km/s at 8 km and 6.5 km/s at 12 km are compatible with previous study (Improta *et al.*, 2003, Boncio *et al.*, 2007).

Then the velocity smoothly increases with depth up to a value of P-wave velocity of about 7 km/s. The distribution of events in depth (4.2c) gives information on the resolved layers. The velocity model is not well resolved for depth greater than 15 km.

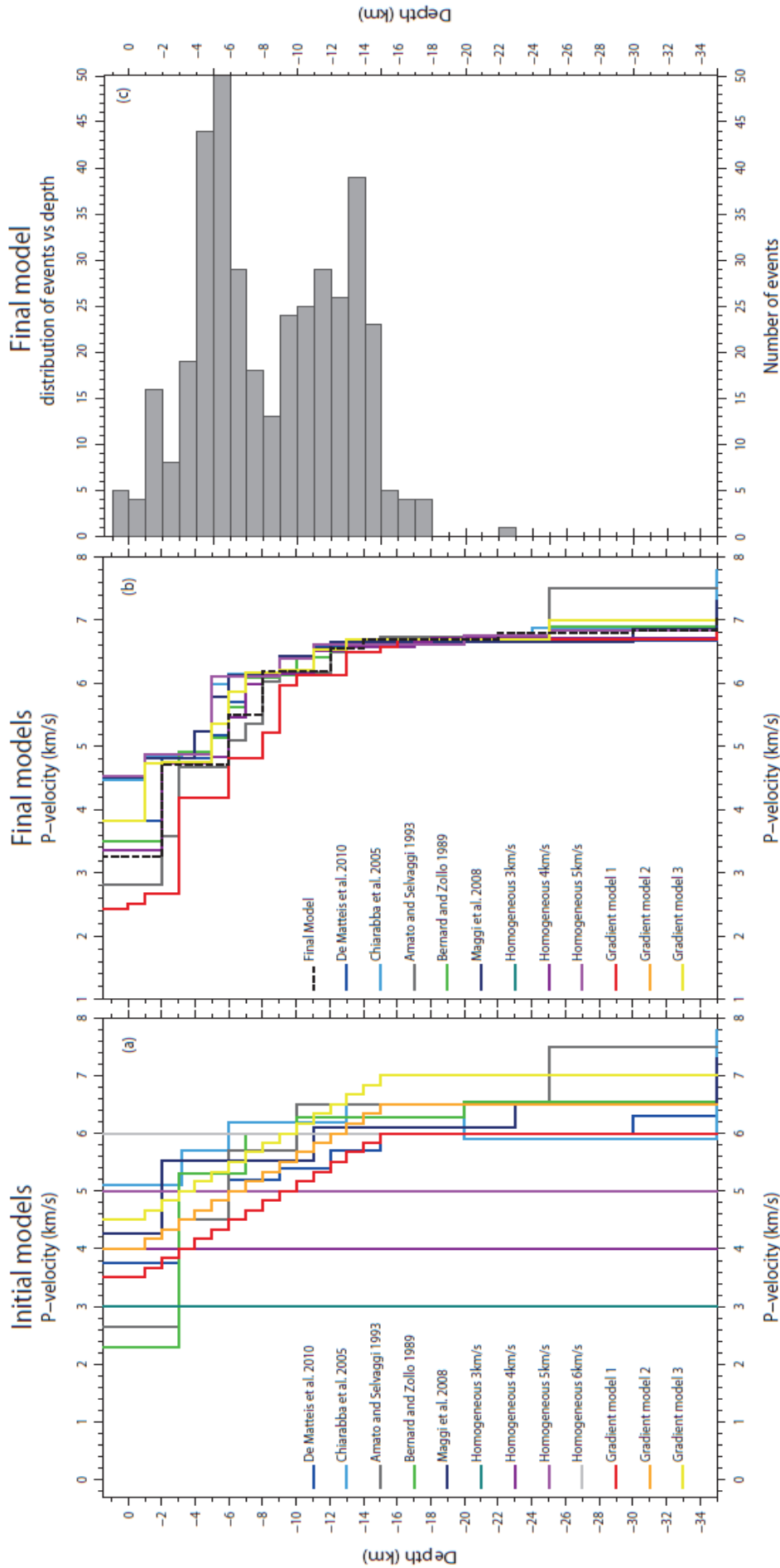


Figure 4.2a. The observed P-wave travel times were inverted to obtain jointly the 1D velocity model, the hypocentral coordinates and the station corrections by using the VELEST algorithm (Kissling *et al.*, 1994). In order to solve the problem of the linearized inverse methods related to the starting velocity model, we performed several inversions using different starting 1D models available from the literature concerning the investigated area (Bernard and Zollo, 1989; Amato and Selvaggi 1993; Chiarabba *et al.*, 2005; Maggi *et al.*, 2009; De Matteis *et al.*, 2010) and various homogeneous and constant gradient velocity models (in picture with different colour)Figure 4.2b. For each starting velocity model the convergence to a stable solution is obtained after several iterations and the final models. The average of the selected velocity models has been used as starting model for a further process of inversion and the result represents the best 1D P-wave velocity model for the study area (black dotted line). We have obtained a RMS reduction of about 61% with a final value equal to 0.12 s. Figure 4.2c The distribution of events in depth: it gives information about the resolved layers.

## 2.1 Hypocenter stability test

We tested the location stability, using the VELEST code, by shifting the initial hypocenter locations randomly in the space before the inversion process.

This provides a way to check the bias in the hypocentral locations and the solution stability of the coupled problem. If the retrieved minimum 1D velocity model is a robust minimum in the solution space, there should be no significant changes in the final hypocentral locations. We generated many dataset adding to the initial hypocenter coordinates random noise ( $\pm 3$  km in both vertical and horizontal directions) according to the average error on earthquake location and we repeated the inversion procedure.

We compared the final locations, obtained starting the inversion process with perturbed earthquakes location, with those obtained starting with the unperturbed locations. In Figure 4.3 grey circles represent the difference between coordinates of the perturbed and the original non-perturbed locations; the black circles are the differences of the final locations

The test revealed fairly stable hypocenter determinations for the most of the events. The difference between the results obtained with non-perturbed starting locations and randomly perturbed ones is smaller than 1 km s for 95% of the events.

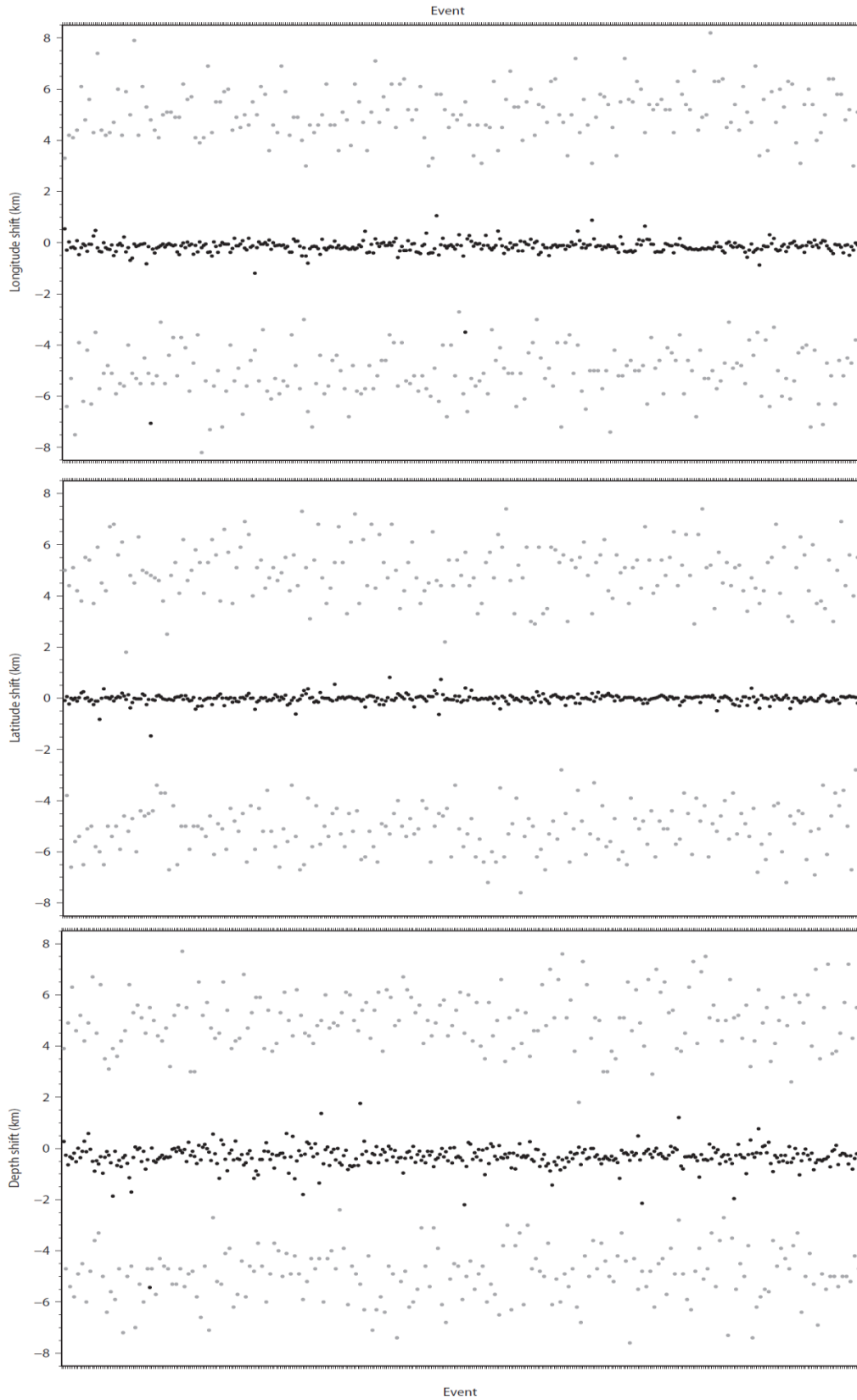


Figure 4.3 Hypocenter stability test. Gray circle represents difference between coordinates of the perturbed and the original non-perturbed initial locations (before the inversion process). Black circle represents difference between coordinates (perturbed - non perturbed) considering the final locations.

## 2.2 Station corrections

Station corrections are integral part of the minimum 1D velocity model since they partly account for the three-dimensionality of the velocity field that cannot be adequately represented by 1D model (Kissling *et al.*, 1995). A change in the velocity structure of the upper layers translates into a more or less constant time-shift for all calculated travel times, which can be compensated by adjusting the station correction.

The VELEST code (Kissling *et al.*, 1995) allows using station elevations for inversion and rays are traced to the true station position. This is an important constrain since in the study area, the elevation of the recording sites ranges from 0.450 to 1.350 km a.s.l. .

Station delays are computed relatively to a reference station, CSG3, whose delay is supposed to be equal to 0. We chose this station because it lies toward the middle of the network, shows a large number of readings with a small error on the observation and it is located in an area where surface geology is known.

The strong lateral velocity variations in the investigated area due to different lithologies varying from Carbonate Platform domain to thrust sheet-top clastic of the shallow subsurface should be accounted for, at least in parts, by the station delays. These are obtained simultaneously with the minimum 1D velocity model. In our minimum 1D model for the Campania-Lucanian region the station located in the northeastern part of the area delayed P-arrivals (positive delays) where we expect low near-surface velocities (Figure 4.4). The southwestern part of the region shows early P-wave arrivals (negative station delays) where rocks with supposedly high P-wave velocity outcrop.

The spatial distribution of station corrections shows a strong lateral variation in a direction orthogonal to the Apenninic chain, which is consistent with the transition between the carbonatic platform outcrops at South-West and the Miocene sedimentary basins at North-East (Figure 4.4a).

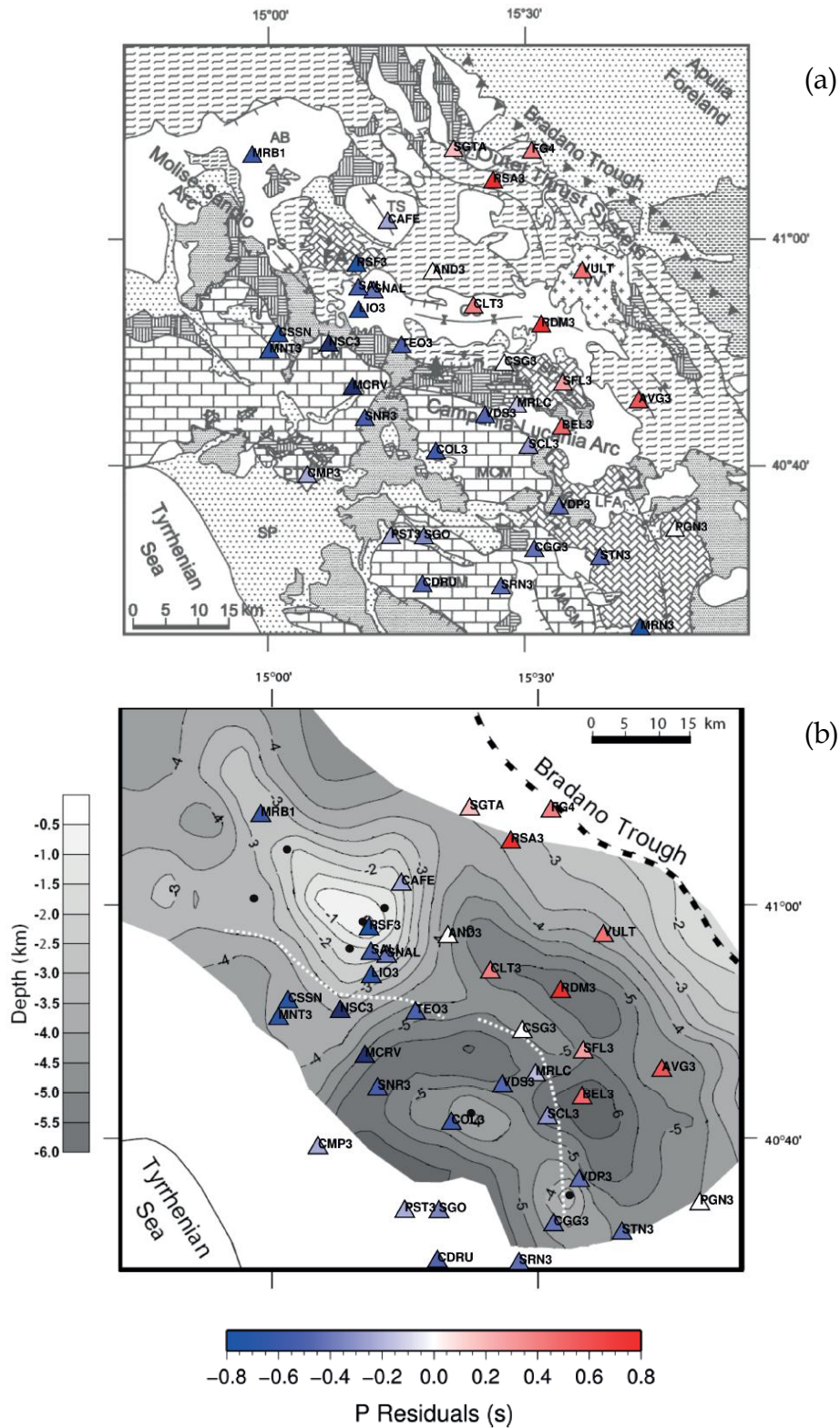


Figure 4.4. Spatial pattern of the station correction. The average value for each considered station is represented. a) comparison of the station corrections distribution with a schematic geological map of the area; in b) comparison with the top of Apulia Carbonate Platform (for more details see Improta *et al.*, 2003).

The comparison of the entity of the retrieved station with the top of the Apula Carbonate Platform obtained by Improta *et al.*, (2003) through a joint interpretation of gravity data, seismic reflection lines and deep wells information highlights that these station delays are clear indicators of strong lateral velocity variations in the near-surface but also likely throughout the crust.

We infact observed a strong correlation with lower depth of the Apula carbonate platform top (4.4b). The rise of this tectono-stratigrafic unit in the Frigento area at NW of the area is underlined by the presence of large negative values of the station corrections (CAFE, RSF3, SNAL, LIO3).

### 2.3 3D P-wave Velocity Model and station corrections interpretation

In order to interpret the observed station corrections pattern we used the three-dimensional crustal velocity model obtained from the inversion of the same data set of P first-arrival travel times by Amoroso (PhD thesis, 2012). The 3D model has been obtained using a linearized, iterative tomographic algorithm (Latorre et al, 2004) in which delay travel times are inverted for both earthquake locations and velocity model parameters at each step of the inversion procedure.

First arrival travel times of wave fronts are computed through a finite difference solution of the eikonal equation (Podvin and Lecomte 1991) in a fine grid of  $0.5 \times 0.5 \times 0.5 \text{ km}^3$ . The latter consists of constant slowness cells computed by trilinear interpolation from the inversion grid. For each event-receiver pair, travel times are recalculated by numerical integration of the slowness field along the previously traced rays (Latorre *et al.*, 2004). Simultaneously, for each node of the inversion grid, travel time partial derivatives are computed for P slowness field, hypocenter location and origin time. The parameters are inverted using the LSQR method of Paige and Saunders (1982). The iteration limit is set to 5000 internal iteration while the number of inversion step is set up to a maximum of 20 iterations. The control of the model roughness is achieved by the requirement

that the Laplacian of the slowness field must vanish during the inversion procedure (Benz *et al.*, 1996, Menke, 1989). The misfit function, defined as the sum of the squared time delay, is a posteriori analyzed and the convergence is usually reached after 10 or 15 iterations. The use of a nodal representation, in which velocity field is reconstructed by three-dimensional grid, is not allowed to introduce a specific geometry of heterogeneities.

Different grid spacings are tested and in particular several inversions were performed progressively decreasing the distance of each node corresponding to increasing the number of parameters. The optimal parameterization was chosen according to the minimum of the Akaike Information Criteria (AIC) (Akaike, 1974). The minimum was obtained for the model with 6x6x2 km<sup>3</sup> grid spacing.

The inversion is performed starting from the best 'Minimum 1D velocity model' with a RMS reduction of about 68% with a final value of 0.1 s.

To verify the spatial resolution of the inferred 3-D model, standard checkerboard test were performed (Amoroso, 2012). A small anomaly pattern is added to grid node values of final velocity models in order to keep the same ray coverage. In Figure 4.5 we display the synthetic (Figure 4.5b) and the recovered pattern (Figure 4.5c). Resolved anomalies are located between 4 and 15 km depth. The anomaly pattern is not recovered at the surface and for depth greater than 15 km. However lateral smearing is detected where lateral distribution is not able to reconstruct small features.

The tomographic image clearly indicates the presence of a strong velocity variation along the direction orthogonal to the Apenninic chain, from 5 to 8-9 km depth, defining two domains characterized by relatively low (3.5 - 4.8 km/s) and high (5.2 - 6.5 km/s) velocity respectively (Figure 4.5a). This is more evident in Figure 4.6 where the retrieved 3D velocity model is superimposed on two schematic geological sections (A-A' and B-B'; Figure 4.6) proposed by Improta *et al.*, (2003) in order to help us to associate the velocity anomalies with the several units. The fault segments are deduced from the model proposed by Pantosti and Valensise (1990).

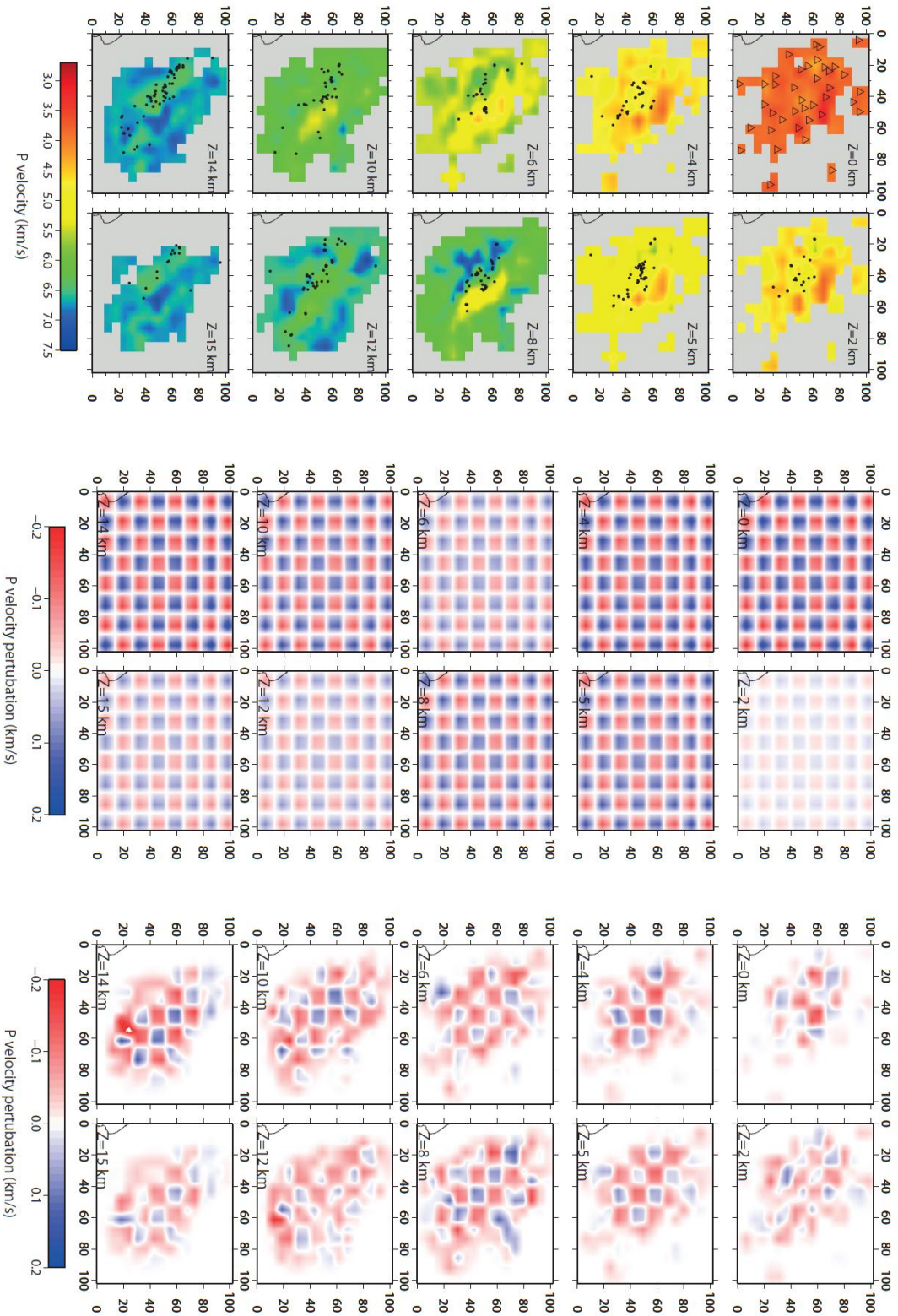


Figure 4.5. Final tomographic model of P velocities and checkerboard test. (a) Map view show velocity layers between 0 and 15 km depth, the regions that are not covered by the ray paths have been masked in grey. (b) Synthetic pattern added to the 3D final tomographic model. (c) Map view at different depth of the recovered pattern.

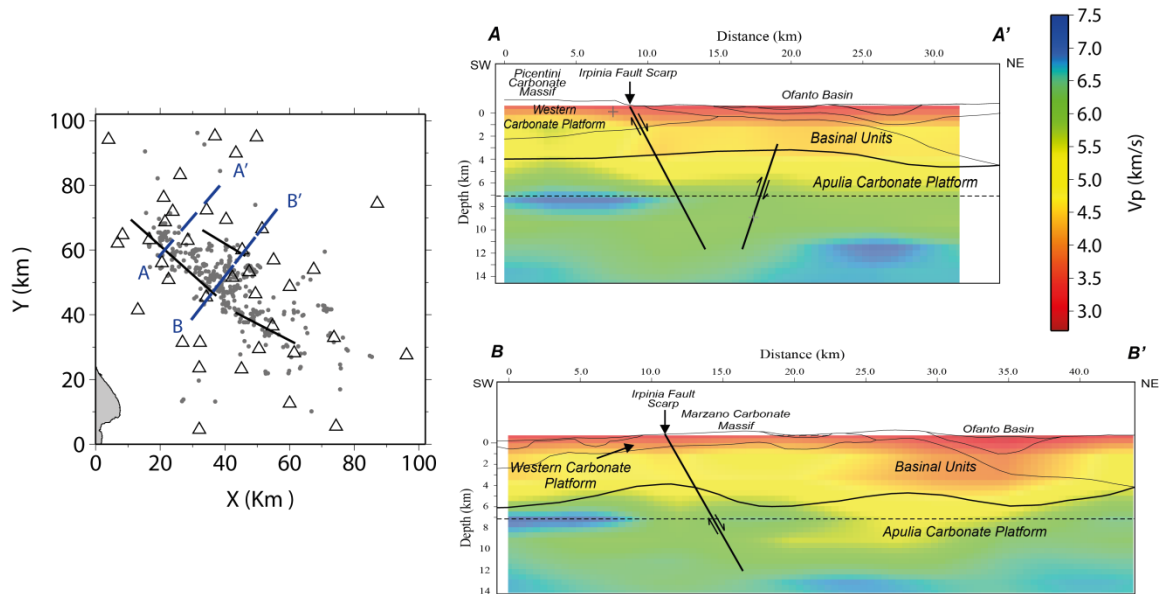


Figure 4.6. The retrieved 3D velocity model is superimposed on two schematic geological sections (A-A' and B-B') proposed by Improta *et al.*, (2003). The fault segments are deduced from the model proposed by Pantosti and Valensise (1990).

Note the general good agreement of the Apulian Carbonate Platform top with the region of the model characterized by high velocity values (6.0-6.5 km/s).

In the section A-A' we see a good correspondence of the Western Carbonate Platform with an high velocity anomaly of about 6 km/s (SW) and a shallow low velocity (3.5 - 4.5 km/s) anomaly in correspondence of the sedimentary basins (NE). This feature is more clear in section B-B' in correspondence of the Ofanto Basin (Figure 4.6).

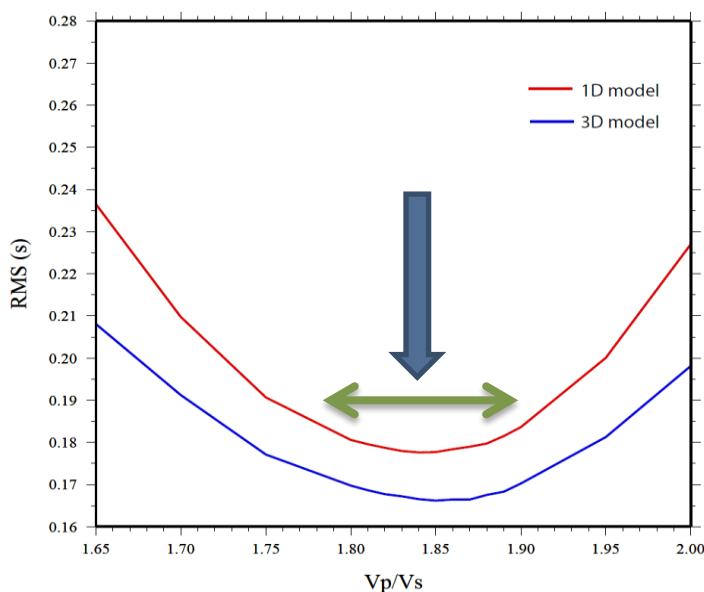
The comparison of retrieved 3D  $V_p$  anomalies with the spatial distribution of 1D derived station corrections confirms that the latter reflects the large-scale geological changes. The spatial pattern of station corrections, in fact, is coherent with the retrieved velocity variation: it is well explained by the strong lateral variation in a direction orthogonal to the Apenninic chain. The retrieved 3D velocity model helps us to give a physical explanation of the station corrections entity and to quantify how deep they are related. It highlights that these station delays are clear indicators of strong lateral velocity variations in the near-surface but also likely throughout the crust until a depth of 5-6 km.

### 3. S-wave velocity structure

To improve the hypocentral determination, using also the S-wave first arrival times, an average  $V_P/V_S$  ratio is computed. The approaches so far described solve for the S-wave model and the P-wave velocity model independently or jointly. It is suitable for cases in which the ratio  $N_p/N_s$  ( $N_p$  and  $N_s$  are the numbers of P and S time readings, respectively) is high and the uncertainties on the S-wave readings are comparable with P uncertainties. In effect, the  $V_P$  model will be constrained by P data that are more numerous and of better quality, and we choose to search the best average  $V_P/V_S$  model considering the best  $V_P$  model as the reference model.

A first evaluation of an average  $V_P/V_S$  ratio has been performed analyzing the “modified Wadati diagram” (Chatelain, 1978). This method has been briefly described in Chapter 3. In an area where there is an extremely variable  $V_P/V_S$  ratio the travel-time residuals computed for the S-wave velocity model derived from P-wave model (using  $V_P/V_S$  calculated with the “modified Wadati diagram”) are not well distributed around zero as well as it was expected.

For this purpose we also analyzed the evolution of RMS of residuals obtained by locating the earthquakes with different values of  $V_P/V_S$  ratio using the NonLinLoc code (Lomax *et al.*, 2000). (Figure 4.7). The analysis is repeated using the minimum 1D velocity model and the retrieved 3D model.



$$RMS_w = \sqrt{\frac{\sum_{i=1}^n w_i (t_i^{calc} - t_i^{obs})^2}{\sum_{i=1}^n w_i}}$$

Figure 4.7 RMS of residuals as function of  $V_P/V_S$  ratio. The red curve is referred to the best 1D velocity model; the blue one to the best 3D velocity model.

The trend of the two curves shows a wide range with minimum RMS. We chose a  $V_p/V_s$  ratio of 1.85. This value is in agreement to that obtained by other studies in the same region ( $V_p/V_s=1.83\pm 0.40$  in Maggi 2008;  $V_p/V_s=1.8\pm 0.1$  in Bernard *et al.*, 1989; Amato and Selvaggi 1993; Bisio *et al.*, 2004; De Matteis *et al.*, 2010).

In literature, whatever the geologic and tectonic framework,  $V_p/V_s$  ratio anomalies ( $\geq 1.7$ ) are systematically interpreted as due to the presence of cracked crustal volumes and/or fluid-saturated zones (Amato *et al.*, 1993; Foulger 1995; Piccinini *et al.*, 1999; Moretti *et al.*, 2004; Ferulano, 2010). In volcanic areas or subduction zones fluids can be even melt (Walck M. C. 1988; Reyners *et al.*, 2006). In the tectonic setting of our study area, i.e., the Southern Apennines upper crust, we suggest, therefore, to explain the observed  $V_p/V_s$  ratio (up to 1.85 or more) as due to the presence of a fractured rock volume possibly saturated by groundwater.

#### 4. Earthquakes Location comparison

In particular in this paragraph the hypocentral parameters were computed using a probabilistic, non-linear model global search earthquake location method (NonLinLoc code; Lomax *et al.*, 2000). This code follows the well-known probabilistic formulation of inverse problems of Tarantola and Valette (1982) and Tarantola (1987). The probability density function (PDF) grid values obtained by the grid search algorithm represent the complete probabilistic spatial solution of the earthquake location problem. The maximum-likelihood point of the complete, non-linear location PDF is selected as an "optimal" hypocenter. To make the location program efficient for complex 3D models, the travel times between each station and all of the nodes of an  $x, y, z$  spatial grid were computed using a 3D version of the Eikonal finite differences scheme of Podvin and Lecomte (1991). To compute the travel times, a regular-sized spatial grid of  $0.5 \text{ km}^3$  was used.

In order to investigate the presence of a systematic shift in the earthquakes position due to the lateral velocity variation not taken into account in the one-

dimensional velocity model (see sketch in Figure 4.8), and to investigate if the introduction of the static corrections can minimize this effect we compared the earthquake locations in the 3D P-wave velocity model (Amoroso, 2011) and in the minimum 1D P-wave velocity model using or not the station correction.

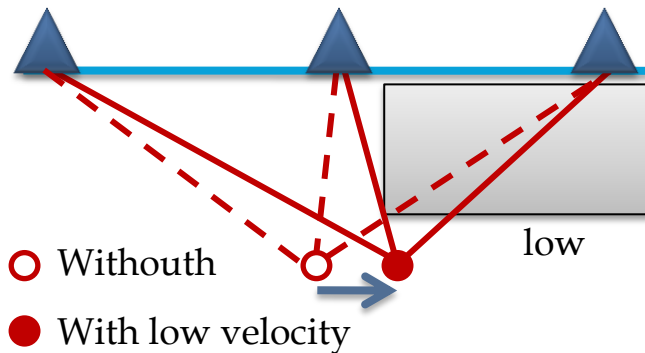


Figure 4.8 Sketch: the location of the earthquakes in our situation may be affected by a systematic error in location calculation, due to the existence of a thick low-velocity layer which is not taken into account in the 1D model.

The analysis is performed on 487 earthquakes with minimum 5P and 2S and  $gap < 200^\circ$  (Matrullo *et al.*, 2011a).

We observed a SW systematic shift of the locations in 1D model respect the locations in 3D model (Figure 4.9). When the station corrections were considered there is a NE systematic shift respect the locations in 3D model (Figure 4.9). This is due to a northeast low-velocity anomaly not considered in the 1D medium as represented in the sketch of Figure 4.8.

It is more clear in the histograms of the differences between the 1D and 3D locations along latitude, longitude and depth where we can quantify the shift respect to the location in the 3D model. The shift appears to be more important along the longitude where is 2 km in average (Figure 4.9c).

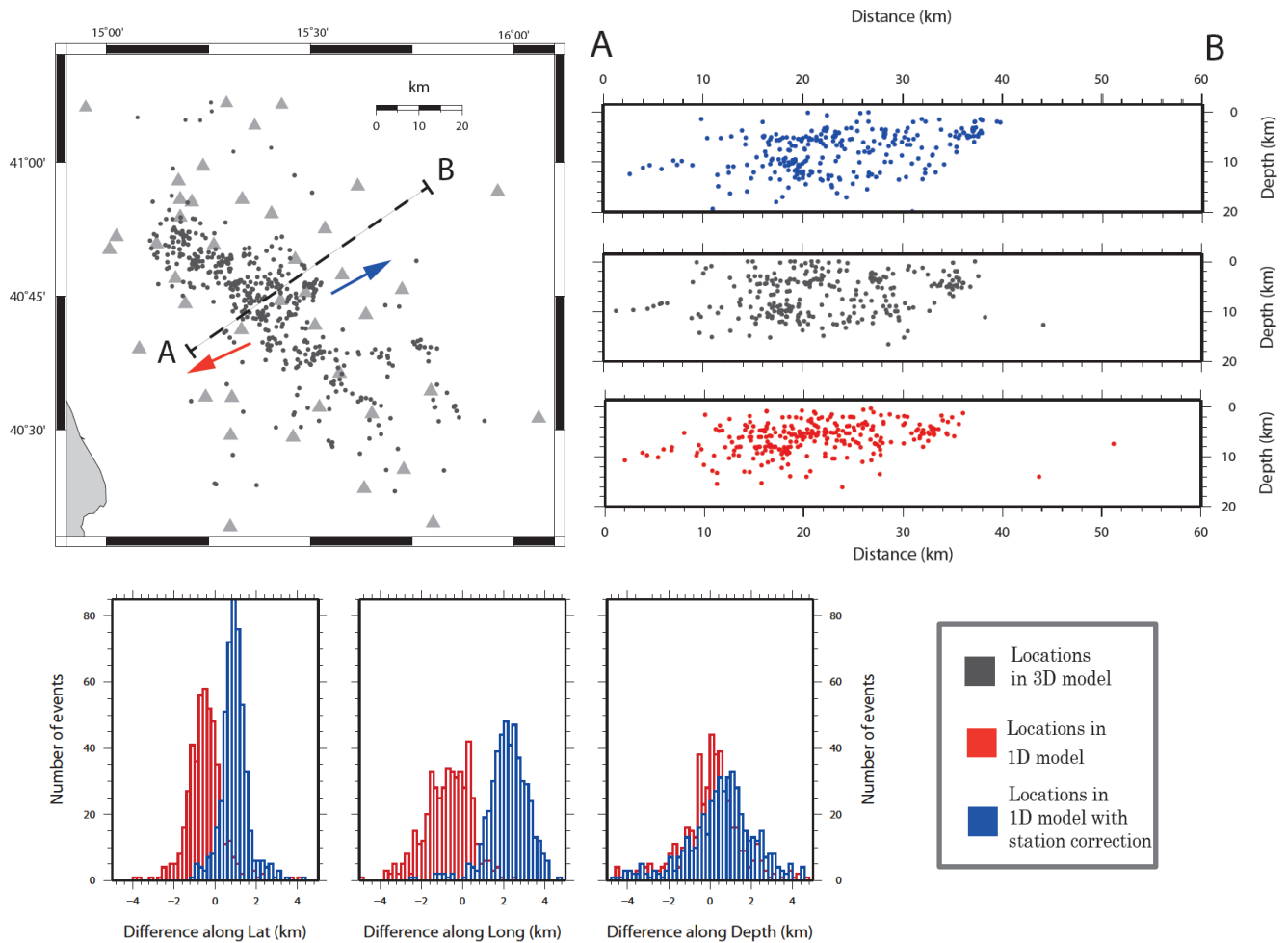


Figure 4.9 In the upper left, an epicentral map of the selected earthquakes (located in the 3D model). The arrows indicates the shift position respect to these. In upper right, a profile with the located earthquakes in the different velocity model. On the bottom the histograms of the differences between the 1D and 3D locations along latitude, longitude and depth.

By analyzing the difference between the observed and computed travel times for the different velocity models as a function of the hypocentral distance, we generally observe a better distribution of P-residuals with respect to the S-residuals (Figure 4.10). Moreover there is a gradual improvement in terms of RMS when we considering the location in the 1D model, the 1D model with the station corrections and finally the 3D tomographic model. Distributions of RMS values for the event locations show a significant variation when we use the 1D model (average RMS=0.25 s) and the 1D model with static corrections (RMS=0.18

s). This RMS value is comparable with the RMS (0.17s) obtained for the earthquakes location in the 3D model.

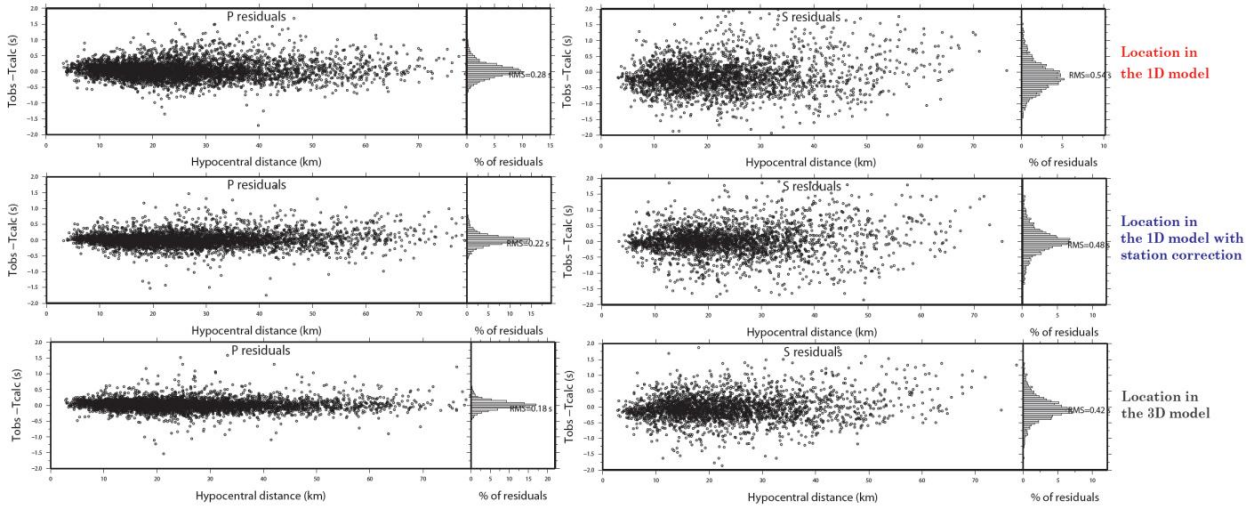


Figure 4.10 The difference between the observed and computed travel times for the different velocity models in function of the hypocentral distance. The histogram of the residuals are shown on the right for each considered case.

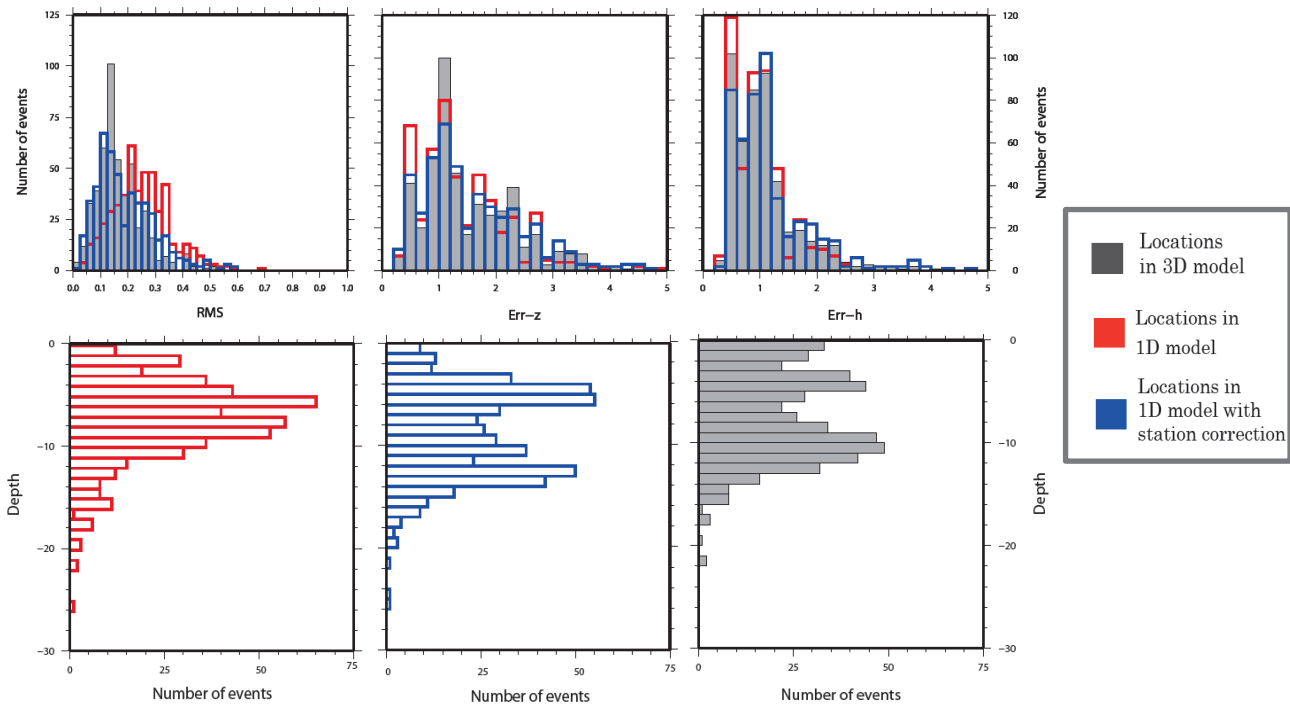


Figure 4.11 On the top: Histogram of RMS, Err-z (error along depth in km) and Err-h (error along horizontal in km). With different color we considered the different locations. On the bottom: the histogram of the events in function of depth.

There is no significative difference for the three models in terms of distributions of vertical (Err-z) and horizontal error (Err-h) (Figure 4.11). Analyzing the distributions of the events with the depth for the three velocity models we conclude that the seismicity appears more concentrated in the first 10 km depth in the 1D velocity model (Figure 4.11). The distributions became bimodal in the 1D model with station corrections and in the 3D model and very similar to each other (Figure 4.11).

## 4.1 Synthetic examples on earthquake location

To understand if the systematic shift is real or an artefact of the several inversion procedures we performed two synthetic examples.

In the first case we supposed 75 seismic sources disposed along three lines dipping north-eastwards (see the Figure 4.12).

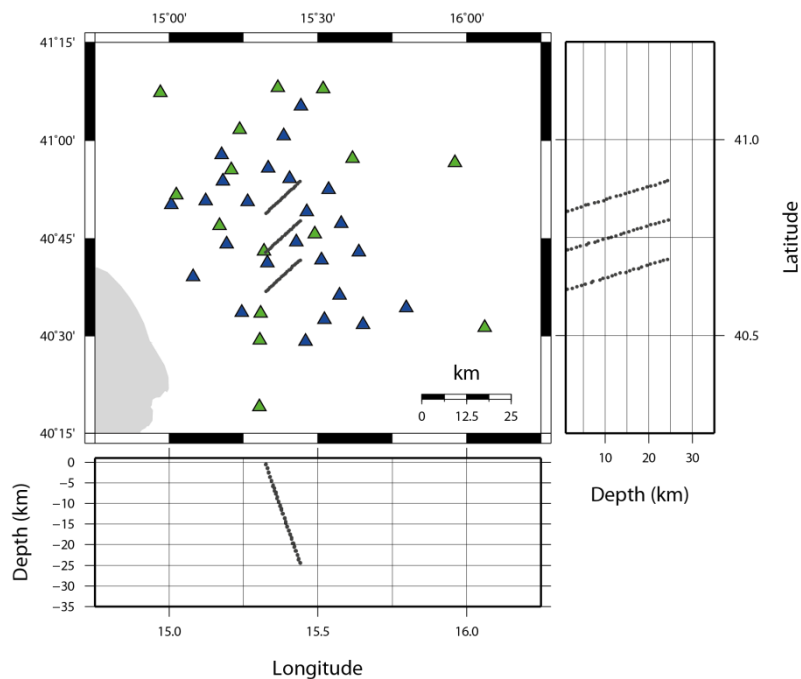


Figure 4.12 Initial configuration of earthquakes for the synthetic example 1. Black circles represent the location of seismic source and triangle the seismic station (in blue ISNet stations; in green INGV stations)

With NLLoc code we computed in the 3D P-wave velocity model the theoretical P and S travel times at 42 stations of ISNet and INGV network as for the real case. We suppose an error less than 0.05 s on the P-arrival time and less of 0.1 s for the S-arrival time to reproduce the different uncertainty that affects the real readings.

After we relocated the sources in the 3D velocity model and in the 1D models (with and without the station correction that we recomputed with VELEST code) and compared the results (Figure 4.13).

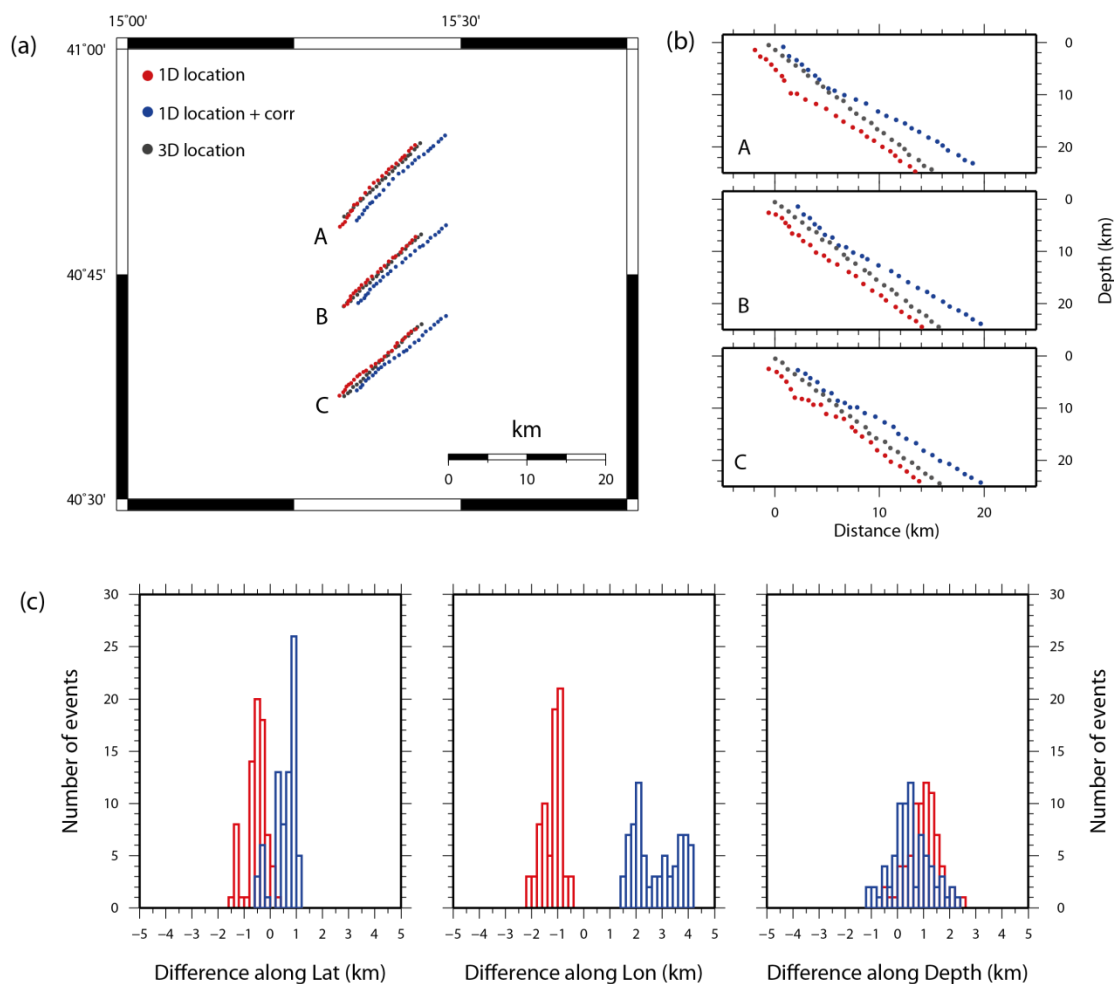


Figure 4.13 Result of synthetic example in plane (a), in three section along the lines of sources (b), and histogram of the difference between the 1D locations (with and without station corrections) and 3D locations along latitude, longitude and depth.

The results of the synthetic test confirm the shift observed in the real case. In particular we remark in the map view of Figure 4.13b a shift of the source positions mainly along E-W direction although the alignment is preserved. In the vertical sections along the lines of sources (Figure 4.13b) the linear distribution of the sources is perturbed and in particular we observe a slight change of the slope at great depth ( $> 10$  km) for the 1D locations with static corrections. The shift is shown in the histograms of the differences between the 1D locations (with and without station corrections) and 3D locations along latitude, longitude and depth (Figure 4.13c).

The vector from the position of the sources located in the 3D model to the position of the sources located in the 1D velocity model (with and without static corrections) along the longitude is shown for each line of sources in Figure 4.14.

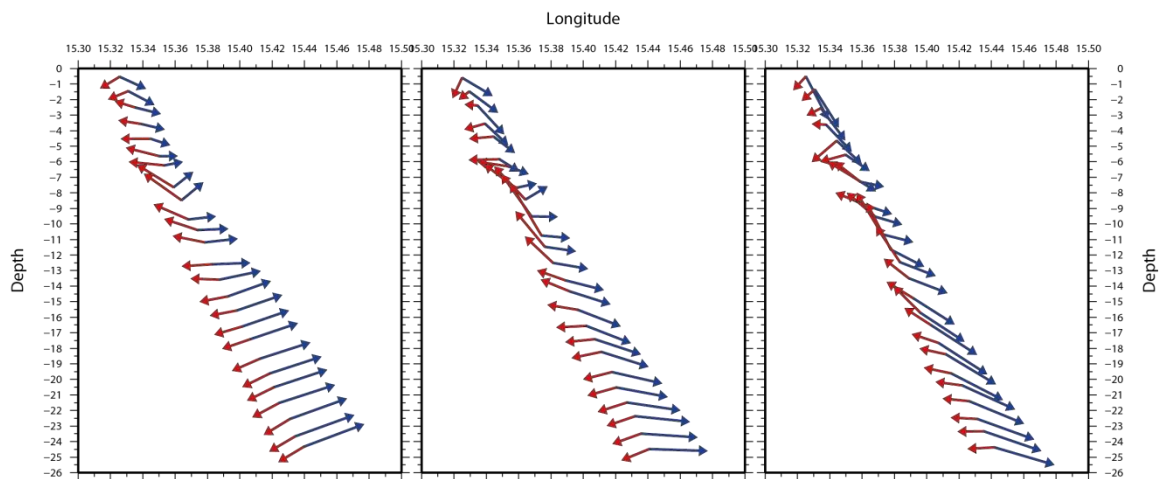


Figure 4.14 The vector from the position of the sources located in the 3D model to the position of the sources located in the 1D velocity model along the longitude. The red vector is referred to the 1D location, the blue color is referred to the 1D location considering the station corrections.

The epicentral shifts are better highlighted performing another synthetic test in which we considered seven sources at fixed depth (7.5 km) along a typical Apenninic alignment (Figure 4.15)

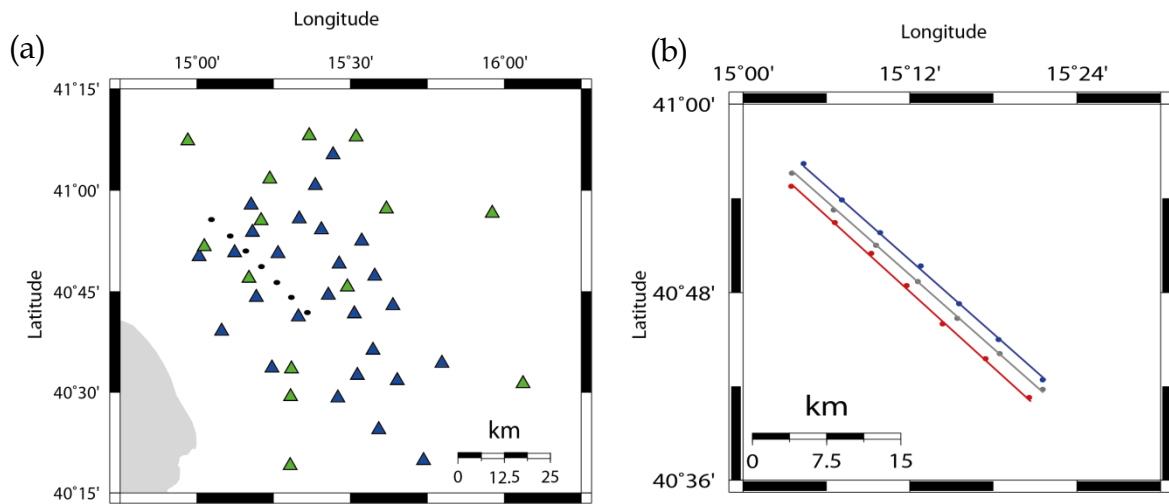


Figure 4.15 Initial configuration of seismic sources (circles) for the synthetic example 2 (a) and final configuration of sources (b) in the 3D model (gray), 1D model (red), and 1D model considering the station corrections (blu). The triangles represent the seismic station (in blu ISNet stations; in green INGV stations)

## 5. HypoDD relocation

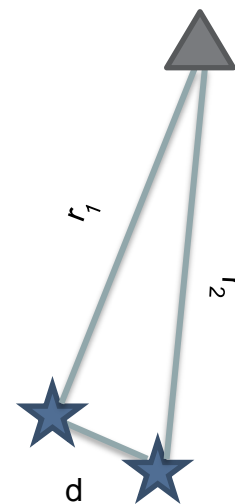
In order to minimize errors due to un-modelled 3D velocity structure and to improve earthquake location we used a double-difference (DD) algorithm (Waldhauser and Ellsworth, 2000). The effects of errors in the knowledge of velocity structure can also be effectively minimized by using relative earthquake location methods.

The fundamental hypothesis on which is based the the double-difference technique (HypoDD, Waldhauser and Ellsworth, 2000) is that hypocentral separation between two earthquakes are small compared to the event-station distance

$$d \ll r_1 \approx r_2$$

and to the scale length of the velocity heterogeneity.

Therefore, the ray paths between the source region and a common station are similar along almost the entire raypath. The difference in travel times for two



events observed at one station can be attributed to the spatial offset between the events with high accuracy (Fréchet, 1985; Got *et al.*, 1994). This is because the absolute errors are of common origin except in the small region where the ray paths differ at the sources. This technique carries out a simultaneous relocation of events with large distance from stations. It is possible to further improve the location precision using waveform cross-correlation methods. Two earthquakes produce similar waveforms at a common station if their source mechanisms are virtually identical and their sources are co-located so that the signal scattering due to velocity heterogeneities along the ray paths is small.

In the linearized approach of earthquake location, a truncated Taylor series expansion is generally used. The resulting problem then is one in which the travel-time residuals,  $r$ , for an event  $i$  are linearly related to perturbations,  $\Delta\mathbf{m}$ , to the four current hypocentral parameters for each observation  $k$ :

$$\frac{\partial t_k^i}{\partial \mathbf{m}} \Delta\mathbf{m}^i = r_k^i \quad (4.2)$$

Where  $r_k^i = (t^{obs} - t^{calc})_k^i$  is the travel time residual for event  $i$  at station  $k$ ,  $t^{obs}$  and  $t^{calc}$  are the observed and theoretical travel time, respectively, and  $\Delta\mathbf{m}^i = (\Delta x_i, \Delta y_i, \Delta z_i, \Delta \tau_i)$  are the perturbation of the four current hypocentral parameters.

Equation 4.2 is appropriate for use with measures arrival times. Considering travel-time differences between events  $i$  and  $j$ , at station  $k$ , the  $(t_k^i - t_k^j)^{obs}$ , the equation (4.2) becomes:

$$\frac{\partial t_k^{ij}}{\partial \mathbf{m}} \Delta\mathbf{m}^{ij} = dr_k^{ij} \quad (4.3)$$

where  $\Delta\mathbf{m}^{ij} = (\Delta x^{ij}, \Delta y^{ij}, \Delta z^{ij}, \Delta \tau^{ij})$  is the change in the relative hypocentral parameters between the two events, and the partial derivatives of  $t$  with respect to  $\mathbf{m}$  are the components of the slowness vector of the ray connecting the source and receiver measured at the source (Aki and Richards, 1980).

We assume constant slowness vector for the two events. This is true for events that are sufficiently close together.  $dr_k^{ij}$  is the residual between observed and calculated differential travel time between the two events defined as:

$$dr_k^{ij} = (t_k^i - t_k^j)^{obs} - (t_k^i - t_k^j)^{calc} \quad (4.4)$$

We define equation (4.4) as a double difference (DD). Applying the Eq. 4.2 to each event and subtracting the two equations we obtain:

$$\frac{\partial t_k^i}{\partial \mathbf{m}} \Delta \mathbf{m}^i - \frac{\partial t_k^j}{\partial \mathbf{m}} \Delta \mathbf{m}^j = dr_k^{ij} \quad (4.5)$$

We minimize the double difference of residuals for pairs of earthquakes at each station by weighted least squares using the conjugate gradients method (LSQR, Paige and Saunders, 1982). The final solutions are found by iteratively adjusting the vector difference between the nearby earthquake pairs. The LSQR method takes advantage of the sparseness of the system of DD-equations and is able to solve a large system efficiently.

## 5.1 Synthetic example

To prove the improvement of the earthquake location in terms of recovery of the systematic shift observed in the absolute location with 1D velocity model, we repeat the synthetic example of the previous paragraph considering 75 sources disposed along three lines (Figure 4.12).

Re-locating the sources with double difference algorithm we observed that the systematic shift relative to the 3D locations becomes less important (Figure 4.16a,b). The initial linear distribution of sources with depth in the vertical section along the sources line is retrieved expect at depth greater than 10 km.

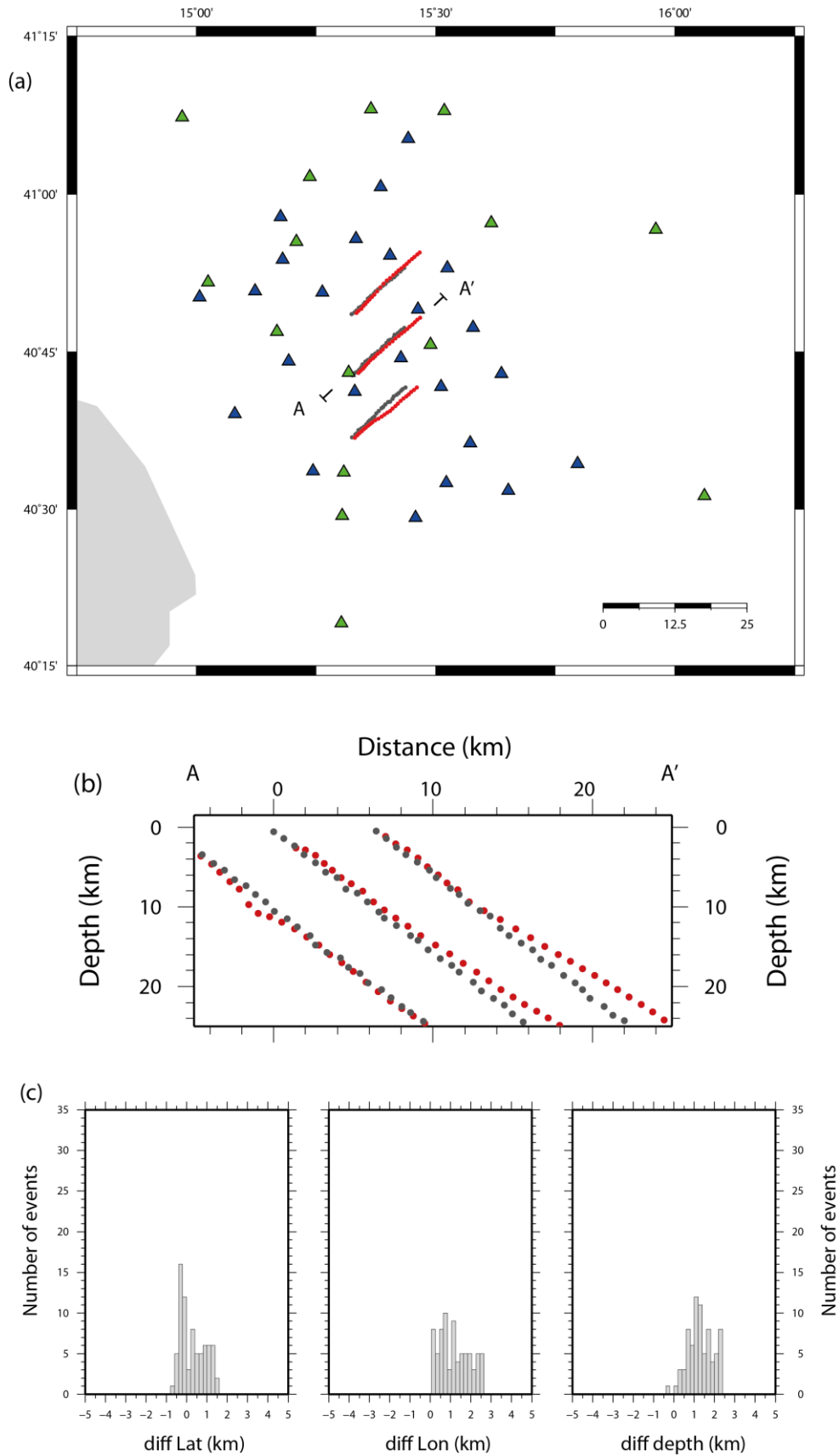


Figure 4.16 Initial configuration of seismic sources for the synthetic example (grey) and HypoDD relocation in red (a), vertical section along the line of sources (b), and histograms of the difference between the HypoDD locations and the true position along latitude, longitude and depth (c).

## 5.2 Double difference location in the studied area

We applied the double-difference technique (HypoDD, Waldhauser and Ellsworth, 2000) to our data set.

We considered restrictive constraints on each events couple, such as a residual threshold of 0.1 s for P and S absolute travel times, a maximum distance of 10 km between linked pairs (to respect the hypothesis that the distance between events is large compared to the maximum distance between event pairs and station) and a minimum of 4 links between the events. Two earthquakes define an events couple when they have at least the fixed minimum number of links where a link means that the two events have been recorded at the same station. Generally an events couple has a strong link when the two events have been recorded at eight common stations. This number is used in problem with more than 10000 earthquakes. In our case we tested that 4 link is an optimal number to select a fairly number of events (for a more detailed description of the HypoDD parameter, see Waldhauser and Ellsworth, 2000)

These constraints reduced the number of useful events from 1312 to 911.

In particular we relocated the event with HypoDD algorithm by dividing the dataset into two subsets: Irpinia cluster and Potenza cluster (in the area: 15.65-15.95 E, 40.55-40.75 N) based on known geological and seismological features of the area. In particular we considered 895 events in the Irpinia region and 60 in Potenza region. And after the relocation process we reduced the number of useful events (854 in Irpinia and 57 in Potenza).

In Figure 4.17 we show the relocated earthquakes for the Irpinia (turquoise) and Potenza region (orange). In a profile EW are plotted all the seismicity to understand the general characteristic of the relocated seismicity. A histogram of the earthquakes as function of depth is shown.

The earthquakes located along the chain (Irpinia region) affect the uppermost 15 km of the crust and their depth distribution is nearly uniform. The cross sections in Figure 4.17 indicate that the seismicity, along the chain, does not occur on a

single fault but in a volume delimited by the faults activated during the 1980 Irpinia earthquake (it will be best described in Chapter 6).

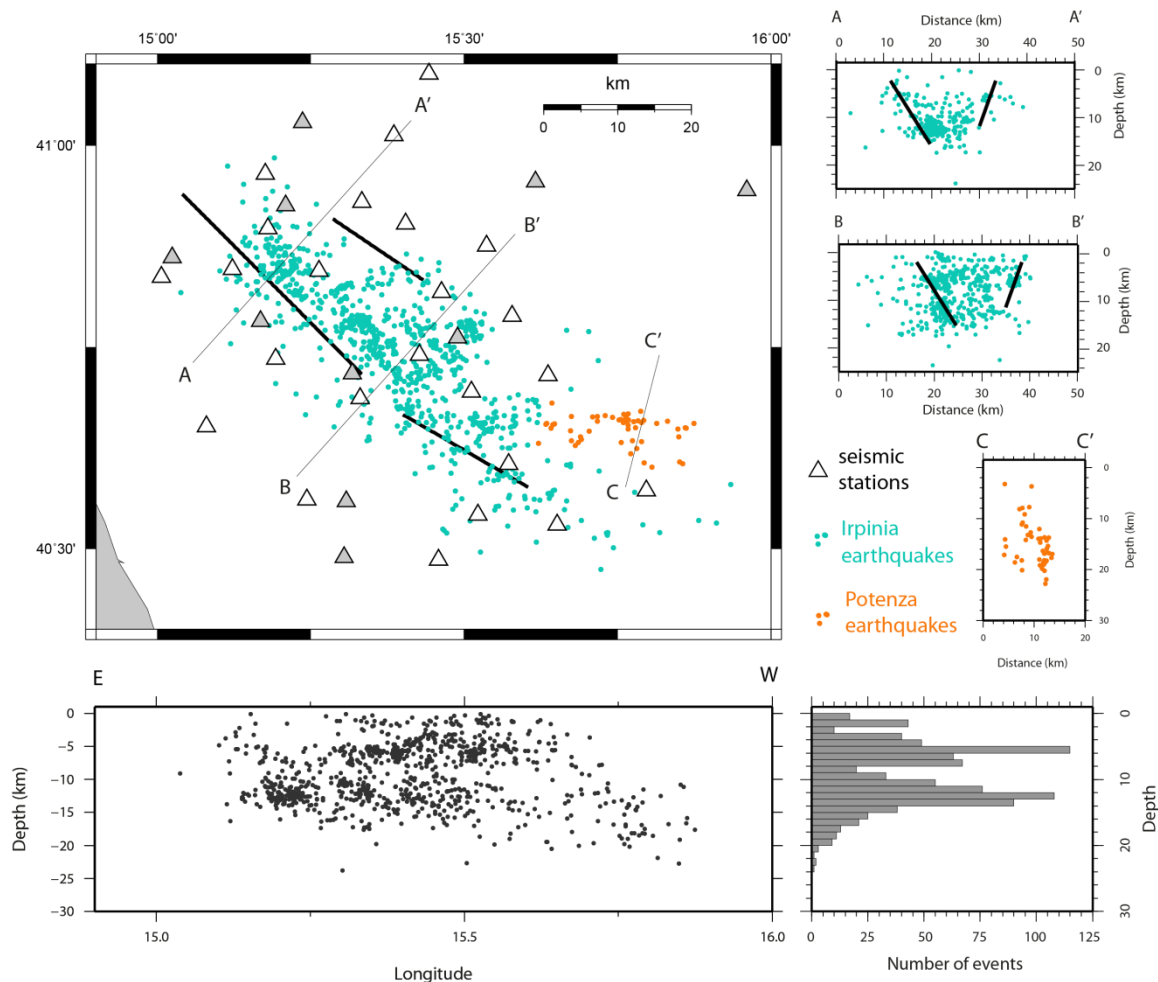


Figure 4.17 Map view of the relocated seismicity from August 2005 to April 2011 by using the double-difference method. The black lines are the surface projection of the three fault segments that ruptured during the 1980 Irpinia earthquake (Bernard and Zollo, 1989). Cross sections of the seismicity along the profiles reported in the map. The width of cross section is 15 km. Black lines represent the projection of the fault segments of the Irpinia earthquake. E-W vertical section of the seismicity and histogram of the events in function of depth.

The seismicity of Potenza region presents different features: epicentral distribution exhibits an alignment approximately along E-W direction. The earthquakes in this region are located at a larger depth, down to 25 km depth and show a sub-vertical alignment. The background seismicity in the Potenza

area delineates an E-W striking structure that cuts off the NW-SE striking, faults along the Apennine chain. This evidence is also consistent with results obtained by Ekstrom (1994) and Di Luccio *et al.*, (2005) who previously analyzed the 1990 and 1991 earthquake sequences.

Figure 4.18 shows the distributions of the error on the events location (along  $x$ ,  $y$  and depth) and the distribution of RMS of time residuals. In turquoise we represent the results for the Irpinia cluster, and in orange for the potenza cluster. The distribution of the RMS (s) is centered around 0.09s for both cases. The error along the direction is for the relocated Irpinia events less than 200m (in average 80m) and became more important for the Potenza earthquakes (300m in average). We note a general improvement of the error passing from the absolute (previous paragraph) to the relative location.

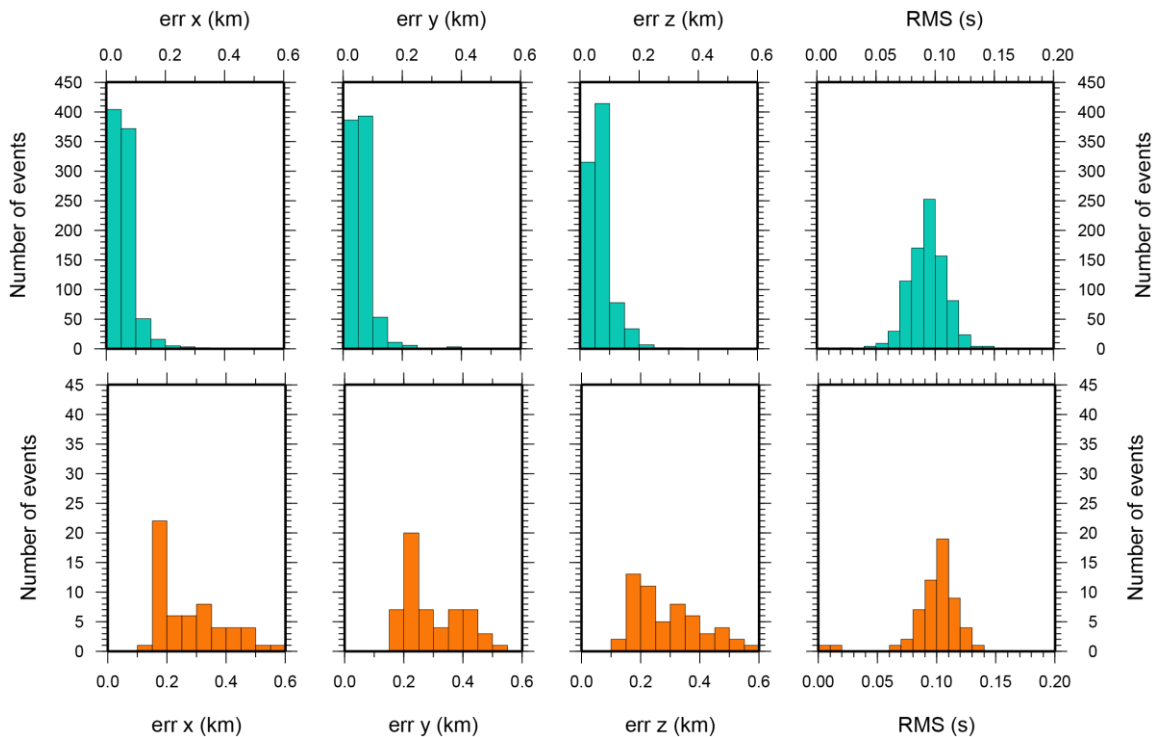


Figure 4.18 distributions of the error on the events location (along  $x$ ,  $y$  and depth) and the distribution of RMS of time residuals for the selected Irpinia earthquakes (turquoise) and Potenza earthquakes (orange).

We underline that the NLLoc error statistics illustrated in the previous chapter are obtained by absolute locations while the HypoDD statistics refer only to relative hypocenter locations.

To better understand the change in location we plot the seismicity before (gray) and after the double difference relocation (red). The seismicity appears more clustered with respect to the initial location. In particular, to understand the improvement of the location, we show in the upper corner of the figure 4.19 an histogram of the RMS (s) for the initial locations (gray) and the hypoDD relocation (red). We obtain an RMS reduction of about 55% with a final value of 0.09 s.

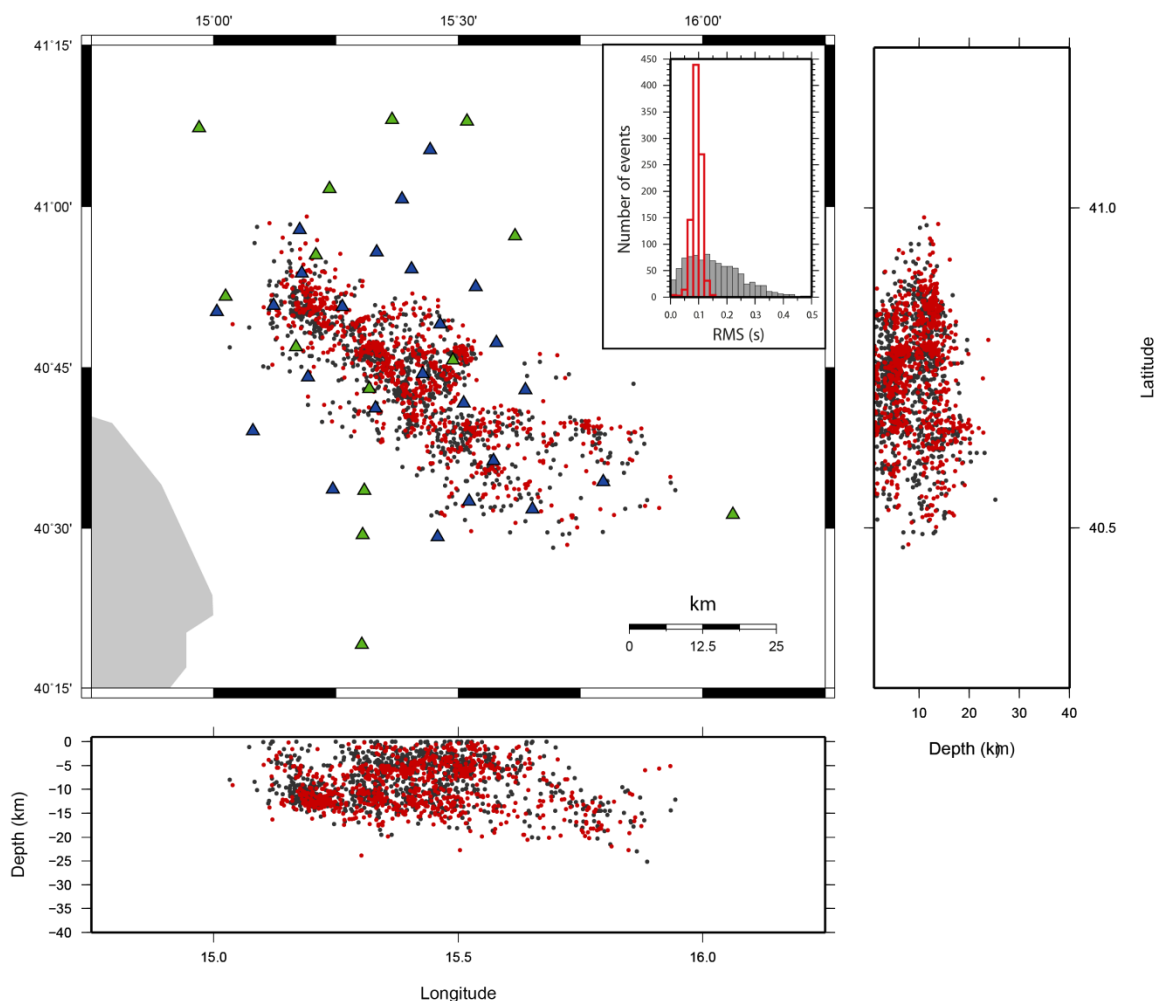


Figure 4.19 The seismicity before (gray) and after the double difference relocation (red). In the upper corner we show an histogram of the RMS (s) in both case (initial and hypoDD location). The station are indicated with triangles (ISNet in blu, INGV in green).

This is more clear in the comparison of the seismicity pattern before (Bulletin location) and after (accurate manually picking of the waveform, velocity model analysis and HypoDD relocation; Figure 4.19). The seismicity pattern after our processing better delineates both the Irpinia and the Potenza fault systems. The seismicity appears more clustered with respect to the Bulletin location.

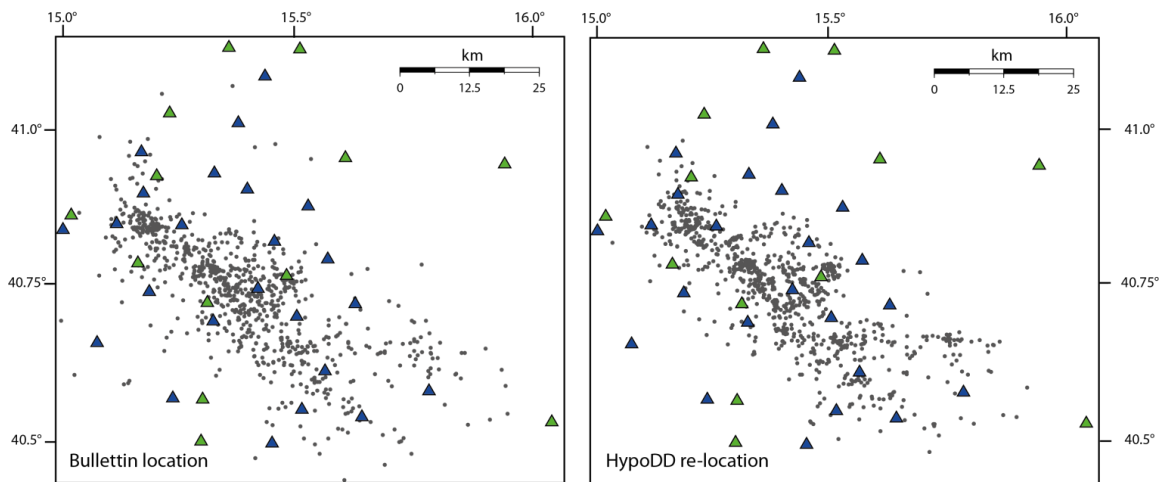


Figure 4.19 Comparison between Bulletin locations (from ISNet and INGV catalogues) and after our processing accurate manually picking of the waveform, velocity model analysis and HypoDD relocation. One notes that relocated events better delineate the Irpinia and Potenza fault systems.

## 6. Discussions and conclusions

The detailed analysis of the background regional microseismicity ( $M < 3$ ) of the Southern Apennines (Italy) is used to determine the 1D velocity structure in a structurally complex area that has three-dimensional peculiarities.

The distribution of station delays, obtained simultaneously with the velocities of the minimum 1D model, shows a strong lateral variation in a direction orthogonal to the Apenninic chain. The comparison of the station corrections distribution with the top of the Apula Carbonate Platform and the entity of the retrieved station corrections highlights that these station delays are clear indicators of strong lateral velocity variations in the near-surface but also likely throughout the crust until a depth of 5-6 km. The availability of a 3D P-wave velocity model provides a physical explanation of the station corrections

distribution and confirms that the station corrections reflect lateral variations of P-wave velocity at great depths.

In this chapter we have analyzed the effects induced on earthquakes location when this important lateral velocity variation is not taken into account. As we expected the relocated seismicity exhibits a SW systematic shift. This problem may be crucial when the location of microearthquakes is used to delineate fault structures.

The station corrections bring a significant increase in the quality of the location: the average RMS of time residuals shows a significant improvement and this result is comparable with that obtained for the 3D locations. Also the main features of the seismicity located in the 1D model with station corrections and in the 3D model are comparable: the distributions of the events are very similar each other both for the depth values and for the bimodal trend observed. This feature is not present in the distribution of the events in depth computed in the 1D velocity model without static corrections.

The inclusion of the station corrections in the location procedures over-corrects the shift in very complex medium: when the station corrections are considered there is a NE systematic shift respects the locations in 3D model. Some synthetic example showed that the use of 1D velocity model with a double difference technique (HypoDD) can overcome in part the problem of not precise knowledge of the propagation medium.

The re-located seismicity with HypoDD well delineate a system of NW-SE striking normal faults along the Apenninic chain and an approximately sub-vertical E-W oriented fault transversely cutting the belt. The seismicity along the chain does not occur on a single fault but in a volume, delimited by the faults activated during the 1980 Irpinia M 6.9 earthquake.

In the Irpinia area, characterized by an extensional stress field, we do not expect to see sharp streaks of microearthquakes as for strike slip faults (Hauksson and Shearer, 2005; Shearer *et al.*, 2005). In fact, the normal faults are gently dipping and epicentral maps could not display linear trends as for near vertical faults;

moreover, in particular in this area, normal fault systems are generated by graben like structure with the presence of several similar trending sub-parallel faults. These combined effects are likely to produce rather cloudy distributions mainly elongated along the dominant fault system strike.

The fault plane solutions and the direction of principal stress axes may provide the evidence for either earthquakes occurring along normal fault dipping planes or/and the presence of a highly organized system of sub-parallel faults occurring in the volume confined within the master faults as shown in the next chapter

Results show that the recent low magnitude earthquakes belongs to the background seismicity and they are likely generated along the major fault segments activated during the most recent earthquakes, suggesting that they are still active today thirty years after the mainshock occurrences.

# Chapter 5

## Focal mechanisms and stress field determination

---

### 1. Introduction

Because of their frequent occurrence, the small earthquakes are particularly important for characterizing regional tectonics and constraining stress orientations (Hardebeck *et al.*, 2002). In the previous chapter we showed that an accurate localization of microearthquakes in the Campania-Lucania region, an area characterized by extensional regime, highlights the existence of a complex fault system but it is necessary to determine the fault plane solutions and the direction of principal stress axes to define the geometry of fault systems and understand the geodynamic acting in the area.

In this chapter, we first illustrate the methodology behind the construction of the focal mechanism and the algorithm used (FPFIT - Reasenberg and Oppenheimer, 1985) and then we apply to our dataset. After we analyze the problem of the stress field determination. We use a method developed by Rivera and Cisternas (1990) in which the first-motion data, instead of previously determined focal mechanisms solutions, are directly used for the inversion. Moreover we compute the confidence limits by using a bootstrap resampling approach in order to get realistic error estimation on the orientation of the three principal axes. Furthermore, we investigate the possibility of a spatial variation of the stress field.

In this chapter we also analyze the sensitivity of first-motion focal mechanisms and stress tensor to various sources of error. The focal mechanism and stress

field parameters depend on the P-wave first-motion polarity observations, the assumed earthquake location and the choice of seismic-velocity model, both of which affect the computed position of stations on the focal sphere. The changes in the best-fitting focal mechanism and stress parameters are complex and nonlinear and can depend on other factors, such as stations coverage and event depth. Changes in event location and in velocity models essentially modify the computed takeoff angles and as a consequence the position of seismic stations on the focal sphere. In particular, only the changes of event position in depth are usually considered because vertical uncertainty is usually much larger than horizontal uncertainty. But several studies demonstrate that the sensitivity of the takeoff angle to the velocity models is usually much greater than the sensitivity to event depth (Hardebeck *et al.*, 2002; Pasquale *et al.*, 2009). We analyze the influence of the velocity model (and consequently the influence of the earthquake location) on the estimated parameters.

## 2. Focal mechanisms

The first motions of P waves have long been used to determine earthquakes focal mechanism using the double-couple model.

First-motion polarities are observed at seismic stations, and the position on the focal sphere for each observation, that is, the azimuth and takeoff angle at which the ray leaves the source, is computed for an assumed location and seismic-velocity model. The initial motion of the P wave determines whether the ray left the source in a compressional (upward first motion at a surface receiver) or dilatational quadrant (downward first motion). The focal mechanism is determined by finding two orthogonal planes that separate these quadrants.

Usually only the lower hemisphere of the focal sphere is plotted (polarities from the upper hemisphere are plotted on the opposite side point of the focal sphere), as most rays at teleseismic distances depart downward from the source. There is no way to tell from these observations alone which of the two nodal planes is the true fault plane and which is the auxiliary fault plane.

The most widely used method for determining focal mechanisms from P-wave polarity data is the FPFIT software package (Reasenber and Oppenheimer, 1985). FPFIT employs a grid search over all possible values of the strike, dip, and rake to identify the best-fitting focal mechanism. The misfit for a given focal mechanism is defined as the number of polarity observations that are inconsistent with the predicted polarity for the quadrant in which they appear, weighted by the quality of the observation and the distance from the nodal planes.

The FPFIT procedure accounts for the possibility of errors in the observed P-wave polarities, but it does not account for possible errors in the computed takeoff angles of the rays. Changes in the assumed source location or the seismic-velocity model alter the pattern of observations on the focal sphere and therefore the best-fitting focal-mechanism solution can change. Focal mechanisms that are stable with respect to polarity errors may be unstable with respect to small changes in location or velocity model and should not necessarily be considered well constrained (for more details on FPFIT code see Reasenber and Oppenheimer, 1985).

## 2.1 Focal mechanisms of the studied area

In our case, the main problem related to the focal mechanisms determination is due to the difficulty of reading the polarity of the first P-arrival times. As we see in the Chapter 3, although the analyzed dataset have a good number of P-wave arrival times (weight  $\propto$  the smaller reading error), to assign to all the readings the polarity was rather difficult due to the small magnitude of the earthquakes.

We perform the polarities reading only for the P-wave arrival time readings with the smaller reading error. Moreover we have chosen, in order to better constrain the focal mechanisms, a minimum of 6 polarities for each event ensuring that the distribution of polarities on the focal sphere was quite heterogeneous. In some cases, in fact, the number of polarity was theoretically sufficient to compute

the focal mechanism, but since the polarity was the same at all stations, it was impossible to well constrain the focal mechanism. We have selected the focal mechanisms with at most only two discrepant polarities, single solutions and when multiple fault plane solutions were available we have selected the solution with the maximum quality factor defined in the code. In this way we have selected 118 well constrained earthquakes. The Figure 5.1a shows an epicentral map of the analyzed earthquakes. A red diamond is present where the focal mechanism was calculated. The Figure 5.1b represents the histogram of the read polarities as function of the number of earthquakes, considering only the events with well constrained focal mechanism.

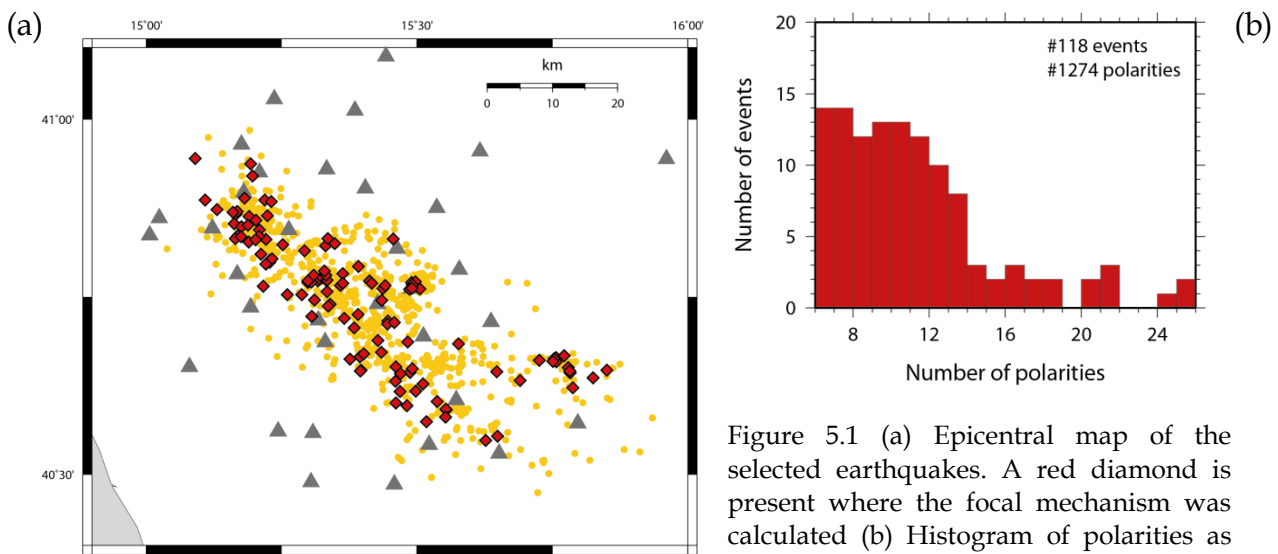


Figure 5.1 (a) Epicentral map of the selected earthquakes. A red diamond is present where the focal mechanism was calculated (b) Histogram of polarities as function of the number of earthquakes.

From a first analysis of focal mechanisms distribution we can see that mostly, fault plane solutions belong to normal component faulting (pure normal fault and normal fault with a strike-slip component). Only some solutions show strike-slip or reverse faulting. This is evident in the diagram of T-axis plunge vs P-axis plunge (Figure 5.2). Most of points (cross in Figure 5.2b) is located in the lower right. This means that the T-axis is nearly horizontal while the P-axis is nearly vertical and so there is a majority of normal-type focal mechanisms. The presence of points on the graph near the origin of the coordinate system indicates the attendance of strike-slip-type focal mechanisms (both P and T-axis

near the horizontal), while the points in the central part of the graph indicate the presence of mixed-type (normal-type with a strike slip component) focal mechanisms. There are no points in the graphs relative to the presence of reverse-type focal mechanisms (T-axis near the vertical and P-axis near the horizontal). A detailed analysis of these values displayed that only 10% of focal mechanisms have plunge of the T axis is greater than  $35^\circ$  (Figure 5.2).

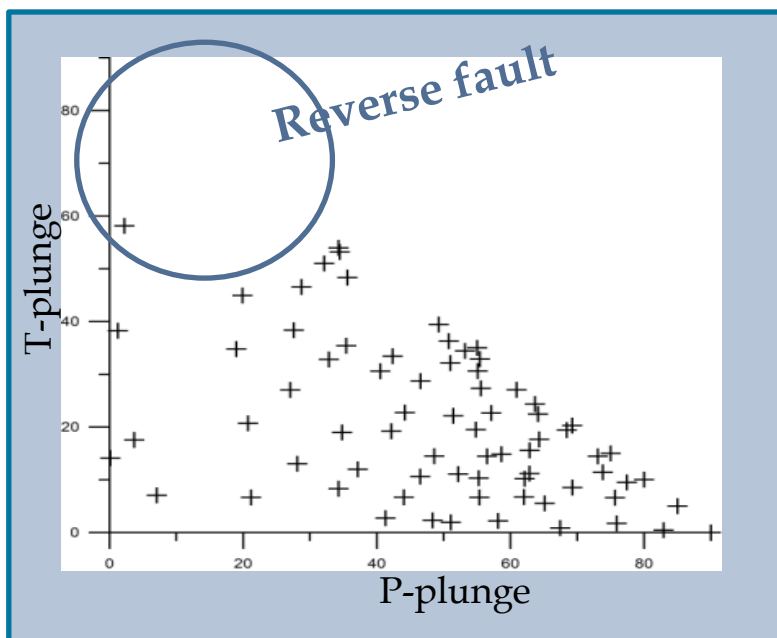


Figure 5.2 Diagram of T-axis plunge as function of P-axis plunge for the selected earthquakes. With a circle we underline the area where we expect reverse solution

As well known, the main difference related to the use of 1D or 3D velocity model lies in the computation of take-off angles. Rose diagram in Figure 5.3 shows that the take-off angles computed using the minimum 1D P-wave velocity model and the double difference location method are clustered around some preferential values ( $45^\circ$  and  $90^\circ$ ). The take-off angles, computed using the 3D velocity model, are more uniformly distributed in the range  $45^\circ$ - $135^\circ$ .

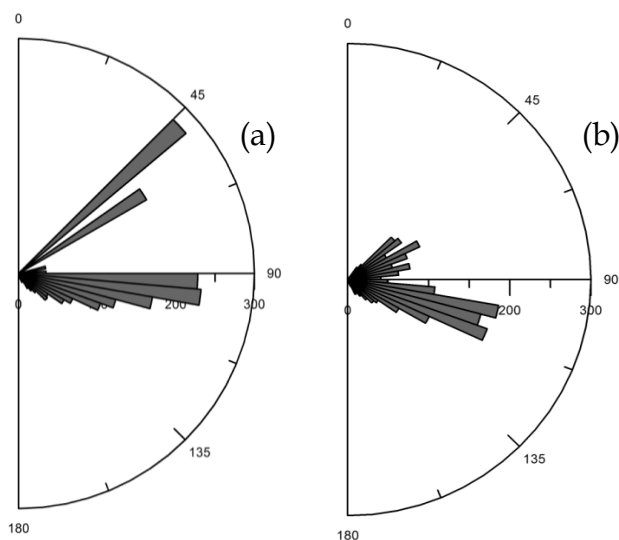


Figure 5.3 Rose diagram for the take-off angles computed using the minimum 1D velocity model and double difference location (a), and (b) the 3D velocity model. The length of the bar is proportional to the number of the data considered (this number is indicated in the horizontal bar in the diagram)

In order to evaluate how these differences between the take-off angles reflect on the focal mechanisms estimation we computed and compared the fault plane solutions of the earthquake located in the minimum 1D velocity model (double difference location) and the 3D velocity model. For simplicity we compare the orientation of the T-axes in the rose diagrams of Figure 5.4.

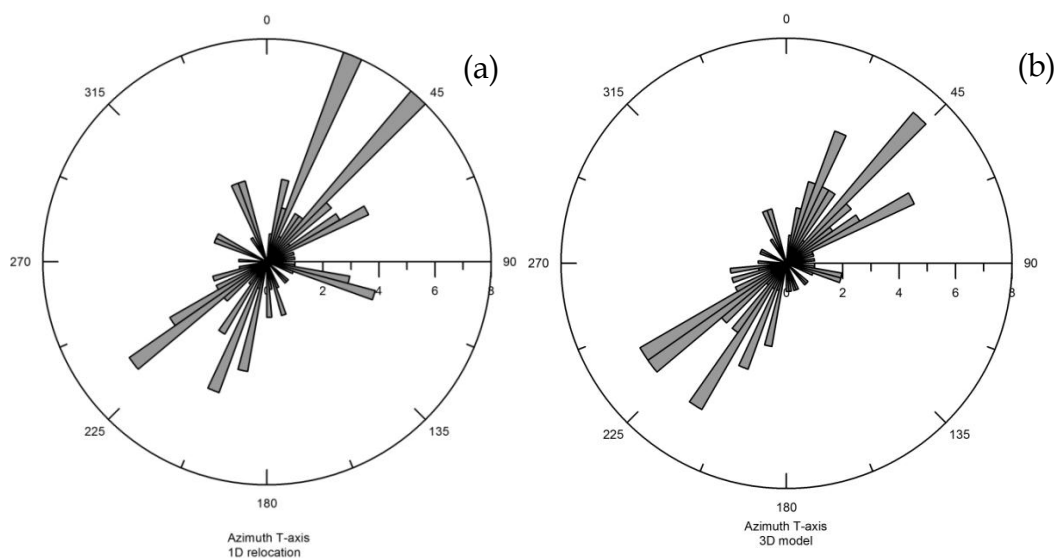


Figure 5.4 Rose diagram of the T-axes orientation for earthquakes located in (a) 1D model and (b) 3D model.

A more intelligible representation of the results is provided by the comparison of the horizontal projections of the T-axes direction (Figure 5.5). The length of the black lines is inversely proportional to the plunge of the T axis: longer lines represent T axes with smaller values of plunge. The T-axes show a predominant NE-SW direction.

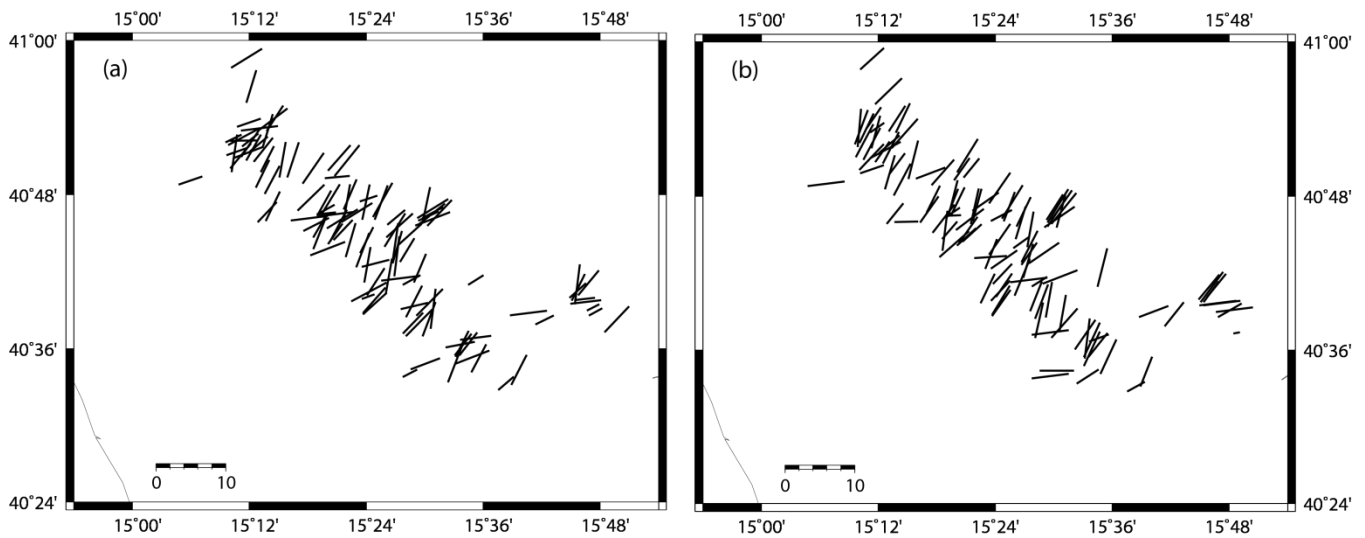


Figure 5.5 Projection of T-axes direction computed in 1D model (a) and 3D model (b). The length of the black lines is inversely proportional to the plunge of the T axis: longer lines represent T axes with smaller values of plunge.

The differences of the take-off angles due to the use of the 1D and 3D velocity models do not substantially modify the focal mechanisms estimation. The principal feature we observe is the coherence in the T-axes direction that are mainly oriented along NE-SW in both cases (1D and 3D velocity models).

A detailed analysis of focal mechanisms allows us to study the pattern of the focal planes (Figure 5.6). In the Irpinia area Figure 5.6a shows that for most focal mechanisms, strikes are parallel to Apenninic chain trend. The projection of focal mechanisms on vertical sections orthogonal to the strike direction enables to verify the coherence between the dip of several fault planes. Figure 5.6b shows several representative vertical cross sections where it's possible to observe that the microearthquakes are distributed along not a single fault plane but on different planes almost parallel to each other (De Matteis et al., 2012 - under revision).

Within the figure 5.6 the focal mechanisms in the Potenza region are highlighted. We can note that in this region the presence of earthquakes with dominant right-lateral slip.

Table 5.1 shows the complete list of the selected earthquake focal mechanisms.

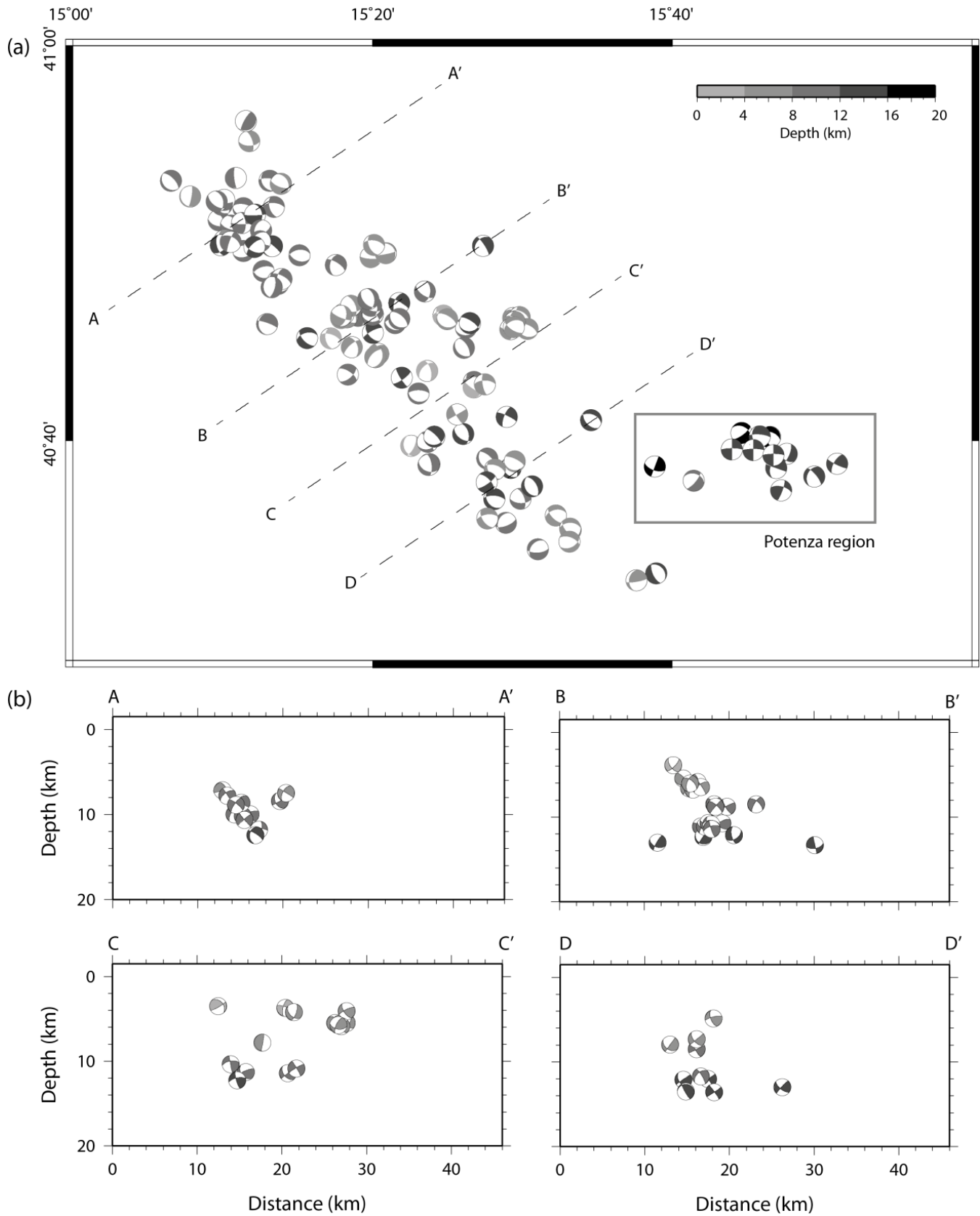


Figure 5.6 Selected focal mechanisms in plan (a) and projection of focal mechanisms in vertical section orthogonal to the strike direction (b). The gray palette table is referred to the depth of the earthquake

## Focal mechanisms of events located in the Irpinia and Potenza areas

YYMMDD	hhmm	seconds	Lat °N	Lon °E	Depth (km)	Strike (°)	Dip (°)	Rake (°)
20060205	1702	59.19	40.81	15.21	11.65	100	35	-70
20060314	0315	03.29	40.82	15.33	06.00	325	20	-40
20060314	1333	42.60	40.83	15.35	07.00	320	15	-30
20060405	1540	03.15	40.72	15.37	12.72	55	75	170
20060507	1427	00.45	40.72	15.45	11.41	145	40	-50
20060517	1033	20.31	40.60	15.54	07.68	255	45	-140
20060624	0722	02.44	40.66	15.38	03.50	25	65	-70
20060717	1515	45.65	40.77	15.49	05.58	305	30	-140
20060717	1656	02.78	40.77	15.50	05.47	295	45	-140
20060827	1300	56.99	40.71	15.38	11.29	270	65	-100
20060915	1755	07.69	40.77	15.36	10.75	270	55	-100
20060917	2151	37.61	40.71	15.45	03.69	355	20	-40
20060926	1629	18.73	40.71	15.46	04.21	270	60	-160
20061201	1538	13.07	40.76	15.44	11.42	305	65	-70
20070127	0420	57.71	40.78	15.36	12.12	300	80	-140
20070217	1754	59.07	40.64	15.49	12.02	325	55	-90
20070220	1027	49.13	40.82	15.25	10.10	110	45	-70
20070302	1729	56.56	40.80	15.23	10.57	275	60	-120
20070416	1931	31.12	40.86	15.22	08.00	275	60	-140
20070427	1733	44.14	40.68	15.58	12.96	290	45	-110
20070618	0538	29.72	40.62	15.47	12.09	140	35	-50
20070829	2010	14.96	40.62	15.50	11.71	340	60	-40
20070911	2003	27.53	40.73	15.39	03.92	345	60	-130
20070911	2247	52.94	40.92	15.20	05.55	90	55	-150
20071206	2125	26.00	40.85	15.16	08.00	100	45	-130
20071218	1638	12.39	40.77	15.32	11.11	140	65	-100
20071227	0545	02.20	40.89	15.22	08.40	150	30	-40
20080321	0800	24.86	40.76	15.33	12.35	140	55	-20
20080527	1619	33.28	40.78	15.32	11.12	275	40	-110
20080528	1022	09.16	40.78	15.32	10.69	270	25	-120
20080602	2311	03.11	40.69	15.48	12.67	295	80	-160
20080623	2204	24.84	40.88	15.23	07.48	110	65	-110
20080627	0532	21.80	40.86	15.19	09.98	280	60	-90
20080629	0138	36.36	40.76	15.51	04.07	295	60	-90
20080904	0231	52.32	40.72	15.31	11.29	50	60	-150
20080910	0819	09.29	40.85	15.18	09.98	105	60	-120
20080913	2041	47.38	40.85	15.19	10.16	90	80	-150
20081006	0227	25.71	40.87	15.17	09.62	140	40	-90
20081014	1805	16.00	40.67	15.43	12.24	125	50	-120
20081023	1602	13.26	40.69	15.43	07.79	150	80	-180
20081103	0524	09.11	40.65	15.46	08.47	310	65	-100
20081108	0924	22.12	40.59	15.55	04.81	150	45	-80
20081119	0500	28.43	40.77	15.41	03.90	270	55	-130
20081119	1917	52.57	40.59	15.55	04.14	135	55	-60
20081122	1453	17.67	40.64	15.47	07.30	145	40	-60
20081125	0743	59.52	40.77	15.42	04.51	110	25	-100
20081225	1156	27.58	40.83	15.34	07.95	280	55	-130
20090226	2126	26.19	40.79	15.39	08.49	125	60	-130
20090427	1923	08.37	40.55	15.65	15.10	155	65	-80
20090513	0313	23.49	40.87	15.17	08.61	95	65	-110
20090515	0851	16.05	40.67	15.39	10.34	325	80	-60
20090518	0001	10.30	40.74	15.34	05.88	340	70	-120
20090518	0202	15.07	40.84	15.17	07.00	165	50	-30
20090518	1626	03.18	40.75	15.31	05.45	340	45	-150
20090522	0859	19.35	40.74	15.34	04.74	20	35	-110
20090625	2304	20.08	40.87	15.16	08.85	345	40	-60
20090706	0630	52.39	40.58	15.55	04.68	290	55	-60
20090715	1825	36.63	40.83	15.22	12.24	180	15	-40
20090725	0656	23.78	40.89	15.18	11.77	35	15	-50
20090727	2156	03.96	40.77	15.49	05.87	300	55	-130
20090901	0453	55.47	40.82	15.29	11.59	190	45	-30
20090928	2257	08.04	40.77	15.22	08.73	290	80	-110

20091005	2336	18.49	40.67	15.40	12.24	315	75	-70
20091116	0904	20.08	40.65	15.40	08.67	355	65	-60
20091116	0913	52.76	40.65	15.40	08.49	115	40	-140
20091203	0506	46.05	40.77	15.36	08.79	130	30	-90
20091204	0008	00.98	40.55	15.63	04.90	80	80	120
20100114	0053	33.99	40.75	15.44	10.87	330	60	-80
20100227	1932	47.94	40.76	15.49	05.50	5	60	-20
20100227	1936	13.17	40.76	15.49	05.75	245	40	-140
20100306	1841	00.82	40.86	15.20	12.42	350	35	-10
20100312	1808	22.27	40.63	15.51	13.55	330	55	-90
20100317	1659	42.73	40.84	15.21	09.50	195	40	-130
20100503	0731	41.67	40.87	15.13	07.71	10	80	-80
20100607	1452	15.33	40.84	15.21	11.53	115	80	-60
20100607	2232	54.55	40.83	15.19	10.78	270	50	-80
20100608	0334	55.43	40.83	15.20	12.42	225	65	-140
20100614	0507	53.30	40.98	15.48	15.58	145	20	-100
20100630	1343	36.34	40.83	15.16	12.51	165	60	-130
20100703	0953	24.87	40.77	15.33	10.87	50	40	-140
20100703	1044	58.41	40.77	15.33	11.39	85	30	-140
20100703	1112	04.75	40.78	15.33	08.49	115	55	-120
20100713	0336	18.78	40.60	15.48	09.40	205	30	-130
20100717	0044	41.53	40.84	15.18	10.13	200	80	-40
20100814	1855	44.29	40.89	15.11	09.68	135	25	-90
20100914	2051	08.16	40.65	15.49	04.85	95	20	-110
20100920	2108	09.08	40.75	15.26	13.02	135	60	-50
20101001	0005	07.71	40.57	15.52	08.55	220	35	-130
20101004	0227	28.79	40.60	15.46	07.95	145	55	-40
20101112	0903	18.64	40.80	15.23	11.38	270	60	-100
20101118	0325	47.03	40.63	15.46	13.49	55	75	-150
20101127	1243	28.29	40.75	15.29	03.86	290	60	-130
20101207	0104	13.89	40.77	15.30	06.58	130	50	-100
20101207	1425	16.46	40.77	15.30	06.76	310	25	-80
20101210	2011	02.90	40.80	15.23	09.83	190	55	-30
20101213	2251	43.13	40.77	15.30	06.46	250	80	-180
20101214	1222	16.21	40.77	15.44	12.60	80	25	-130
20110103	1255	55.65	40.94	15.19	11.74	60	15	120
20110107	2111	39.65	40.78	15.31	06.46	105	45	-130
20110112	0037	51.68	40.77	15.30	06.05	10	50	-20
20110123	0600	31.31	40.80	15.22	10.66	15	65	-80
20110222	1144	12.19	40.79	15.33	08.79	140	50	-110
20110316	1307	14.16	40.83	15.46	13.31	220	35	-20
20110329	0149	17.27	40.94	15.09	06.82	270	75	-10
20060507	0946	21.14	40.66	15.76	14.00	285	80	-100
20060507	1011	32.34	40.67	15.76	13.40	275	75	-120
20071020	0244	32.59	40.66	15.76	14.51	270	80	-180
20080225	0540	08.79	40.66	15.75	17.45	285	50	-140
20080225	0542	48.03	40.66	15.75	15.99	270	80	-180
20080923	0152	30.91	40.64	15.78	14.00	200	45	0
20081114	2044	51.09	40.65	15.78	15.99	270	80	-180
20090519	1044	10.38	40.67	15.75	18.17	300	40	-30
20090630	2107	34.83	40.64	15.65	17.72	110	60	-180
20100201	0142	00.29	40.63	15.69	10.75	285	35	-30
20100602	0452	06.03	40.65	15.85	14.98	210	65	10
20100602	0453	11.37	40.64	15.82	15.55	205	35	-30
20110130	0612	29.95	40.65	15.78	14.09	135	45	-150
20110218	0636	31.96	40.62	15.79	13.76	20	80	30

Table 5.1 Focal mechanisms of events occurred in the Irpinia (blue) and Potenza (green) areas. Strike, dip, and rake angles are referred to one of the two nodal planes.

### 3. Stress inversion

Since the P and T axes of focal mechanism do not necessarily coincide with the maximum and minimum compressive stress orientations, we performed a stress tensor inversion to retrieve the principal stress directions (McKenzie, 1969). We used the algorithm developed by Rivera and Cisternas (1990) described in the paragraph 4.1 of the Chapter 1.

The data are the raw first-motion polarities for a set of events.

The model parameters are the 3 orientation parameters,  $\phi, \theta, \psi$  for the stress tensor, 1 parameter for the stress ratio R and 2N parameters,  $\phi_{si}$  and  $\delta_i$  with  $i=1,2,\dots,N$ , for the fault planes ( $\phi_{si}$  and  $\delta_i$  are strike and dip of the fault plane of event  $i$ , and N is the number of events used for the inversion).

The likelihood function  $L(m)$  is defined to measure the misfit between the first-motion data and the predicted polarities. In the definition of L the contribution of each polarity is weighted as a function of the amplitude of the predicted P-wave radiation pattern

An initial model ( $\phi, \theta, \psi, \theta_R, \phi_{si}$  and  $\delta_i$ ) is modified in an iterative process until a given convergence criterium is satisfied.

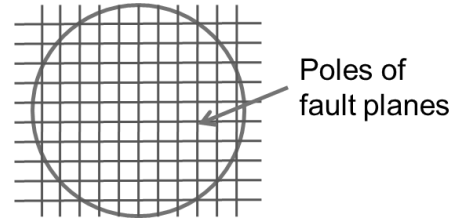
We use here an analogy with mechanics (mass) or with electrostatics (charge). We compute the tensor of inertia or the second order moment of the "charge" distribution. Positive polarities are assimilated to positive masses (or positive charges) and negative polarities correspond to negative masses (or negative charges). For a given event we compute the inertia tensor as:

$$I_{ij} = \sum_k p^{(k)} x^{(k)}_i x^{(k)}_j \quad (5.1)$$

where  $p^{(k)}$  is the sign of polarity "k" and  $x^{(k)}_i$  is the "i" component ( $i=1,2,3$ ) of the unit vector pointing to polarity "k" on the unit sphere. If the focal sphere is well covered by polarities, the three eigenvalues of the inertia tensor  $I_{ij}$  will point to the P, N, and T axis of the focal mechanism.

If instead of summing of the polarities of a single event, we sum over the polarities for the whole population (in a way this is like making a composite focal mechanism), we will have an average inertia tensor. We will use this average inertia tensor to define a preliminary stress tensor to be used as starting point for the iteration process. From this we compute the initial three Euler's angles ( $\phi$ ,  $\theta$ ,  $\psi$ ) and we fixed  $\theta_R$  to zero.

By using a grid search method we found the optimal fault plane that produces the best fit of the polarity data for a given stress tensor.



For each event ( $je$ ) we made a grid search for the pole of the fault plane ( $\phi_s, \delta$ ).

For each station ( $jp$ ) we computed the amplitude using the equation (1.36)

$$A_P(je)(jp) = 2 (r^t n) (r^t t) \quad (5.2)$$

and we estimated a factor of quality  $qe(je) = \sum A_P(je)(jp) \cdot \text{pol}(je)(jp)$

For each event we selected the fault plane ( $\phi_s, \delta$ ) which provides the maximum of quality factor.

### 3.1 Bootstrap method, confidence ellipses and error estimation

The ability to define meaningful confidence regions is equally as important as the ability of an inversion to find an acceptable "best" answer (Micheal 1987). This is especially important if we are looking for variations in the stress field. The main problem with computing the confidence limits is that we do not know the true errors in the data and that these errors may be significantly non-Gaussian (Gephart and Forsyth, 1984).

In our case we decided to compute the confidence limits on the parameters of the model by a statistical tool known as bootstrap resampling.

The bootstrap method was introduced by Efron (1979) in the late 70's. It is a valuable technique when there is not a clear analytical theory to obtain the

estimation of accuracy of a measurement. The most common application of the bootstrap method is the estimation of the standard errors and confidence intervals. It should be underlined that we must consider both the confidence level (e.g. 68.3%,90%,95.4%, 99%) and the shape of the confidence region. The aim of the confidence region is to give information about the reliability of a parameter. In one dimension, the convention is to use a segment centered on the measured value, while increasing the size we use ellipse or ellipsoid.

From a theoretical point of view confidence limits would be computed by repeating an experiment many times. To simulate a repetition of an experiment, we resample data (polarities) randomly from the original dataset. Essentially, this new dataset will have the same number of data as the original dataset, but will have same polarities repeated two or more times while other polarities will be absent. For example, if we suppose a sample like this:  $x=(a,b,c,d,e)$ ; a possible bootstrap resampling could be:  $x^*=(d,b,c,c,a)$  or  $x^{**}=(a,a,a,a,a)$ .

We re-grouped the polarities for event and we inverted this dataset for the stress field, and repeated this process several times. We obtain three distribution of point for the three principal axes. We still used the concept of inertia tensor. We define for each principal axis  $k$  the inertia tensor  $I_{ij} = \sum_k x_i^k x_j^k$ . And across the definition of the eigenvalues and eigenvectors of this tensor we obtain the center of the distribution and the “confidence ellipse” around it (e.g. 1-sigma, 2-sigma). The eigenvectors of the inertia tensor give information about the orientation of the ellipses and the eigenvalues control the dimension of the semi-axes. The method we are using to define the ellipse (through the inertia tensor of the population of the corresponding axis) works properly if the distribution is not very different from a gaussian.

This formulation of the error is innovative respect the original formulation which provided the variance for each stress angular parameter. The errors in this sense are not immediately related to the errors on the direction of main axes of the stress tensor. In addition, the original error analysis by Rivera *et al.*, suffers of non-normalization. Their confidence regions have the proper shape and

orientation but their size is only useful in a relative sense (to compare one earthquake with another).

In the present approach, by using the bootstrap method, we obtain confidence regions which are properly normalized and can be immediately interpreted in terms of probability.

In addition the error on R is defined by:

$$\sigma_R = \frac{1}{2} * \sqrt{3} * [1 + \tan^2(\theta_r)] * \sigma_{\theta_R} \quad (5.3)$$

Where  $\sigma_{\theta_R}$  is the standard deviation on  $\theta_R$  and remembering that

$$R = \frac{1}{2} [1 + \sqrt{3} * \tan(\theta_r)]$$

### 3.2 Stress inversion for the studied area

To estimate the stress field in the Campania-Lucanian region, we inverted the dataset of the selected earthquakes (where focal mechanism is available Figure 5.1) located with the double difference code using the minimum 1D P-wave velocity model and a value of  $V_p/V_s = 1.85$ .

We apply the bootstrap procedure, as we described in previous paragraph, we verified that the inversion parameter distributions show a “gaussian-like distribution”. In order to choose the optimal number of resampling in the bootstrap procedure we tested different resampling and the results indicate that the solution becomes stable from 500 resampling. This is clear in Figure 5.6 that shows the average value of Euler’s angles ( $\phi$ , phi;  $\theta$ , theta;  $\psi$ , psi) and the shape factor ( $\theta_R$ , thetaR) after the inversion with the associated error for different number of bootstrap resampling of the initial data (polarities). The estimation becomes stable considering high value of resampling.

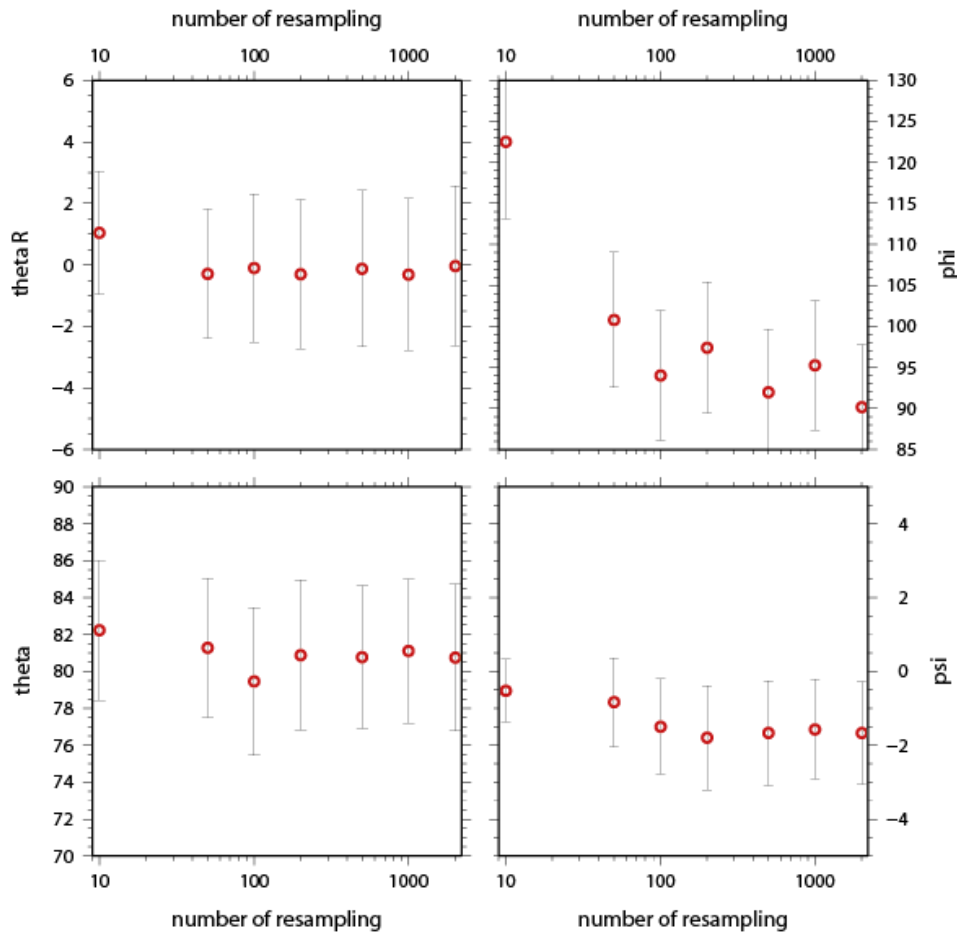


Figure 5.7 The average value of several angular parameters after the inversion (red point) with the associated error (black bar) for different number of bootstrap resampling of the initial data (polarities). To better understand the difference the scale of the graphic is semi-logarithmic.

Furthermore, to ensure that the inversion worked properly we performed several synthetic examples, considering extensional, compressional and pure strike-slip stress regime.

Figure 5.8 shows a typical representation of the inversion results: the principal stress axes ( $\sigma_1$ ,  $\sigma_2$ ,  $\sigma_3$ ) with different colors, their confidence ellipses (1-sigma and 2-sigma) and the result of each resampling are plotted into the lower hemisphere stereonet plot (Matrullo *et al.*, 2011b). The result of the inversion for each bootstrap resampling is represented in several shades of gray (from dark referred to  $\sigma_1$  to light referred to  $\sigma_3$ ).

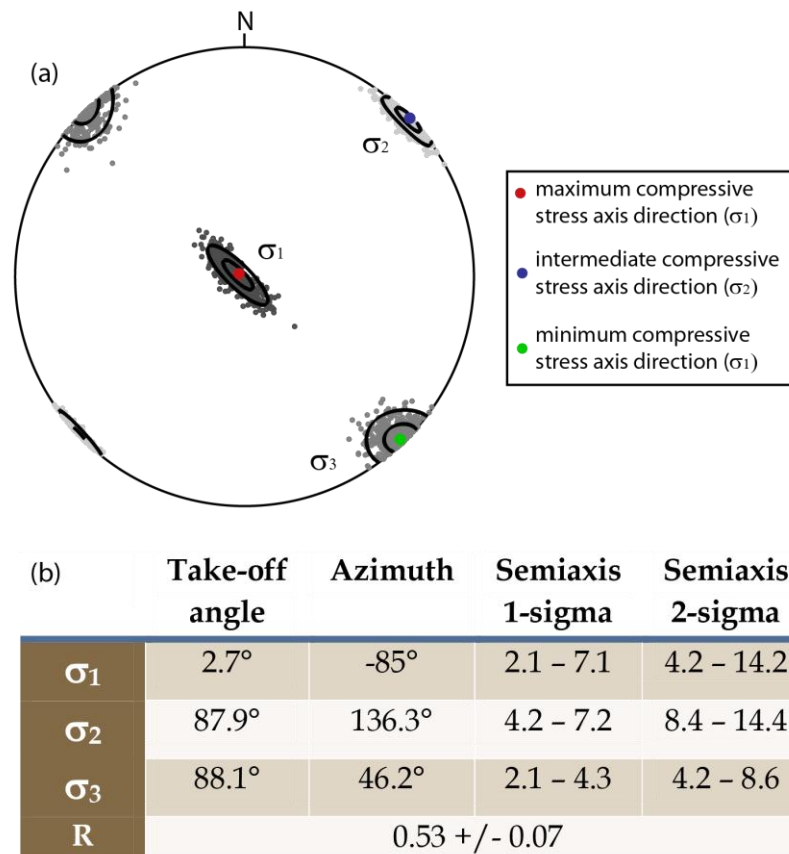


Figure 5.8 Result of the stress inversion in the Campania - Lucania region. In the stereonet plot, different colors (red, blue and green) represent the 3 principal axes (the center of the distribution). The result of the inversion for each bootstrap resampling is represented in several shades of gray (from dark referred to  $\sigma_1$  to light referred to  $\sigma_3$ ). We represent also the confidence ellipses (1-sigma and 2-sigma). In table we specify the values.

Using the whole data set, results show a regional stress field characterized by a nearly horizontal NE-SW minimum compressive stress axis ( $\sigma_3$ ), a maximum compressive stress axis ( $\sigma_1$ ) that is nearly vertical, and an nearly horizontal NW-SE intermediate stress axis ( $\sigma_2$ ). While axis  $\sigma_3$  is horizontal with a very small error on its dip and azimuth, the axis  $\sigma_1$  shows a large error for dip.

From the analysis of the polarities coherence, we obtain 70% of the computed polarities in agreement with the observed polarities.

The retrieved regional stress tensor is typical of an extensional regime along NE-SW direction. It confirms and generalizes the results obtained with other data and methods such as in-situ stress data analysis, GPS data and the focal mechanisms of strong-to-moderate earthquakes (Figure 5.9).

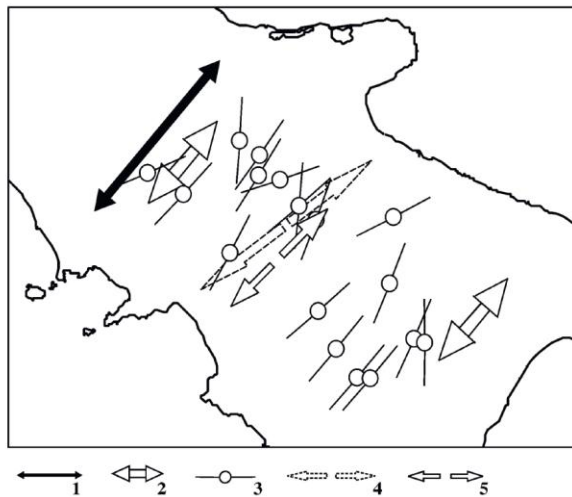


Figure 5.9 Stress field orientations obtained from former studies using: 1 GPS data (Anzidei *et al.*, 2001) ; 2 strong earthquakes (Montone *et al.*, 1999); 3 breakout data (Montone *et al.*, 1999); 4 focal mechanisms of the Southern Apennines earthquakes (Frepoli *et al.*, 2000); 5 focal mechanisms of the November 23, 1980 aftershocks (Pasquale *et al.*, 2009).

### 3.3 Velocity model influence on stress parameters

In this paragraph we analyzed the influence of the velocity model on the estimated stress parameters

The basic effects on stress field parameters depend on the P-wave first-motion polarity observations and on the position of these observables on the focal sphere. Changes in event location and in the velocity model can alter the computed position of rays on the focal sphere and therefore, the best fitting stress field. In particular as we explained in previous paragraph, the main difference related to the use of different velocity model lies in the computation of take-off angles, especially if we considered 1D or 3D parameterizations.

To better quantify the take-off angle variation on the estimated parameters, we considered the location using different velocity models proposed for the studied area by several authors (Bernard *et al.*, 1989; Amato *et al.*, 1993; Chiarabba *et al.*, 2005; Maggi *et al.*, 2009; De Matteis *et al.*, 2010) and an homogeneous model (for the details see chapter 4).

A comparison between the takeoff angles computed with the different models is shown in Figure 5.9. The computed takeoff angle versus the distance from the epicenter to the station (DIST) for the different seismic velocity models ("minimum" 1D velocity model, 3D velocity model, 1D literature velocity

models and different homogeneous and gradient model shown in chapter 4), are shown for different source depths (0-2 km; 2-4 km; 4-6 km; 6- 8 km; 8-10 km; 10-12 km; 12-16 km; 16-20km) in a global sketch. We confirm that the use of different velocity models can modify the take-off angles between 10 and 60 degrees (in few cases). The discrepancy between the takeoff angles computed from the different models for each range of source depth increase with the distance. Furthermore this quantity decreases with increasing hypocentral depth. For the source located within 10-20km respect the station and/or at a source depth of at least 16 km, the discrepancies between the computed takeoff angles in different model are within  $10^\circ$  of each other.

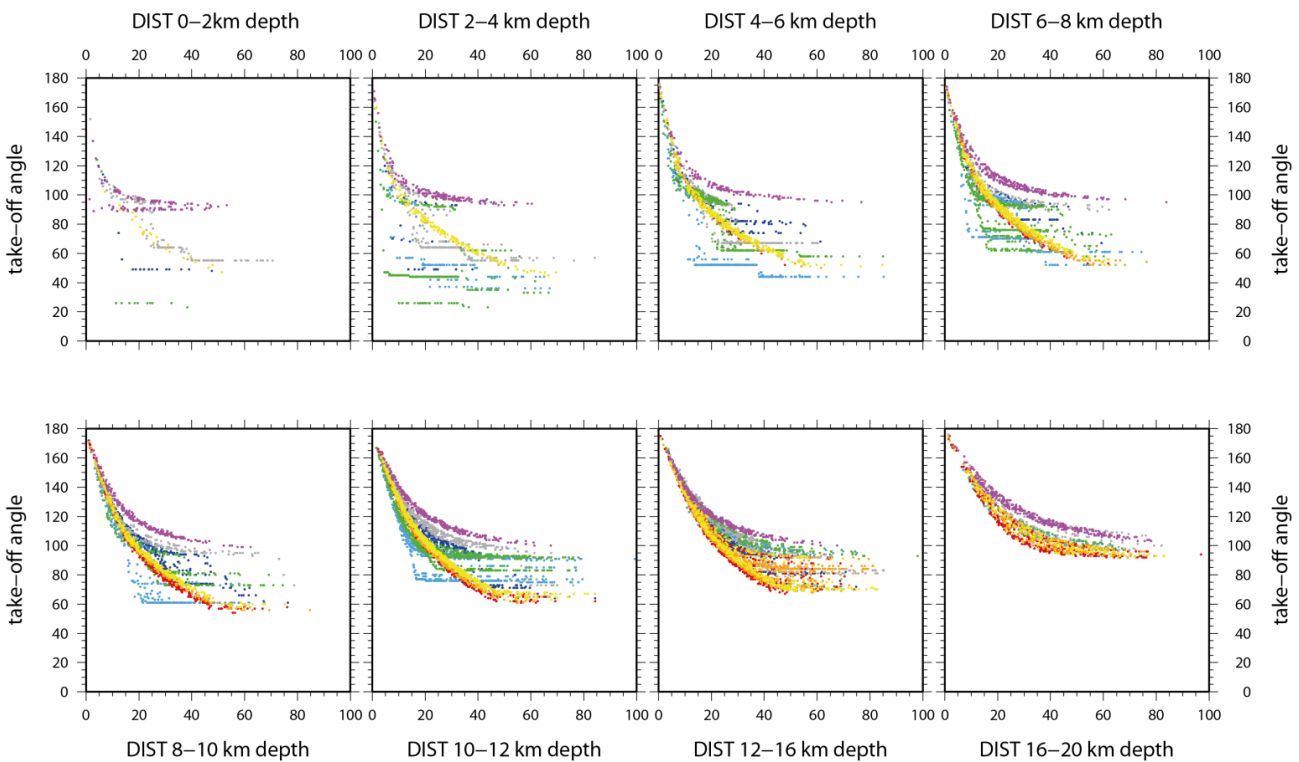


Figure 5.10. The computed takeoff angle versus DIST (the distance from the epicenter to the station) for the different seismic velocity models shown in Figure 4.2 (see cap. 4 for the detailed colours) , for eight different source depths: (a) 0-2 km; (b) 2-4 km; (c) 4-6 km; (d) 6- 8 km; (e) 8-10 km; (f) 10-12 km; (g) 12-16 km; (h) 16-20km. Takeoff angle is measured up from downward vertical.

Figure 5.11 shows the histogram of the difference between the take-off angles computed with the reference velocity models (“minimum” 1D and 3D model) and the different literature velocity models.

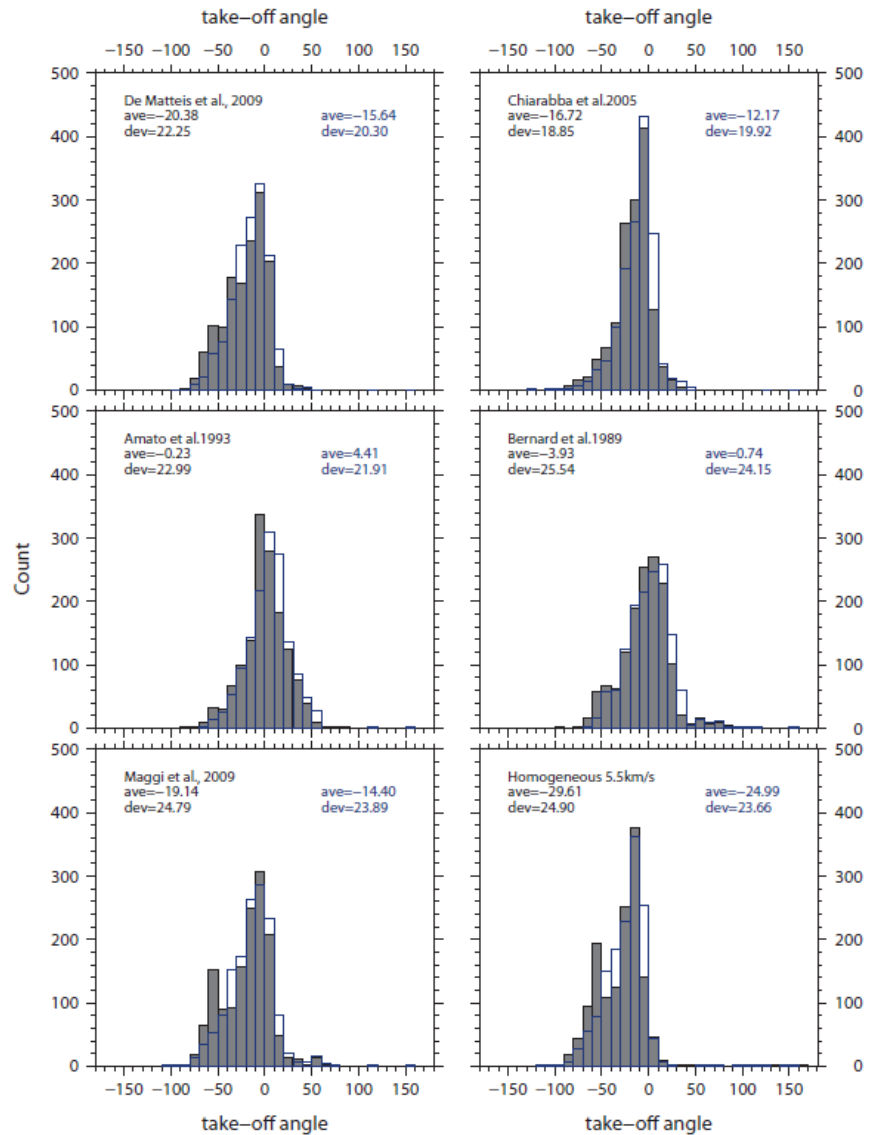


Figure 5.11  
The difference between take-off angle computed using reference velocity models (1D in grey and 3D in blue) and the different 1D velocity models. The mean angular difference (ave) and the standard deviation (dev) is also reported.

The use of different velocity models modifies the take-off angles of about 20 – 30 degrees (with 83% of take-off angle differences within 20° of each other and 90% within 30°).

To understand the influence of the take-off angle uncertainty on the stress parameters, we perform several inversion considering the earthquakes located in the “minimum” 1D model (DD location) and in the 3D model, considering (a) the original data, (b) adding to the take-off angles a perturbation randomly

chosen in the range  $\pm 20$  degrees and (c) adding to the take-off angles a perturbation randomly chosen in the range  $\pm 30$  degrees (Matrullo *et al.*, 2011b).

The results of these inversions indicate that the take-off angle uncertainty increases the error on the directions of the three principal axes especially for the intermediate and maximum axes as we can see in Figure 5.12b,c (the results of the inversion for 1D velocity model are shown on the top, and for the 3D model on the bottom).

Moreover, the errors on the direction of the principal stress axes for the three examined cases is always a little bit smaller, especially for the maximum and minimum principal axes directions, for the 3D velocity model (Figure 5.12a bottom) compared to the 1D model (Figure 5.12b top).

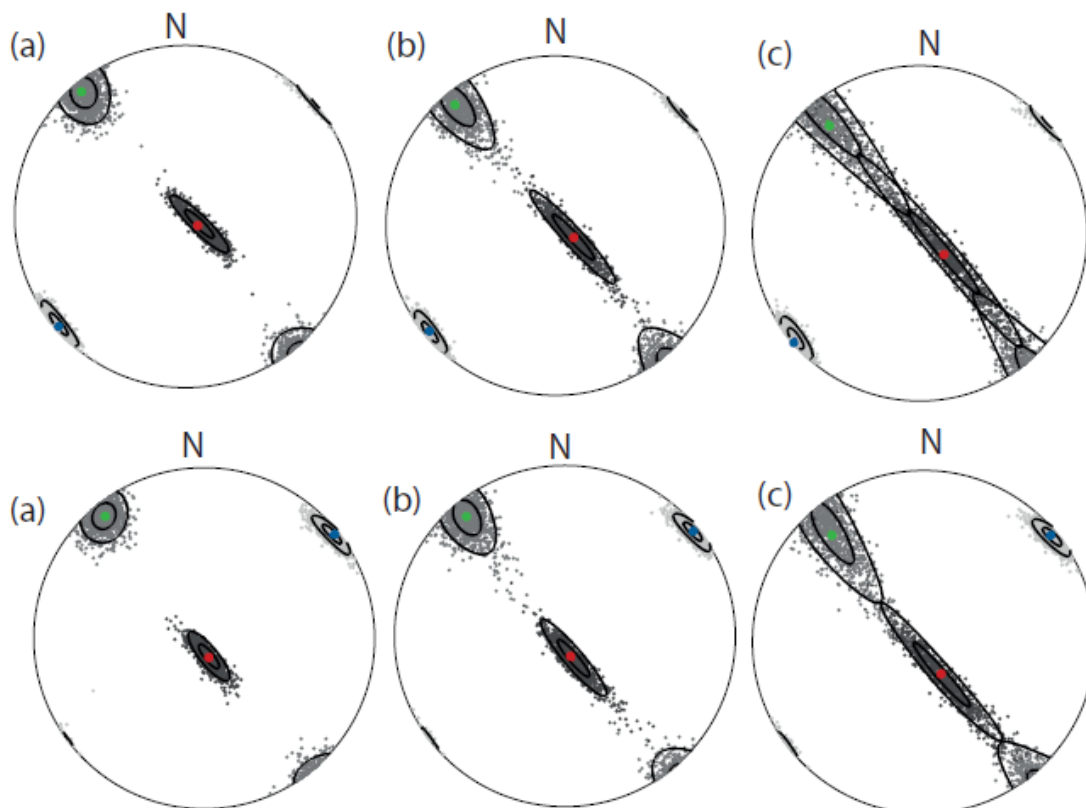


Figure 5.12 Comparison between the stress field result from a subset of earthquakes located with reference 1D model (top) and in 3D model (bottom) from: Original data (a); Adding a randomly take-off angle perturbation in a range  $\pm 20$  degrees (b) and  $\pm 30$  degrees (c).

### 3.4 Analysis on spatial variations of the stress fields

In cases where, we suspect that the stress tensor is not homogeneous, and if the dataset is large enough, we may explore the region by moving several spatial windows and verify the behaviour of the inverted stress tensor as a function of the position of the windows.

And so, taking into account the different kinematics that characterize the earthquakes occurring along the chain, in the Irpinia area (Figure 5.14a, turquoise) , and the seismic cluster E-W elongated in the Potenza area (Figure 5.14a, orange), we subdivided our data set in two sub-sets and inverted separately.

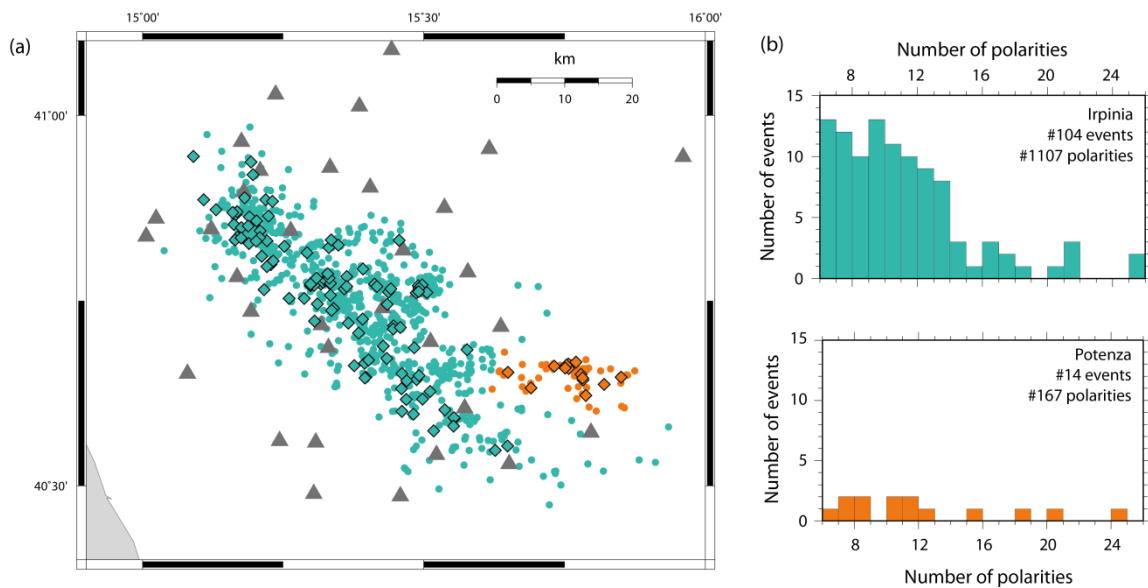


Figure 5.14 (a) Epicentral map of the Irpinia cluster (turquoise) and Potenza cluster (orange). (b) Histogram of the number of earthquakes as a function of the number of polarities for the two subset of events.

Stress tensor orientation retrieved for the Irpinia cluster is essentially the same as for the whole data set indicating an extensional stress field NE-SW oriented. (Figure 5.15a). While, the stress tensor obtained from the inversion of Potenza cluster indicates a strike-slip regime with  $\sigma_3$  and  $\sigma_1$  nearly horizontal, NE-SW and NW-SE trending, respectively (Figure 5.15b).

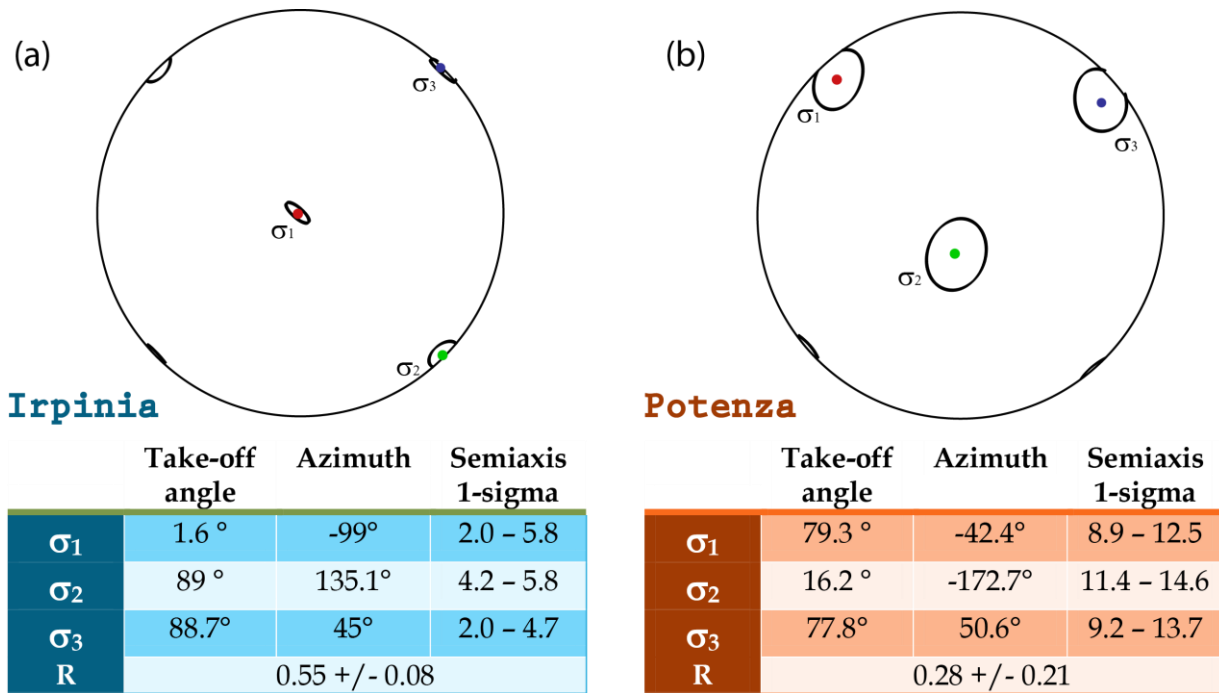


Figure 5.15 Result of the stress inversion for the Irpinia ad Potenza region. In the stereonet plot, different colours (light blu for the Irpinia and orange for the Potenza region) represent the 3 principal axes (the center of the distribution). We represent also the confidence ellipses (1-sigma). In table we specify the several value.

By dividing the dataset the solution for the Irpinia cluster appears slightly better constrained in terms of error on the direction of principal axes respect the inversion of the whole data set.

But from the analysis of the polarity coherence (score: number of the computed polarity in agreement with the observed polarity) we obtain for the regional stress tensor a score of 70%, for the Irpinia cluster 70% and for Potenza cluster 74%. In addition, we verified that the P-wave polarities from the micro-earthquakes in the Potenza region are well explained by both a unique regional extensional stress and the local strike-slip regime retrieved from the inversion of the Potenza cluster.

In conclusion, we obtain two models mathematically equivalent that well explain the observed data (De Matteis *et al.*, 2012 under revision).

If we process the P-wave polarities from the micro-earthquakes in the Potenza region together with those of the Irpinia area we get the same stress field like from the inversion of the Irpinia cluster only.

If we process the P-wave polarities from the micro-earthquakes in the Potenza region separately from Irpinia we obtain a different stress regime.

The analysis of the stress inversion from earthquakes seems does not discriminate the dynamic model that explains the two observed different faulting styles. We must emphasize that this is probably due to the limited data in the region of Potenza. On the other hand the presence of the two possible stress fields implies to consider the possible variation of the field moving from the inner part of the chain to the external part, and (considering the large depth in the Potenza earthquakes) in deep, as explained in the next chapter.

#### 4. Discussion and conclusion

Low magnitude seismicity gives information about the stress regime presently acting in a structurally complex region of Southern Apennines, and on the geometry of the fault systems.

The map of the focal mechanisms, the surface projection of the T-axes together with the projection of the focal mechanisms on the cross sections, indicate that the microseismicity in the Irpinia area is not randomly distributed but occur on sub-parallel fracture planes highly organized. The focal mechanisms in the area reveal the presence of a normal fault system (Irpinia) and a dextral strike slip fault (Potenza) at greater depth.

We used the technique developed by Rivera *et al.*, (1990) to obtain the stress tensor from first P motion polarities for source-station pairs. In order to get a realistic error estimation on the orientation of the three principal axes, we computed the confidence limits by using a bootstrap resampling approach.

The regional stress tensor we found is typical of an extensional regime along a NE-SW direction. These findings indicate the existence of an extension

perpendicular to the axis of the belt that is well known in the study area (Montone *et al.*, 1999; Anzidei *et al.*, 2001; Frepoli *et al.*, 2000; Montone *et al.*, 2004, Pasquale *et al.*, 2009; Maggi *et al.*, 2009).

Taking into account for the different kinematics that characterize the earthquakes occurring in the Irpinia area and in the Potenza area, we performed an analysis on the spatial variation of the stress field.

We found two different stress fields:

- an extensional stress field, with the minimum compressive axis NE-SW oriented, which is responsible for the NW-SE striking normal faults system located along the Apenninic chain;
- a strike slip stress field in the Potentino area responsible for earthquakes with dominant right-lateral slip on a E-W fault. The retrieved strike-slip regime is in agreement with the presence of a composite seismogenic source on which the M 5 1990 and 1991 earthquake sequences originated.

These observations call in question the possible spatial variation in the tectonic regime from the inner to the external part of the chain as well as in depth.

In addition, it is well known that earthquake location and velocity model may influence the computed point of intersection of rays with the focal sphere, and so can alter the P-wave first-motion polarity position on the focal sphere. And so we studied the influence of the velocity model on the estimated focal mechanisms and stress parameters and we concluded that its main effect is on the computation of take-off angles. The differences of the take-off angles do not substantially modify the results both for focal mechanisms and for the retrieved stress tensor. Specifically, errors on take-off angles slightly increase only the error on the principal stress axes direction, but do not modify the principal stress axes orientation.

# Chapter 6

## Seismotectonic implications

---

### 1. Introduction

In this chapter we propose our interpretation of the results presented in the previous chapters.

The current stress field and related seismogenic faults that characterize the Southern Apennines (Italy), a structurally complex area with high seismic potential, have been studied through the analysis of the microseismicity ( $M < 3$ ) recorded by a local seismic network projected *ad hoc* to monitor the Irpinia area. The new and more accurate seismicity location, along with the computed focal mechanisms, well correspond to a NW-SE striking normal fault system along the axis of the Apennine chain, and to an approximately E-W striking, strike-slip fault system, oblique with respect to the main trend of the belt. It has to be noticed that these fault systems correspond with those responsible for the 1980 and 1990-91 earthquakes, but in this work they have been independently depicted by the microseismicity distribution.

In particular, the microseismicity along the chain axis identifies the hanging wall volume delimited by the normal fault system (thus by the main fault and its antithetic one) responsible for the 1980 Irpinia M 6.9 earthquake. We verified that the analyzed low magnitude earthquakes can be positively ascribed to the background seismicity rather than to the aftershock sequence, and that they are likely generated at the hanging wall of the Irpinia major fault segments, suggesting that this fault system is active still today, thirty years after the mainshock occurrence. In the same way, we ascribed to the background seismicity the microseismicity along the 1990-91 Potenza seismogenic fault

system, suggesting that this E-W striking, subvertical, right-lateral structure is still active twenty years later.

In the following sections, we will discuss the aforementioned points from a seismotectonic and geodynamic point of view.

## **2. Fault identification and regional stress field from the analysis of background microseismicity**

For the investigated area, we showed that the earthquakes recorded in the last 20 years do not match the Omori's law rate decay. We proved, therefore, that the current seismic events can be ascribed to the background seismicity rather than be interpreted as aftershocks of previous large earthquakes. This gives a new perspective to the application of the high quality records of background seismicity for the identification and characterization of active fault systems, which can integrate the information provided by low magnitude seismicity about the active stress regime. We want to emphasize here the novelty of the contribution obtained from the analysis of background microseismicity in studies of active tectonics.

The accurate seismicity location shows a cloudy distribution of the hypocenters, mainly NW-SW-elongated along the core of the Apennine chain, and an approximately E-W-oriented in the Potenza area, where the distribution obliquely cut the mountain belt (Figure 6.1a).

In Figure 6.1c, the distribution of the 1980 aftershocks is projected on a regional cross section and it allows a comparison with the analyzed background microseismicity. The figure 6.1a suggests that the recent low magnitude seismicity follows the same aftershock pattern, with a main elongation parallel to the strike of the fault segments activated during the 1980 Irpinia earthquake. The earthquakes occurring at the core of the Apennine chain affect the uppermost 15 km of the crust. As we can notice in figure 6.1c, where we indicate schematically the lithology of reference, most the earthquakes occur in carbonate rocks and underlying crystalline basement. In general, the depth distribution is nearly

uniform but in the Sele River Valley area, where a seismic gap in the upper about 8 km depth is observed, which is likely due to the presence of a thick sedimentary cover probably infilling a paleo-valley. This is consistent with what observed by Amato and Selvaggi (1993).

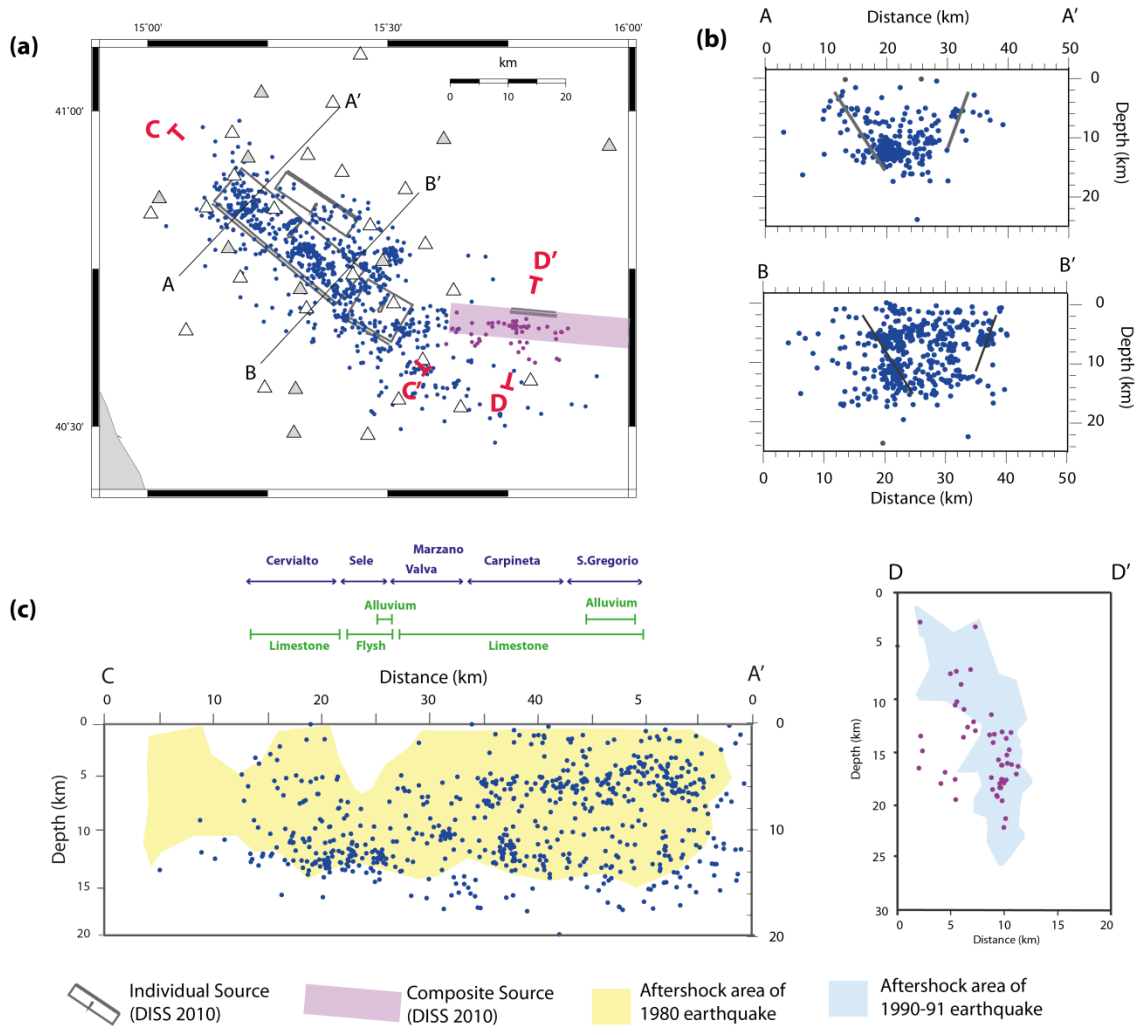


Figure 6.1 Map view of the relocated seismicity from August 2005 to April 2011 by using the double-difference method. The black lines are the surface projection of the three fault segments that ruptured during the 1980 Irpinia earthquake. b) Cross sections of the seismicity along the profiles reported in the panel a). The width of cross section is 15 km. Grey lines represent the projection of the fault segments of the Irpinia earthquake. c) Earthquake cross sections along the profiles reported in the map. Aftershock of 1980 and 1990-91 earthquakes are also shown.

The hypocentral distribution of the microseismicity is consistent with what observed from classical instrumental seismicity in the same areas, both for the depth values and for the bimodal trend. The latter has been explained by Boncio *et al.*, (2007) in terms of rheological profiles, and this interpretation can be reasonably applied to our data as well, although keeping into account the

uncertainties in the focal depths. In detail, Boncio and coworkers analyze the crustal structure of the Southern Apennines and the rheological layering along a crustal section by computing rheological profiles. The higher depths of the earthquakes in the Potenza area (>15 km) with respect to those in Irpinia, as well as the confinement within a relatively narrow depth range, are explained by the crustal rheology, which consists of a strong brittle layer at mid crustal depths, sandwiched between two plastic horizons.

This articulated rheological stratification is typical of the central part of the Southern Apennine crust, where the Apulia crust is overthrust by the Apennine units. This strong brittle layer is also supposed to act as a stress guide able to laterally transmit the deviatoric stresses responsible for the strike-slip regime in the Apulia crust, and may explain the close proximity (nearly overlapping) of the strike-slip and normal faulting regimes in the Southern Apennines (Boncio *et al.*, 2007).

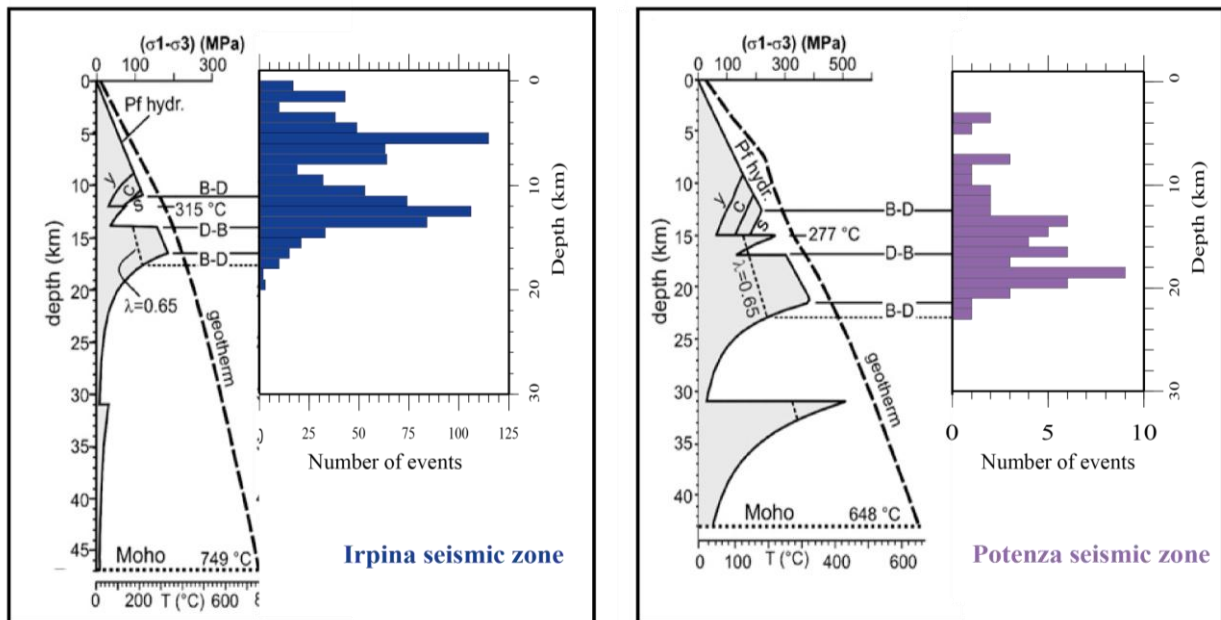


Figure 6.2 (modified from Boncio *et al.*, 2007) The geotherms and rheological profiles for the Irpinia seismic zone and Potenza seismic zone are compared with the distribution of the seismicity in depth we found. The temperatures calculated at the base of sediments and at the Moho are indicated. Different flow strengths of carbonates are compared:  $y$ =Yule marble;  $c$ =Carrara marble;  $s$ =Solnhofen limestone. B-D=brittle-ductile transition; D-B=ductile-brittle transition. The bottom of the brittle layer for both hydrostatic (Pf hydr.) and supra-hydrostatic ( $\lambda=0.65$ ) pore-fluid pressure is indicated.

Dealing with the fault geometry as depicted by low magnitude background microseismicity, we first remark that in Irpinia, an area characterized by extensional stress field, we do not expect to see a microearthquakes distribution in sharp streaks as in case of strike-slip faults (Hauksson and Shearer, 2005; Shearer *et al.*, 2005). Normal faults generally dip from  $50^{\circ}$  to  $70^{\circ}$ . Therefore, even in case of hypocentral distribution strictly following a normal fault plane, the epicentral map could not display linear trends as for near vertical faults. Moreover, in particular in this area, normal fault systems display a graben-like structure, with similar trending sub-parallel faults, both synthetic and antithetic. For these reasons, the microearthquakes epicentral map shows a cloudy distribution, mainly elongated in accordance with the main fault system. In addition, the hypocentral distribution shown in the cross sections of Figure 6.1b suggests that the recorded seismicity does not occur on a single fault plane, but in a volume delimited by the faults activated during the 1980 Irpinia earthquake, and which correspond to the hanging wall of the graben-like structure defined by the NE-dipping faults of the first shock and of the second shock at 19 seconds, and by the SW-dipping antithetic fault responsible for the shock at 38 seconds.

In this perspective, the fault plane solutions provide constraints on the compatibility of the kinematics of the analyzed microearthquakes compared with the Irpinia fault system kinematics. Moreover, they prove the occurrence of a highly organized system of sub-parallel active faults in the volume confined within the faults of the graben-like structure.

Of course, there is a variability in the fault plane solutions: majority of focal mechanisms shows a dominant normal faulting kinematics ranging from normal dip-slip to transtensional kinematics. In spite of this, both the focal mechanisms and the related T axes projected in map, as well as with the projection of the focal mechanisms on the cross sections (Figure 6.3 a,b), all indicate that the microseismicity in the Irpinia area is not randomly distributed but occurs on sub-parallel fault planes highly organized inside the volume delimited by the faults of the 1980 earthquake (De Matteis *et al.*, 2011).

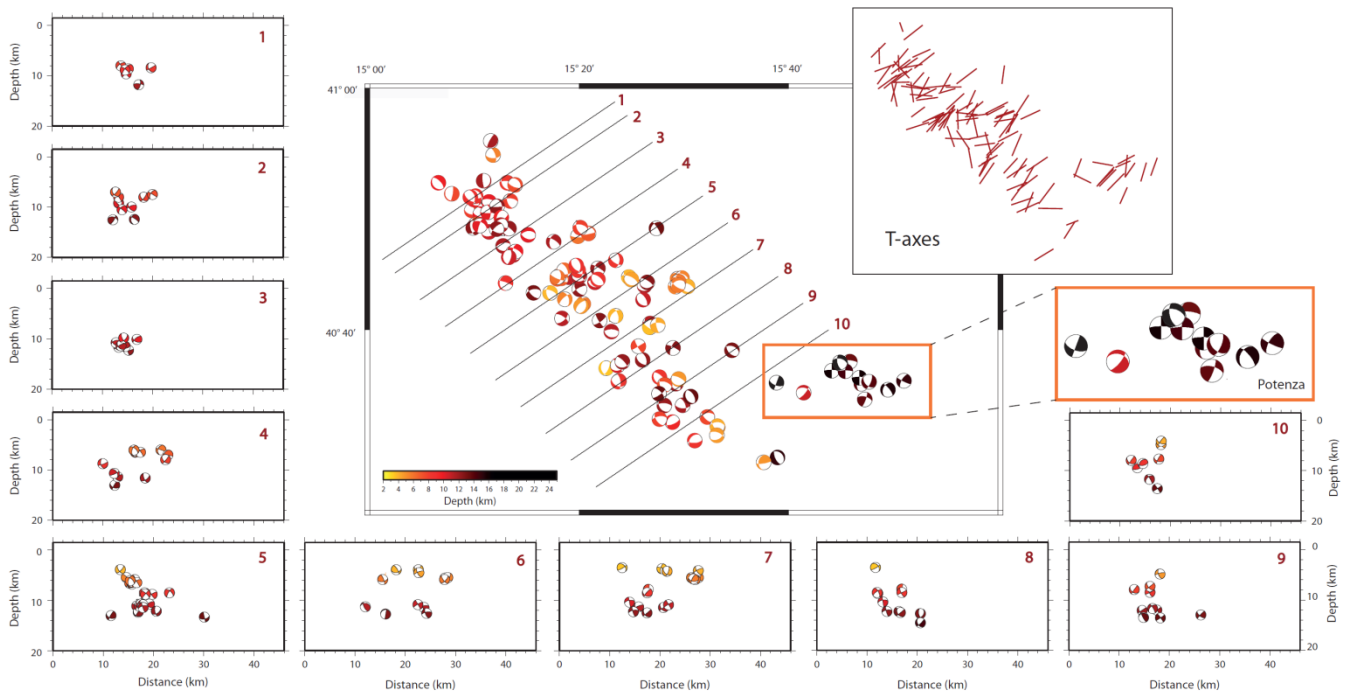


Figure 6.3 Map view of the 118 selected focal mechanisms, and the surface projection of the T axes orientation in the inset of the panel. The length of the bar is inversely proportional to the plunge of the T axis. Projection of the focal mechanisms onto the vertical sections indicated in the map are also shown. A zoom on Potenza region is performed.

Moving to the SE of the study region, the background seismicity in the Potenza area shows that the NW-SE-striking normal fault system occurring along the Apennine chain axis gives place to an E-W striking structure. Moreover, most of the focal mechanisms along this structure in the Potenza area show strike-slip kinematics on N-S left-lateral and E-W right-lateral nodal planes (Figure 6.3). This evidence is consistent with the results obtained by Ekstrom (1994) and Di Luccio *et al.*, (2005) for the 1990 and 1991 earthquake sequences.

Projecting our data onto a schematic geological cross section at regional scale (e.g., Menardi Noguera and Rea, 2000; Butler *et al.*, 2004) where classical instrumental seismicity of Southern Apennines is also shown (after Valensise *et al.*, 2004, redrawn), one can observe that the seismicity we analyzed reproduces the same pattern. In particular, the analyzed background microseismicity occurs in the range 10–24 km depth, therefore within the basement underlying the buried Apulia Platform, as the 1990–91 Potenza sequence and the 2002 Molise earthquakes, and shows a sub-vertical focal alignment. The seismogenic layer in this area is ca. 20–25 km thick.

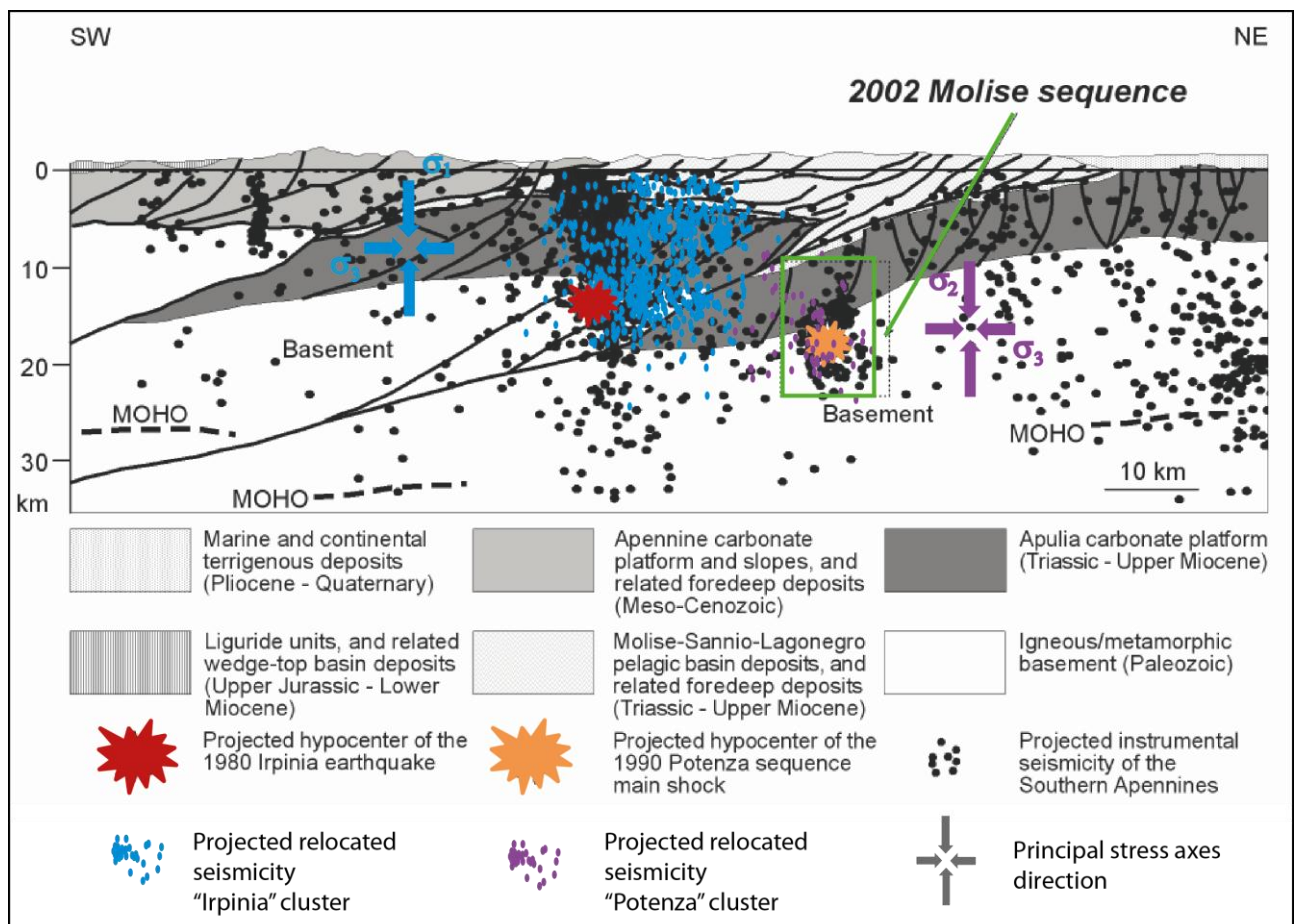


Figure 6.4 Modified from Di Bucci *et al.*, 2006. Schematic structural cross-section across the study area [after Menardi Noguera and Rea, 2000, simplified and redrawn]. Instrumental seismicity of the Southern Apennines and our analyzed seismicity is shown (after Valensise *et al.* [2004], redrawn). The 2002 earthquakes fall in the crustal volume outlined by a green line in the cross-section. Notice that the sequence took place at a depth in the range 10–24 km according with the Potenza relocated seismicity. The thickness of the seismogenic layer is of ca. 20–25 km. The principal stress axes direction obtained from this study is also shown

### 3. Seismotectonic and geodynamic interpretation

Our study confirms that the background microearthquake activity in the studied sector of the Apennine chain is controlled by two major fault systems: a set of sub-parallel, NW-SE trending normal faults and an E-W oriented strike-slip fault, oblique with respect to trend of the chain. The geological scheme in Figure 6.5 gives a global view of the current fault setting and the related stress regimes in the studied area (De Matteis *et al.*, 2011).

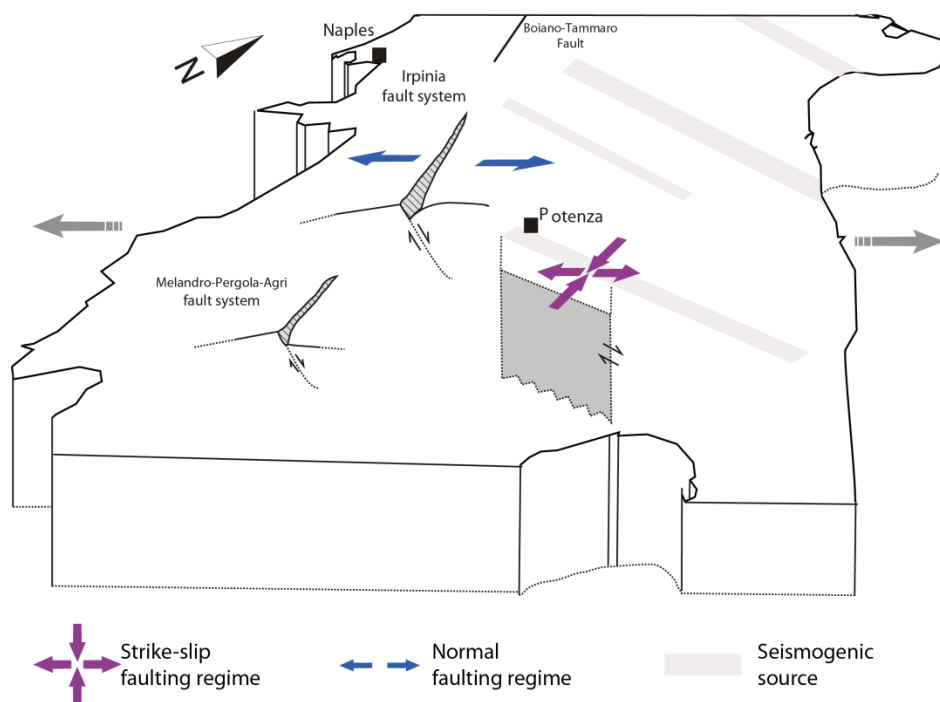


Figure 6.5 Cartoons showing the main results of this study in relation to the seismogenic sources and stress regime of the southern Apennines. Grey arrows indicate the regional stress regime, violet arrows the Potenza stress regime, blue arrows the Irpinia regime.

A regional stress tensor with a nearly horizontal minimum stress axis,  $\sigma_3$ , perpendicular to the axis of the belt (Figure 6.5 in grey) is retrieved. This stress tensor is consistent with the results obtained from the analysis of other geological, breakout and seismic data (Pantosti and Valensise, 1990; Frepoli and Amato, 2000; Montone *et al.*, 2004; DISS Working Group, 2010; Pasquale *et al.*, 2009) acquired along the Apennines.

As also suggested by previous active stress field analysis (Montone *et al.*, 2004),

however, the study area includes the boundary between two different tectonic regimes, i.e., extensional to the west, in correspondence with the Apennine chain axis, and strike-slip to the east, from the frontal part of the orogenic wedge to the foreland. As a matter of fact, if we take into account the different kinematics of the earthquakes in the Irpinia area with respect to what observed for the seismic cluster in the Potenza area, we can subdivide our data set in two sub-sets and invert them separately. As a result, the stress tensor retrieved for the Irpinia cluster corresponds to that characterizing the whole data set, whereas the stress tensor obtained from the inversion of Potenza cluster indicates a strike-slip regime with nearly horizontal  $\sigma_3$  and  $\sigma_1$ , NE-SW and NW-SE trending, respectively (Figure 6.5 violet). These two stress tensors have variances comparable with that obtained for the stress field inversion from the whole data set.

Also in our case, therefore, the results obtained inverting separately the Irpinia and Potenza clusters display the existence of two local stress fields, suggesting a transition from a normal faulting regime (Figure 6.5 blue), acting in the inner sector of the chain, to a strike-slip regime in the Potenza region (Figure 6.5 violet). Both the stress fields associated with the NW-SE normal fault system and to the EW strike-slip fault are characterized by a nearly horizontal minimum compressive stress axis,  $\sigma_3$ , with approximately the same NE-SW direction. On the other hand the vertical stress axis is, of course,  $\sigma_1$  for the normal faults, and  $\sigma_2$  for the strike-slip faults. From the inner sector of the belt to the external margin, therefore,  $\sigma_3$  remains nearly the same, while there is a switch between  $\sigma_1$  and  $\sigma_2$ .

The analysis of the stress inversion from earthquakes cannot discriminate the dynamic model that explains the two observed tectonic styles. The P-wave polarities from the micro-earthquakes in the Potenza region are well explained by both a unique regional extensional stress field and a local strike-slip regime as retrieved from the inversion of the Potenza cluster.

On the one hand, applying the Ockham's razor to interpret our data, we could conclude that a unique, dominant SW-NE extensional regional stress field is enough to explain the microearthquake generation along both the NW-SE striking normal faults and the E-W striking right-lateral faults. E-W oriented faults inherited from previous tectonic regimes could be reactivated under a normal faulting regime. For instance, Nostro *et al.*, (1997) analyzed the static stress changes on the Potenza fault zone, due to the occurrence of the 1980 Irpinia earthquake, and showed that E-W striking right-lateral faults are favourably oriented with respect to the total stress resulting from the extensional regional stress field and the coseismic stress induced by the 1980 earthquake. In this perspective, a single regional stress field allows a unified interpretation for the two different faulting styles characterizing the earthquakes that occur along the chain and the E-W fault dissecting the belt (De Matteis *et al.*, 2012 under revision).

On the other hand, several E-W striking, right-lateral seismogenic faults are present in the Apulia foreland, both exposed and buried, and they have been interpreted in a more comprehensive model available in literature, which predicts a lateral and depth change of the regional stress field, extensional along the chain and strike-slip eastwards and down-depth, including in the Potenza area (Di Bucci and Mazzoli, 2003; Valensise *et al.*, 2004; Di Bucci *et al.*, 2006; Boncio *et al.*, 2007; Meletti *et al.*, 2008).

Major E-W oriented shear zones have been singled out roughly between the latitudes 40°30'N and 42°30'N, both on-shore and off-shore [Di Bucci and Mazzoli, 2003; Valensise *et al.*, 2004, and references therein]. Among them, the best constrained runs through the source region of the 2002 Molise earthquakes (Vallée and Di Luccio, 2004), continues toward the east crossing the mesoseismal area of the 1627 Gargano earthquake, then connects with the Mattinata fault and the Gondola line off-shore. This shear zone, which we will refer to as Molise-Gondola shear zone, can be considered as representative of all the other,

generally less detailed, parallel shear zones (Di Bucci *et al.*, 2006, with references).

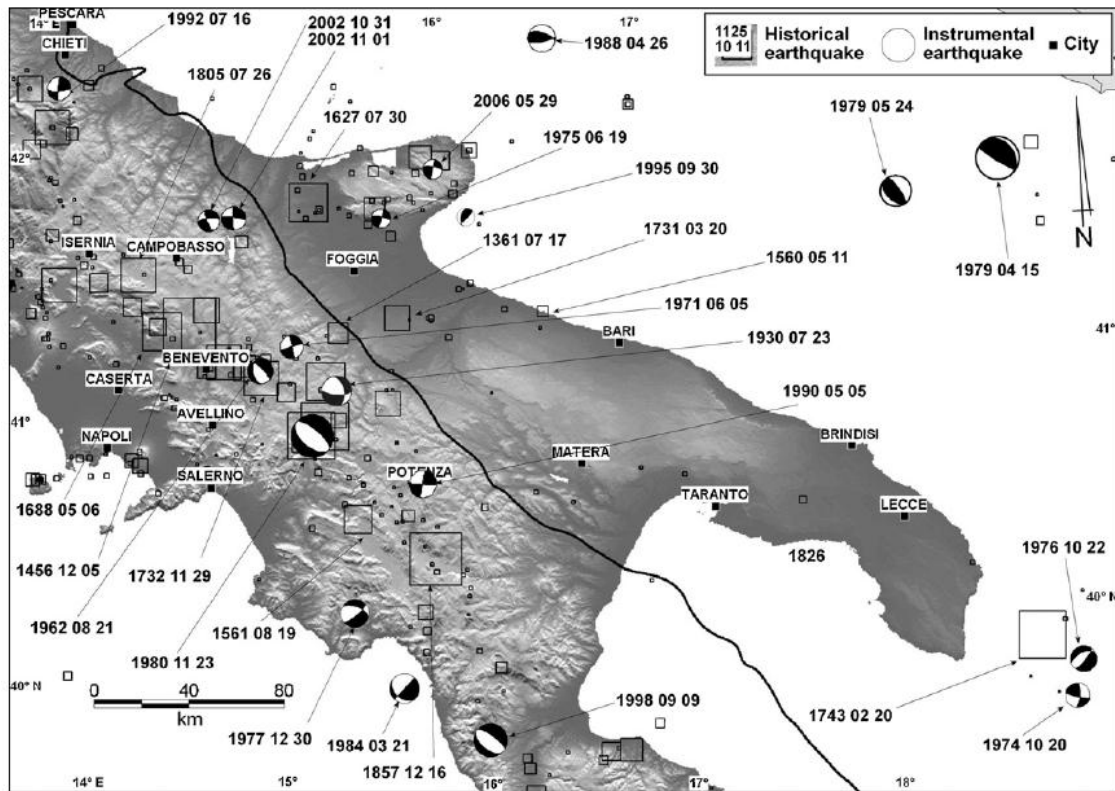


Figure 6.6 Historical and instrumental earthquakes of the Central and Southern Apennines ( $M > 4.0$ ; Gruppo di Lavoro CPTI, 2004; Vannucci and Gasperini, 2004; Pondrelli *et al.*, 2012; Fracassi and Valensise, 2007). The size of the square symbols is proportional to an equivalent magnitude derived from intensity data. The black thick line is the outer front of the Southern Apennines buried below the foredeep deposits (from (from Di Bucci *et al.*, JoG, 2011).

An analogy between the current strike-slip tectonic regime acting in the Potenza region and the similar stress field of the Gargano seismic zone has been proposed also by Boncio *et al.*, (2007).

In this framework, a more recent interpretation (Di Bucci *et al.*, 2010) compares the Molise-Gondola Shear Zone with the N-S striking, left-lateral Vizzini-Scicli Shear Zone in the Sicilian foreland, to recognize the role of the Africa-Eurasia plates NW-SE convergence (well established, based on GPS and VLBI data: e.g., DeMets *et al.*, 1990; Ward, 1994; Zarracoa *et al.*, 1994; Hollenstein *et al.*, 2003; McClusky *et al.*, 2003) in controlling the seismotectonics of the Italian peninsula.

We can compare the Potenza seismogenic zone with these two major shear zones which cut foreland areas and exhibit remarkable similarities.

The database of individual seismogenic sources (DISS working Group, 2010) indicates, for the Potenza area, the presence of a composite seismogenic source identified on the basis of geological, geophysical, and seismological data and associated to moderate magnitude earthquakes ( $M > 6$ ). We already mentioned how some authors pointed out that the seismicity of this region is similar to the one observed in the Gargano area to the northeast, where strike-slip focal mechanisms of instrumental seismicity match with the known E-W striking Mattinata fault, characterized by dominant right-lateral strike-slip motions (Doglioni *et al.*, 1994; Valensise *et al.*, 2004; Di Luccio *et al.*, 2005). There is a general consensus that E-W striking structures, cutting the foreland crust, are older, pre-existing faults inherited at least since Mesozoic times, and that the widespread seismicity associated is due to their reactivation under the present-day stress field (e.g., Di Bucci *et al.*, 2010; Latorre *et al.*, 2010). This seismicity mainly occurs at depths between, let's say, 10 and 25 km.

Moreover, the "Potenza" earthquakes were generated within the most internal buried foreland, where it tends to deepen below the outer front of the Apulia antiformal stack (i.e., the deepest part of the Apennine chain; Boncio *et al.*, 2007). This means that, where present, right-lateral E-W striking shear zones could be active at least as far as the buried Adriatic foreland is not involved in thrusting.

With respect to the Apennine chain, the foreland buried below the outer front of the Apulia antiformal stack is the most internal structural domain where active tectonics and seismicity are known to occur along E-W striking shear zones. As mentioned before, along the axis of the Apennine belt strong earthquakes on NW-SE normal faults are in fact the expression of active extension characterized by a SW-NE striking  $\sigma_3$ . This seismicity is generated by faulting within the uppermost 15 km of the crust (Valensise *et al.*, 2004), and is best represented by the 1980 Irpinia earthquake ( $M_s = 6.9$ ; Gruppo di Lavoro CPTI [1999]), that nucleated at about 13 km depth (Boschi *et al.*, 1993).

On these bases, we can hypothesize that the behavior of the Potenza fault system is similar to the 2002 Molise seismogenic faults within the Molise Gondola shear

zone (Mostardini and Merlini, 1986; Butler *et al.*, 2004), as already proposed by some investigators (Di Bucci and Mazzoli, 2003; Valensise *et al.*, 2004; Boncio *et al.*, 2007). As for the 1990-91 Potenza sequence and for the 2002 Molise sequence, also for the 1851 and 1930 previous earthquakes, epicenters locate immediately west of the Southern Apennines thrust front and east of the chain axis (Pino *et al.*, 2008), i.e., where at depth the foreland is buried and inflected under the orogenic wedge but still not involved in thrusting.

In a broader view, we can now include in our comparison of the Potenza fault system with the Molise-Gondola shear zone also Vizzini-Scicli shear zone (Figure 6.7).

Firstly, the Molise-Gondola and Vizzini-Scicli shear zones are comparable from a geometric and kinematic point of view; both are more than 100 km long and formed by 30–50 km long fault systems, which in some cases can be further subdivided into 10–15 km long fault segments, exhibit high-angle fault planes and are dominantly strike slip. In this perspective, the Potenza fault system, E-W striking, 20 km long, within a seismogenic layer about 25 km thick, displaying strike-slip kinematics, can be compared with the fault systems forming the two major shear zones.

Secondly, the Molise-Gondola and Vizzini-Scicli shear zones are also located in similar tectonic environments. Both extend from an open foreland area to the outer front of a fold-and-thrust belt. In detail, both shear zones display two fault systems in the foreland, the first of which is submerged (Gondola Fault Zone and Scicli offshore, respectively) whereas the second one is exposed in the mainland (Mattinata Fault and Scicli onshore, respectively). From this point of view, the Potenza fault system can be compared to the 2002 Molise fault system in the Molise-Gondola shear zone, whereas no equivalent structure is known at the northern tip of the Vizzini-Scicli shear zone. Moreover, with respect to the 2002 Molise fault system, the Potenza fault system is located in a more internal and deeper part of the buried Apulia foreland.

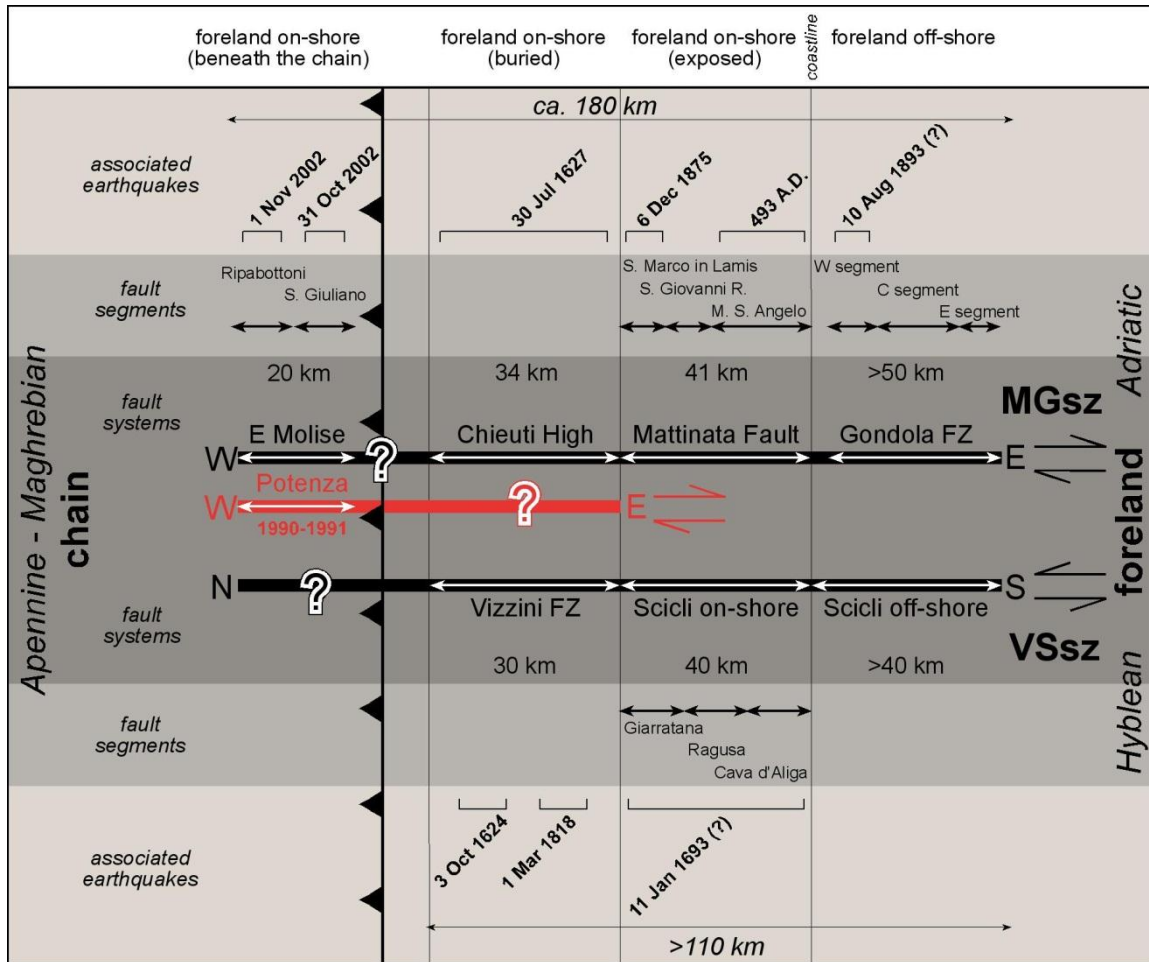


Figure 6.7 The Potenza fault system –in red– projected onto a schematic comparison between the Molise-Gondola and Vizzini-Scicli shear zones (modified from Di Bucci *et al.*, 2010). Each shear zone is formed by fault systems, each of which is further subdivided into fault segments, that is, segments that may rupture during individual damaging earthquakes or during a complex sequence. The double white arrows bound individual fault systems. Where defined, the segments forming each fault system have also been reported.

Finally, the Molise-Gondola and Vizzini-Scicli shear zones display present-day activity due to reactivation of regional structures inherited at least since Mesozoic times. These large regional fault zones, which dissect the foreland crust, have experienced long lasting activity under different tectonic regimes, that is to say, with different kinematics at different times. For both, the inception of the present day activity and thus the most recent slip reversal occurred at about the same time, around the beginning of the Middle Pleistocene. Also the Potenza fault system is located in correspondence with an E-W striking regional tectonic structure, which is exposed in correspondence of the town of Matera, to

the east of Potenza. In analogy with the other shear zones, we could therefore speculate about the Potenza fault system as well as part of an inherited tectonic structure.

An interesting point regards the seismogenic potential of the fault structure as defined by the background seismicity distribution in the Potenza area. The EW alignment extends for a length of about 20 km, including the epicentral area of the 1990 and 1991 Potenza seismic sequences. Assuming that this alignment is the expression of a single, active fault segment, and applying the empirical relation by Wells and Coppersmith (1994), we obtain a seismogenic potential corresponding to magnitudes up to ca. 6.3, a value that is larger than those recorded in this area during the last centuries. The most relevant historical earthquakes occurred in 1826 (M 5.7) and 1963 (M 5.3). Their magnitudes have led to propose that faults in this area are not capable to produce events with intensities higher than VII (CPTI, 2004). Stronger events may have occurred, however, in a longer time span, not covered by available earthquake catalogues.

#### 4. Final remarks

As mentioned in the previous section the role of the Africa-Eurasia convergence in the recent tectonic evolution of the central Mediterranean has been investigated (Di Bucci *et al.*, 2010) by focusing on current fault activity in two sectors of the Adriatic-Hyblean foreland of the Apennine-Maghrebian chain, as they allowed tectonic evidence for relative plate motions to be analyzed aside from the masking effect of other more local tectonic phenomena (e.g., subduction, chain building, etc.).

The selected foreland areas exhibit remarkable similarities, including an unexpectedly high level of seismicity and the presence of the Molise-Gondola and Vizzini-Scicli shear zones since the Mesozoic. From the analysis of the tectonic framework, active tectonics, and seismicity of each of the foreland areas,

highlighting the evolution of the tectonic understanding, current strains at midcrustal levels seem to respond to the same far field force oriented NNW-SSE to NW-SE, similar to the orientation of the Africa-Eurasia convergence. The conclusion is that this convergence plays a primary role in the seismotectonics of the central Mediterranean and is partly accommodated by the reactivation of large Mesozoic shear zones. The tectonic effects of the current Africa-Eurasia convergence are interpreted as a unifying key for understanding the long wavelength seismotectonics of the central Mediterranean, whereas different geodynamic models are available in literature for each of the mentioned shear zones of parts of them (e.g., Doglioni *et al.*, 1994; Catalano *et al.*, 2008).

The activity of the Potenza fault system is well compatible with this geodynamic interpretation. Figure 6.8 schematizes the relation between Africa-Eurasia relative motion and strike-slip motion along the Molise-Gondola and Vizzini-Scicli shear zones and the Potenza fault system, as well as the extensional regime along the chain axis. It's clear from our analysis as well that two active deformation styles can be recognized along the southern part of the Italian which share the same SW-NE striking  $\sigma_3$ .

The reason for the shift between  $\sigma_1$  and  $\sigma_2$ , which is responsible for the two tectonic regimes (vertical  $\sigma_1$  for the extension and vertical  $\sigma_2$  for the transurrence) is still matter of debate and this finding is out of the scopes of this thesis. We can speculate, however, on a possible explanation of this occurrence. We know that the Southern Apennines are experiencing widespread uplift since Middle Pleistocene, and that this uplift is maximum along the core of the chain (Dramis, 1992; Bordoni and Valensise, 1998). We think that the same vertical force which causes the chain uplift could add stress to the vertical  $\sigma_2$  that characterizes the foreland areas, changing it into  $\sigma_1$ ; the lithostatic load of the chain may have a minor role in this process. The reasons for this uplift are themselves matter of debate. Just to give two examples among the available models, we remind the elastic rebound of the lithosphere, due to the slab detachment occurred at the end of the Lower Pleistocene (Patacca and Scandone,

1989), or the asthenospheric wedging underneath the chain, due to the eastward mantle flow interacting with a west-dipping, non-detached slab (Doglioni, 1994).

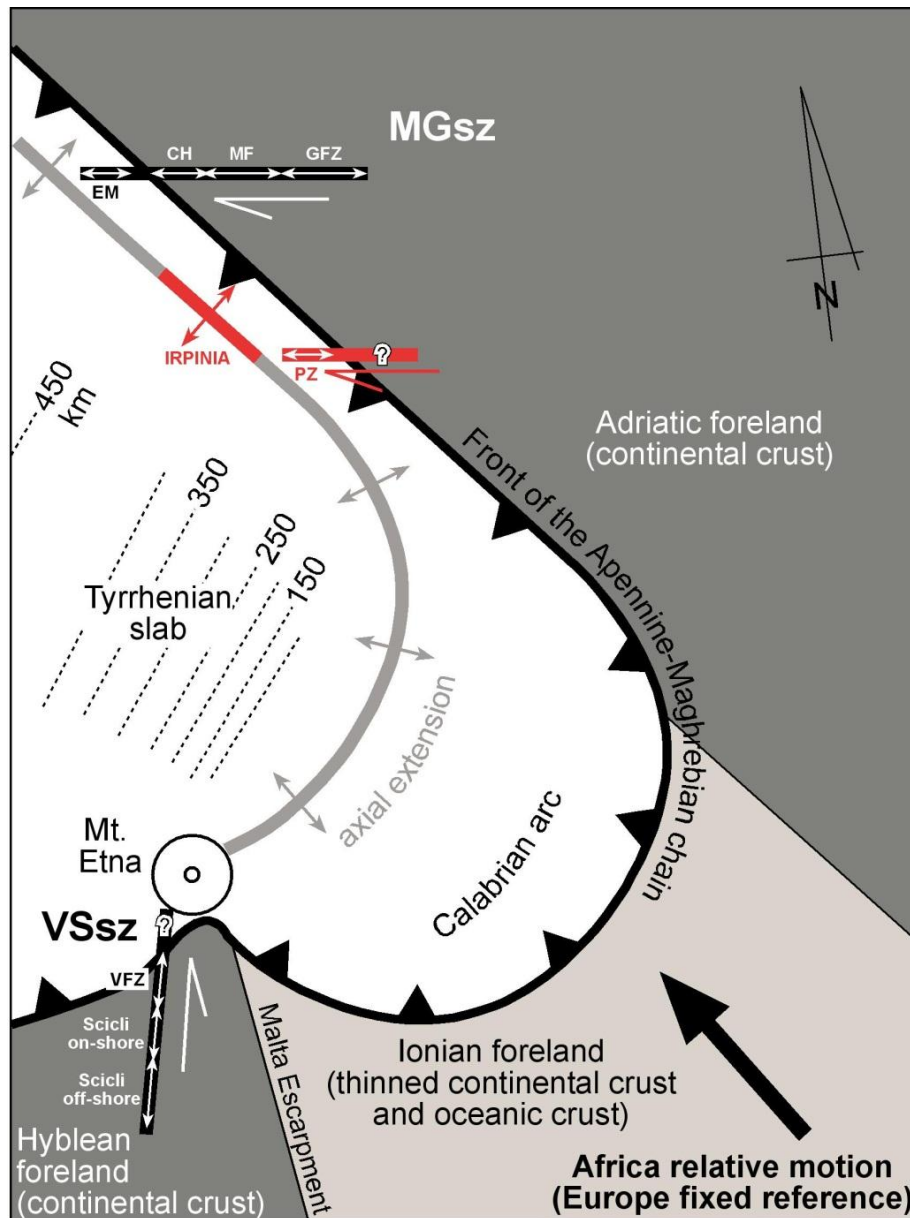


Figure 6.8 The Potenza and Irpinia fault systems projected onto a geodynamic model proposed by Di Bucci *et al.* (2010), which includes a schematic representation of the location and current kinematics of the the Molise-Gondola and Vizzini-Scicli shear zones. Dashed lines are depth contours of the subducting slab (from D'Agostino and Selvaggi, 2004). A gray line runs along the axis of the Apennine- Maghrebian chain, which is currently undergoing extension. The relative Africa plate motion (thick black arrow) is from Devoti *et al.* (2008). Fault systems: EM, Eastern Molise (2002 earthquakes sources); CH, Chieuti High; MF, Mattinata Fault; GFZ, Gondola Fault Zone; VFZ, Vizzini Fault Zone.

To conclude, the geodynamic setting of the Southern Apennines could be explained as due to the juxtaposition of various first order structures, including (1) the Adriatic foreland; (2) the Tyrrhenian Sea, a young oceanic type basin that is still undergoing significant stretching; (3) the Southern Apennines, a continuous fold-and-thrust belt with variable strike, degree of shortening and uplift rates. We suppose that the NW-SE-striking Africa-Eurasia convergence acts in the background of all these structures, playing a primary and unifying role in the seismotectonics of the whole region. The interaction of these shear zones with the Apennine chain, however, still remains to be elucidated.

## Conclusion

The aim of this work was to show that refined analyses of background, low magnitude seismicity allow to delineate the main active faults and to accurately estimate the directions of the regional tectonic stress that characterize the Southern Apennines (Italy), a structurally complex area with high seismic potential.

Thanks the presence in the area of an integrated dense and wide dynamic network projected *a hoc* to monitor the studied area, was possible to analyzed an high quality microearthquake data-set. We performed very accurate arrival time and polarities of the P-wave first motion readings in order to improve the accuracy in velocity model, location, focal mechanism and stress field estimation.

The determination of a reference 1D P-wave velocity model together with the associated station corrections is carried out. The station delays, whose spatial distribution shows a strong lateral variation in a direction orthogonal to the Apenninic chain, have been interpreted thanks to the well-known geological knowledge of the area and the availability of a 3D velocity model.

We also studied the influence of the use of 1D model to represent the true 3D velocity distribution of a geologically complex area in the earthquake locations. Some synthetic example showed that the use of 1D velocity model with a refined technique (double difference; HypoDD) can overcome in part the problem of a poor representation of the propagation medium.

Based on the result of refined seismicity location and focal mechanisms we delineated a system of NW-SE striking normal faults along the Apenninic chain and an approximately E-W oriented, strike-slip fault, transversely cutting the belt. Our study confirms that the background microearthquake activity in the

studied sector of the Apenninic chain is controlled by these two major fault systems.

We proved that the earthquakes recorded in the last 20 years do not match the Omori's law rate decay. And so, this evidence demonstrated that the current seismic events can be ascribed to the background seismicity rather than be interpreted as aftershocks of previous large earthquakes. In this sense, this study gives a new perspective to the application of the high quality records of low magnitude background seismicity for the identification and characterization of active fault systems. We want to emphasize here the novelty of the contribution obtained from the analysis of background microseismicity in studies of active tectonics.

Results show that three decades after the 1980 Irpinia earthquake the background, low magnitude seismicity and the related stress field are closely linked with the major fault segments activated during the 1980 and 1990 mainshocks, and delineate their geometries, extents and mechanisms.

The seismicity along the chain does not randomly distributed but occurs on sub-parallel fault planes highly organized inside the volume delimited by the normal fault system of the 1980 Irpinia M 6.9 earthquake. In the same way, moving to SE of the study region we observed that the background seismicity along the 1990-91 Potenza seismogenic fault system, have an E-W striking, subvertical, right-lateral structure is still active twenty years later this event.

In order to better understand the geodynamic acting in the area we determine the direction of principal stress axes. A method to obtain the stress tensor from first P motion polarities for source-station pairs was applied and a technique to define realistic error estimation on the orientation of the three principal axes was implemented.

From the stress tensor analysis a regional stress tensor with a nearly horizontal minimum stress axis,  $\sigma_3$ , perpendicular to the axis of the belt is retrieved. This is consistent with the results obtained from the analysis of other geological, breakout and seismic data (Pantosti and Valensise, 1990; Frepoli and Amato, 2000; Montone *et al.*, 2004; DISS Working Group, 2010; Pasquale *et al.*, 2009) acquired along the Apennines.

The observations of the different kinematics that characterize the earthquakes occurring in the Irpinia area and in the Potenza area call in question the possible spatial variation in the tectonic regime from the inner to the external part of the chain. Considering the data separately, we found two different stress fields:

- a SW-NE-striking extensional regime in correspondence of the core of the Apennines fold-and-thrust belt;
- a strike-slip regime that exhibits SW-NE-striking minimum horizontal stress towards the Apulia foreland.

The geodynamic setting of the considered region is due to the juxtaposition of various first order structures, including the Adriatic foreland and the Southern Apennines, a continuous fold-and-thrust belt with variable strike, degree of shortening and uplift rates.

In particular, we suggest that the NW-SE-striking Africa-Eurasia convergence acts in the background of all these structures, playing a primary and unifying role in the seismotectonics of the whole region.



## Bibliography

- Akaike H. (1974). A new look at the statistical model identification. *IEEE Trans. Autom. Control* , 6, 716-723.
- Aki, K. and P. Richards. (1980). *Quantitative Seismology*. San Francisco: W. H. Freeman.
- Alessio, G., E. Esposito, A. Gorini, S. Porfido. (1995). Detailed study of the Potentino seismic zone in the Southern Apennines, Italy. *Tectonophysics*, 250, Issues 1-3, 113-134.
- Amadei B. and O. Stephansson. (1997). *Rock stress and its Measurements*. London: Chapman & Hall.
- Amato A., Azzara R., Basili A., Chiarabba C., Cocco M., Di Bona M., Malagnini L., Scardella M., and Selvaggi G. (1993). Lo sciame sismico dei Colli Albani. *Geologica Romana*, 29, 277-280.
- Amato, A., Selvaggi, G., . (1993). Aftershock location and P-wave velocity structure in the epicentral region of the 1980 Irpinia earthquake. *Ann. Geofis.*, 36 (1), 3- 15.
- Amoroso, O. (2012). *Ph. D. thesis in Geophysics: "Three dimensional seismic imaging and earthquake in a complex, segmented fault region in Southern Apennines "*. Bologna: Università di Bologna.
- Anderson E.M. (1951). *The dynamics of faulting and dike formation with application to Britain*. Oliver and Boyd.
- Angelier, J. . (1984). Tectonic analysis of fault slip data sets . *J. Geophys. Res.*, 89, 5835-5848.
- Angelier, J. , A. Tarantola, B. Valette, and S. Manoussis. (1982.). Inversion of field data in fault tectonics to obtain the regional stress, I, Single phase fault populations A: new method of computing the stress tensor,. *Geophys. J. R. Astron. Soc*, 69, 607-621.
- Anzidei M, Baldi P, Casula G, Galvani A, Mantovani E, Pesci A, et al. (2001). Insights into present-day crustal motion in the central Mediterranean area from GPS surveys. *Geophys J Int* , 146:98-110. doi:10.1046/j.0956-540x.2001.01425.x.
- Armijo, R. and A. Cisternas . (1978). Un probleme inverse en microtectonique cassante, *C. R. Acad. Sci. C. R. Acad. Sci. Paris* , 287(D), 595-598.
- Armijo, R., E. Carey, and A, Cisternas. (1982). The inverse problem of microtectonics and the separation of tectonic phases. *Tectonophysics* , 82, 145-160.
- Benz, H., B. Chouet, P. Dawson, J. Lahr, R. Page, and J. Hole. (1996). Three-dimensional p and s wave velocity structure of redoubt volcano, alaska. *J. Geophys. Res.* , 101 (B4), 8111-8128.
- Bernard, P., Zollo, A. (1989). The Irpinia (Italy) 1990 earthquake: detailed analysis of a complex normal fault. *J. Geophys. Res.*, 94, 1631- 1648.

- Bisio L., D. G. (2004). Three-dimensional earthquake locations and upper crustal structure of the Sannio-Matese region (Southern Italy). *Tectonophysics*, 385, 121-136.
- Boncio, P., Mancini, T., Lavecchia, G., Selvaggi, G. (2007). Seismotectonics of strike-slip earthquakes within the deep crust of southern Italy: Geometry, kinematics, stress field and crustal rheology of the Potenza 1990-1991 seismic sequences (Mmax 5.7). *Tectonophysics*, 445, 281-300.
- Bordoni, P. & Valensise G. (1998). Deformation of the 125 ks marine terrace in Italy: tectonic implications. Coastal Tectonics. In I. S. Stewart, *Geological Society, London, Special Publications* (p. 146, 71-110).
- Boschi, E., D. Pantosti, D. Slejko, M. Stucchi, and G. Valensise (Eds.) . (1993). Special issue on the meeting "Irpinia dieci anni dopo", Sorrento 1990. *Ann. Geofis.*, 36(1), 351 pp.
- Boschi, E., E. Guidoboni, G. Ferrari, D. Mariotti, G. Valensise, and P. Gasperini. (2000). Catalogue of strong Italian earthquakes from 461 B. C. to 1997. *Ann. Geophys.*, 43(4), 608 - 868.
- Bott, M. H. (1959). The mechanics of oblique slip faulting. *Geol. Mag.*, 96, 109-117.
- Brillinger, D. R., A. Udias, and B. A. Bolt. (1980). A probability model for regional focal mechanism solution. *Bull. Seism. Soc. Am.* , 70, 149-170.
- Brudy M., Zoback M.D., Fuchs K., Rummel F., Baumgartner J. (1997). Estimation of the complete stress tensor to 8 km depth in the KTB scientific drill holes: Implication for crustal strength. *J. Geophys. Res.*, 102, 18453-18475.
- Bufo, E. (1985). Metodos para la determinacion del mecanismo focal de los terremotos a partir de la polaridad de las ondas P. In D. M. A. Udias, *Mecanismo de los Terremotos y Tectonica* (p. 117-139). Madrid: Editorial de la Universidad Complutense.
- Buland R. (1976). The mechanics of locating earthquakes. *Bulletin of the Seismological Society of America*, vol. 66 no. 1 173-187.
- Butler R. W. H., Mazzoli S., Corrado S., De Donatis M., Scrocca D., Di Bucci D., Gambini R., Naso G., Nicolai C., Shiner P. & Zucconi V. (2004). Applying thick-skinned tectonic models to the Apennine thrust belt of Italy - Limitations and implications. In: K. McClay (Ed.) - Thrust tectonics and hydrocarbon systems. *American Association of Petroleum Geologists Memoir*, 84, 647-667.
- Cao, A., and S. Gao. (2002). Temporal variation of seismic b-values beneath northeastern Japan island arc. *Geophys. Res. Letts.* , 29, no. 9, 1334.
- Carrozzo, M.T., Chirenti, A., Luzio, D., Margiotta, C., Quarta, T. (1981). Carta gravimetrica d'Italia: tecniche automatiche per la sua realizzazione. *Proc. of the I Annual Meeting of the National Geophys. Group, Rome, Italy*, pp. 132- 139.
- Casero, P., Roure, F., Endignoux, L., Moretti, L., Muller, C., Sage, L., Vially, R., . (1988). Neogene geodynamic evolution of the Southern Apennines. *Mem. Soc. Geol. Ital.*, 41, 109- 120.

- Casero, P., Roure, F., Vially, L. (1991). Tectonic framework and petroleum potential of the Southern Apennines. In: Spencer, A.M. (Ed.), *Generation, Accumulation, and Production of Europe's Hydrocarbon. European Association of Petroleum Geoscientists, Special Publication, vol. 1. Oxford University Press, Oxford, UK*, pp. 381-387.
- Casnadei, R. (1988). Subsurface basin analysis of fault-controlled turbidite system in Bradano Trough, Southern Adriatic foredeep, Italy. *Bull. Am. Assoc. Pet. Geol.*, 72 (11), 1370-1380.
- Castello B., Selvaggi G., Chiarabba C., Amato A. (2005). CSI Catalogo della sismicità italiana 1981-2002. *INGV-CNT*.
- Catalano, S., G. De Guidi, G. Romagnoli, S. Torrisi, G. Tortorici, and L. Tortorici. (2008). The migration of plate boundaries in SE Sicily: Influence on the large-scale kinematic model of the African promontory in southern Italy. *Tectonophysics*, 449, 41-62.
- Catalano, S., G. De Guidi, G. Romagnoli, S. Torrisi, G. Tortorici, and L. Tortorici. (2008). The migration of plate boundaries in SE Sicily: Influence on the large-scale kinematic model of the African promontory in Southern Italy. *Tectonophysics*, 449,41-62.
- Cavinato G.P. and De Celles P.G. . (1999). Extensional basins in the tectonically bimodal central Apennines fold-thrust belt, Italy: response to corner flow above a subducting slab in retrograde motion. *Geology*, 27, 955-988.
- Chatelain, J.L. (1978). *Etude fine de la sismicité en zone de collision continentale à l'aide d'un réseau de stations portables: la région Hindu-Kush-Pamir, Thèse de 3<sup>ème</sup> cycle*. Toulouse.: Univ. Paul Sabatier.
- Cherchi A. and Montadert L. (1982). Oligo-Miocene rift of Sardinia and the early history of the Western Mediterranean Basin. . *Nature*, 298, 736-739.
- Chiarabba, C., Amato, A. (1994). From tomographic images to fault heterogeneities. *Ann. Geofis.*, 37 (6), 1481-1494.
- Chiarabba, C., Amato, A., Megrhraoui, M. (1996 ). Imaging seismogenic structures with local earthquake tomography. . *Phys. Chem. Earth* , vol 21, No 4, pp. 247-251.
- Chiarabba, C., Jovane, L., Di Stefano, R. (2005). A new view of Italian seismicity using 20 years of instrumental recordings. *Tectonophysics*, 395, 251-268.
- Chiaraluce L., Ellsworth W. L., Chiarabba C. and Cocco M. (2003). Imaging the complexity of an active normal fault system: The 1997 Colfiorito (central Italy) case study. *Journal of Geophysical Research* , VOL. 108, NO. B6, 2294, doi:10.1029/2002JB002166.
- Cinque, A., Patacca, E., Scandone, P., Tozzi, M. (1993). Quaternary kinematic evolution of the Southern Apennines. Relationship between surface geological features and deep lithospheric structures. *Ann. Geofis.*, 36 (2), 249-260.

- Cocco, M., C. Chiarabba, M. Di Bona, G. Selvaggi, L. Margheriti, A. Frepoli, F.P. Lucente, A. Basili, D. Jongmans, and M. Campillo, . (1999). The April 1996 Irpinia seismic sequence: evidence for fault interaction. *J. Seism.*, 3, 105–117.
- Cocco, M., Pacor, F. (1993). The rupture process of the 1980, Irpinia, Italy earthquake from the inversion of strong motion waveforms. *Tectonophysics* , 218, 157–177.
- CPTI WORKING GROUP . (1999). Catalogo Parametrico dei Forti Terremoti Italiani (GNDT-ING-SGA-SSN). *Ed. Compositori, Bologna*, pp. 88.
- Crosson RS. (1976). Crustal structure modelling of earthquake data. Simultaneous least squares estimation of hypocentre and velocity parameters. *J Geophys Res*, 81:3036–3046.
- D’Addezio, G., Pantosti, D. and Valensise, G. (1991). Paleoearthquakes along the Irpinia fault at Pantano di San Gregorio Magno (southern Italy). *Il Quaternario*, 4, 121–136.
- D’Agostino, N., A. Avallone, D. Cheloni, E. D’Anastasio, S. Mantenuto, and G. Selvaggi. (2008). Active tectonics of the Adriatic region from GPS and earthquake slip vectors . *J. Geophys. Res.*, 113, B12413, doi:10.1029/2008JB005860.
- D’Agostino, N., and G. Selvaggi . (2004). Crustal motion along the Eurasia-Nubia plate boundary in the Calabrian Arc and Sicily and active extension in the Messina Straits from GPS measurements. *J. Geophys. Res.*, 109, B11402, doi:10.1029/2004JB002998.
- D’Agostino, N., J. A. Jackson, F. Dramis, and R. Funicello . (2001). Interactions between mantle upwelling, drainage evolution and active normal faulting: An example from the central Apennines (Italy). *Geophys. J. Int.*, 147, 475 – 497.
- D’Argenio, B., Pescatore, T., Scandone, P. (1974). Schema geologico dell’Appennino Meridionale (Campania e Lucania). *Atti del Convegno: Moderne Vedute Sulla Geologia dell’Appennino Meridionale. Accad. Naz. Lincei.*, vol. 183, pp. 49–72.
- De Matteis R., Amoroso O., Matrullo E., Stabile T.A., Rivera L., Zollo A. (2011). Analysis of background microseismicity for crustal velocity model, fault delineation and regional stress direction in Southern Apennines, Italy. *AGU Fall Meeting, San Francisco, USA, 5 - 9 December, 2011.*
- De Matteis R., Matrullo E., Rivera L., Stabile T.A., Pasquale G., Zollo A. (2012 - under revision). Fault delineation and regional stress direction from the analysis of background microseismicity in Southern Apennines, Italy. *BSSA.*
- De Matteis, R., A. Romeo, G. Pasquale, G. Iannaccone, and A. Zollo. (2010). 3D tomographic imaging of the southern Apennines (Italy): a statistical approach to estimate the model uncertainty and resolution. *Stud. Geophys. Geod.*, 54, 367–387.
- Della Vedova B., G. Pellis, J.P Foucher, J.-P Rehault . (1984). Geothermal structure of the Tyrrhenian Sea . *Marine Geology*, Volume 55, Issues 3–4, Pages 271–289 .

- DeMets, C., R. G. Gordon, D. F. Argus, and S. Stein. (1994). Effect of recent revisions to the geomagnetic reversals time scale on estimates of current plate motions. *Geophys. Res. Lett.*, 21, 2191-2194, doi:10.1029/94GL02118.
- Deschamps A. and King G. C. P. . (1984). Aftershocks of the Campania-Lucania (Italy) earthquake of 23 November 1980. *Bulletin of the Seismological Society of America*, vol. 74 no. 6 2483-2517.
- Devoti D., F. Riguzzi, M. Cuffaro, and C. Doglioni (2008). (s.d.). New GPS constraints on the kinematics of the Apennines subduction. *Earth Planet. Sci. Lett.* 273, 163-174.
- Di Bucci D. and S. Mazzoli. (2003). The October-November 2002 Molise seismic sequence (Southern Italy); an expression of Adria intraplate deformation. *J. Geol. Soc. London*, 160 (4), 503-506.
- Di Bucci D., Caputo R., Mastronuzzi G., Fracassi U., Sansò P. & Selleri G. (2011). First evidence of Late Quaternary tectonics from quantitative joint analysis in the southern Adriatic foreland (Italy). In C. D. Piccardi L., "Active Tectonics of the Circum-Adriatic Region" (p. 51 (2-3), 141-155. doi: 10.1016/j.jog.2010.01.012). *Journal of Geodynamics*.
- Di Bucci D., P. Burrato, P. Vannoli, and G. Valensise. (2010). Tectonic evidence for the ongoing Africa-Eurasia convergence in central Mediterranean foreland areas: A journey among long-lived shear zones, large earthquakes, and elusive fault motions. *JGR*, VOL. 115, B12404, doi:10.1029/2009JB006480, 2010.
- Di Bucci, D., A. Ravaglia, S. Seno, G. Toscani, U. Fracassi, and G. Valensise. (2006). Seismotectonics of the southern Apennines and Adriatic foreland: Insights on active regional E-W shear zones from analogue modeling. *Tectonics*, 25, TC4015, doi:10.1029/2005TC001898.
- Di Luccio, F., E. Fukuyama and N.A. Pino. (2005). The 2002 Molise earthquake sequence: what can we learn about the tectonics of Southern Italy? *Tectonophysics* , 405, 141-154.
- DISS Working Group . (2010). Database of Individual Seismogenic Sources (DISS), Version 3.1.1: A compilation of potential sources for earthquakes larger than M 5.5 in Italy and surrounding areas. <http://diss.rm.ingv.it/diss/>. *INGV*.
- Doglioni, C. (1996). Geological remarks on the relationships between extension and convergent geodynamic settings. *Tectonophysics*, 252, 253- 268.
- Doglioni, C., Mongelli, F., Pieri, P. (1994). The Puglia uplift (SE Italy): an anomaly in the foreland of the Apenninic subduction due to buckling of a thick continental lithosphere. *Tectonics* , 13, 1309-1321.
- Douglas A. (1967). Joint Epicentre Determination. *Nature*, 215, 47 - 48.
- Dramis F. (1992). Il ruolo dei sollevamenti tettonici a largo raggio nella genesi del rilievo appenninico. *Studi Geologici Camerti*, volume speciale (1992/1), 9-15.
- Efron B. (1979). Bootstrap Methods: Another Look at the Jackknife. *Ann. Statist.* , Volume 7, 1-26.

- Ekstrom G. (1994). Teleseismic analysis of the 1990 and 1991 earthquakes near Potenza. *Ann. Geofis.*, XXXVII, 1591-1599.
- Ellsworth W. L. (1977). *Three-dimensional structure of the crust and mantle beneath the island of Hawaii*. Cambridge: Ph.D. Thesis, Massachusetts Institute of Technology.
- Ellsworth, W. L., and X. Zhonghuai. (1980). Determination of the stress tensor from focal mechanism data (abstract). *Eos Trans AGU*, (p. 61, 1117 1980).
- Engelder T. (1993). *Stress Regimes in the Lithosphere*. Princeton, New Jersey: Princeton.
- Evans, R., Asudeh, I., Crampin, S. and Üçer, S. B. . (1985). Tectonics of the Marmara Sea region of Turkey: new evidence from microearthquake fault plane solutions. *Geophys. J. Royal Astr. Soc.*, 83: 47-60.
- Ferulano F. (2010). Sintesi di 18 anni di registrazione della rete sismologica Eni nell'Area di Correggio (Mo). *Atti del 29° Convegno GNGTS*, (p. 56-58.).
- Foulger G. R., Miller A. D., Julian B. R., and Evans J. R. (1995). Three-dimensional vp and vp/vs structure of the Hengill Triple Junction and geothermal area, Iceland, and the repeatability of tomographic inversion. *Geophys. Res. Lett.*, 22 (10), 1309-13.
- Fracassi, U., and G. Valensise . (2007). Unveiling the sources of the catastrophic 1456 multiple earthquake: Hints to an unexplored tectonic mechanism in southern Italy. *Bull. Seismol. Soc. Am*, 97, 725-748, doi:10.1785/0120050250.
- Fréchet, J. (1985). *Sismogenèse et doublets sismiques. Thèse d'État*. Université Scientifique et Médicale de Grenoble.
- Frémont M. and Malone S.D. (1987). High Precision Relative Locations of Earthquakes at Mount St. Helens, Washington. *JOURNAL OF GEOPHYSICAL RESEARCH*, VOL. 92, NO. B10, PP. 10,223-10,236.
- Frepoli A, Amato A. (2000). Spatial variation in stress in peninsular Italy and Sicily from background seismicity. *Tectonophysics* , 317:109-124. doi:10.1016/S0040-1951(99)00265-6.
- Frepoli, A. and A. Amato. (2000). Spatial variation in stresses in Peninsular Italy and Sicily from background seismicity. *Tectonophysics*, 317, 109-124.
- Galadini F., Meletti C., Rebez A. (2000). *“Le ricerche del GNDT nel campo della pericolosità sismica (1996-1999)”*. Roma: CNR - Gruppo Nazionale per la Difesa dai Terremoti.
- Galadini, F. . (1999). Pleistocene changes in the central Apennine fault kinematics: A key to decipher active tectonics in central Italy. *Tectonics* , 18(5).
- Gephart JW, Forsyth DW. (1984). An improved method for determining the regional stress tensor using earthquake focal mechanism data: application to the San Fernando earthquake sequence. *J Geophys Res*, 89:9305-9320.

- Gomberg, J. S., K. M. Shedlock, and S. W. Roecke. (1990). The effect of S-wave arrival times on the accuracy of hypocenter estimation. *Bull. Seismol. Soc. Am.*, 80, 1605–1628.
- Got, J. L., Fréchet, J., Klein, F.W. (1994). Deep fault plane geometry inferred from multiplet relative location beneath the south flank of Kilauea. *J. Geophys. Res.*, 99, pp. 15375–15386.
- Gruppo di Lavoro, Catalogo Parametrico dei Terremoti Italiani (CPTI). (2004). *Catalogo Parametrico dei Terremoti Italiani, versione 2004 (CPTI04)*. <http://emidius.mi.ingv.it/CPTI04/> (last acces. Bologna, Italy: Istituto Nazionale di Geofisica e Vulcanologia,).
- Gueguen, E., C. Doglioni, and M. Fernandez. (1998). On the post-25 Ma geodynamic evolution of the western Mediterranean. *Tectonophysics*, 298, 259–269.
- Gutenberg B. and C.F. Richter. (1954). *Seismicity of the Earth and Associated Phenomena, 2nd ed.* . Princeton, N.J.: Princeton University Press.
- Hardebeck, J. L. and P. M. Shearer. (2002). A new method for determining first-motion focal mechanisms. *Bull. Seism. Soc. Am.*, 92, 2264–2276.
- Hauksson, E., and P. Shearer. (2005). Southern California hypocenter relocation with waveform cross-correlation, part 1: Results using the double-difference method. *Bull. Seismol. Soc. Am.*, 95, 896– 903.
- Hollenstein, C., H.-G. Kahle, A. Geiger, S. Jenny, S. Goes, and D. Giardini. (2003). New GPS constraints on the Africa-Eurasia plate boundary zone in southern Italy. *Geophys. Res. Lett.*, 30(18), 1935, doi:10.1029/2003GL017554.
- Hurukawa, N. and Imoto, M. (1992). Subducting oceanic crusts of the Philippine Sea and Pacific plates and weak-zone-normal compression in the Kanto district, Japan. . *Geophysical Journal International*, 109: 639–652. doi: 10.1111/j.1365-246X.1992.tb00122.x.
- Improta L., Bonagura M., Captano P., Iannaccone G. (2003). An integrated geophysical investigation of the upper crust in the epicentral area of the 1980, Ms=6.9, Irpinia earthquake (Southern Italy) . *Tectonophysics*, 361 (2003) 139– 16.
- Jaeger J.C. and N.G.W. Cook. (1971). *Fundamental of rock mechanics*. London: Chapman and Hall.
- Jenny S. , Goes S. , Giardini D. , Kahle H.-G. (2006). Seismic potential of Southern Italy. . *Tectonophysics* , 415 81 – 101.
- Kissling E. (1988). Geotomography with local earthquake data. . *Rev Geophys*, 26:659–698.
- Kissling E. (1995). *Velost user's guide. Internal report.* . ETH Zurich, pp 26: Institute of Geophysics,.
- Kissling, E., Ellsworth, W.L., Eberhart-Phillips, D., Kradolfer, U. (1995). Initial reference models in local earthquake tomography. *J. Geophys. Res.*, 99, 19635–19646.

- Latorre, D., A. Amato, and C. Chiarabba. (2010). High-resolution seismic imaging of the Mw5.7, 2002 Molise, southern Italy, earthquake area: Evidence of deep fault reactivation. *Tectonics*, 29, TC4014, doi:10.1029/2009TC002595.
- Latorre, D., Virieux, J., Monfret, T., Monteiller, V., Vanorio, T., Got, J.-L. and Lyon-Caen, H. (2004). A new seismic tomography of Aigion area (Gulf of Corinth-Greece) from a 1991 dataset. *Geophys. J. Int.*, 159, 1013-1031.
- Lavecchia G. (1988). The Tyrrhenian-Apennines system: structural setting and seismotectogenesis. *Tectonophysics*, 147, 263-296.
- Lay T. and Wallace T. C. (1995). *Modern global seismology*. Academic Press.
- Lee W. H. K., Stewart S. W. (1981). Principles and applications of microearthquake networks. *Advances in geophysics*.
- Lin, G., P. Shearer, and E. Hauksson. (2007). Applying a three-dimensional velocity model, waveform cross correlation, and cluster analysis to locate southern California seismicity from 1981 to 2005. *J. Geophys. Res.*, 112, B12309.
- Lockner D.A., and Beeler N. (2002). Rock Failure and Earthquakes. In H. K. William H.K. Lee, *Earthquake and engineering seismology* (p. 32, 505-537). San Diego, California: Elsevier Science.
- Lomax, A., J. Virieux, P. Volant, and B.C. Thierry. (2000). *Probabilistic earthquake location in 3D and layered models*. Dordrecht: Kluwer Academic.
- Lucente F.P., Chiarabba C. e Cimini G. (1999). Tomographic constraints on the geodynamic evolution of the Italian region. *Journal of Geophys. Research*, 104, B9, 20, 307-20, 327.
- Luongo G. (s.d.). La città e i suoi rischi naturali. In A. Vallario, *Dissesto idrogeologico in Campania* (p. 2002). CUEN.
- Maggi, C., Frepoli, A., Cimini, G. B., Console, R., Chiappini, M. (2009). Recent seismicity and crustal stress field in the Lucanian Apennines and surroundings areas (Southern Italy): seismotectonic implications. *Tectonophysics*, 463, 130-144.
- Malinverno A. e Ryan W.B.F. (1986). Extension in the Tyrrhenian Sea and shortening in the Apennines as a result of arc migration driver by sinking of the lithosphere. *Tectonics*, 5, 227-245.
- Matrullo E., Amoroso O., De Matteis R., Satriano C., Zollo A. (2011a). 1D versus 3D velocity models for earthquake locations: a case study in Campania-Lucania region (Southern Italy). *EGU General Assembly April 3-8, 2011*, (p. Vol. 13, EGU2011-9305). Vienna.
- Matrullo E., Rivera L., De Matteis R., Zollo A. (2011b). Stress inversion from initial polarities of a population of earthquakes: application to the Irpinia region (Southern Apennines). *EGU General Assembly - April 3-8, 2011*, (p. Vol. 13, EGU2011-808). Vienna.

- McClusky, S., R. Reilinger, S. Mahmoud, D. Ben Sari, and A. Tealeb. (2003). GPS constraints on Africa (Nubia) and Arabia plate motions. *Geophys. J. Int.*, 155(1), 126 – 138.
- McKenzie, D. P. (1969). The relation between fault plane solutions for earthquakes. *Bull. Seismol. Soc. Am.*, 59, 591-601.
- Meletti C., Galadini F., Valensise G., Stucchi M., Basili R., Barba S., Vannucci G., Boschi E. (2008). A seismic source zone model for the seismic hazard assessment of the Italian territory. *Tectonophysics*, 450, 85-108.
- Menardi Noguera, A., & Rea, G. (2000). Deep structure of the Campanian-Lucanian Arc (southern Apennines). *Tectonophysics*, 324, 239-265.
- Menke W. (1989). *Geophysical Data Analysis: Discrete Inverse Theory*. Academic Press.
- Micheal AJ. (1984). Determination of stress from slip data: faults and folds. *J Geophys Res*, 89:11517-11526.
- Micheal AJ. (1987a). Use of the mechanisms to determine stress: a control study. . *J Geophys Res*, 92:357-368.
- Micheal AJ. (1987b). Stress rotation during the Coalinga aftershock sequence. *J Geophys Res*, 92:7963-7979.
- Michelini A. and Lomax A. (2004). The effect of velocity structure errors on double-difference earthquake location. *GRL*, VOL. 31, L09602.
- Montone P, Amato A, Pondrelli S. (1999). Active stress map of Italy. . *J Geophys Res*, 104:25595-25610.doi:10.1029/1999JB900181.
- Montone, P., M. T. Mariucci, S. Pondrelli, and A. Amato . (2004). An improved stress map for Italy and surrounding regions (central Mediterranean). *J. Geophys. Res.*, 88, 6415-6429.
- Moretti M., De Gori E. C., and Chiarabba C. (2004). Confronto di metodologie di tomografia sismica locale nella definizione della struttura crostale di un'area di Lacuna sismica (CDC). *Atti del 23° Convegno GNGTS*.
- Moser, T.J., T. van Eck and Nolet, G., . (1992). Hypocenter determination in strongly heterogeneous earth models using the shortest path method. *J. Geophys. Res.*, 97, 6563-6572.
- Mostardini, F., & Merlini, S. . (1986). Appennino centro-meridionale. Sezioni geologiche e proposta di modello strutturale. *Memorie della Società Geologica Italiana*, 35, 177-202.
- Murru, M., R. Console, G. Falcone. (2009). Real time earthquake forecasting in Italy. *Tectonophysics*, 470, Issue 3-4, 214-223,.
- Nakamura K. (1977). Volcanoes as possible indicators of tectonic stress orientations-principle and proposal . *J. Volcanol. Geotherm. Res.*, 2, 1-16.

- Nicolich. (1989). Crustal structures from seismic studies in the frame of the European geotrasverse (southern segment) and CROP projects. *The lithosphere in Italy, Advances in Earth Science Research. It. Nat. Lith. Progr., Mid-term Conf. Rome, 5-6 May*; edited by A. Boriani, M. Bonafede, G.B. Piccardo and G.B. Vai, Atti Conv. Lincei, 80, 41-61.
- Nostro, C., M. Cocco, and M. E. Belardinelli . (1997). Static Stress Changes in Extensional Regimes: An Application to Southern Apennines (Italy). *Bull. Seismol. Soc. Am.*, Vol. 87, No. 1, pp. 234-248.
- Olivieri M., R.M. Allen, and G. Wurman. (2008). The Potential for Earthquake Early Warning in Italy Using ElarmS. *Bulletin of the Seismological Society of America*, Vol. 98, No. 1, pp. 495-503.
- Omori F. (1894). On the aftershocks of earthquakes. *Journal of the College of Science, Imperial University of Tokyo*, 7:111-200.
- Paige, C. and Sanders, M. A. (1982). LSQR: An algorithm for sparse linear equation and sparse least squares. *Trans. Math. Software*, 8, 43-71.
- Pantosti D., Schwartz D.P., Valensise G. . (1993). Paleoseismology along the 1980 surface rupture of the Irpinia fault: Implications for earthquake recurrence in the Southern Apennines, Italy. *J. Geophys. Res.*, 98, 6561-6577.
- Pantosti, D., Valensise, G., . (1990). Faulting mechanism and complexity of the November 23, 1980, Campania- Lucania earthquake, inferred from surface observations. *J. Geophys. Res.* , 95 (15), 319-341.
- Pasquale, G., R. De Matteis, A. Romeo, and R. Maresca. (2009). Earthquake focal mechanisms and stress inversion in the Irpinia Region (southern Italy). *J. Seism.*, Vol. 13, 107-124, DOI 10.1007/s10950-008-9119-x.
- Patacca E. and Scandone P. (1989). Post-Tortonian mountain building in the Apennines: the role of the passive sinking of a relic lithospheric slab. In M. B. eds A. Boriani, *The Lithosphere in Italy: Advances in Earth Science Research* (p. Vol. 80, pp.157-176 ). Rome: Accademia Nazionale dei Lincei.
- Patacca, E. and Scandone P. (2001). Late thrust propagation and sedimentary response in the thrust belt - foredeep system of the Southern Apennines (Pliocene-Pleistocene). . In G. M. Vai, *Anatomy of an Orogen: The Apennines and Adjacent Mediterranean Basins*. (p. pp. 401-440.). Dordrecht, Netherlands: Kluwer Academic Publishers.
- Patacca, E., Sartori, R., Scandone, P. (1990). *Adjacent Mediterranean Basins*. Dordrecht, Netherlands: Kluwer Academic Publishers.
- Patacca, E., Scandone, P. (1987). Post-Tortonian mountain building in the Apennines. The role of the passive sinking of a relic lithospheric slab. In A. B. Boriani, *The Lithosphere in Italy. Accad. Naz. Lincei* (p. vol. 80, pp. 157-176.).
- Patacca, E., Scandone, P., Ballatalla, M., Perilli, N., Santini, U. (1992). The Numidian-sand event in the Southern Apennines. *Mem. Soc. Geol. Padova* , 43, 297-337.

- Pavlis G. L. (1986). Appraising earthquake hypocenter location errors: a complete, practical approach for single event locations. *Bulletin of the Seismological Society of America*, 76, pp. 1699–1717.
- Pavlis G. L. (1992). Appraising relative earthquake location errors . *Bulletin of the Seismological Society of America*, vol. 82 no. 2 836-859 .
- Piccinini D., Chiaraluce M., and Ripepe M. . (1999). Analisi dei foreshocks della sequenza sismica Umbro-Marchegiana del Settembre 1997. *Atti del 18° Convegno GNGTS*.
- Pino, N. A., B. Palombo, G. Ventura, B. Perniola, and G. Ferrari. (2008). Waveform modeling of historical seismograms of the 1930 Irpinia earthquake provides insight on “blind” faulting in Southern Apennines (Italy). *J. Geophys. Res.*, 113, B05303, doi:10.1.
- Podvin, P. and Lacomte, I., . (1991). Finite difference computation of traveltimes in very contrasted velocity models: A massively parallel approach and its associated tools. *Geophys. J. Int.*, 105, 271-284.
- Pondrelli, S., Morelli, A., Ekström, G., Mazza, S., Boschi, E., Dziewonski, A.M.,. ( 2002). European–Mediterranean regional centroid-moment tensors: 1997–2000. *Phys. Earth Planet. Inter.* , 130, 71–101.
- Pondrelli, S., S. Salimbeni, G. Ekström, A. Morelli, P. Gasperini, and G. Vannucci . (2006). The Italian CMT dataset from 1977 to the present. *Phys. Earth Planet.* , In. 159, no. 3/4, 286–303, doi 10.1016/j.pepi.2006.07.008.
- Presti D., Toise C., De Natale G. (2004). Probabilistic location of seismic sequence in heterogeneous media. *BSSA*, Vol.94, N.6, pp. 2239-2253.
- Pujol, J. (1988). Comments on the joint determination of hypocenter and station corrections. *Bull. Seism. Soc. Am.* , 78, 1179–1189.
- Reasenber, P. A., and Oppenheimer, D. (1985). FPFIT, FPLOT, and FPPAGE: Fortran computer programs for calculating and displaying earthquake fault-plane solutions. *U.S. Geological Survey Open-File Report* , 85-739.
- Reyners M., Donna E.P, Stuart G., and Yuichi N. . (2006). Imaging subduction from the trench to 300 km depth beneath the central North Island, New Zealand, with Vp and Vp/Vs. *Geophys. J. Int.*, 165 (2), 565-583. Doi: 10.1111/j.1365246X.2006.02897.x.
- Rigo, A., Lyon-Caen, H., Armijo, R., Deschamps, A., Hatzfeld, D., Makropoulos, K., Papadimitriou, P. and Kassaras, I. (1996). A microseismic study in the western part of the Gulf of Corinth (Greece): implications for large-scale normal faulting mechanisms. *Geophys. J. Int.*, 126: 663–688.
- Rivera L. and Cisternas A. (1990). Stress tensor and fault plane solution for a population of earthquakes. *Bulletin of the Seismological Society of America*, Vol. 80, No. 3, pp. 600-614.

- Rivera L. and Kanamori H. (2002). Spatial heterogeneity of tectonic stress and friction in the crust. *GRL*, Vol. 29 N.6.
- Rosenbaum G. and Lister G.S. (2004). Neogene and Quaternary rollback evolution of the Tyrrhenian Sea, the Apennines, and the Sicilian Maghrebides. *Tectonics*, Vol. 23, TC1013, doi:10.1029/2003TC001518.
- Roure, F., Casero, P., Vially, R. (1991). Growth processes and mélangé formation in the Southern Apennines accretionary wedge. *Earth Planet. Sci. Lett.* , 102, 395– 412.
- Royden, L., Patacca, E., Scandone, P. (1987). Segmentation and configuration of subducted lithosphere in Italy: an important control on thrust-belt and foredeep-basin evolution. *Geology*, 15, 714–717.
- Rubin, A. M., D. Gillard, and J. L. Got . (1999). Streaks of microearthquakes along creeping faults. *Nature*, 400, 635– 641.
- Ruff, L. J. (2002). State of stress within the earth. In H. K. William H.K. Lee, *Earthquake and Engineering Seismology part A* (p. 33, 539-556). San Diego, California: Elsevier Science.
- Scandone P. (1980). Origin of the Tirrenian Sea and Calabrain Arc. *Boll. Soc. Geol. It*, 98, 27-34.
- Scarfì L., S. Imposa, R. Raffaele, A. Scaltrito. (2009). Crustal seismic velocity in the Marche region (Central Italy): computation of a minimum 1-D model with seismic station corrections. *Environ Geol*, 56:1115–112.
- Scrocca. (2010). Southern Apennines: structural setting and tectonic evolution. In A. P. Marco Beltrando, *The Geology of Italy* (p. vol. 36, paper 13). Journal of the Virtual Explorer, Electronic edn.
- Scrocca D., Carminati E., Doglioni C. . (2005). Deep structure of the southern Apennines, Italy : Thin - skinned or thick skinned ? *Tectonics*, vol. 24 pp. 1-20. .
- Shearer P., Hauksson E., and Lin G. (2005). Southern California Hypocenter Relocation with Waveform Cross-Correlation, Part 2: Results Using Source-Specific Station Terms and Cluster Analysis. *Bulletin of the Seismological Society of America*, Vol. 95, No. 3, pp. 904–915, doi: 10.1785/0120040168.
- Shearer P.M. (1997). Improving local earthquake locations using the L1 norm and waveform correlation application to the Whittier Narrows, California, aftershock sequence. *Journal of Geophysical Research*, 102.
- Shearer, P. M. (2009). *Introduction to Seismology, second edition*. Cambridge: Cambridge University Press.
- Shiner P., Beccacini A. e Mazzoli S. (2004). Thin-skinned versus thick-skinned structural models for Apulian carbonate reservoirs: constraints from the Val d'Agri Fields, S Apennines, Italy. *Marine and Petroleum Geology* 21, 805–827.
- Suarez, G., T. Monfret, G. Wittlinger, C. David. (1990). Geometry of subduction and depth of the seismogenic zone in the Guerrero gap, Mexico. *Nature*, 345, 336-338.

- Tarantola A. (1987). *Inverse problem theory: Methods for data fitting and model parameter estimation*. Amsterdam: Elsevier .
- Tarantola A. and Valette B. (1982). Inverse Problems = Quest for Information. *Journal of Geophysics*, 50, p. 159–170.
- Thurber C. H. (1983). Earthquake Locations and Three-Dimensional Crustal Structure in the Coyote Lake Area, Central California. *Journal of Geophysical Research*, VOL. 88, NO. B10, PP. 8226-8236.
- Thurber CH . (1992). Hypocentre–velocity structure coupling in local earthquake tomography. . *Phys Earth Planet Int*, 75:55–62.
- Turcotte D., Schubert G. (2002). *Geodynamics*. Cambridge: Cambridge University Press.
- Utsu, T. (1961). A statistical study of the occurrence of aftershocks. *Geophysical Magazine* , 30:521-605.
- Utsu, T.; Ogata, Y.; Matsu'ura, R.S. (1995). The centenary of the Omori formula for a decay law of aftershock activity. *Journal of Physics of the Earth*, 43: 1-33.
- Valensise, G., D. Pantosti and R. Basili . (2004). Seismology and tectonic setting of the 2002 Molise, Italy, earthquake. *Earthquake Spectra*, 20, S23.
- Valensise, G., Pantosti, D. (2001). The investigation of potential earthquake sources in peninsular Italy: a review. *Journal of Seismology* , 5 (3), 287–306.
- Vallée, M., and F. Di Luccio. (2005). Source analysis of the 2002 Molise, southern Italy, twin earthquakes (10/31 and 11/01). *Geophys. Res. Lett.*, 32, L12309, doi:10.1029/2005GL022687.
- Vannucci, G., Gasperini, G. (2004). The new release of the database of Earthquake Mechanisms of the Mediterranean Area. *Ann. Geophys.*, (EMMA version 2). 47 (1) with CD-Rom.
- Vanorio, T., Virieux, J., Capuano P., and Russo G. (2005). Three-dimensional seismic tomography from P wave and S wave microearthquake travel times and rock physics characterization of the Campi Flegrei Caldera . *Journal of Geophysical Reserach*, Vol. 110, B03201.
- Vassallo M., G. Festa and A. Bobbio. (2012 in press). Seismic Ambient Noise Analysis in Southern Italy. *BSSA*, Vol. 102, No. 2.
- Walck M.C. (1988). Three-Dimensional Vp/Vs Variations for the Coso Region, California. *J. Geophys. Res.*, 93 (B3), 2047-2052. Doi: 10.1029/JB09iB03p02047.
- Waldhauser F. (2002). Fault structure and mechanics of the Hayward Fault, California, from double-difference earthquake locations. *Journal of Geophysical Research*, VOL. 107, NO. B3.
- Waldhauser F. and W. L. Ellsworth. (2000). A double-difference earthquake location algorithm: Method and application to the northern Hayward Fault, California. *Bull. Seismol. Soc. Am*, 90, 1353– 1368.

- Ward, S. N. . (1994). Constraints on the seismotectonics of the central Mediterranean from very long baseline interferometry. *Geophys. J. Int.*, 117, 441 - 452.
- Weber E., Iannaccone G., Zollo A., Bobbio A., Cantore L., Corciulo M., Convertito V., Di Crosta M., Elia L., EMolo A., Martino C., Romeo A., Satriano C. (2007). An advances seismic network in Southern Apennines (Italy) for seismicity investigations and experimentation with earthquake early warning. *Seismological Research Letters*, 78 (6): 622-634.
- Wells, D. L., and K. J. Coppersmith . (1994). New empirical relationships among magnitude, rupture length, rupture width, rupture area, and surface displacement. *Bull. Seismol. Soc. Am.*, 84, 974-1002.
- Westaway R. & Jackson J. (1987). *The earthquake of 1980 November 23 in Campania-Basilicata (Southern Italy)*. *Geophys. J. R. Astr. Soc.*: 90, 375-443.
- Wiemer, S., and M. Wyss . (2002). Minimum magnitude of completeness in earthquake catalogs: examples from Alaska, the Western United States and Japan. *Bull. Seismol. Soc. Am.*, 90, no. 4.
- Wittlinger, G., Herquel G., and Nakache, T. (1993). Earthquake location in strongly heterogeneous media. *Geophys. J. Int.*, 115, 759-777.
- Zarraoa, N., A. Rius, E. Sardo'n, and J. W. Ryan. (1994). Relative motions in Europe studied with a geodetic VLBI network. *Geophys. J. Int.*, 117, 763 - 768.
- Zoback M.L. (1992). First and second order patterns of tectonic stress: The World Stress Map Project. *J. Geophys. Res.*, 97, 11703-11728.
- Zoback M.D. and Zoback M.L. (2002). State of stress in the Earth's Lithosphere. In H. K. Willian H.K. Lee, *Earthquake and Engineering Seismology part A* (p. 34, 559 - 568). San Diego, California: Elsevier Science.
- Zollo, A., G. Iannaccone, M. Lancieri, L. Cantore, V. Convertito, A. Emolo, G. Festa, F. Gallovic', M. Vassallo, C. Martino, C. Satriano, and P. Gasparini. (2009). Earthquake early warning system in southern Italy: Methodologies and performance evaluation. *Geophys. Res. Lett.* , 36, L00B07, .

## Acknowledgments

*I would like to thank my tutor Prof. Raffaella De Matteis for having followed me in these three years, for her invaluable advices and for the patience she has always shown towards me. She is a very nice person and woman besides being a good scientist. I recognize in her a strong ability to transmit all her knowledge to her students.*

*I'm grateful to the RISSC-Lab of the University Federico II of Naples, in the persons of Prof. Aldo Zollo and Prof. Giovanni Iannaccone, for giving me the chance to work on the data of ISNet Network, as well as to work in one of the most advanced research groups in Seismology (RISSC-Lab).*

*I would like to thank my supervisor Dr. Antonio Emolo for his availability. Special thanks are given to Prof. Aldo Zollo for fruitful scientific discussions and advices.*

*I am grateful to Dr. Claudio Satriano because I think that I never thanked him enough for believing in me from the beginning. Thanks for helping me in my choices as well as in the early stages of this work.*

*I want to thank all the professors who helped me in the writing of this thesis.*

*I am grateful to Prof. Luis Rivera ("Luigi") for his availability and his teachings, and for making my stay in Strasbourg comfortable as well as fruitful.*

*I thank Daniela Di Bucci for the great help for the geological framework and interpretation of results.*

*I would like to thank all my colleagues of the RISSC-Lab, and in particular Antonella Orefice, Ernestina Lucca, Mauro Caccavale and Giuseppe Pasquale for sharing with me the whole or part of this long experience, Simona Colombelli for a final review of the manuscript, and thanks to Ortensia Amoroso for the 3D velocity model computation.*

*Thanks to all the Ph.D. students and Post Doc of the Strasbourg University (especially to Zacharie Duputel and Marco Calò) for welcoming me as one of them and for not making me feel alone in a foreign country.*

*At last but not least, I wish to express my profound gratitude to my family, my friends and my affections which are all a part of me. Thank you for their advices and encouragement, and for putting up with me all this time.*